CERN-ACC-2015-0144

EuCARD-2
Enhanced European Coordination for Accelerator Research & Development
Scientific Monograph

Vol. 32 - Thermo-Mechnical Studies of Large Hadron Collider Collimators in Accident Scenarios

Cauchi, Marija (University of Malta)

17 September 2015

The EuCARD-2 Enhanced European Coordination for Accelerator Research & Development project is co-funded by the partners and the European Commission under Capacities 7th Framework Programme, Grant Agreement 312453.

This work is part of EuCARD-2 Work Package **1: Management and Communication (MANCOM)**.

CERN-ACC-2015-0144

UNIVERSITY OF MALTA
L-Università ta' Malta

Thermo-Mechanical Studies of Large Hadron Collider Collimators in Accident Scenarios

Marija Cauchi

Department of Mechanical Engineering
Faculty of Engineering
University of Malta

Department of Microelectronics & Nanoelectronics
Faculty of Information & Communications Technology
University of Malta

A dissertation submitted to the University of Malta for the degree of
Doctor of Philosophy

August 2015

The research leading to the results of this thesis has received funding from the European Commission under the FP7 Research Infrastructures projects EuCARD (grant agreement no. 227579) and EuCARD-2 (grant agreement no. 312453). The financial support of CERN and the University of Malta is also acknowledged.

UNIVERSITY OF MALTA
L-Università ta' Malta

CERN

EuCARD

EuCARD²

SEVENTH FRAMEWORK
PROGRAMME

UNIVERSITY OF MALTA
FACULTY OF ENGINEERING

DECLARATION

Student's Code: 22588(G)

Student's Name & Surname: Marija Cauchi

Course: Doctor of Philosophy in Mechanical Engineering

Title of Thesis:

Thermo-Mechanical Studies of Large Hadron Collider Collimators in Accident Scenarios

I hereby declare that I am the legitimate author of this Thesis.

I further confirm that this work is original and unpublished.

Signature of Student

MARIJA CAUCHI
Name of Student

Date

Copyright Notice

No portion of the work referred to in the thesis has been submitted in support of an application for another degree or qualification of this or any other university or other institute of learning.

Signature:

Date:

“Nothing in life is to be feared, it is only to be understood. Now is the time to understand more, so that we may fear less.”

Marie Curie

Abstract

The performance of the Large Hadron Collider (LHC) strongly depends on the correct functionality of the LHC collimation system. With a nominal stored beam energy of 362 MJ and a beam momentum of 7 TeV/c, beam accident scenarios must be studied well to assess if the collimator design is robust against possible error scenarios in operation. One of the serious accident scenarios in the LHC is an asynchronous beam dump. While the primary and secondary collimators are designed to withstand such beam impacts, there may be machine conditions that expose the metal-based tertiary collimators (TCTs) and put them at risk of damage.

A numerical finite element (FE) model is thus developed in this thesis and applied to investigate the thermo-mechanical response of a TCT in novel jaw error cases derived from an asynchronous beam dump accident. The effectiveness of operating with tilted collimator jaws is identified and it is found that a jaw inclination of -1 mrad can mitigate the damage caused by an accidental beam impact on a TCT. The thermo-mechanical response of TCTs to proton and $^{208}\mathrm{Pb}^{82+}$ ion beam impacts is also compared and it is concluded that heavy ion operation in the LHC poses no additional challenges on the structural integrity of TCTs during a beam impact. The developed FE model is complemented by the commissioning of thermal and structural characterisation campaigns of the TCT jaw insert material (INERMET$^{®}$ 180) under varying temperature and strain-rate conditions. Moreover, a dedicated beam experiment at the CERN High Radiation to Materials (HiRadMat) facility has successfully validated the reliability of the developed FE model, thus giving confidence in the prediction of damage by such numerical simulations.

The work presented in this thesis provides a more thorough understanding of the thermo-mechanical behaviour of TCTs during beam impact in accident scenarios. This is achieved by taking into account all relevant collimator damage limits in a detailed study of various relevant scenarios for the operation of the LHC and its risk optimisation.

Acknowledgements

I would like to first and foremost express my special appreciation and thanks to my supervisors Ralph W. Assmann (CERN), Pierluigi Mollicone (University of Malta) and Nicholas Sammut (University of Malta) for their guidance and motivation throughout my PhD. I am also greatly indebted to Alessandro Bertarelli, Federico Carra and Stefano Redaelli for ideas, discussions and advice whenever needed. Special additional thanks goes to Luisella Lari for providing me with input data for my simulations.

I am also very grateful to various present and past colleagues in the LHC collimation and FLUKA teams at CERN. Special thanks goes to Oliver Aberle, Roderik Bruce, Francesco Cerutti, Alessandro Dallocchio, Nicola Mariani, Aurilien Marsili, Adriana Rossi, Belen Salvachua and Daniel Wollman for their help and support. The work of H. Richter and D. Campanini in developing and making available FLUKA-ANSYS® interfaces is also acknowledged.

The contribution and various inputs of Ilias Efthymiopoulos and Adrian Fabich during the planning and logistics phase of the collimator experiment at the HiRadMat facility are greatly appreciated. Acknowledgements go to the support of SPS operators, especially that of Karel Kornelis, in preparing the beams for the HiRadMat experiment. Special thanks also to Alessandro Masi, Jerome Lendaro, Richard Bebb, Chris Theis and Kurt Weiss for their technical support during the setup of the experimental installation and for their help during the post-irradiation analysis of the tested collimator.

I would also like to acknowledge the contributions of Wolfgang Hohenauer from the Energy Department at the Austrian Institute of Technology as well as Martina Scapin and Lorenzo Peroni from the DYNLab at the Politecnico di Torino for the useful discussions and the results provided as part of the commissioned material characterisation tests of the collimator jaw insert material.

I would like to express my thanks to fellow PhD students and friends Nicholas Aquilina, Florian Burkart, Daniel Deboy, Steffen Hillenbrand, Ernesto de Matteis, Daniele Mirarchi, Giuseppe Montenero, Elena Quaranta, Michaela Schuman, Claudia Tombasco, Alan Tua and Gianluca Valentino for making my stay at CERN, away from home, an enjoyable learning experience. A word of mention also goes to my fellow colleagues Redeemer Axisa, Brian Ellul, Robert Farrugia and Paul Refalo for welcoming me in Room 217 at the Department of Mechanical Engineering, Faculty of Engineering, University of Malta and for their help whenever needed.

This PhD is the result of many years of hard work. It has been a difficult yet wonderful experience which has led to a lot of learning and personal development. A special thanks goes to my family. Words cannot express how grateful I am to my parents and my brother Ruben whom I could always rely on during my discouraging moments, and without whose love and continuous solace this work would not have been a success. And last but not least, I would like to express heartfelt gratitude to my fiancé Darren for his great support, patience and understanding, and for unconditionally being there for me ever since the start of this long journey, thank you.

Contents

List of Figures

List of Tables

List of Acronyms

1D 1-Dimensional

2D 2-Dimensional

3D 3-Dimensional

ALICE A Large Ion Collider Experiment

ATLAS A Toroidal LHC Apparatus

BBA Beam-Based Alignment

BC Boundary Condition

BCC Body-Centred Cubic

BCT Beam Current Transformer

BLM Beam Loss Monitor

BPM Beam Position Monitor

C-C Carbon-Carbon Composite

CERN Conseil Européen pour la Recherche Nucléaire

CMS Compact Muon Solenoid

CPU Central Processing Unit

DAQ	Data Acquisition
DOF	Degree of Freedom
DSC	Differential Scanning Calorimetry
E-M	Electro-Magnetic
EMD	Electro-Magnetic Dissociation
EOS	Equation of State
ESU	Equipment Specific Uncertainty
FCC	Face-Centred Cubic
FE	Finite Element
FEA	Finite Element Analysis
FEM	Finite Element Method
Fermilab	Fermi National Accelerator Laboratory
h-A	Hadron-Nucleus
HERA	Hadron-Electron Ring Accelerator
HiRadMat	High Radiation to Materials
IP	Interaction Point
IR	Interaction Region
ITS	Integration Time Step
J-C	Johnson-Cook
LD	Left Downstream

LFA Laser Flash Analysis

LHC Large Hadron Collider

LHCb Large Hadron Collider beauty

LU Left Upstream

LVDT Linear Variable Differential Transducer

MCS Multiple Coulomb Scattering

MKB Diluter Dump Kicker

MKD Ejection Dump Kicker

MPS Machine Protection System

MSD Ejection Dump Septum

NRMSE Normalised Root Mean Square Error

OFE Oxygen-Free Electronic

PET Positron Emission Tomography

PID Proportional-Integral Derivative

PIM Powder Injection Moulding

PS Proton Synchrotron

RD Right Downstream

RF Radio Frequency

RMS Root Mean Square

RU Right Upstream

S-L Steinberg-Lund

SC Superconducting

SPS Super Proton Synchrotron

TCDI Target Collimator Dump Injection Transfer Line

TCDQ Target Collimator Dump Quadruple

TCDS Target Collimator Dump Septum

TCLA Target Collimator Long Absorber

TCLI Target Collimator Long Injection Protection

TCP Target Collimator Primary

TCS Target Collimator Secondary

TCT Target Collimator Tertiary

TDE Dump for Ejected Beam

UHV Ultra-High Vacuum

UTS Ultimate Tensile Strength

WWW World Wide Web

XRD X-Ray Diffraction

Z-A Zerilli-Armstrong

Nomenclature

Nb	Niobium
Ti	Titanium
$\mathcal{L}$	Luminosity
β	Beta function
β^*	Beta star (β calculated at the interaction point)
c	Speed of light
1σ	1 standard deviation
Z	Atomic number
p	Proton
W	Tungsten
Cu	Copper
Ni	Nickel
Fe	Iron
Ag	Silver
σ-ϵ	Stress-strain

σ_{c}	Critical stress
ϵ_{c}	Critical strain
σ	Beam size
σ_{x}	Beam size in the x-direction
σ_{y}	Beam size in the y-direction
T	Temperature
T_{max}	Maximum temperature
T_{ref}	Reference temperature
P_{max}	Maximum power density
τ_{shock}	Thermal shock duration
c_{p}	Specific heat capacity
k	Thermal conductivity
ρ	Density
κ_{cc}	Thermal diffusivity
α	Coefficient of linear thermal expansion
L_0	Original length
ΔL	Change in length
$\Delta L/L_0$	Linear thermal expansion
E	Young's Modulus
ν	Poisson's ratio
σ_{yield}	Yield strength
ϵ_{el}	Elastic strain

ϵ_{pl}	Plastic strain
$\{T\}$	Temperature DOF vector
$\{\dot{T}\}$	Time derivative of the temperature DOF vector
$\{u\}$	Displacement DOF vector
$\{\dot{u}\}$	First time derivative of the displacement DOF vector
$\{\ddot{u}\}$	Second time derivative of the displacement DOF vector
$[C_{\text{thermal}}]$	Thermal specific heat matrix
$[k_{\text{thermal}}]$	Thermal conductivity matrix
$\{Q_{\text{heatgen}}\}$	Heat generation rate nodal load vector
$\{Q_{\text{convection}}\}$	Convection nodal load vector
$\{Q_{\text{flux}}\}$	Heat flux nodal load vector
$[M]$	Mass matrix
$[C]$	Damping matrix
$[K]$	Structural stiffness matrix
$\{F_{\text{thermal}}\}$	Thermal strain nodal load vector
$\{F_{\text{pressure}}\}$	Pressure nodal load vector
$\tau_{\text{diffusion}}$	Characteristic thermal diffusion time
l	Typical dimension along which heat diffusion is computed
t	Time
t_{flex}	First period of flexural oscillation
M	Mass
L	Length

I	Cross-sectional inertia
Δt	Integration time step
L_{mesh}	Typical mesh size in the structural solution
c_{sound}	Speed of sound
θ	Jaw-beam angle
T_{melt}	Melting temperature
X_i	Physical quantity
n	Number of individual measurements
q_i	Arithmetic mean of n individual measurements
$s(q_{i,k})$	Standard deviation of the individual measurements
$u(q_i)$	Uncertainty of arithmetic mean
y	Output estimate
$u_c(y)$	Standard uncertainty of the output estimate
R	Reference measurement
S	Specimen measurement
Lit	Reference data from literature
K_{R}	Correction function
$P(T)$	Temperature-dependent position
B	Base-line measurement
Q	Heat energy
V	Volume
h	Height of samples for thermal diffusivity measurements

$\dot{\epsilon}$	Strain-rate
F	Load
A_0	Original cross-sectional area
σ_{eng}	Engineering stress
ϵ_{eng}	Engineering strain
σ_{true}	True stress
ϵ_{true}	True strain
I	Intensity
I_{equiv}	Equivalent intensity
$\langle\delta_{\text{p}}^2\rangle^{1/2}$	RMS momentum spread
$\frac{dE}{dx}$	Ionisation energy loss gradient
A	Atomic mass

List of Publications

The following publications are the result of the work of this thesis.

Journal Publications

1. **M. Cauchi**, R.W. Assmann, A. Bertarelli, F. Carra, F. Cerutti, L. Lari, P. Mollicone, S. Redaelli, N. Sammut, "Thermomechanical Response of Large Hadron Collider Collimators to Proton and Ion Beam Impacts", *Phys. Rev. ST Accel. Beams*, 18, 041002 (2015).
2. **M. Cauchi**, R.W. Assmann, A. Bertarelli, F. Carra, L. Lari, P. Mollicone, A. Rossi, N. Sammut,"Thermomechanical Assessment of the Effects of a Jaw-beam Angle during Beam Impact on Large Hadron Collider Collimator", *Phys. Rev. ST Accel. Beams*, 18, 021001 (2015).
3. R. Bruce, R. W. Assmann, V. Boccone, C. Bracco, M. Brugger, **M. Cauchi**, F. Cerutti, D. Deboy, A. Ferrari, L. Lari, A. Marsili, A. Mereghetti, D. Mirarchi, E. Quaranta, S. Redaelli, G. Robert-Demolaize, A. Rossi, B. Salvachua, E. Skordis, C. Tambasco, G. Valentino, T. Weiler, V. Vlachoudis, and D. Wollmann,"Simulations and Measurements of Beam Loss Patterns at CERN Large Hadron Collider", *Phys. Rev. ST Accel. Beams*, 17, 081004 (2014).
4. **M. Cauchi**, O. Aberle, R.W. Assmann, A. Bertarelli, F. Carra, K. Cornelis, A. Dallocchio, D. Deboy, L. Lari, P. Mollicone, S. Redaelli, A. Rossi, B. Salvachua, N. Sammut,"High Energy Beam Impact Tests on a LHC Tertiary Collimator at the

CERN High-Radiation to Materials Facility", *Phys. Rev. ST Accel. Beams*, 17, 021004 (2014).

Conference Proceedings

1. **M. Cauchi**, O. Aberle, R.W. Assmann, A. Bertarelli, F. Carra, A. Dallocchio, D. Deboy, L. Lari, P. Mollicone, S. Redaelli, A. Rossi, B. Salvachua, N. Sammut,"High Energy Beam Impact Tests on a LHC Tertiary Collimator at CERN HiRadMat Facility", in *Proceedings of 4th International Particle Accelerator Conference, Shanghai, China*, pp. 954-956, May 2013.
2. **M. Cauchi**, R.W. Assmann, A. Bertarelli, F. Carra, F. Cerutti, L. Lari, P. Mollicone, N. Sammut, "Preliminary Comparison of the Response of LHC Tertiary Collimators to Proton and Ion Beam Impacts", in *Proceedings of 4th International Particle Accelerator Conference, Shanghai, China*, pp. 3412-3414, May 2013.
3. D. Deboy, O. Aberle, R.W. Assmann, F. Carra, **M. Cauchi**, J. Lendaro, A. Masi, S. Redaelli,"Remote Estimation of Collimator Jaw Damages with Sound Measurements during Beam Impacts", in *Proceedings of 4th International Particle Accelerator Conference, Shanghai, China*, pp. 951-953, May 2013.
4. S. Redaelli, R.W. Assmann, G. Bellodi, K. Brodzinski, R. Bruce, F. Burkart, **M. Cauchi**, D. Deboy, B. Dehning, E.B. Holzer, J. Jowett, L. Lari, E. Nebot Del Busto, M. Pojer, A. Priebe, A. Rossi, M. Sapinski, M. Schaumann, R. Schmidt, M. Solfaroli, G. Valentino, R. Versteegen, J. Wenninger, D. Wollmann, M. Zerlauth, "Quench Tests at the Large Hadron Collider with Collimation Losses at 3.5 Z TeV", in *Proceedings of the 52nd ICFA Advanced Beam Dynamics Workshop on High-Intensity and High-Brightness Hadron Beams, Beijing, China*, pp. 157-161, September 2012.
5. **M. Cauchi**, R.W. Assmann, A. Bertarelli, R. Bruce, F. Carra, A. Dallocchio, L. Lari, N. Mariani, P. Mollicone, A. Rossi, N. Sammut,"Preliminary Thermo-Mechanical Analysis of Angular Beam Impact on LHC Collimators", in *Proceedings of 3rd*

International Particle Accelerator Conference, New Orleans, Louisiana, USA, pp. 550-552, May 2012.

6. L. Lari, R.W. Assmann, R. Bruce, **M. Cauchi**, A. Faus-Golfe, A. Rossi,“Improved Robustness of the LHC Collimation System by Operating with a Jaw-Beam Angle”, in *Proceedings of 3rd International Particle Accelerator Conference, New Orleans, Louisiana, USA*, pp. 553-555, May 2012.

7. **M. Cauchi**, R.W. Assmann, A. Bertarelli, R. Bruce, F. Carra, A. Dallocchio, D. Deboy, L. Lari, N. Mariani, P. Mollicone, A. Rossi, N. Sammut,“Preliminary Assessment of Beam Impact Consequences on LHC Collimators”, in *Proceedings of 2nd International Particle Accelerator Conference, San Sebastian, Spain*, pp. 1617-1619, September 2011.

8. G. Bellodi, R.W. Assmann, R. Bruce, **M. Cauchi**, J.M. Jowett, G. Valentino, D. Wollmann, “First Ion Collimation Commissioning Results at the LHC”, in *Proceedings of 2nd International Particle Accelerator Conference, San Sebastian, Spain*, pp. 1813-1815, September 2011.

To Mum & Dad, Ruben and Darren

…for always being there

Chapter 1

Introduction

1.1 CERN and the Large Hadron Collider

1.1.1 General overview

The European Organisation for Nuclear Research (CERN) [1] was one of Europe's first ventures to probe the fundamental structure of the universe by studying the basic constituents of matter. The cutting-edge research taking place at the CERN laboratory is made possible by the presence of some of the world's largest and most complex scientific instruments and technologically advanced facilities.

CERN has been the place of many important particle physics discoveries for which scientists have received prestigious awards throughout the years. The most recent achievement is the Nobel Prize in Physics 2013 awarded to François Englert and Peter W. Higgs for the prediction of the Higgs Boson. The prediction of this fundamental particle was recently confirmed through its discovery at CERN's Large Hadron Collider (LHC) [2]. Moreover, there have also been spin-off discoveries during research in particle physics at CERN, with the most prominent technological applications being the development of the World Wide

Web (WWW), touch screens and positron emission tomography (PET) scanners used in the field of medical imaging [1].

The LHC is regarded as CERN's flagship project as it is CERN's newest and most powerful accelerator [3]. The LHC relies on several older accelerators such as the linear accelerator and booster ring, the Proton Synchrotron (PS) and the Super Proton Synchrotron (SPS) to get its protons up to speed (Figure 1.1). The LHC has four main particle physics experiments to analyse the debris from particle collisions. These experiments are ATLAS (A Toroidal LHC Apparatus) [4], ALICE (A Large Ion Collider Experiment) [5], CMS (Compact Muon Solenoid) [6] and LHCb (Large Hadron Collider beauty) [7], each of which has a different contribution to particle physics knowledge [8].

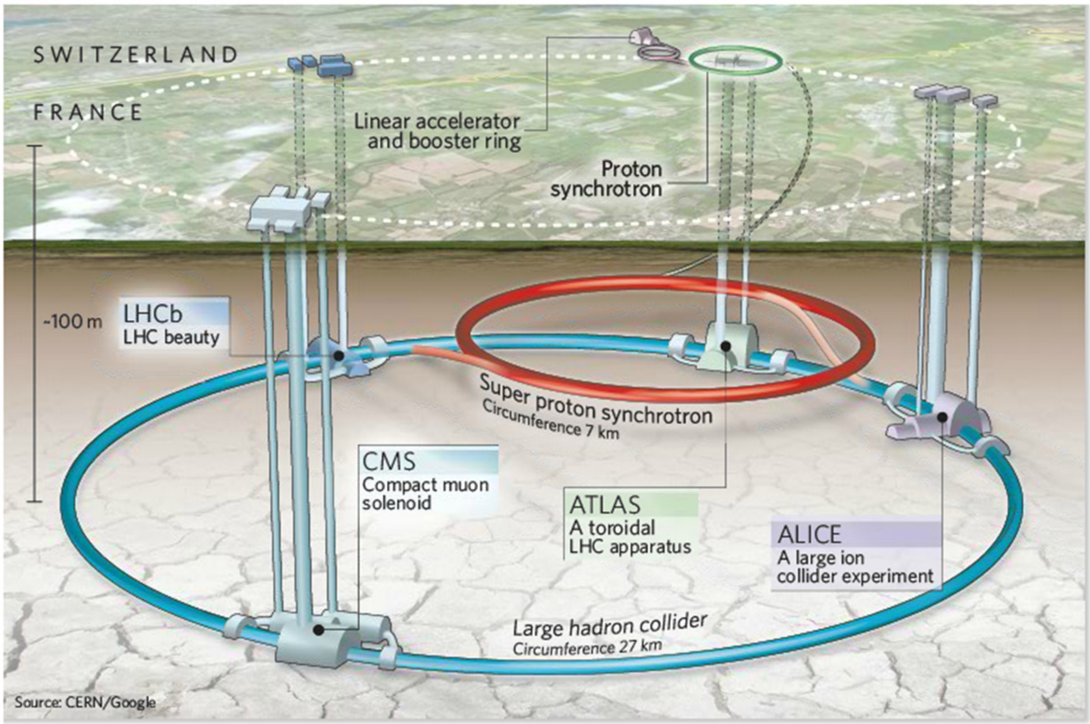

Figure 1.1: The accelerator complex at CERN. Each accelerator boosts the speed of a beam of particles before injecting it into the next accelerator in the sequence. The LHC is the ultimate stage within this complex [8].

The LHC is a circular particle accelerator installed in an underground tunnel with a circumference of 26.659 km (Figure 1.2), in which two beams of subatomic particles - either protons or lead ions - travel in a vacuum chamber, gaining energy with every lap. It is estimated that the protons have to circulate in the LHC for around 20 minutes before reaching the required maximum energy. Inside the accelerator, the two high-energy particle beams travel at close to the speed of light before they are made to collide. The counter-rotating beams travel in separate beam pipes kept at an ultra-high vacuum (UHV) of the order of 10^{-10} to 10^{-11} mbar [9].

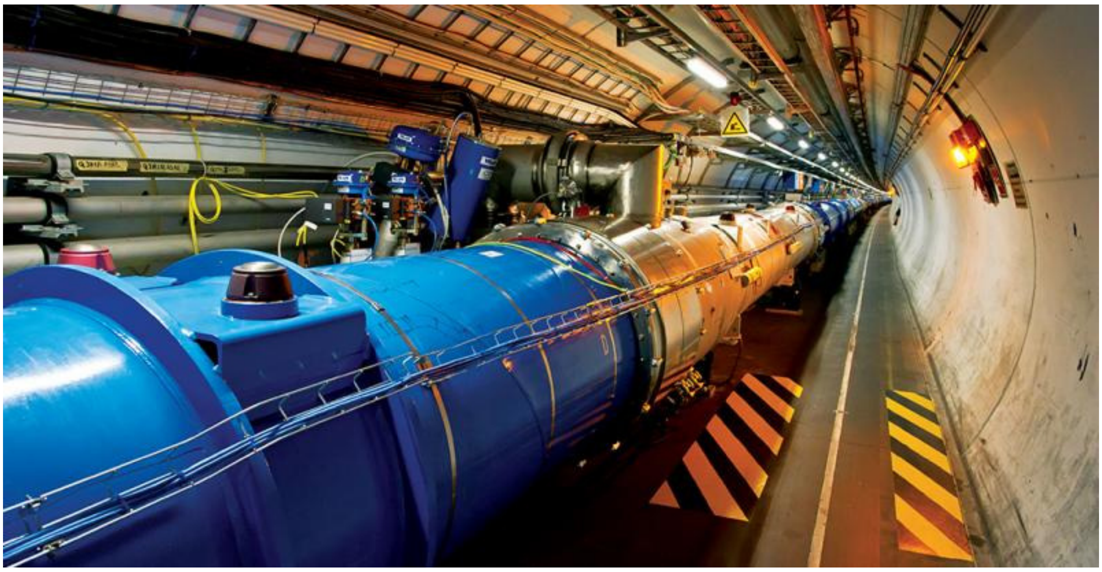

Figure 1.2: The LHC - the world's largest and most powerful particle accelerator. It consists of a 27 km ring of superconducting magnets together with a number of accelerating structures to boost the energy of the particles along the way. The LHC first started up on 10 September 2008 and it remains the latest addition to the CERN's accelerator complex [9].

The LHC consists of eight straight sections, called interaction regions (IRs), and eight arcs (Figure 1.3). Each IR houses either one of the four main experiments dedicated to the LHC (IR1, IR2, IR5, IR8) or other equipment such as the superconducting (SC) accelerating radio frequency (RF) system installed in IR4, the beam extraction system in IR6, and injection devices in IR2 and IR8. IR3 and IR7 are dedicated to the LHC collimation system.

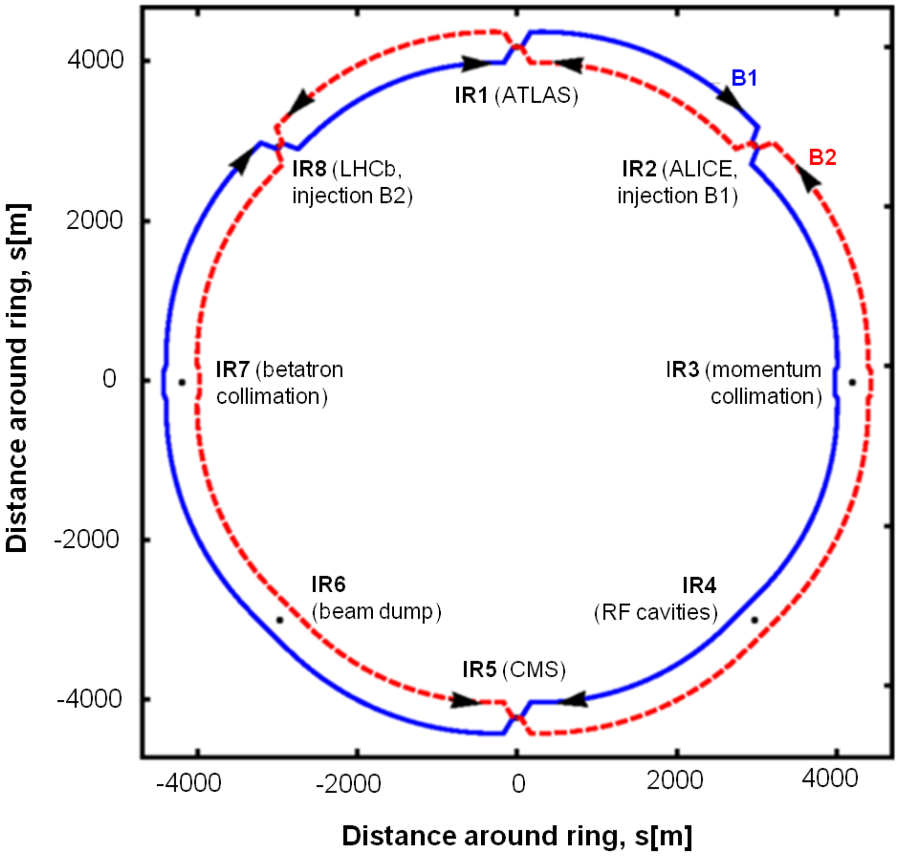

Figure 1.3: Basic schematic layout of the LHC with experimental insertions and utilities (the separation of the two rings is not to scale). Beam 1 (B1) and Beam 2 (B2) circulate in a clockwise and anticlockwise direction respectively, and they collide at the four LHC experiments: ATLAS, ALICE, CMS and LHCb [10].

The particle beams are accelerated through the use of electric fields in SC RF cavities (Figure 1.4) while steering and focusing of the beams are achieved by dipole and quadrupole SC magnets respectively [9]. These electromagnets need to maintain a strong magnetic field of 8.33 T in order to keep the particle beams on course around the LHC's 27 km ring. Large electric currents (approximately 11,850 A) in the magnet coils are consequently needed to create such intense magnetic fields.

The use of SC materials, for instance niobium-titanium (Nb-Ti) for the LHC's magnet coils, has proven to be the best way of having a very high and stable magnetic field to guide the particles around the ring whilst focusing them around the beam core. Superconductivity is not possible without the use of cryogenic systems and thus the Nb-Ti wires of the magnet coils must be kept at low temperatures in order to reach a SC state. This would then allow

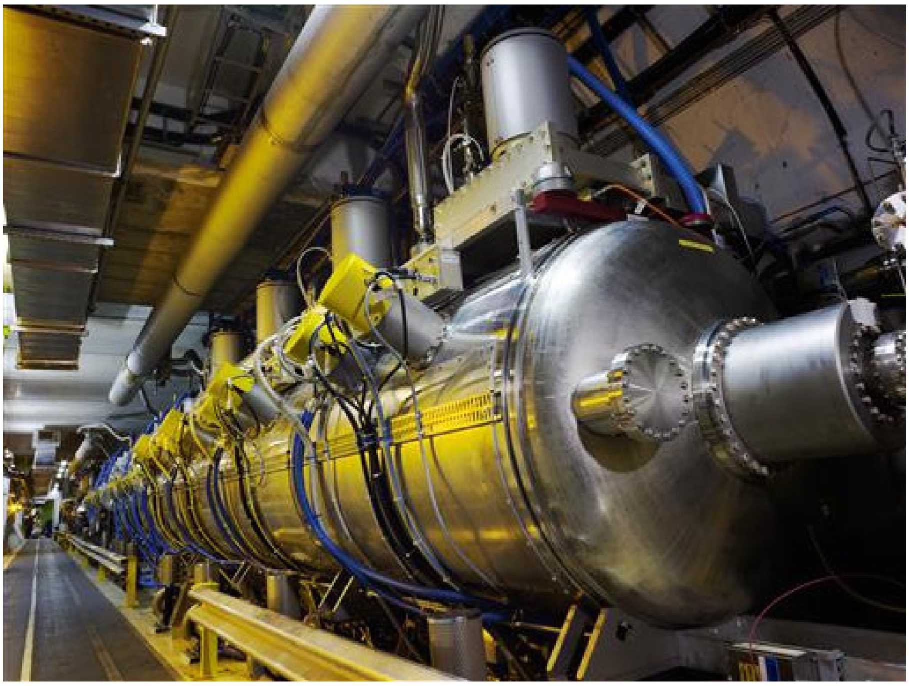

Figure 1.4: Superconducting radio frequency cavities located in IR4. These cavities give the required energy kick to the particles [11].

them to efficiently conduct electricity with negligible electrical resistance or loss of energy. Most of the LHC's SC magnets are therefore required to be maintained at a temperature of 1.9 K (-271.25 °C) which is achieved through the use of a closed liquid-helium system [12].

All the controls for the LHC accelerator, its services and technical infrastructure are managed from the CERN Control Centre. From this centre, the two beams inside the LHC are brought into collision at very high energy at four different locations that represent the main LHC experiments (Figure 1.3). These four locations are known as the interaction points (IPs) [9]. Any particles created in the collisions are then analysed using special detectors [13].

Some important parameters of the LHC - both the operational parameters in 2011 and 2012, and the nominal design values - are summarised in Table 1.1. It can be seen that the design bunch intensity has been surpassed during LHC operation in 2011 and 2012.

Moreover, the achieved luminosity is almost as high as the design value in spite of a lower energy and fewer bunches used during past LHC operation.

Table 1.1: LHC proton running conditions for the collection of physics data during 2011 and 2012 operation, and for nominal design parameters. The peak luminosity ($\mathcal{L}$)[1] and beta-star (β^*)[2] refer to the high luminosity experiments ATLAS and CMS.

Parameter	**2011**	**2012**	**Nominal**
Beam energy [TeV]	3.5	4	7
Number of bunches	1380	1380	2808
Average bunch intensity [10^{11} p]	1.20	1.40	1.15
Peak stored energy [MJ]	112	146	362
Horizontal and vertical β^* [m]	1.50, 1.00	0.60	0.55
Peak luminosity $\mathcal{L}$ [10^{34} cm^{-2}s^{-1}]	0.35	0.77	1.00

Ultimately, each of the two LHC beam pipes is designed to handle a stored beam energy of up to 362 MJ (equivalent to 3.00×10^{14} protons at 7 TeV) such that the LHC can achieve centre-of-mass collision energies of up to 14 TeV. The design stored energy of the LHC beams is at least two orders of magnitude larger than in previous hadron machines with SC magnets such as the Tevatron[3] and the HERA[4] [14]. Comparing transverse energy densities in Figure 1.5, it can be observed that the LHC advances the state-of-the-art by even three orders of magnitude, from 1 MJ/mm^2 to 1 GJ/mm^2 [15], thus making the LHC beams highly destructive.

---

[1] The luminosity $\mathcal{L}$ is a measure of the rate of the number of particle collisions that can be produced in a detector per cm^2.

[2] The betatron (β) function is an optical amplitude function that describes the transverse oscillations in a particle's motion. Of particular significance is the value of the β function calculated at the collision point, known as β^*. A smaller β^* is essential to achieve a higher peak luminosity.

[3] The Tevatron is a circular particle accelerator at Fermilab (Fermi National Accelerator Laboratory) in the United States.

[4] The HERA is a hadron-electron ring accelerator at the German Electron Synchrotron - DESY.

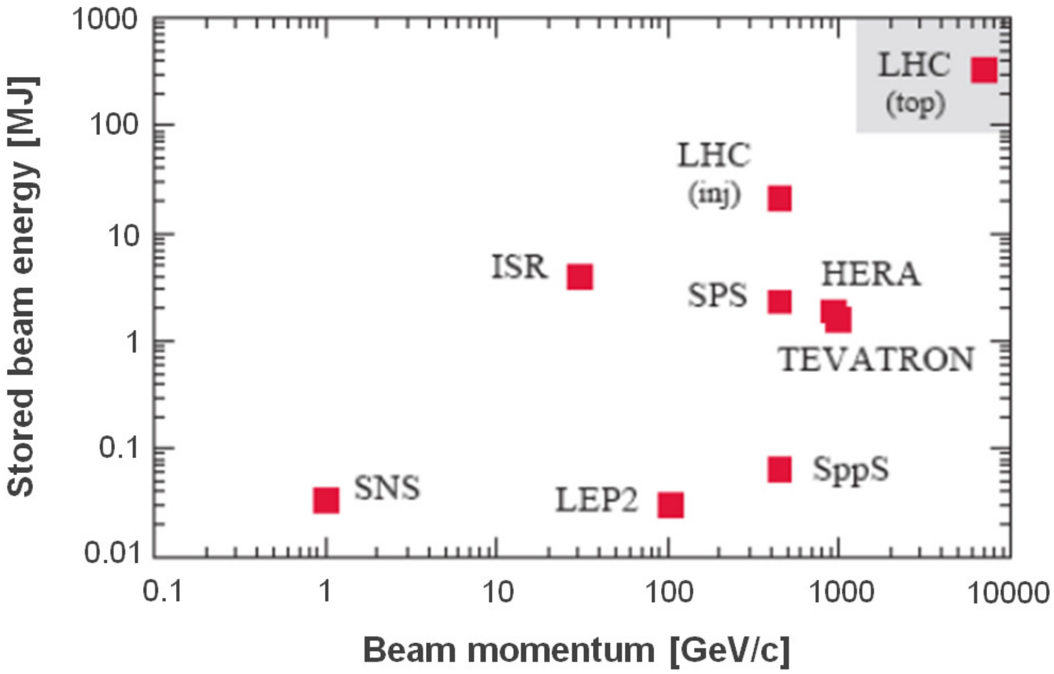

Figure 1.5: Stored beam energy versus beam momentum in different proton colliders [15].

The design LHC beam consists of 2808 bunches with a nominal bunch intensity of 1.15×10^{11} protons. Nominally, the core of each high-energy bunch has a cross-section that can be described by a 2-dimensional (2D) Gaussian distribution (Figure 1.6). The nominal bunch spacing for the LHC is 25 ns, while the bunch duration is 1 ns as calculated from the root mean square (RMS) value of the bunch length (4σ length for Gaussian distributions) [3].

It is unavoidable that beam losses occur during collider operation. In fact, as the bunches rotate within the LHC ring, processes such as the long-range beam-beam effect [16], intra-beam scattering [17, 18] and noise on the RF and orbit feedback systems, cause a slow diffusion of particles out of the beam core. Particles at the edges of the spatial distribution then tend to escape from the proper trajectory and consequently form a beam halo. Lost beam halo and particle interactions at the experiments make the beam lifetime finite [19]. Moreover, more rapid beam losses can occur during changes of the LHC machine configuration in the operational cycle or through beam instabilities.

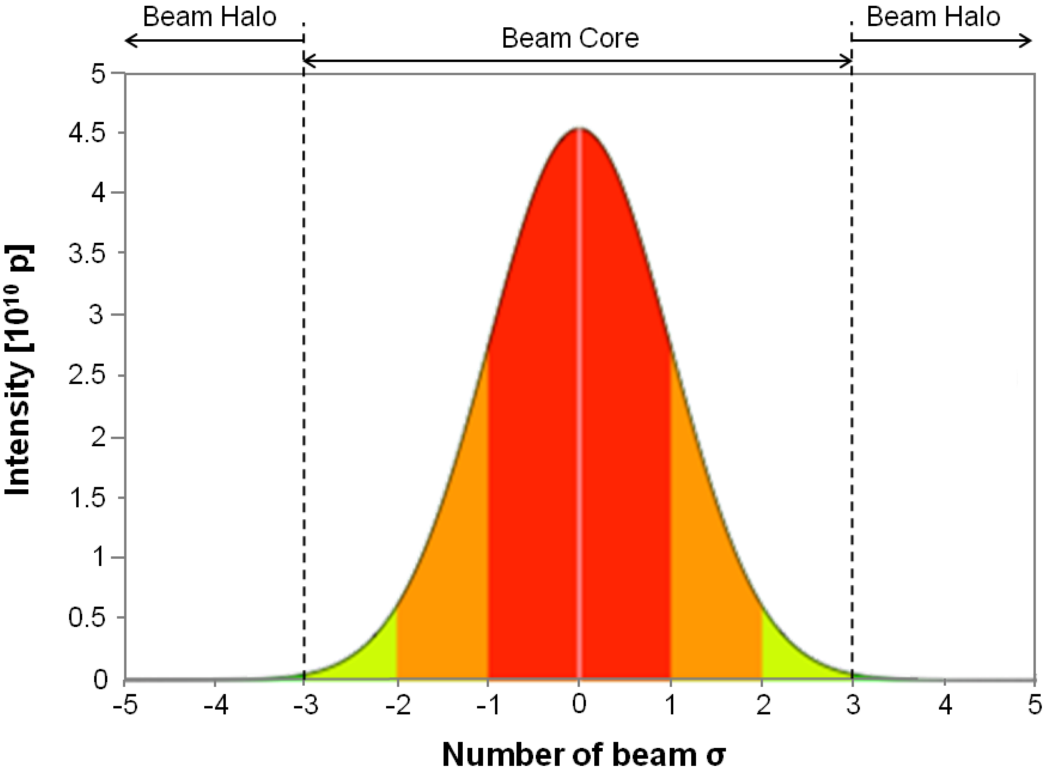

Figure 1.6: The Gaussian distribution in the transverse plane of a high-energy particle beam made up of 1 nominal bunch (1.15×10^{11} p). The beam core and halo regions are shown. One standard deviation (1σ) of the Gaussian beam comprises approximately 68% of all particles. The beam core is usually defined as 0 - 3σ (99.7% of all particles) while the region $> 3\sigma$ surrounding the dense beam core represents the beam halo.

As already mentioned, one of the LHC operational requirements is that the SC magnets must be kept at cryogenic temperatures in order to benefit from their SC state. Although beam losses cannot be completely suppressed, they must be reduced as much as possible and sensitive equipment, particularly the SC magnets, must be protected. This is because such events can have consequential problems such as beam-induced quenches[5] of the SC magnets [20] or even destruction of parts of the accelerator.

---

[5] A magnet quench represents a transition of the magnet from a SC to a normal-conducting state. This will result in very high resistances and unstable magnetic fields.

To prevent beam-induced magnet quenches and other damage, the LHC has a system of about 4000 beam loss monitors (BLMs) installed around the ring. These BLMs detect losses during operation [21, 22] and trigger a beam dump if the losses exceed pre-determined safety thresholds. As shown in Figure 1.7, BLMs are mounted on the outside of the cryostat of all quadrupoles in the LHC as well as on all collimators and other elements that have been identified as potentially critical.

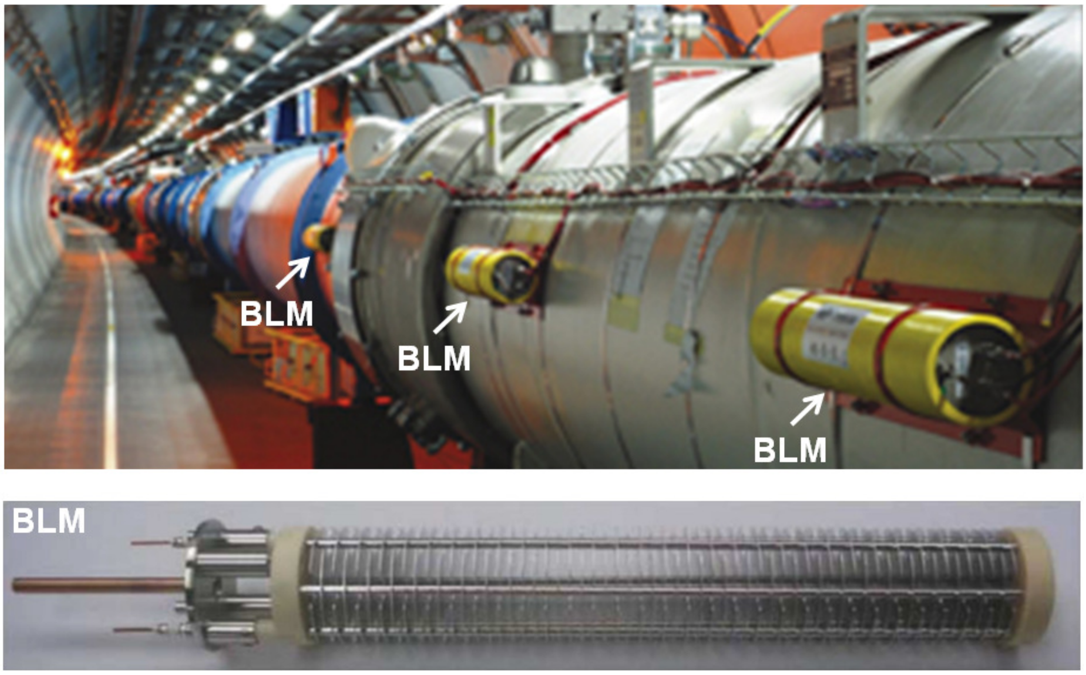

Figure 1.7: BLM detectors in the LHC. BLMs (yellow insulation, mounted on a red support) installed on the outside of the cryostat of an LHC quadrupole magnet and horizontally aligned to the beam pipe (top), and a BLM ionisation chamber without its casing showing its inside structure (bottom). The radiation dose on the BLMs over 20 years of LHC operation is estimated at 2 × 10^8 Gy in the collimation sections and 2 × 10^4 Gy at the other locations [23, 24].

The BLMs are ionisation chambers that are 50 cm long and filled with nitrogen. The lost beam particles initiate hadronic showers through the magnets and other machine components. Since the BLMs are mounted on the outside of the accelerator equipment, they intercept and measure only secondary shower particles [23]. A beam dump is triggered when a BLM detects a loss above a certain threshold and the beam is extracted before the magnetic field is significantly altered by a developing quench. The dump thresholds have been determined from the quench levels of the SC magnets and from Monte Carlo simulations of the ratio between temperature rise in the coils and energy deposition in the BLM gas volume [20, 25, 26].

As a matter of fact, the SC magnets in the LHC would quench if small amounts of energy, induced by a local transient beam loss of a 10^{-9} fraction of the full beam at 7 TeV (amounting to an order of 10^6 protons), are deposited into the SC magnet coils [20]. When losses occur in a SC magnet, the coils are heated by the induced hadronic and electro-magnetic (E-M) showers, and a temperature rise of around 2 K can cause a quench in the magnets operating at 1.9 K. Beam-induced quenches and other equipment damage are to be avoided during collider operation since they might lead to LHC machine downtime, which in turn compromises the time available for collecting physics data.

Thus, these issues established the need for the development of a powerful collimation mechanism [27] in order to ensure stable running conditions which are not interrupted by quenches or damaging events. The continuously repopulated beam halo has to be safely removed by the LHC collimation system in order to protect the accelerator against unavoidable regular and irregular beam losses, as well as to ensure the proper functionality of the LHC.

1.1.2 The LHC collimation system

The LHC collimation system is the largest and most advanced installation of this kind ever built. This system has been installed in the LHC in order to tightly control all beam losses by ensuring beam halo cleaning and machine protection [27]. The cleaning efficiency of the collimation system is defined as the ratio of the highest loss in the collimators to the highest loss in the cold regions (where the SC magnets are located) of the LHC [28]. The LHC collimation system must ensure efficient ($> 99\%$ in all conditions) cleaning of the beam halo during the full LHC beam cycle [29]. This is crucial for handling the high-intensity LHC beams and for enabling the LHC to reach its full potential during regular operation, especially in terms of luminosity performance [30, 31].

During the first LHC run in 2009-2013 (called Run 1), the LHC collimation system has been very successful in protecting the cold magnets. No beam-induced quenches have occurred during physics operation with colliding beams in spite of more than 100 MJ being routinely stored over many hours. The stored energy of the two counter-rotating beams can be seen in Figure 1.8 for all physics fills[6] in 2011 and 2012.

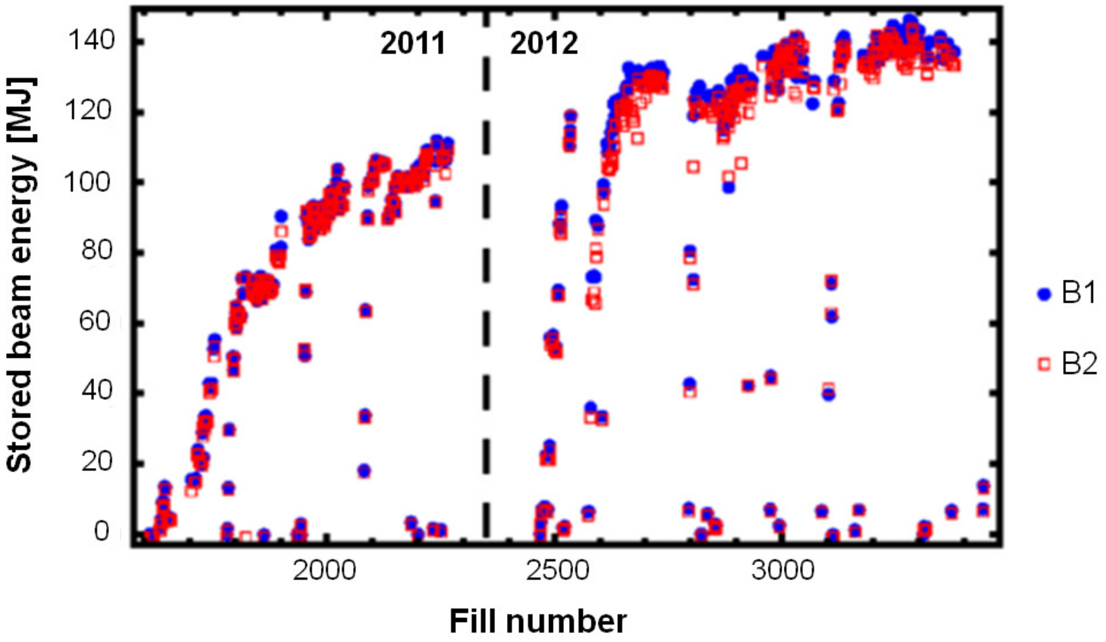

Figure 1.8: Stored beam energy for Beam 1 (B1) and Beam 2 (B2) at the beginning of each LHC physics fill in 2011 and 2012 with proton collisions. The operational energy was 3.5 TeV in 2011 and 4 TeV in 2012. At the beginning of each year, a gradual ramp-up in intensity was performed for machine protection reasons [10].

---

[6] A physics fill refers to the period between injection and dump when the LHC is running in good stable and controlled conditions for collecting physics data.

The LHC collimation system consists of several collimators placed all around the LHC ring (Figure 1.9) . Collimators can be installed in vertical (90°), horizontal (0°) and skew (45°, 135°) configurations in order to maximise cleaning efficiency all around the particle beam axis (Figure 1.10). In this way, the collimation system keeps the highly energetic beam under control by ensuring that any unavoidable occurring particle losses stay at a safe level.

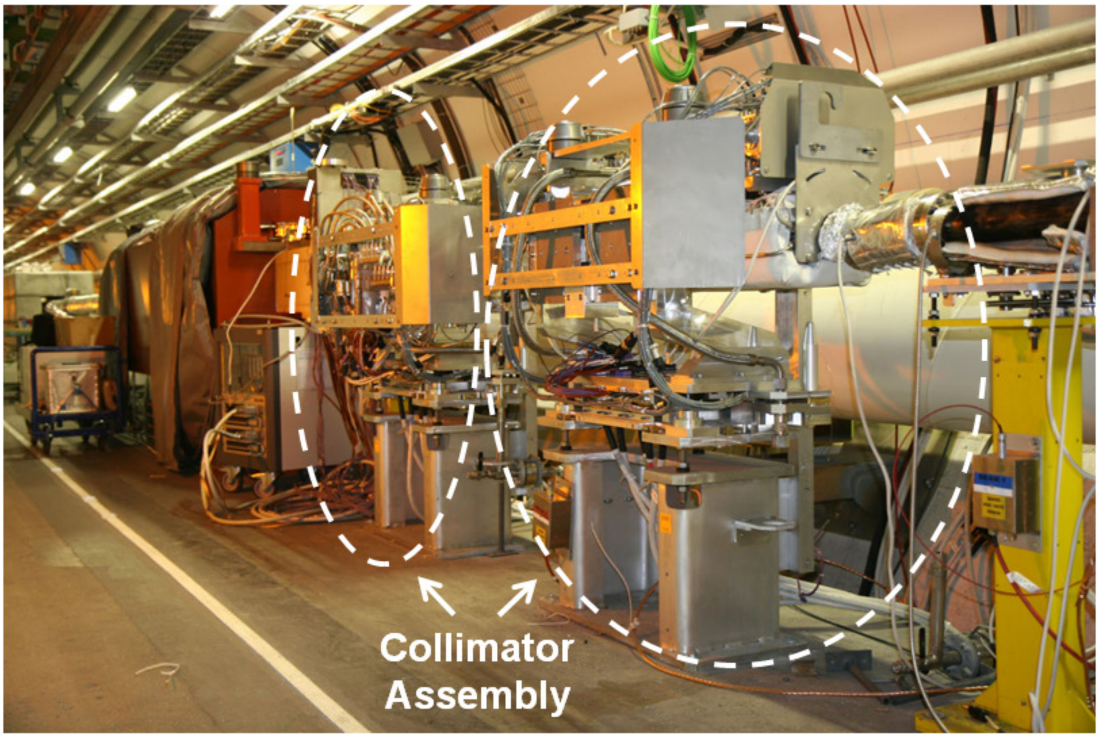

Figure 1.9: Photograph of two installed ring collimator assemblies in the LHC [32].

The LHC requires collimation during all stages of operation to protect its elements, unlike previous colliders, such as the Tevatron, where the main purpose of collimation was to reduce experimental background. In the LHC, the collimation system forms an important part of the machine protection system (MPS). The collimation system used for the LHC Run 1 is shown in Figure 1.11. It consists of 108 collimators and absorbers, of which 100 are movable collimators installed in seven out of eight LHC IRs as well as in the transfer lines [15].

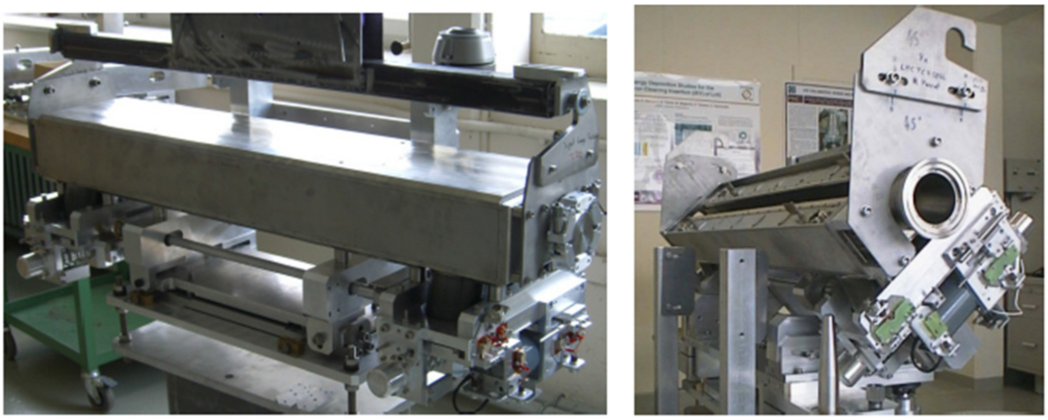

Figure 1.10: Photograph of a horizontal (left) and a skew (right) LHC collimator. The latter has the vacuum tank open to show the two movable jaws [32].

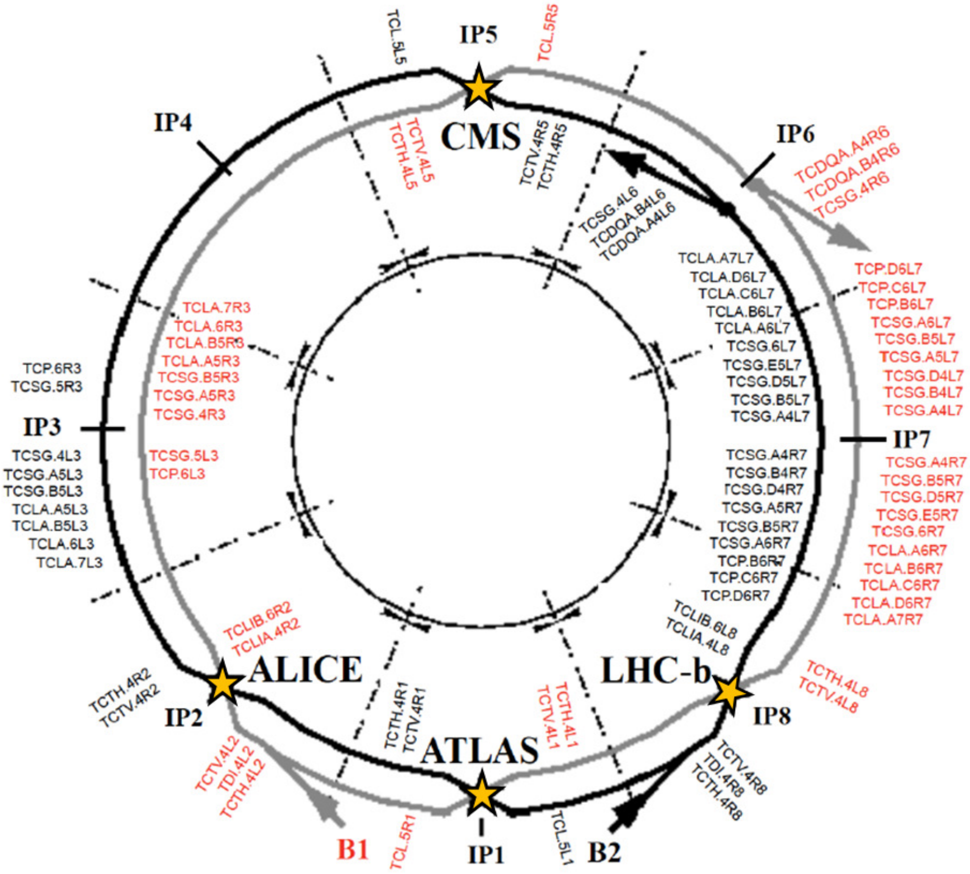

Figure 1.11: Sketch of the LHC collimator layout used during Run 1. Collimators are installed on both beam lines all around the LHC ring. They are located mainly in IR3 and IR7 where they ensure momentum and betatron cleaning of the particles respectively. Collimators also protect the four experiments (ATLAS, ALICE, CMS and LHCb), the beam dump (IR6), and the transfer line regions. Collimators for Beam 1 (red) and Beam 2 (black) are distinguished (adapted from [29]).

The LHC collimation system implements a multi-staged beam cleaning process (Figure 1.12) in order to efficiently remove particles that would otherwise be lost in the machine. The halo collimation is achieved by several stages, with the primary collimators (TCPs) being closest to the beam, followed by the secondary collimators (TCSs) and the so-called active absorbers (TCLAs) that are set at larger apertures.

A three-staged system of this kind is installed in dedicated warm insertions, both in IR3 and IR7. The IR3 and IR7 collimators have different functions and are used for off-momentum and betatron cleaning respectively. While the system in IR3 is built to intercept losses only in the horizontal plane (off-momentum protons), the larger system in IR7 has a good coverage of the whole transverse space. For optimal performance, the beam halo particles should first hit a TCP, and the other collimators should then only intercept halo particles that have already been scattered in, and escaped out from, upstream collimators.

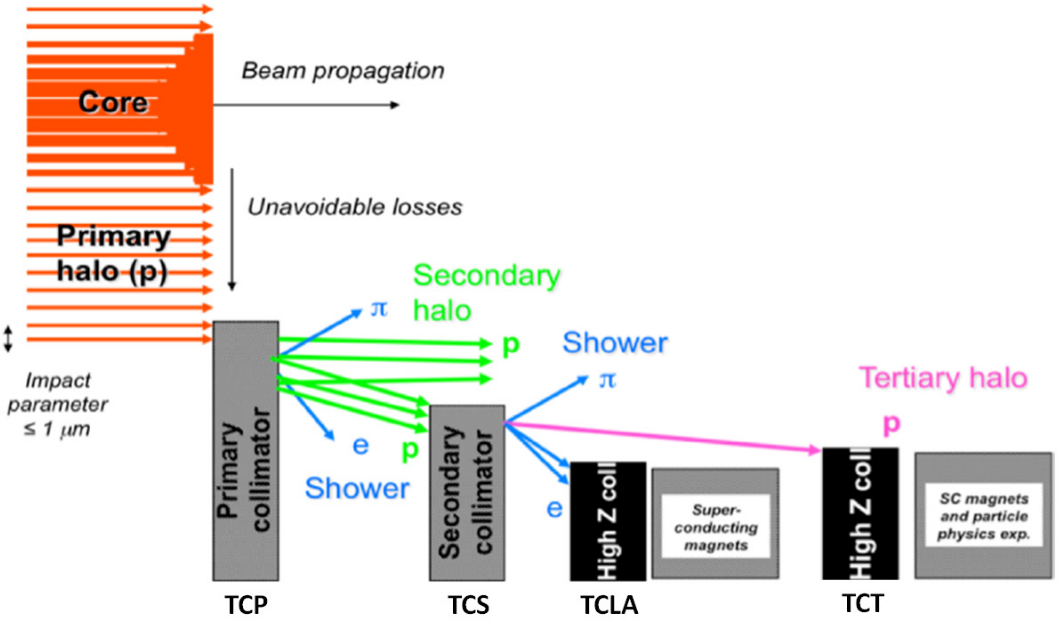

Figure 1.12: Qualitative schematic diagram of the LHC multi-staged collimation system. It can be observed that the beam halo particles diminish from left to right, i.e. from TCP to TCS to TCLA/TCT, as the collimators serve their function in intercepting and stopping particles of the external beam halo (adapted from [33]).

Before high-intensity beams are allowed in the LHC machine, the cleaning performance of the collimation system is qualified. This is done by provoking beam losses with a safe low-intensity beam and observing the resulting loss pattern on the BLMs around the ring [34–36]. Such beam losses can be created by two methods, which are either by driving the beam onto the third order resonance or else by using a white-noise excitation from the transverse damper. The losses are then plotted as a function of the s-coordinate around the ring in the form of a loss map (Figure 1.13). Both methods produce similar loss maps [37].

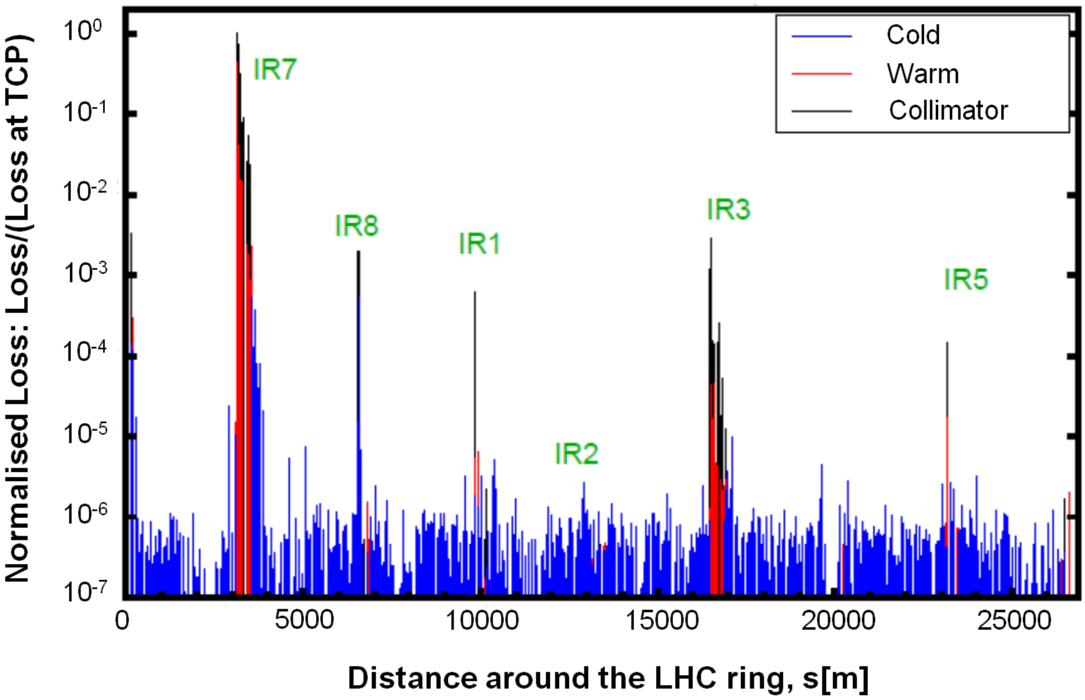

Figure 1.13: An example of a beam loss distribution map around the LHC measured with the BLMs using a 1.3 s integration time. This is taken from a qualification loss map of the betatron collimation system performed on 11 March 2011. The correct hierarchy of the collimation system should be regularly qualified in order to ensure that the highest loss is always located at the TCP, followed by the TCS and then the TCLA/TCT [10].

The TCP and TCS collimators have been designed to withstand beam losses of 90 kW (corresponding to 1 hour beam lifetime at design conditions) and 10-second bursts of losses up to 450 kW. Being closest to the beam, the TCPs and TCSs intercept large beam losses and are thus made of a carbon-carbon composite (C-C) whose high melting temperature and low energy absorption (3% for 1 m) make such collimators robust against beam damage. This is however achieved at the expense of lower collimation efficiency and higher impedance. The TCLAs are then meant to catch both scattered primary beam and shower debris from upstream collimators. TCLAs are high-Z collimators where Z represents the atomic number of the collimator material; they are in fact made of a tungsten heavy alloy to adequately stop the incoming energy. However, they are not as robust as C-C collimators and thus they should never intercept primary beam losses. To protect the TCLAs, the collimator hierarchy must be guaranteed as the TCLAs would suffer damage if hit by one or several high-energy and high-intensity proton bunches.

In addition to these dedicated collimation insertions (IR3 and IR7), there are also collimators in all other IRs, except IR4 which houses the SC accelerating RF cavities and feedback systems. In particular, there are the tertiary collimators (TCTs), built with the same design and materials as the TCLAs, and installed about 150 m upstream of the collision points at all experiments. The TCTs are meant to intercept the tertiary halo close to the particle physics experiments and the sensitive triplet magnets. They provide local protection of the quadrupole triplets in the final focusing system and are also essential for decreasing the experimental background [38].

Other special collimators around the ring intercept debris originating from beam-beam collisions at the experiments. There are also dump protection collimators (TCDQs) installed at the beam extraction in IR6 to serve as protection against mis-kicked beams in case of extraction failures. Similarly, there are injection protection collimators (TCLIs) installed in IR2 and IR8, and transfer line collimators (TCDIs) in the transfer lines between the SPS and the LHC [27].

As shown in Figure 1.12, collimators are strategically positioned to provide passive protection for other critical structures such as the downstream SC magnets [39]. Most of the beam is expected to be safely disposed of by the beam dump system in IR6. However, if the mis-injected or mis-dumped beams make it past the IR3 and IR7 collimators, they can reach the experiments. In such an event, the TCTs are the last line of defence for the triplet quadrupoles and the particle physics experiments.

The design of the LHC collimation system has been a complex task as there is no single collimator solution that fulfils all the design goals for LHC collimation. Hence, the effort to design, develop, optimise and operate the powerful LHC collimation mechanism is crucial. This design must take into account all relevant requirements concerning robustness, performance, fabrication, installation, maintenance, machine protection and beam operation [32]. Design work on an appropriate collimation system has, in fact, continuously evolved over the years since 1990 [15, 40, 41], thus reflecting both the difficulties involved to meet the LHC requirements as well as the challenge of advancing the state-of-the-art beam cleaning and collimation into a new regime.

1.2 Project description and objectives

The operation of the LHC in terms of reliability and achieved luminosity strongly depends on the performance and correct functionality of the LHC collimation system [42]. The requirements to handle the high-intensity beams circulating in the LHC can be demanding. In the field of high-energy physics, studying the thermal and mechanical response of structures subjected to rapid internal heating is of paramount importance as short duration impacts induced by high-energy particle beams on structures occur frequently in modern accelerators.

Being the closest elements to the proton beam, the collimator jaws are continuously exposed to direct interaction with high-energy particles. The variations in thermal load due to particle loss on the collimator jaws are described by a time constant, which can range from seconds to hours in the case of nominal operation. On the other hand, the relevant time scale for energy deposition during a beam accident scenario is on the order of nanoseconds or microseconds. This very fast energy deposition provokes a thermo-dynamic response of the collimator structure in which the robustness of the collimators plays an important role. As the material of the collimator jaw cannot respond to the rapid increase in temperature [43] caused by the hadronic shower, structural deformations can occur [44]. This study investigates collimator damage under such conditions.

One of the serious beam accident scenarios identified in the LHC corresponds to an asynchronous trigger of the beam dumping system [45]. In an asynchronous beam dump, one or more high energy density bunches might directly impact a collimator, possibly with serious consequences [46]. While the carbon collimators (TCDQs, TCPs and TCSs) are designed to withstand full bunch beam impacts without permanent damage, this is not the case for metal-based collimators like the TCTs in the experimental regions that protect the SC triplet magnets [47]. Even though the machine configurations [48] are chosen to minimise this risk in a way that it can only occur in case several combined failures occur at the same time [49], it is important to understand the implications of such an event on a TCT as it may lead to serious limitations of the overall LHC performance. The results are thus an important input in the risk assessment for possible operation scenarios of the LHC.

The materials involved in high-energy and high-intensity beam impacts operate under extreme conditions, in which the possibility to perform experimental tests is limited. For this reason, it is evidently very important to develop reliable methods and accurate computational models that can be efficiently applied to estimate the damage occurring during an accidental beam impact.

In this perspective, a numerical finite element method (FEM) approach is developed and presented in this thesis. Sequential, fast-transient, thermo-structural analyses are performed in the elastic-plastic domain in order to evaluate the thermo-mechanical response of TCTs to beam impact as a consequence of an asynchronous beam dump accident. This thesis presents several novel case studies representing different realistic beam impact scenarios. A number of FEM simulations are carried out by varying beam energy and impact conditions, thereby allowing the identification of different damage levels for the TCT. Such case studies include:

- The evaluation of the effectiveness, from a collimator damage point of view, of operating with tilted collimator jaws in case of a direct impact of one high-intensity LHC bunch on a TCT
- The evaluation and comparison of the thermo-mechanical response of a TCT in case of critical beam load cases involving proton and heavy ion beam impacts

In order to achieve these goals and implement a reliable FEM approach, the above-mentioned analyses need to be complemented by:

- A dedicated beam experiment set up at the CERN High Radiation to Materials (HiRadMat) facility in order to obtain a thorough integral assessment of beam accident scenarios involving a complete TCT and to benchmark numerical simulations
- Material characterisation tests in order to obtain a full thermo-physical and structural characterisation of the TCT jaw insert material (INERMET® 180) in order to be able to correctly reproduce the material behaviour in the FEM simulations

As a conclusion, an analysis of the thermal and structural response of TCTs to rapid energy deposition resulting from an asynchronous beam dump accident is presented, from which the most critical and interesting cases are then identified. Such work will thus help to achieve a more reliable understanding of the thermo-mechanical behaviour of TCTs in accident scenarios and will give an initial insight on the operational constraints of the LHC by taking into account all relevant collimator damage limits.

1.3 Structure of the thesis

This thesis is structured as follows. An introduction to CERN and the LHC is provided in Chapter 1. The LHC design parameters and the consequences of abnormal beam losses are discussed, accompanied by an overview of the beam loss monitoring system in the LHC.

In this perspective, the LHC collimation system is introduced as a powerful mechanism that protects the accelerator against unavoidable beam losses, thus ensuring the proper functionality of the LHC. The design of the collimation system with a multi-staged beam cleaning approach and a brief description of its qualification are explained. The goal of this thesis is set to investigate the thermo-mechanical effects provoked by high-energy particle beams during different novel impact scenarios on TCTs. This is defined together with the motivation for this work and the expected project objectives.

The mechanical design of the collimation system poses a serious challenge. This is expanded upon in detail in Chapter 2 by presenting the main features and characteristics in the mechanical design of collimators, with a special emphasis on TCTs. The different thermal load conditions on the collimator jaw inserts and the resulting modes of damage are also discussed, with a focus on accidental beam loss scenarios. It is shown that various detailed studies have been carried out over the years to evaluate the damage in metal structures subjected to high energy deposition. An overview of the work presented in this thesis in relation to such studies is then given at the end of Chapter 2.

Chapter 2 serves as a useful introduction to better understand the numerical approach adopted in this study to achieve the objectives of this thesis. The numerical FEM method described in Chapter 3 has found an important application in the study of LHC collimators. An explanation of the simulation chain used is given, starting from Monte Carlo based simulations and followed by FEM thermo-mechanical studies.

Chapter 4 starts off with a detailed description of the asynchronous beam dump accident scenario considered in this thesis. This is followed by thermo-mechanical studies of a TCT in novel jaw error cases with the aim of analysing the effectiveness of operating with tilted collimator jaws in case of a direct impact of an LHC bunch on a TCT. The results for the transient thermal analyses as well as for the dynamic and quasi-static structural analyses are presented and discussed.

Material characterisation tests of the TCT jaw insert material (INERMET® 180) have been commissioned in order to be able to implement a more reliable material model in the

FEM simulations. The methodologies and results of the thermo-physical and structural material characterisation campaigns, which are performed at different temperature and strain-rate conditions, are presented in Chapter 5.

Chapter 6 describes a dedicated beam experiment set up at the CERN HiRadMat facility in order to complement and benchmark the advanced numerical simulations of beam accident scenarios involving a complete TCT. The experimental setup and the installation layout are first presented. This is followed by a summary of the tests performed and the main beam test results, including outcomes from visual inspection. A comparison of these experimental results with numerical simulations is discussed, together with other experimental outcomes.

Chapter 7 deals with the comparison between proton and heavy ion beam impacts on TCTs. A concise overview of the physical interaction processes occurring when both particle types traverse the collimator material is initially given. Using the new material characterisation measurements of INERMET® 180 as described in Chapter 5, the thermo-mechanical response of TCTs to critical beam load cases is fully evaluated and compared in case of both proton and heavy ion beam impacts.

A summary of the work achievements and the main contributions of this study to the development of the research field are finally presented in Chapter 8. This chapter also provides concluding remarks and suggestions for future work.

Chapter 2

The LHC Collimation System

2.1 Introduction

As described in Chapter 1, various types of collimators are installed in the LHC in order to ensure the multi-staged beam cleaning process of the collimation system. The mechanical design and layout of the collimation jaw assembly depend on the collimator's function and thus vary for primary (TCP), secondary (TCS) and tertiary (TCT) collimators. Since this study deals particularly with horizontal TCTs, this chapter will focus on the mechanical design of such collimators.

A detailed description of the mechanical design of TCTs, together with the potential damage mechanisms as a result of rapid energy deposition during an accident scenario, are presented. This is followed by a short discussion of the various studies that have already been performed to evaluate the damage in metal structures subjected to high energy deposition by particle beams. An overview of the state-of-the-art contribution of the work presented in this thesis in relation to the development of the research field is finally given.

2.2 Mechanical design of LHC collimators

2.2.1 General layout and design

The present LHC collimator design is the result of the analysis of a wide range of options and alternatives [50]. Each LHC collimator (Figure 2.1) is made up of a support table on which the vacuum tank and the actuation mechanism are pre-aligned and positioned using a plug-in system. This plug-in external alignment system allows a quick and simple positioning of the collimator assembly in the LHC machine.

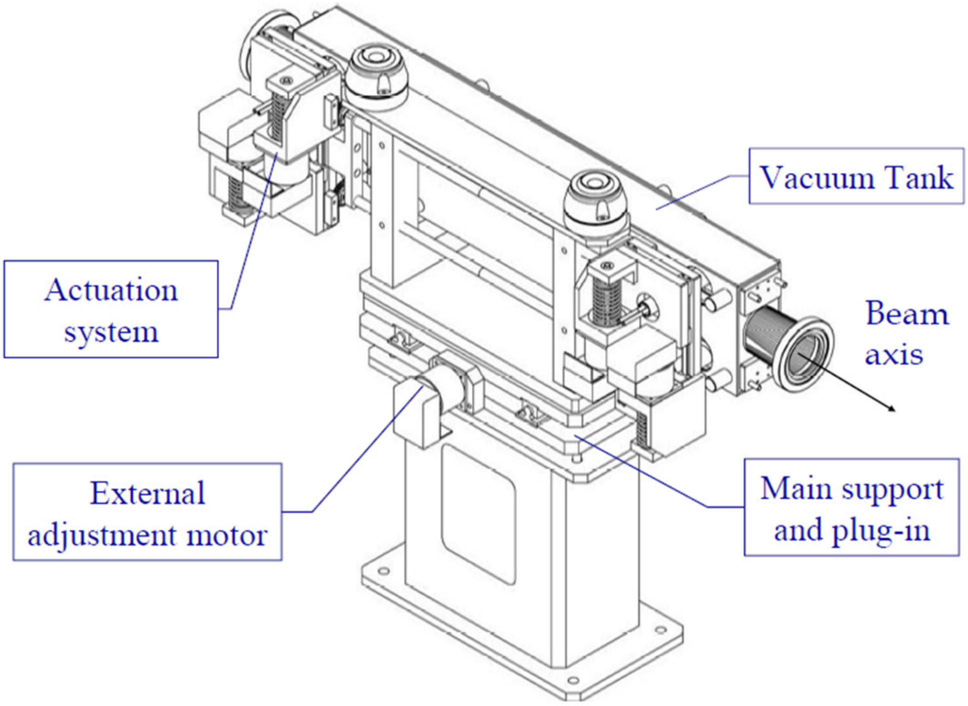

Figure 2.1: 3D CAD assembly of a full LHC collimator (vertical configuration) on its support (adapted from [27]).

The vacuum tank is of a traditional structural design. It is manufactured in AISI 316L stainless steel and is mainly electron-beam welded. The rotation of the vacuum tank is used to define a horizontal, vertical or skew collimator configuration. The tank is supported by brackets, whose design depends upon the collimator orientation. A stepper motor allows transverse displacements of the whole collimator tank by 10 mm, giving the possibility to expose a new jaw surface in case of a beam impact where the initial impact area is damaged. The particle beam enters/exits longitudinally into/out of the vacuum tank through the connections at the extremities, as illustrated in Figures 2.1 and 2.2 [27].

Inside the vacuum tank, there are two collimation jaw assemblies that are considered the core of the system as they are the components that interact directly with the particle beams (Figure 2.2) [27]. The flat top length[1] of the jaws is always 1.0 m, except for TCPs (0.6 m) and TCDIs (1.2 m). The flange-to-flange length of a collimator is 1.48 m [30]. Each jaw is cooled by the water of the general cooling circuit of LHC Sectors 3 and 7 [51].

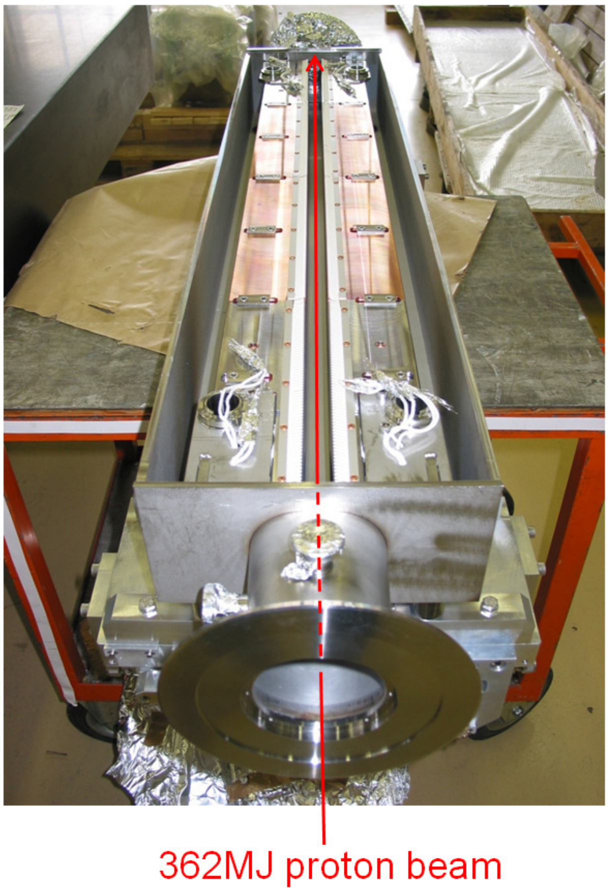

Figure 2.2: Plan view into the open vacuum tank of an LHC collimator during production. The collimator is exhibited in a horizontal configuration since the two collimation jaw assemblies are located on the left and right sides of the beam within the vacuum tank (adapted from [32]).

---

[1] The flat top length of the collimator jaw is the total jaw length excluding the tapering at the upstream and downstream parts of the jaw.

The collimator jaws are the components closest to the LHC beam, separated from one another by a gap as small as 2 - 3 mm at 7 TeV (Figure 2.3) [39]. The LHC collimators not only need to be very robust but also quite long (because of the high-energy protons) and very precise (because of the small collimation gaps) at the same time. The small minimum gap size and the small beam size at the collimators imply tight mechanical tolerances [27]. Other important collimator specifications can be found in [30].

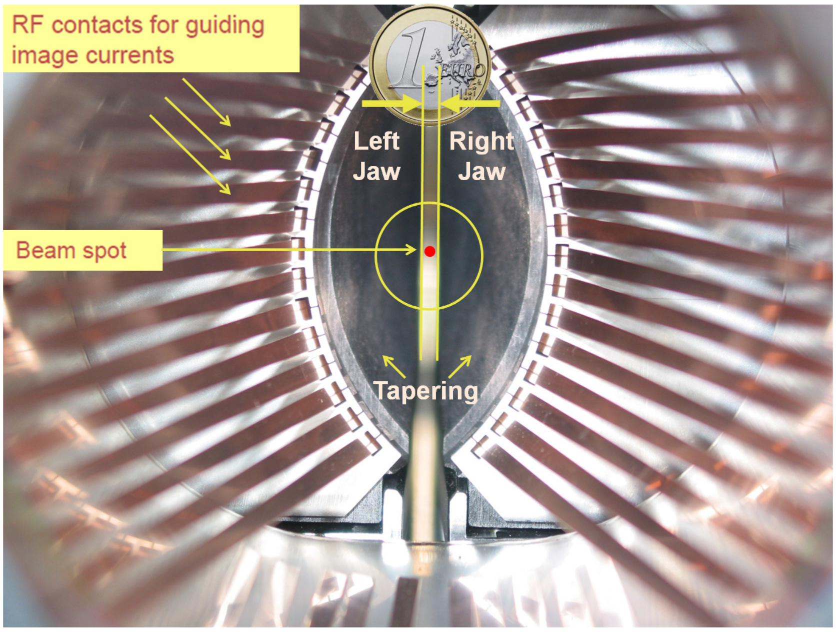

Figure 2.3: View along the beam path in a horizontal collimator. A typical LHC gap size at 7 TeV is shown. At nominal conditions, the machine aperture is equivalent to the size of the Iberian Peninsula on a 1€ coin. Beam image currents are guided by the RF fingers that are visible at the tank entry. The tapering at the upstream part of the collimator jaws is also indicated (adapted from [30, 52].)

An internal alignment system comprises two independent stepper motors per jaw (Figure 2.4). These motors allow both the lateral displacement (with a nominal stroke of 30 mm plus 5 mm of extra stroke beyond the beam axis) and the angular adjustment of the water-cooled parallel jaws with respect to the beam [27]. Switches limit the stroke of the jaw movement to the valid range, including limits on the jaw gap through anti-collision switches [33]. Moreover, excessive tilt of the jaw is prevented by a rack and pinion system [51]. Each motor directly drives a table via a roller screw/nut set, which allows the precise positioning of the jaw supporting axle. Each table is mounted on anti-friction linear guide-ways. The support shafts, located at each end of the vacuum tank, are passed through flexible vacuum bellows that deform with jaw movements and guarantee vacuum tightness [33].

Another technical feature of the LHC collimator design is a precise actuation system that is pre-loaded by return springs to make it play-free. The return springs also ensure a semi-automatic mechanical return of the jaw in case of motor failure [51]. Furthermore, a misalignment prevention device assures the alignment of the jaws with a high precision. This is crucial for beam-based alignment (BBA) procedures as the jaws must have the ability to be remotely moved with good precision. Reproducibility of the collimator settings is also vital in order to avoid lengthy re-optimisation procedures [27]. Figure 2.4 shows in more detail how the jaw assemblies are supported at the extremities by two shafts that transmit the movement given by the actuation system.

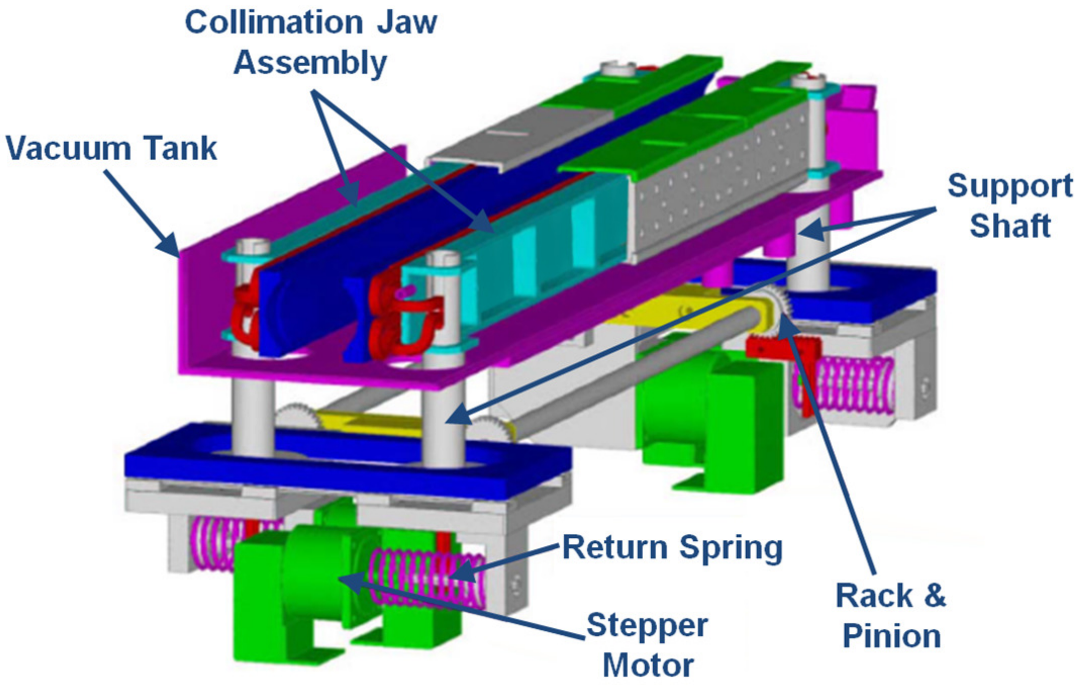

Figure 2.4: An LHC collimator (horizontal configuration). The jaw assemblies, enclosed in the vacuum tank, are supported at the extremities by two shafts that transmit the movement given by the actuation system (adapted from [27]).

Collimator settings are crucial for the safety of the LHC accelerator, the experiments and the collimation system itself. A full control system [53] is thus in place to ensure that beam dumps are triggered through the LHC beam interlock system in case of measurements of jaw positions, collimator gaps or temperature that go beyond specified safe limit functions, or in case of detection of abnormal beam load conditions. The collimators are thus equipped with sophisticated instrumentation (Figure 2.5) that provides extensive diagnostics information [27], including:

- Position of each motor and jaw support point
- Independent measurements of the collimator gap at both extremities of the collimator tank (average gap and angle between the two jaws)
- Independent measurements of one jaw position at both extremities of the collimator tank
- Temperature of each collimator jaw at both of its extremities
- Temperature of the cooling water at inlet and outlet
- Signals from various switches (in, out, anti-collision)
- Microphone signals from sensors installed close to the TCPs in the LHC tunnel
- Flow of cooling water per collimator

Separate control paths and hardware controls are used to drive the stepping motors and to independently monitor the actual movements of the collimator jaws with high precision sensors [54]. The position control is guaranteed by motor encoders and position sensors, known as linear variable differential transducers (LVDTs), that are mounted on each collimator. These sensors measure the position of the four jaw extremities in each tank, and the upstream and downstream gaps defined by the jaws. Temperature sensors monitor the temperature of the collimator jaws by means of cables passed through the tank with vacuum feed-throughs, while microphones are used to detect any shock waves induced by beam hits [55]. In addition, an efficient collimator control system requires the knowledge of beam parameters such as beam position, beam size and beam divergence at each collimator.

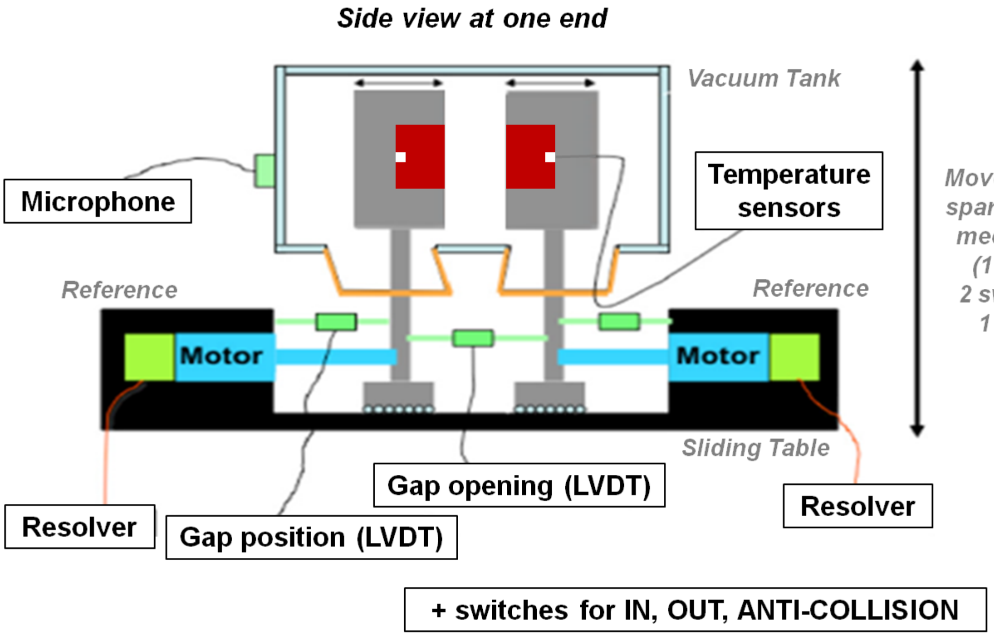

Figure 2.5: Illustration of the mechanical concept for a horizontal LHC collimator. It can be observed that the LHC collimator design has the unique feature of allowing the measurements of the collimation gap seen by the beam from outside of the beam vacuum (adapted from [33]).

These are obtained through links to other measurement devices such as BLMs, beam current transformers (BCTs) and beam position monitors (BPMs) [33, 53].

Additionally, the LHC beam pipe is an UHV system and the collimators must not disturb the vacuum performance. For this reason, the outgassing rates of the collimator jaws are optimised by an in-situ high temperature bake-out process at 300 °C prior to installation in the LHC [27]. Moreover, vacuum studies [56, 57] have been performed to show that the chosen collimator jaw design and materials are compatible with the LHC UHV requirements.

It can be concluded that the LHC collimators must act as high precision devices [33]. Their mechanical design is thus a very challenging aspect in order to ensure that collimators can withstand the demanding requirements of the high-intensity LHC beams [27].

2.2.2 Collimation jaw assembly

The collimation jaw assembly of a horizontal TCT will now be presented in more detail. The mechanical design of the jaw assembly is deemed very important because it is the basis of the thermo-mechanical analyses that will be presented in the following chapters.

Like most collimators, the TCT (Figure 2.6) consists of two parallel symmetrical jaws contained in a vacuum tank, with the beam passing through the centre of the jaw gap. For optimal performance, the jaws have to be centred around the actual orbit through a BBA procedure [58]. Each TCT jaw (Figure 2.7) has a total length of 1.2 m (1 m active length + 0.1 m tapering at the upstream and downstream parts of the jaw). A detailed view of the layout of a TCT jaw assembly is shown in Figure 2.8.

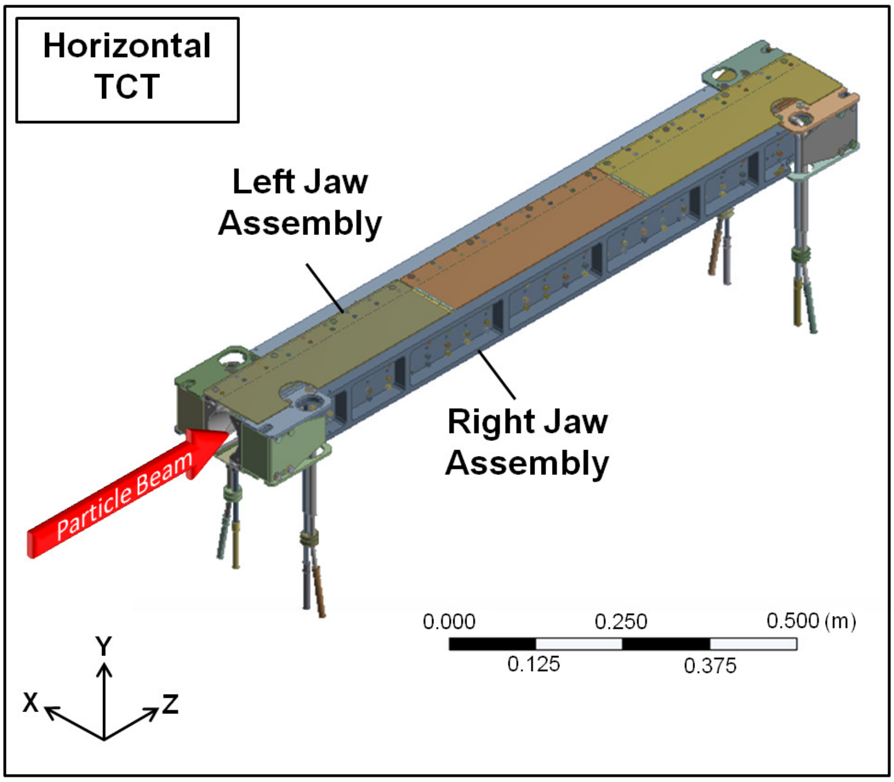

Figure 2.6: A 3D model of a horizontal TCT in ANSYS® DesignModeler.

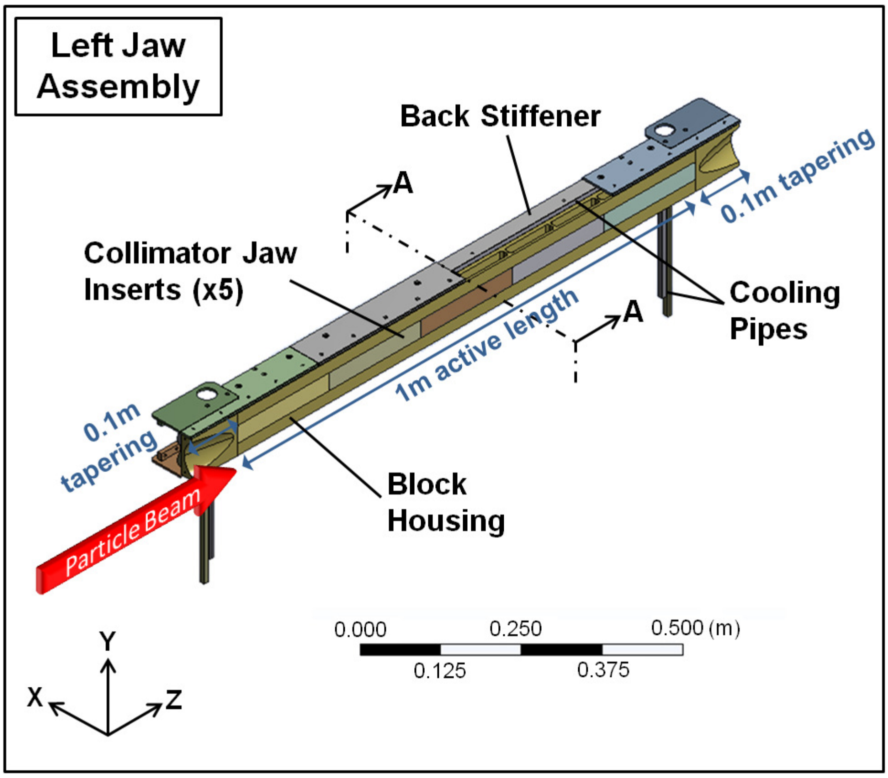

Figure 2.7: A 3D model of the left jaw assembly (as seen by the incoming beam) of a horizontal TCT in ANSYS® DesignModeler.

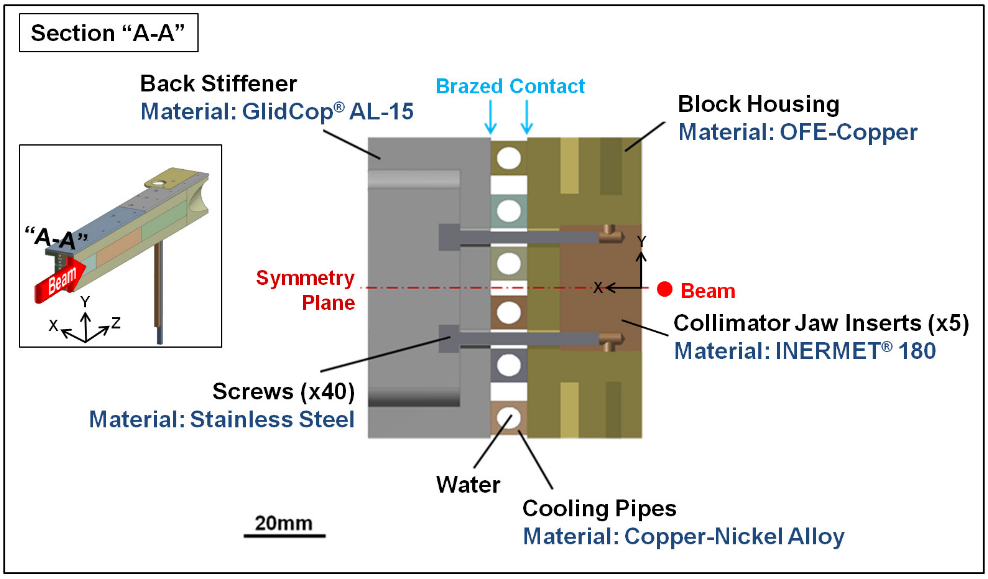

Figure 2.8: Detailed cross-section (Section A-A from Figure 2.7) in the x-y plane of the TCT left jaw assembly. The orientation of the left jaw assembly with respect to the beam is shown in the inset.

As can be observed from Figures 2.7 and 2.8, the jaw assembly is a multi-component system consisting of the following parts:

- **Collimator Jaw Inserts**: The collimator jaw inserts are the components that have direct interaction with the high-energy particle beams and are thus continuously subject to thermal loads due to particle losses on the jaw. There are five collimator jaw inserts per jaw, each having a rectangular cross-section of 20 mm × 34 mm and a length of 200 mm. In the case of TCTs, these collimator jaw inserts are made of a tungsten heavy alloy with the commercial name of INERMET® 180 [59]. These five blocks are then placed into a copper housing and fixed with stainless steel screws to the jaw assembly.

- **Block Housing**: The block housing serves to give the required structural support to the collimator jaw assembly. It has a C-shaped cross-section with a sequence of ribs disposed over the length. The tapering at the ends of the block housing (Figure 2.7), together with the RF fingers (Figure 2.3) [60], have the function to allow for a smooth geometrical transition from the flat jaws to the round flanges and the beam pipe. Such a transition minimises impedance and consequently reduces beam energy loss, local heating and coupled bunch instabilities [61]. The block housing is made of oxygen-free electronic copper (OFE-Cu) and it is brazed to the cooling pipes.

- **Cooling Circuit**: The cooling circuit acts as a heat exchanger and is essential for the evacuation of the heat deposited on the jaw inserts. It consists of two pipes per jaw, brazed on one side to the block housing and on the other to the back stiffener, and one additional pipe for the collimator tank. The inlet water temperature is 27 °C. Each pipe is made of a Cu-Ni alloy and has three turns to increase the heat exchange capability. The water cooling pipes have an internal circular cross-section with a diameter of 6 mm and an external square shape in order to ease the brazing and avoid harmful air traps.

The design water flow rate is 5 l/min per pipe, leading to a total flow rate of 25 l/min per collimator and a design flow velocity of approximately 3 m/s. The flow velocity is in fact rather high and might lead to erosion-corrosion problems on the soft copper pipe bends. However, such a flow velocity is necessary both to ensure the evacuation of the anticipated high heat loads as well as to minimise temperature gradients and to limit thermally induced deformations. The flow rate can be adjusted for each collimator by specific flow-fix valves [27].

- **Back Stiffener**: The back stiffener is the component that keeps together all the elements making up the jaw assembly. It is made of an alumina dispersion strengthened copper with the commercial name of GlidCop® AL-15.

The screwed tungsten-copper and the brazed copper-copper interfaces play a critical role in the cooling process since they present a higher resistance to heat flow compared to the components themselves. To avoid excessive deformations of the jaw and to ensure the correct functioning of the collimator, the thermal conductance at these interfaces must be high.

The block housing, the cooling pipes and the back stiffener are brazed together with a silver alloy, thus creating a single body. It is expected that the thermal conductance value may vary across different interface sections. This is because of imperfections of the brazed contact, possibly due to small variations in the brazing process or different flatness tolerances of the contact interfaces.

On the other hand, silver-coated stainless steel (A4-100) screws are used to establish a good contact pressure between the jaw inserts and the copper block housing. Due to the difference in thermal expansion coefficients between the tungsten heavy alloy and OFE-Cu, such a design allows for relative slipping between the two surfaces [51]. Moreover, the reason for having five jaw inserts is to limit the effects of the thermal expansion that would otherwise result in large thermal deformations in case of one long jaw insert.

In a screwed contact, the thermal conductance is a function of the pressure at the contact interface and should be such that it ensures proper heat conduction between the two surfaces. An appropriate thermal conductance value permits the heat deposited by the beam on the collimator jaw inserts to be efficiently removed by the cooling system, limiting the jaw temperature in operation and the thermally induced deformations. Screwed contacts bring new challenges when compared to brazed contacts such as the fact that the thermal contact depends on the screw pre-load, and on the risk of stress relaxations at the interfaces, especially during the high temperature bake-out cycles.

2.2.3 Collimator materials

As already explained in Section 2.2.2, the components of the jaw assembly are composed of different materials. This sub-section briefly discusses the thermo-physical and mechanical properties of these materials, giving also a motivation for their choice in the collimation jaw assembly [62]:

- **INERMET® 180**: Being the most important components of the whole collimation assembly, the material of the collimator jaw inserts will be discussed in more detail in Chapter 5. The composition of INERMET® 180 is 95 wt.% W - 3.5 wt.% Ni - 1.5 wt.% Cu. Tungsten is the main component of the alloy and is the reason for its overall high density (18,000 kg/m^3). The brittle tungsten grains are held together by a copper-nickel alloy that serves as a binder matrix, giving the alloy its ductility and machinability. In particular, INERMET® 180 has been chosen as the material for the collimator jaw inserts due to its good resistance to high temperature thermal shocks and its low coefficient of thermal expansion, both of which ensure a high geometric stability [59].

- **OFE-Copper**: This type of material generally refers to a group of wrought high conductivity copper alloys that have been electrolytically refined in order to reduce the level of oxygen to a practically negligible value. In fact, OFE-Cu is considered a 99.99% pure copper material with 0.0005% oxygen content, thus guaranteeing the good inherent properties of elemental copper. Such properties include high ductility, high electrical and thermal conductivity, high impact strength, ease of welding/brazing/soldering and low relative volatility under high vacuum. Moreover, OFE-Cu is essential to prevent oxidation when the metal heats up during the brazing process, resulting in a stronger and more durable joint.

- **Copper-Nickel Alloy**: A copper-nickel alloy with a composition of 90 wt.% Cu - 10 wt.% Ni has been chosen for the cooling pipes due to its good resistance to the corrosion provoked by the cooling water, thereby maintaining a good thermal conductivity.

- **Alumina Dispersion Strengthened Copper**: This material, having the commercial name of GlidCop® AL-15, is widely used for high temperature applications. Dispersion strengthening is the mechanism of strengthening metals, in this case copper, by adding dispersed second phase material, such as alumina. The thermal and electrical conductivities of GlidCop® AL-15 are similar to those of copper; however, it has a higher yield strength. A very important characteristic of such a material is that it does not undergo thermal softening and it retains its good mechanical properties even at high temperatures. This is considered critical as the collimator jaw assembly must be submitted to a bake-out process at a high temperature before being installed in the tank in order to respect the constraints imposed by the UHV requirements.

- **Stainless Steel**: The conventional choice of stainless steel for the screw material is due to the fact that the screws are not exposed to the highest thermal loads within the collimator structure and thus thermal conductivity does not play a very important role in this case.

2.2.4 Thermal loads on collimators

The proximity of the collimator jaw inserts to the high-energy LHC beam implies that the inserts are continuously exposed to intense thermal loads in different working conditions. The resulting particle beam losses define different load cases for the LHC collimation system. The type of load condition then influences the approach adopted to obtain the solution of the thermo-mechanical problem involved [27].

In design working conditions, a steady-state thermal load is deposited on the collimator jaws as the latter continuously interact with particles belonging to the external beam halo. A second load case foresees that, starting from a nominal steady-state condition, an increase of the beam loss takes place as a consequence of an error in the control of beam dynamics. From a thermo-mechanical point of view, the second load case implies that, starting from a nominal proton loss condition (approximately 90 kW corresponding to 1 hour beam lifetime at design conditions), the energy deposition increases by a factor of 5 up to 450 kW over a transient period of 10 s, after which the nominal condition will be recovered [27].

However, the load case that will be studied in this thesis is one that arises from an accident scenario and thus, abnormal beam loss processes must be taken into account. In these cases, particle beam impacts occur on the collimator jaws, resulting in very fast energy deposition and consequently provoking a thermo-mechanical dynamic response of the structure. Figure 2.9 summarises the power deposition profiles as a function of time for the different thermal loads on the collimators that have just been explained.

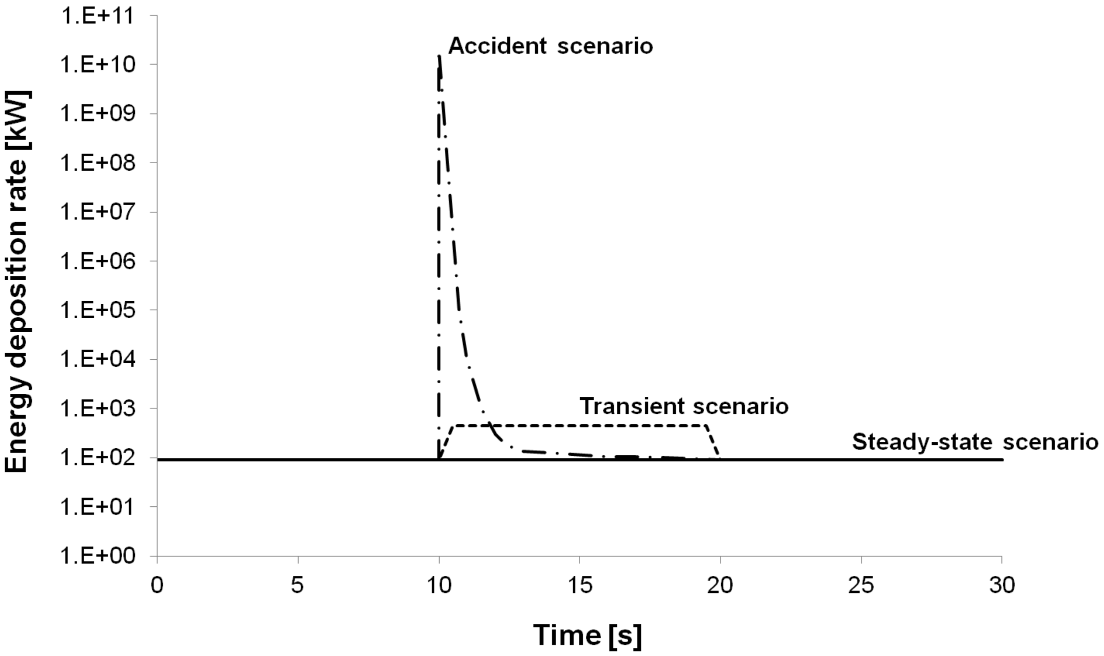

Figure 2.9: Logarithmic power deposition as a function of time for steady-state, slow transient and fast transient (i.e. accident scenario) thermal loads.

2.2.5 Functional requirements

The design of the LHC collimators must comply with the very demanding specifications [39] resulting from the high-energy beam handled in the LHC. The main design requirements are the following:

- **Temperature**: The temperature increase on the collimator jaws should not exceed the limit of 50 °C in nominal steady-state conditions.
- **Geometric Stability**: The deflection of the collimator jaws due to thermal loads must not exceed the limit of 40 μm over a length of 1.2 m of the whole jaw assembly in nominal steady-state conditions.
- **Robustness**: High robustness in case of accident scenarios is also required as collimators must survive particle beam impacts keeping their correct functionality.

2.3 Effects due to rapid energy deposition

2.3.1 Beam-matter physical interactions

Beam-matter interaction processes take place whenever particles strike a surface. Physical interactions between particle beams and solids entail several complex phenomena in the domain of particle physics. Particle cascades with a large spectrum of energies are normally produced and the FLUKA code [63, 64] is able to accurately simulate each of these processes through its embedded models. The effects of such phenomena vary from the heating of components to the perturbation of electronics and displacement damage [65]. A short review of the passage of charged particles through matter can be found in [66].

When a high-energy proton hits a material block, all or part of its energy is dissipated through different processes. It could interact with a nucleus and produce many secondary particles, which later also interact until the residual energy per particle becomes negligible. Such processes are important both in terms of the local heat deposition inside the material as well as the resulting secondary scattering processes that occur. In fact, the final energy deposition in the material is, to a large extent, due to the E-M shower[2] which is developed together with the hadronic shower[3] initiated by nuclear inelastic reactions [67]. These are combined with various other physical processes, all of which release kinetic energy to the lattice of the hit structure.

Ultimately, almost all the deposited energy is converted to heat, resulting in the development of intense thermal loads within the collimator jaws in various working conditions. The energy deposited in matter then leads to a temperature increase that is greatly influenced by the particle shower developed within the jaw as well as by the properties of the jaw material [43].

---

[2] E-M showers are produced by a particle that interacts primarily or exclusively via the E-M force, usually a photon or electron.

[3] Hadronic showers are produced by hadrons (i.e. nucleons and other particles made of quarks) and proceed mostly via the strong nuclear force.

Figure 2.10 shows the traces produced by a 6 GeV proton in liquid argon. Different kinds of processes can be observed including hadron-nucleus (h-A) interactions, E-M showers, decay of unstable nuclei, multiple elastic and inelastic scatterings of impinging particles, ionisation (dE/dx and δ)[4] and low energy neutron interactions.

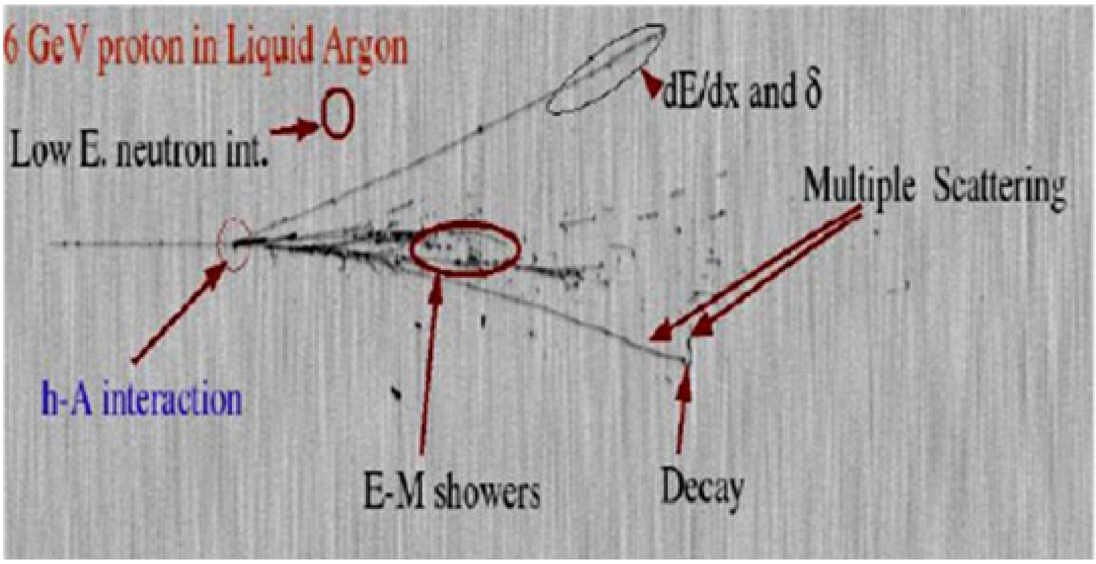

Figure 2.10: Traces of a 6 GeV proton in liquid argon. The different physical processes initiated by a hadron-nucleus (h-A) interaction are indicated [52].

2.3.2 Thermal and structural effects

The absorption of intense high-energy proton bursts with a duration of several microseconds causes a considerable temperature increase of the same rise-time inside the intercepting material. During this short period, thermal expansion of the irradiated material is partly prevented, thus provoking dynamic structural responses within the impacted structure [44].

---

[4] The energy loss due to ionisation of a particle traversing matter is given by dE/dx. During the ionisation process, orbiting electrons are knocked out of atoms by the interaction with the very fast travelling charged particles. The δ-ray production is then characterised by the very fast electrons produced as a result of ionisation.

The intensity and the time-scale of the response can be categorised based on several parameters mainly: deposited energy, maximum energy deposition, interaction duration and strength of the impacted material. In fact, three dynamic regimes can be identified with increasing deposited energy (Figure 2.11).

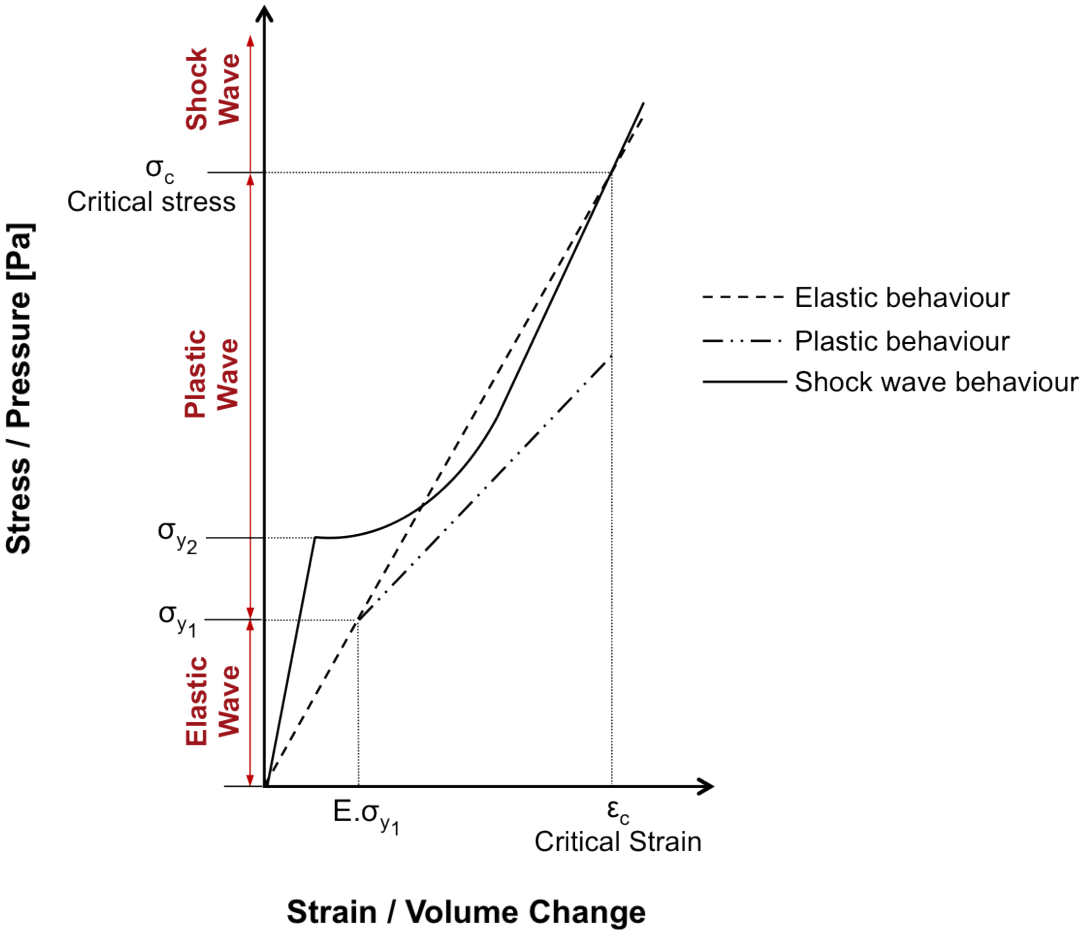

Figure 2.11: Material model for the stress-strain curve (or pressure-volume change curve) showing the different dynamic regimes resulting from the rapid interaction of high-energy particle beams with matter (adapted from [47]).

The three identified dynamic regimes [47] are:

- **Stress Waves in the Elastic Domain**: This regime is encountered in case of relatively low-energy impacts during which dynamic stresses do not exceed the material yield strength. Any changes of density are negligible and pressure waves propagate at the elastic speed of sound without plastic deformation. Such phenomena can be very well-treated with standard implicit finite element (FE) codes (such as ANSYS® [68]) [69] or even with analytical tools [44, 70].
- **Stress Waves in the Plastic Domain**: In this regime, the dynamic stresses exceed the material yield strength and plastic stress waves appear propagating at velocities slower than the elastic speed of sound. Changes in density can still be considered negligible; however, permanent deformations appear within the affected structure. Such a dynamic response can still be reasonably well-treated with standard implicit FE codes (such as ANSYS®) [71, 72].
- **Shock Waves**: This regime comprises deposited energies that are high enough to provoke strains and stresses above a critical threshold (ϵ_c, σ_c). An energetic shock wave is then formed which propagates at a velocity higher than the speed of sound, potentially leading to severe damage within the affected component. The energy deposited by the proton bunches leads to strong heating that generates a pressure in the beam-heated region. This high pressure then generates a strong outgoing shock wave that moves the material outwards, thus leading to a strong density reduction along the target axis. As a consequence, the protons that are delivered in subsequent bunches, together with the particle shower they generate, penetrate deeper into the target, causing significant range lengthening. The latter is the so-called tunnelling effect [73].

  In the case of shock waves, which are characterised by a sharp discontinuity in pressure, density and temperature across their front, explicit codes (such as LS-DYNA® [74] and AUTODYN® [75]) provide a better approach towards a reliable solution. In fact, a novel category of numerical tools, called hydrocodes, have been developed to study very fast and intense loading on materials and structures. Such hydrocode simulations [47] account for changes in the state of the material and the presence of shock waves. These new wave propagation codes are highly non-linear FE tools using explicit time integration schemes. They are capable of managing very high plastic deformations at elevated strain rates, the latter being encountered in phenomena where very short and energetic particle impacts lead to material melting.

2.3.3 Damage mechanisms

The interaction between high-energy particle beams and solids can be considered, from a structural point of view, as an energy deposition inducing a sudden non-uniform temperature increase. This provokes a dynamic response of the structure entailing thermal stress waves and thermally induced shock vibrations, or even failure of the component. The materials placed close to the beam are used at, or even beyond, their damage limits. The pressure and temperature of the material at the beam impact location increase and the material could arrive at its melting temperature or vaporise. The material in this region is thus characterised by high values of plastic strain, strain-rate and temperature [76].

Different methods of damage [77] exist for the impacted structure:

1. **Melting**: Melting of the material occurs when the energy intensity deposited on the component is such that the developed temperature increases beyond the melting temperature of the material (Figure 2.12). In this case, the shear strength of the molten elements becomes zero and the material starts to behave like a fluid.
2. **Erosion**: The erosion of elements in the numerical model becomes effective if the value of density is such that the material cannot support tensile load any more. The expansion in the material resulting from the strong outgoing shock wave leads to a significant reduction in density and pressure such that the erosion criteria may be satisfied.

3. **Spallation**: Spallation is an important mode of material failure during high velocity impact. The spallation of elements occurs if the calculated hydrostatic tensile stress grows beyond a fixed limit. Spallation is the process of internal failure or rupture of condensed media through the nucleation, growth and coalescence of defects, such as micro-cracks, due to stresses in excess of the tensile strength of the material (Figure 2.13).

4. **Cumulative Damage**: The calculation of the cumulative damage is performed for the part of the component that is still solid. Resulting cumulative damage includes potential residual stress levels and permanent deformations of the structure [77].

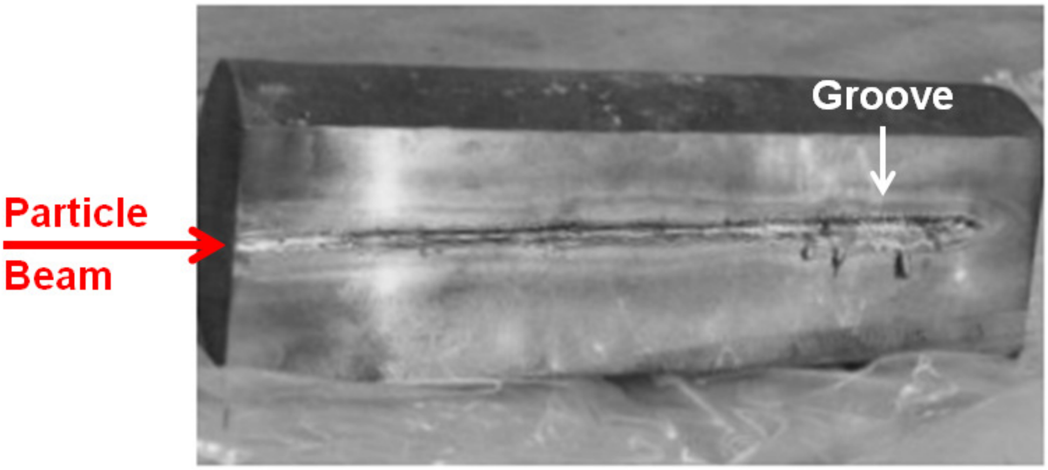

Figure 2.12: Melting effects caused by a high-energy particle beam impact on a metal structure. The molten region results in the formation of a groove within the structure [78].

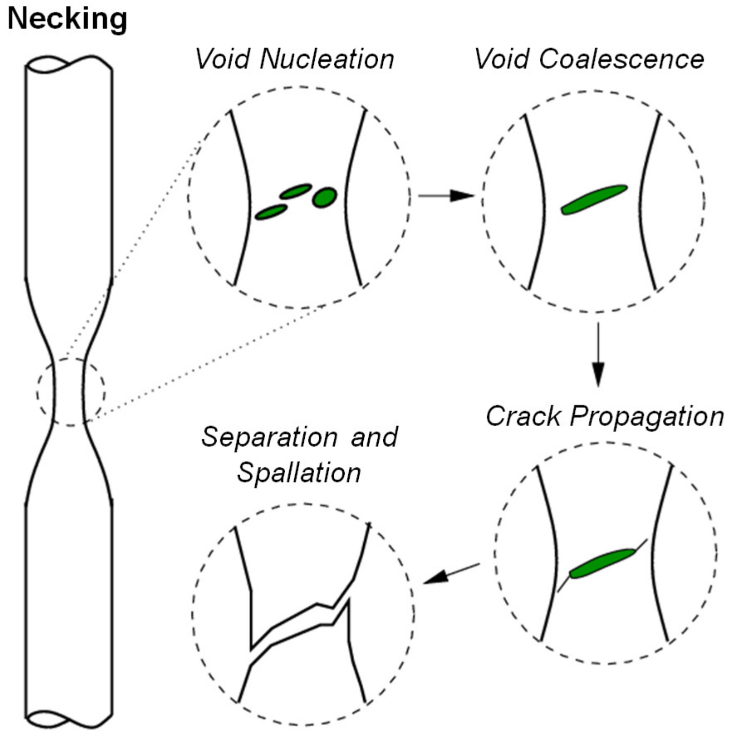

Figure 2.13: Schematic diagram showing the steps of ductile fracture in pure tension. Sequential stages of spallation as a consequence of the beam impact include the appearance of micro-cracks, the coalescence of micro-cracks into one major crack and finally spallation.

A sintered material such as INERMET® 180 can undergo fracture failure in different modes which then affect the resulting strength and ductility of the material. Four possible fracture paths [79] are:

1. **Intergranular tungsten fracture**: the separation between tungsten grains at their interface
2. **Interfacial tungsten-matrix decohesion**: the separation at the interface between tungsten and binder phases
3. **Tungsten cleavage**: the cleavage inside a tungsten grain
4. **Matrix failure**: the ductile rupture of the matrix

The integrity of the tungsten-matrix interphase boundaries established during processing is also of major importance in determining the resultant mechanical properties. The precipitation of a brittle intermetallic third phase along these boundaries poses a serious potential source of embrittlement in liquid-phase sintered alloys. X-ray diffraction (XRD) analysis would play an important role in the evaluation of any unwanted phases including such brittle intermetallics [80].

The random distribution of voids (typical size < 1 μm), both in the grains and along the grain boundaries, contribute to the overall spallation of the material. Apart from the original distribution of voids present in the material during the shock loading, more voids are also generally nucleated during the spallation process. Under the reflected tensile wave, the voids grow bigger and interact with each other resulting in void coalescence and the formation of micro-cracks, which eventually lead to the overall observed spallation (Figure 2.13) . Conventional void growth mechanisms, such as vacancy diffusion and shock heating, cannot account for the void growth process under high strain-rate tension loading as produced by the reflection of a shock wave at a free surface [81]. Lubarda et al. [82] proposed a dislocation-emission-based mechanism for void growth, considering prismatic and shear dislocation loops.

Experimental studies on the behaviour of a tungsten-sintered alloy by Rohr et al. [83] show that no necking or limited necking occurs at room temperature in quasi-static conditions. However, as the deformation increases and the critical fracture stress is reached, micro-cracks start to nucleate preferentially at the grain-matrix interfaces and the grain-grain boundaries (Figure 2.14). This is due to the fact that micro-crack propagation along an interface or a boundary is subject to less resistance when compared to propagation through the matrix or grain body themselves.

On increasing the load stress, these initiated micro-cracks begin to propagate in accordance with the local loading and material conditions. Even under heavy deformation conditions, both the separation along the grain-matrix interface and along the grain-grain boundaries remain the major modes of failure [79]. This was also confirmed by Pasalic et al. [84] who concluded that the most frequent fracture mode in tension is intergranular failure at the tungsten-tungsten interfaces. At high strain-rates the material softens, subsequently

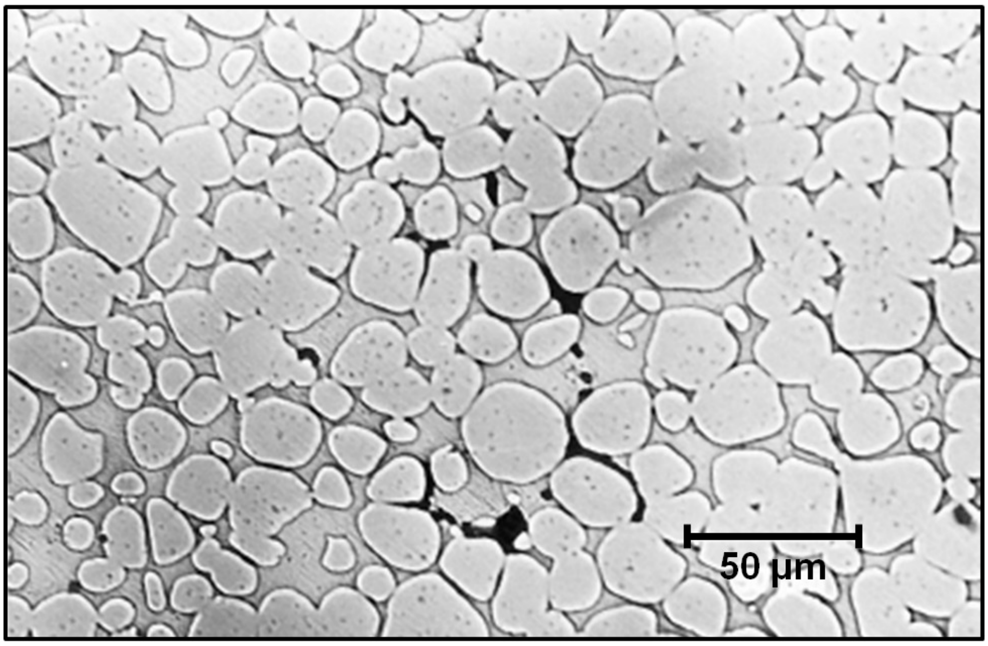

Figure 2.14: An optical micrograph showing the micro-crack features of a tungsten heavy alloy specimen (W-Ni-Fe alloy in this case). It can be observed that initial cracking occurs preferentially either at the tungsten-tungsten grain boundaries or at the tungsten-matrix interfaces. The 'dimpled' appearance of the microstructure is due to the presence of voids both in the grains and in the matrix [79].

increasing the strain and in this case, the weakest points are once again the interfaces between the tungsten grains where failure starts in the direction perpendicular to the loading direction [85]. Moreover, microstructure observations revealed that micro-crack density and grain deformation increase with strain-rate and temperature until catastrophic crack propagation occurs [79].

In the case of a beam impact on a collimator, the generated pressure waves reach the component's free external surfaces in a very short time. The compressive pulses that result from the impact are reflected from these surfaces after which they interact to generate a region of high tensile stress in the material that then causes the formation of spalls. Many spall events can eventually lead to the fragmentation of the material [86].

The part of the component close to the area of impact could be subjected to considerable values of hydrostatic tensile stress caused by the propagation of pressure waves. In this part, if the material is solid and if the tensile load exceeds one of the criteria identified in the spall model explained below, the material spalls and loses its strength. A spall model is thus used to represent the material failure under hydrostatic tensile loads and can include any one of the following three types of spallation criteria [77]:

- **Pressure limit model**: this limits the minimum hydrostatic pressure to a specified cut-off value within the model. If a pressure that is more tensile than this limit is calculated, this model resets the pressure value to the specified minimum value for that element within the model. With this model, the deviatoric stresses are unaffected if the pressure reaches the pressure cut-off value and the latter remains unchanged throughout the analysis.
- **Maximum principal stress model**: this detects spall if the maximum principal stress within the model exceeds a limiting value, such as the ultimate tensile strength (UTS) of the material.
- **Hydrostatic tension spall model**: this limits the minimum pressure value like the pressure limit model. However, in this case, once spall is detected for an element within the model, the deviatoric stresses are reset to zero for that element, resulting in the elimination of elements that are not carrying any load. Moreover, the pressure is required to be compressive and if hydrostatic tension is calculated, then the pressure is reset to zero for that element within the model.

2.4 State-of-the-art and current studies

The energy stored in a single beam of the LHC particle accelerator is equivalent to about 80 kg of TNT explosive. This large amount of energy, which is stored in a transverse beam area with a typical value of 0.3 mm × 0.3 mm, is potentially destructive for accelerator equipment directly impacted by particle beams. This is the case during uncontrolled beam loss due to a failure in the MPS. As a matter of fact, various detailed studies have been carried out over the years to evaluate the damage in metal structures subjected to high energy deposition due to particle beams. Different approaches can be found in literature to solve similar problems. A short discussion about these approaches developed by different research centres will now be presented.

A lot of work has been performed in this field by Tahir et al. [73, 87–89], with the aim to obtain an estimate of the scale of damage resulting from a failure in the LHC MPS. In particular, a solid cylindrical copper target, irradiated by 100 LHC bunches at 7 TeV, was assessed in [43] by carrying out 3-dimensional (3D) energy deposition calculations with FLUKA. This was followed by 2D numerical simulations of the hydrodynamic and thermodynamic response of the target using the BIG-2 code [90]. The model includes a sophisticated multi-phase semi-empirical equation of state (EOS)[5] to describe the target behaviour during the different phases of heating and expansion. Using this approach, the authors estimated that the penetration depth of the LHC protons will be between 10 m and 40 m in the solid copper target. The numerical simulations also showed that the density decreases at the inner part of the beam-heated region because of the outgoing shock wave in the transverse direction. This results in the tunnelling effect which means that the proton bunches that will be subsequently delivered in the later part of the pulse will penetrate further into the target.

As a result of the density variation, the intensity and structure of the particle cascade will also change and this will influence the energy deposition. The previously adopted methodology was thus further extended by performing a calculation of the particle cascade using a dynamic density distribution. This was presented by Tahir et al. in [91] where detailed numerical simulations of the full impact of one LHC beam on a cylindrical solid carbon target were carried out.

The energy deposition was first evaluated with the FLUKA code. This was then directly used as input in the BIG-2 code to study the corresponding thermodynamic and hydrodynamic response of the target that leads to a reduction in the density. The modified density distribution was then used again in FLUKA to calculate a new energy loss distribution and the two codes were thus run iteratively. The authors concluded that a

---

[5] An EOS is a constitutive relation between state variables and describes the state of the matter.

suitable iteration step is considered to be the time interval during which the target density along the axis decreases by 15% - 20%. The simulations suggest that the full LHC proton beam penetrates up to 25 m in solid carbon whereas the range of the shower from a single proton, or the hydrodynamic tunnelling effect, is just about 3 m.

Moreover, detailed studies [92] were also carried out by Tahir's team on a cylindrical tungsten target that has been facially irradiated by the full SPS beam. The beam comprised 288 bunches of 450 GeV/c protons with three different focal spot sizes determined by $\sigma = 0.088$ mm, 0.280 mm and 0.880 mm respectively. The numerical simulations of hydrodynamic and thermodynamic response have shown that the target will be completely destroyed in these cases, generating large samples of high energy density matter.

The phenomenon of significant hydrodynamic tunnelling due to hydrodynamic effects was further investigated through a dedicated novel experiment [93] carried out at the experimental HiRadMat facility [94] at CERN. The impact of the 440 GeV proton beam generated by the SPS on extended solid copper cylindrical targets was studied. Substantial hydrodynamic tunnelling of the protons in the target material was observed, leading to significant lengthening of the projectile range. Such experimental results were in good agreement with the theoretical predictions obtained through numerical simulations presented in [91].

Damage evaluation in copper and tungsten metal structures subjected to high energy deposition due to particle beams has also been thoroughly studied by Peroni et al [76, 77, 95, 96]. Similar to the approach by Tahir et al, the evaluation of thermal loads on the hit material was performed using the Monte Carlo based statistical code FLUKA. The energy map, which takes into account all the particles in the cascade generated by the interaction between the proton beam and the target, was then used as input for thermo-structural studies. These studies were however carried out via the FE code LS-DYNA. The validation of the numerical procedure was first performed on a simplified geometry, consisting of a copper cylindrical bar that was facially irradiated by 8 bunches at 7 TeV, each of them having 1.11×10^{11} protons. A Lagrangian 2D axi-symmetric model was used with an explicit time integration scheme. Since the simplified model represented the irradiated part of a bigger component, the external surface was modelled with a non-reflection boundary in order to simulate the presence of other material.

The thermo-mechanical response of the hit material was studied by Peroni's group by taking into account both the hydrodynamic behaviour using a dedicated EOS and the deviatoric behaviour using a dedicated material model. The material models used for the description of the mechanical strength behaviour of the material were either the Johnson-Cook (J-C) or the Steinberg-Lund (S-L) models in which damage criteria and spall models were introduced. The EOS used in the numerical simulations was a polynomial EOS that was linear in energy, whose coefficients were calculated by fitting a multi-phase tabular EOS for each energy level. The results in [77] show that the copper component is damaged until a maximum radius of 4 mm while in the longitudinal direction, the proton beam impact causes the perforation of the material. The FLUKA/BIG-2 and FLUKA/LS-DYNA approaches by Tahir et al. and Peroni et al., respectively, are compared in [97] and good agreement is achieved.

Peroni et al. then applied the same method to simulate the beam impact against a real complex TCT geometry [78]. The implemented Lagrangian 3D numerical model still represented a simplified structure with respect to the full TCT geometry. However, it considered the presence of two different material parts - an internal tungsten part (the hit part) and an external C-section in copper - and the contact between the different model components. The simulation provides the impact of 8 bunches each having 1.13×10^{11} protons at 5 TeV.

Following the energy deposition, a shock wave is generated which moves from the tungsten region to the copper part. Due to the significant difference in impedance between the two materials (copper and tungsten), the shock wave is in part reflected at the interface with the potential spallation of tungsten and the reduction of the pressure level transmitted to copper. The temperature is limited to the normal melting temperature of tungsten since in the hit zone it could reach several thousands of K (plasma condition). The level of stress is high in the tungsten part resulting in heavy deformation after the beam impact. In the melted part of the component, the Von Mises stress is zero and the behaviour is purely hydrostatic. On the other hand, the Von Mises stress reaches the maximum value behind the shock wave profile. The authors also developed a FLUKA/LS-DYNA coupling approach [98, 99] in order to take into account the dynamic density distribution.

A. Dallocchio studied the problem of rapid internal heating of beam-like structures through an analytical approach [70, 72]. The proposed method allows to quickly evaluate the temperature field, the quasi-static and dynamic thermal stresses as well as the thermally induced vibrations provoked by particle beam impacts. Analytical solutions were used as a benchmark to qualify numerical FE tools and to identify their limit of applicability. The commercial code ANSYS® was used to study the thermo-mechanical behaviour of TCSs. The thermo-structural effects provoked by high-energy particle beams on the carbon-carbon jaw of such collimators was evaluated in case of steady-state and slow transient thermal loads as well as in case of an abnormal beam loss resulting from an injection error. Comparison with experimental measurements resulted in good agreement and thus confirmed the validity of the adopted analytical and numerical approaches.

A similar approach was carried out in [100, 101]. However, in this research, the energy calculation as a result of a high-energy beam impact on a solid material is performed via the MARS code [102] instead of FLUKA. The temperature rise is calculated from the energy map and then used either in LS-DYNA for an explicit analysis or in ANSYS® for an implicit analysis in order to calculate the dynamic stresses in the target.

A number of simulations have also been carried out by A. Bertarelli et al. in [47] in order to identify different damage levels for the TCT up to catastrophic failure. It has been concluded that thermally induced dynamic phenomena up to the melting point of metals can be reasonably well-treated with standard FE codes. However, advanced wave propagation codes, known as hydrocodes, become necessary when changes of state and density occur. Following the energy deposition calculation by FLUKA, a thorough numerical analysis of a TCT was carried out using the AUTODYN® code.

The CERN team led by Bertarelli studied several asynchronous beam abort cases with different values of beam emittance, energy and intensity. It has been found that single-bunch accidents at 3.5 TeV and 7 TeV, at all beam emittances, induce jaw damage which does not require collimator replacement as an appropriate spare surface (with the required flatness) can be obtained by shifting the full collimator. The size of the damaged region is already much larger than the beam size so that no sensible difference is found when varying the beam emittance. Multi-bunch accidents always require collimator replacement. Risk of very severe damage leading to long LHC downtime has been estimated for impacts with more than 4 bunches at 5 TeV, with risk of water leakage detected for an impact with 8 bunches at 5 TeV. For the multi-bunch cases, it was implicitly assumed that the density variation caused by preceding bunches is negligible: this only holds for a limited number of bunches (up to 8 bunches at 5 TeV) after which density changes become too large to be disregarded.

An overview of the research contribution given by the study presented in this thesis will now be introduced. The purpose of this work is to advance the knowledge on the robustness of TCTs by investigating their thermo-mechanical response in novel beam impact scenarios. This is achieved through the use of advanced simulation techniques applied to a complex 3D model. The numerical simulations are performed on the whole collimator jaw assembly, taking into account the jaw insert blocks, the block housing, the cooling circuit and the back stiffener, together with all respective contact interfaces. The starting point of the analysis is the energy deposition map on the component, that is calculated and provided in collaboration with another member of the research team (L. Lari, CERN) using the FLUKA code. The energy deposition distributions are converted into thermal power distributions, and are then used as an input to the thermo-structural analyses that are performed using the commercial code ANSYS®.

A numerical FEM approach is developed and presented in this thesis. Sequential fast-transient thermo-structural analyses are performed in the elastic-plastic domain in order to correctly evaluate the thermo-mechanical response of TCTs to beam impact. The thermal problem is first solved to obtain the temperature distribution as a function of space and time. The results of the temperature analysis are then used as body loads for the structural analysis so that the dynamic thermal stresses and displacements are evaluated. Finally, a quasi-static step is necessary in order to calculate potential permanent deformations of the structure.

The focus of this study is an asynchronous beam dump accident with a single dump module pre-fire, which is one of the most serious accident scenarios identified in the LHC. This work presents novel case studies of realistic proton beam impact scenarios on TCTs as a result of an asynchronous beam dump. Slight angular misalignment errors of the collimator jaw are taken into account and different cases are derived scanning through different jaw angles and varying beam energies. Moreover, since the LHC is also designed to bring into collision heavy ions, this work also investigates, for the first time, the effects of direct ion beam impacts on collimators. This is considered a new vital case to study, as the ion loss case can result in different damage aspects for the collimator due to the different particle-collimator interaction mechanisms for protons and lead ions. The developed FEM approach is used to evaluate the thermo-mechanical response of TCTs in these critical beam load cases.

This work also describes how a thorough integral assessment of beam accident scenarios involving a complete TCT is achieved through the design and setting up of a dedicated beam experiment at the CERN HiRadMat facility. The main aim of the experiment was to address the effects of an asynchronous beam dump considering a relevant nominal 7 TeV case as well as to benchmark simulations for the LHC cases at 5 TeV that have been considered during the LHC Run 1 [47]. A complementary dedicated experiment [103] has also been carried out at the same facility in order to address novel materials of interest for collimators like dispersion-strengthened copper, molybdenum, and metal-diamond/metal-graphite composites.

Additionally, reliable FEM simulations are strongly dependent on a correct material model. Temperature-dependent thermal and structural properties are required in FEM calculations with large temperature variations. However, such properties were not available for the collimator jaw insert material, INERMET® 180, and as previously described, studies on TCTs have in fact always been performed assuming pure tungsten as the material of the jaw inserts, instead of INERMET® 180. Material characterisation tests on INERMET® 180 have thus been commissioned as part of this study in order to obtain a full thermo-physical and structural characterisation of this alloy over a wide range of temperatures and strain-rates. The obtained material properties are presented in this thesis and subsequently used for the material model of the jaw inserts in the FEM simulations.

2.5 Conclusions

The overview of the LHC collimation system serves as a useful introduction to better understand the numerical approach adopted in this study for investigating the thermo-mechanical effects provoked by high-energy particle beams during an impact on collimators. The functional specifications of LHC collimators pose a serious challenge to the mechanical design of these components. This chapter has presented the main features and characteristics of the technical concept addressing these requirements. The different thermal load conditions on the collimator jaw inserts and the resulting damage mechanisms have also been discussed, with a focus on accidental scenarios with abnormal beam losses.

Moreover, it has been shown that various detailed studies have been carried out over the years to evaluate the damage in metal structures subjected to high energy deposition by particle beams. Different methodologies have been adopted and it has been concluded that it is very difficult to accurately predict the structural efficiency and robustness of such metal structures. This is because beam-induced damage for high-intensity and high-energy scenarios occurs in a regime where practical experience does not exist. Additionally, an overview of the scientific contribution given by the study presented in this thesis has been discussed and it has been shown that this work will advance the knowledge on the thermo-mechanical response of TCTs in various relevant scenarios for the operation of the LHC and its risk optimisation. This will be achieved through the use of advanced simulation techniques that take into account all relevant collimator damage limits.

Chapter 3

Numerical Modelling Approach

3.1 Introduction

The interaction of high-energy particle beams with matter provokes a sudden non-uniform temperature increase on the hit structure. This gives rise to thermal stresses and deformations that may affect the integrity or the proper functionality of the hit equipment. As the collimator is a multi-component system composed of different materials and contact interfaces, a numerical FEM approach, rather than an analytical analysis, was used to study the response of the collimator to an asynchronous beam abort. The implementation of such an approach is imperative for an in-depth study of the fast and complex thermo-mechanical phenomena induced within the impacted structure [72]. In this respect, a numerical FEM approach found direct application in the frame of the LHC collimation project [51].

3.2 Simulation framework

3.2.1 Energy deposition maps

A detailed energy deposition map is essential to correctly simulate thermal loads as an input for thermo-mechanical calculations of complex structures. In this study, the evaluation of the thermal loads on the collimator jaw inserts was done using the Monte Carlo based statistical code FLUKA. A FLUKA model of the jaw inserts was set up in collaboration with another member of the LHC collimation research team (L. Lari, CERN) and full shower simulations provided the spatial distribution of the energy deposition (in GeV/cm^3/proton) for the defined accident cases (Figure 3.1).

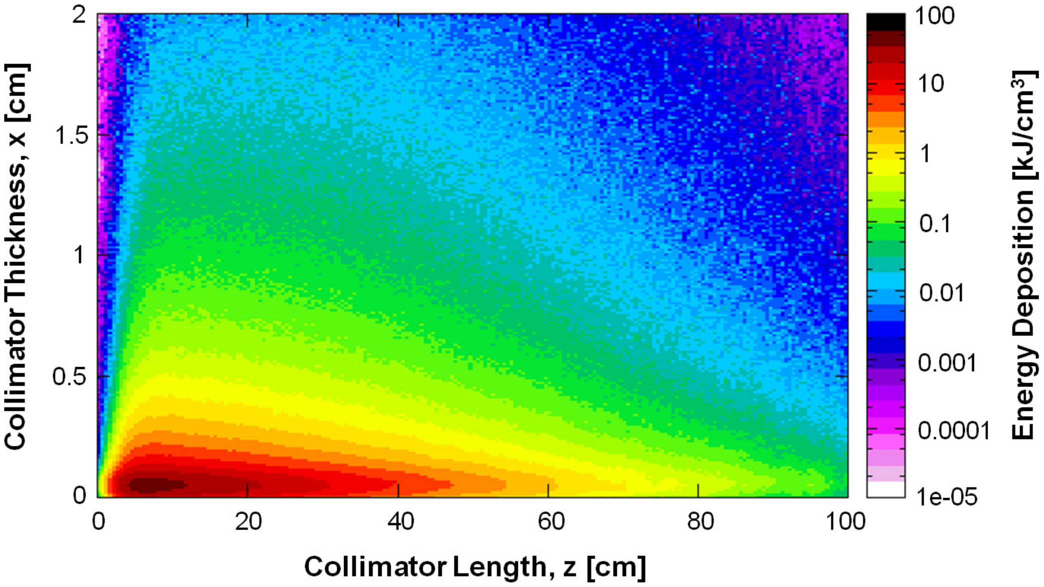

Figure 3.1: An example of an energy deposition map for an x-z cross-section of the collimator jaw inserts along the symmetry plane (y=0) at the end of the energy deposition (t = 1 ns). This example represents the case of 1 nominal LHC bunch of protons (1.15×10^{11} protons) at 7 TeV with a beam size of 0.30 mm (σ_x) × 0.30 mm (σ_y) directly hitting the tungsten jaw inserts. The beam impact parameter (transverse distance to the point of first contact of the beam with the collimator) is set to 0.5 mm (results obtained in collaboration with L. Lari, CERN).

The FLUKA calculation takes into account a large number of primary particles (around 200,000 in the case studies presented in this thesis). This ensures that statistical errors, related to the adopted scoring mesh, are kept to a minimum over the whole target component. Additionally, statistical errors should have much lower values in the region with peak energy deposition. The results are then normalised to one ideal proton. This means that, by sampling from a Gaussian distribution, adding all contributions up, and dividing these by the number of sampled particles, the FLUKA result turns out to be representative of the whole distribution. The FLUKA maps can then be rescaled by the real bunch intensity.

3.2.2 Thermo-mechanical analyses

The FLUKA maps were then processed via a dedicated sub-routine in order to obtain the correct input thermal load, in terms of power density distribution (in W/m^3), for the FEM solution. The single impact parameters, which could be varied in order to generate different energy deposition scenarios from the same FLUKA output file, included the number of bunches, the number of particles per bunch and the impact duration.

Non-linear transient thermo-mechanical analyses were then performed to correctly evaluate the temperature distribution and other thermally induced effects as a function of time. Such analyses were conducted exploiting the implicit FE code ANSYS® and the steps involved in these detailed analyses are explained in Section 3.3. A summary of the used simulation chain is depicted in Figure 3.2.

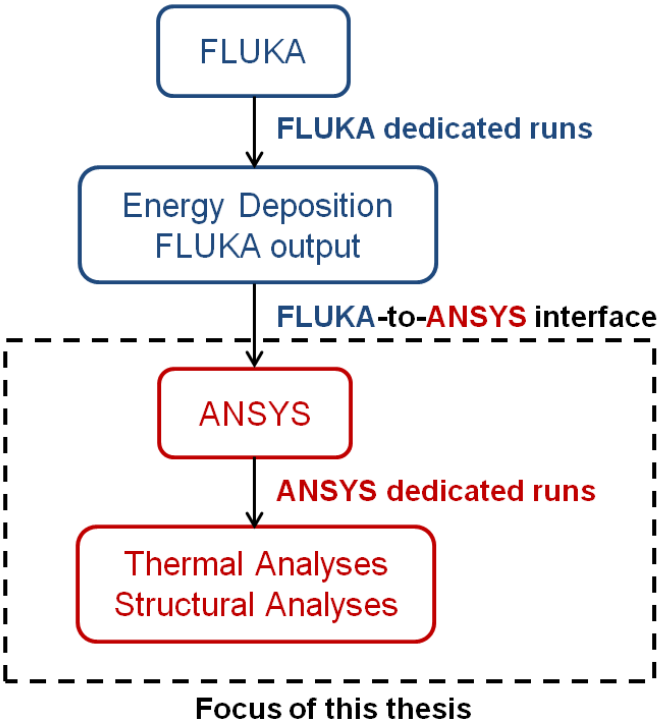

Figure 3.2: The simulation chain showing the inputs and outputs of the FE code ANSYS®. The FLUKA simulations are performed in collaboration with another member of the LHC collimation research team. The focus of this thesis is the thermo-mechanical analyses with ANSYS®.

3.3 Finite element modelling

3.3.1 Geometry and component setup

This study focuses on beam accidents involving horizontal TCTs due to the fact that an asynchronous beam dump accident can only act on the horizontal plane, as will be explained in Section 4.2.1. A detailed 3D model of a horizontal TCT collimator jaw assembly was imported into the FE program ANSYS®. The considered beam impact leads to a symmetrical energy deposition in the longitudinal (x-z) plane of the collimator jaw. Since both the collimator model (Figure 3.3) and the FLUKA shower distribution (Figure 3.4) were symmetric about the mid-plane of the jaw inserts (y=0), it was only necessary to model the upper or lower half of the collimator jaw structure (Figure 3.5).

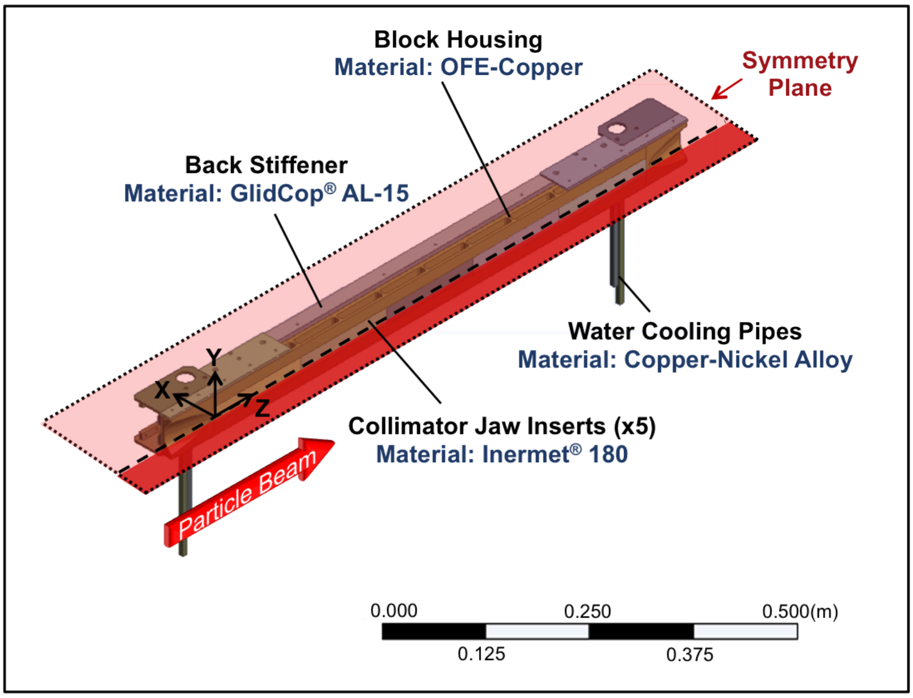

Figure 3.3: A 3D model of the left jaw assembly of a TCT (as seen by the incoming beam). The symmetry plane (x-z plane) is shown in red.

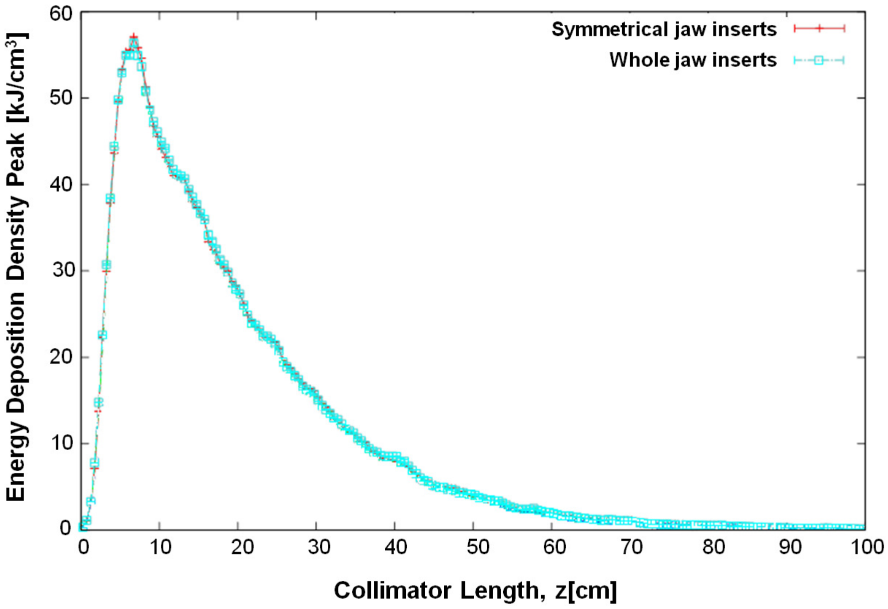

Figure 3.4: Comparison of the energy deposition density peak profiles for a whole collimator model and a symmetrical model (cut at y=0 plane), with both cases having the same mesh density. It can be observed that the two models have an identical energy deposition density peak profile, thus justifying the use of symmetry.

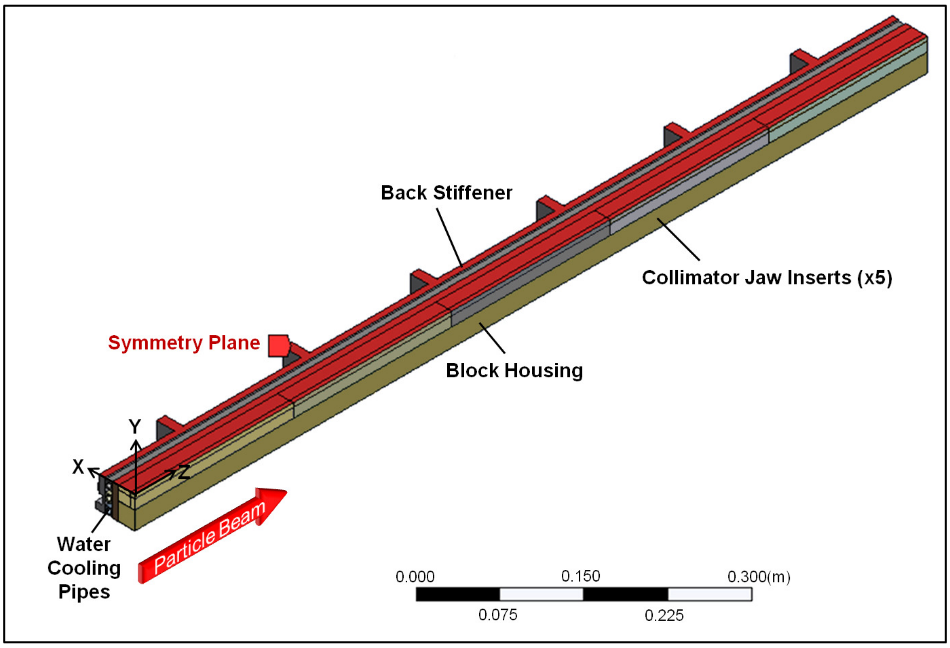

Figure 3.5: A 3D model of the lower symmetrical half of the left jaw assembly of a TCT (as seen by the incoming beam). The symmetry plane (x-z plane at y=0) is shown in red. This is the model used for the sequential thermal and structural analyses in ANSYS®.

These symmetry conditions considerably reduced the computational time necessary to perform the calculation without compromising accuracy. Moreover, FEM simulations were only performed on either the left or the right collimator jaw assembly; in fact, this choice does not make a difference since the two jaw assemblies are symmetrical with respect to the beam.

Furthermore, in the ANSYS® calculation, the contact interfaces between the various components were also modelled. The brazed contact surfaces between the cooling circuit and the block housing/back stiffener were modelled to never slip, meaning that the copper housing, the cooling circuit and the back stiffener were fixed despite any other deformation of the collimator. The thermal conductance value at these contact interfaces was estimated experimentally [104], from which it was decided to use a conservative value of 5000 W/m^{2}K in the numerical simulations.

Similarly, the effect of the stainless steel screws between the copper housing and the jaw inserts was modelled with a thermal conductance value estimated experimentally at 10,000 W/m^{2}K [104]. These experimental measurements are backed up by analytical studies [105, 106] in which all the calculations of tightening torque and pre-load are done according to the German Standard VDI 2230.

The stainless steel screws were not physically modelled and the screwed tungsten-copper contact interfaces were modelled to never slip similar to the brazed contact surfaces. Although OFE-Cu has a larger coefficient of thermal expansion when compared to INERMET® 180, the temperature rise on the copper block housing is insignificant when compared to that on the jaw inserts during the considered asynchronous beam dump accident. This means that while the jaw inserts will undergo thermal expansion, this is not the case for the copper block housing. The result is that the jaw inserts will expand and will force the copper block housing to expand with them such that the block housing (and consequently the brazed cooling pipes and back stiffener) must exhibit the same deformation as the jaw inserts, as the latter are not allowed to slip in the FE model. This is not fully the case in reality as the jaw inserts are allowed to undergo some relative slipping and the block housing is not forced to take the full deformation of the inserts. However, this assumption is considered acceptable given that the FE model represents a conservative approach and gives the correct deformation of the jaw inserts that are ultimately the components whose behaviour is of most interest.

Moreover, no contact interface was modelled between the collimator jaw inserts themselves. This means that in the FE model, the inserts were allowed to expand into each other. In reality, the inserts are machined with a length of 200 mm and a tolerance of between -0.1 mm and -0.2 mm, meaning that there is a gap of at least 0.1 mm between each two inserts. It will be shown in Sections 4.4.2 and 7.4.2 that the total longitudinal deformation of the collimator jaw assembly due to the particle beam impact in the studied jaw error cases is, in fact, smaller than 0.1 mm, thus confirming that no contact model was necessary.

3.3.2 Finite element discretisation

In finite element analysis (FEA), a mesh convergence sensitivity study is required to find a satisfactory balance between accuracy and computational resources. An initial mesh convergence study had to be carried out in FLUKA in order to obtain convergence of the energy deposition values. FLUKA simulations were carried out for different mesh densities of a particular case, from which it was concluded that a mesh size of 0.1 mm (x) × 0.1 mm (y) × 5 mm (z) on the jaw inserts was the minimum required so that a further mesh refinement did not increase the estimated peak power density by more than 10% [52].

The mesh density of the collimator jaw inserts for the thermal analyses was then set equal to that used in the FLUKA model in order to obtain one-to-one mapping of the energy deposition values between the FLUKA and ANSYS® models. This finest mesh size of 0.1 mm (x) × 0.1 mm (y) × 5 mm (z) was implemented within a region of 5 mm (x) × 5 mm (y) around the beam impact location in order to correctly capture the maximum energy deposition on the jaw inserts (Figure 3.6). Once energy deposition distributions were known, the maximum temperature T_{max} at the end of the heat load deposition could be verified (assuming adiabatic conditions) with a simple analytical calculation given by Equation 3.1 [107, p. 71]:

$$T_{\mathrm{max}} = \frac{P_{\mathrm{max}}\,\tau}{\rho \int_{T_{\mathrm{ref}}}^{T_{\mathrm{max}}} c_{\mathrm{p}}(T)\,\mathrm{d}T} + T_{\mathrm{ref}}, \tag{3.1}$$

where P_{max} [W/m^3] is the maximum power density, τ_{shock} [s] is the thermal shock duration, and T_{ref} [°C] is the reference temperature. The density ρ [kg/m^3] refers to the initial condition of the material (solid state at the nominal density) and the heat capacity at constant pressure (c_{p} [J/kgK]) can be integrated as a function of temperature.

Good agreement between the analytical and numerical values for T_{max} proved the choice of a sufficiently fine mesh at the location of the beam impact. Since all the jaw error cases to be simulated in this study deal with a beam impact parameter of 0.5 mm in the x-direction, this region of fine mesh proved to be sufficient for all load cases, thus enabling

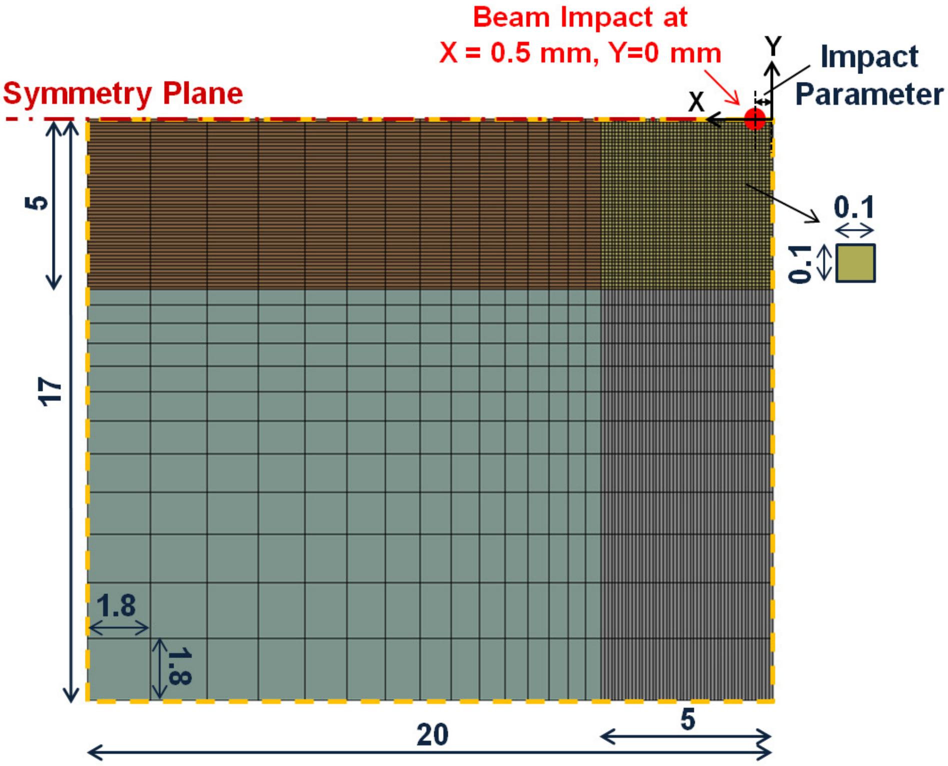

Figure 3.6: A detailed cross-sectional (x-y) view of the collimator jaw inserts as discretised for the thermal analyses. All dimensions are in mm.

the same mesh configuration to be used for the different cases. The rest of the jaw inserts, together with the remaining collimator components (the block housing, the water pipes and the back stiffener), were then discretised with a coarser mesh due to computational requirements (Figure 3.7).

Furthermore, different meshes were employed for the jaw inserts in the thermal and structural analyses. A mesh convergence study was carried out in ANSYS® to justify the choice of the transverse discretisation density for the collimator jaw inserts in the structural solution. A number of different transverse mesh sizes were considered for a particular case, with the finest achievable transverse mesh size being limited to 0.5 mm × 0.5 mm from a computational resources point of view. The imported body temperatures (Figure 3.8), together with the Von Mises stress at a point within the area of interest and the central processing unit (CPU) time of calculation (Figure 3.9), were monitored for the different mesh sizes.

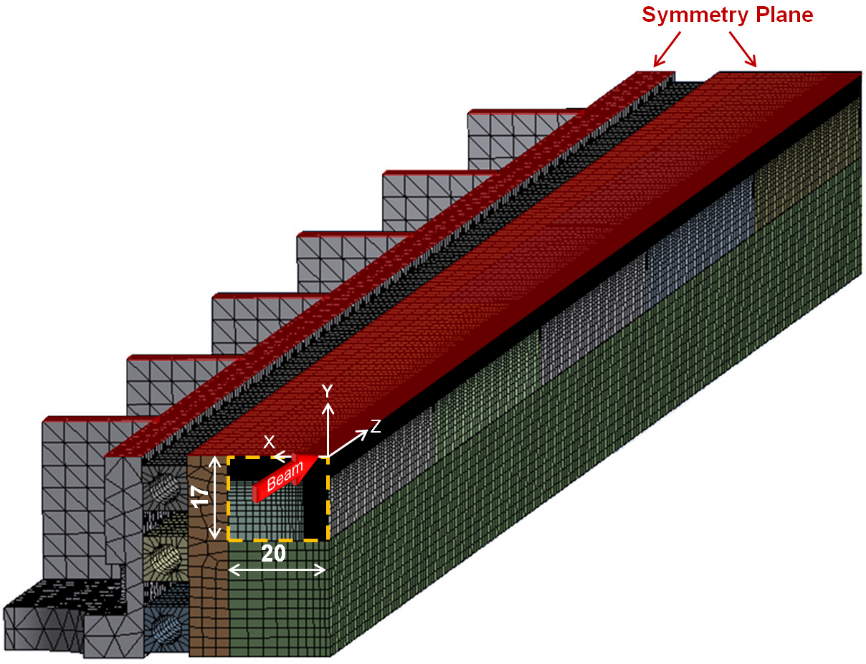

Figure 3.7: FE discretisation of the whole collimator jaw assembly for the thermal analyses. All dimensions are in mm. The total number of elements used for the whole model during the thermal analyses was 1,056,265.

Figure 3.8 highlights that no significant difference is obtained in the imported temperature profile on a mesh refinement beyond a transverse mesh size of 1 mm × 1 mm. Moreover, Figure 3.9 shows that a refinement of the transverse mesh size beyond 1 mm × 1 mm would adversely affect the CPU time of calculation, and that the Von Mises stress values differ by only 8% on doubling the mesh size from 0.5 mm × 0.5 mm to 1 mm × 1mm when compared to the 62% difference on doubling the mesh size from 2 mm × 2 mm to 4 mm × 4 mm. It was thus concluded that a mesh size of 1 mm (x) × 1 mm (y) × 5 mm (z) for the structural solution (Figure 3.10) would be the best compromise to ensure sufficient convergence of stresses while keeping the interpolation errors of the temperature mapping and the solution processing time to a minimum. Contact elements were also implemented between the different component interfaces as identified in Section 3.3.1.

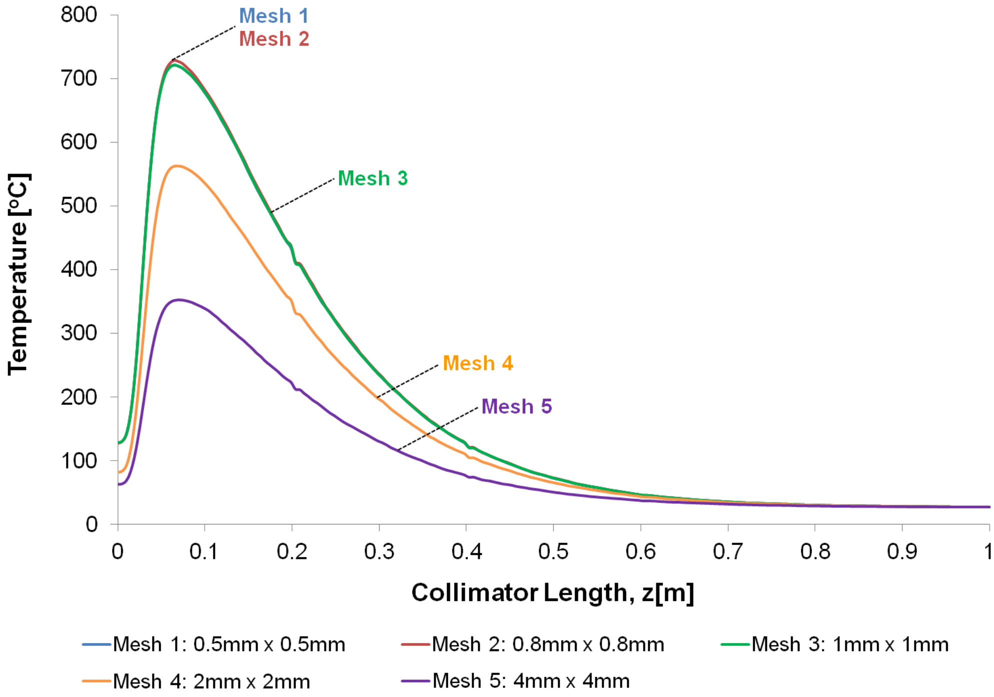

Figure 3.8: Temperature profiles along the collimator length as mapped from the thermal (fixed transverse mesh size: 0.1mm × 0.1mm) to the structural solution (varying transverse mesh sizes).

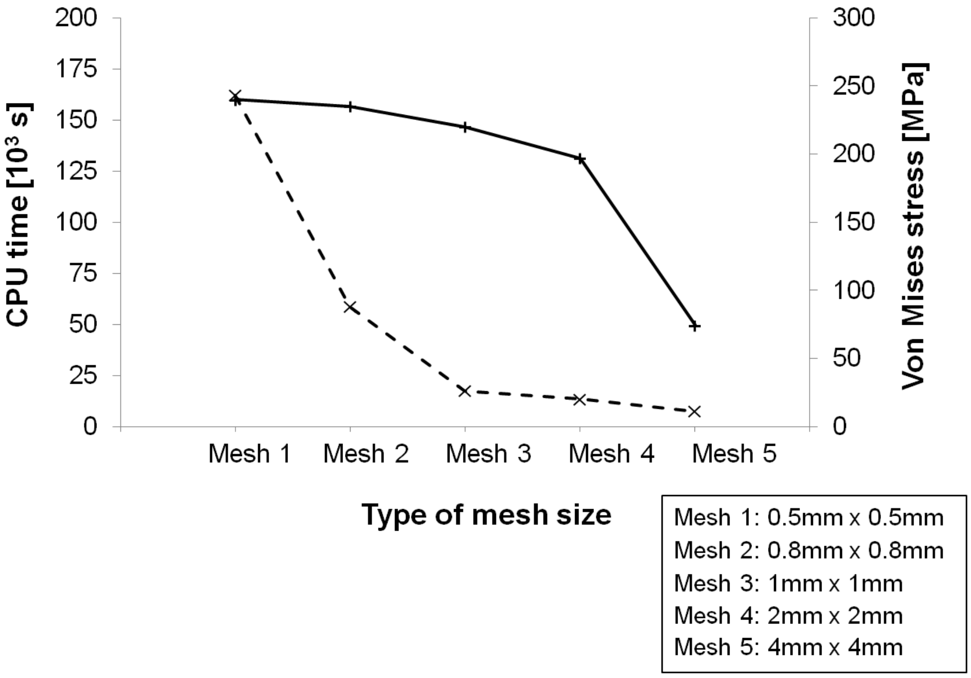

Figure 3.9: Mesh convergence study in the structural analyses. The convergence of the Von Mises stress is monitored together with the CPU time of calculation for different transverse mesh sizes.

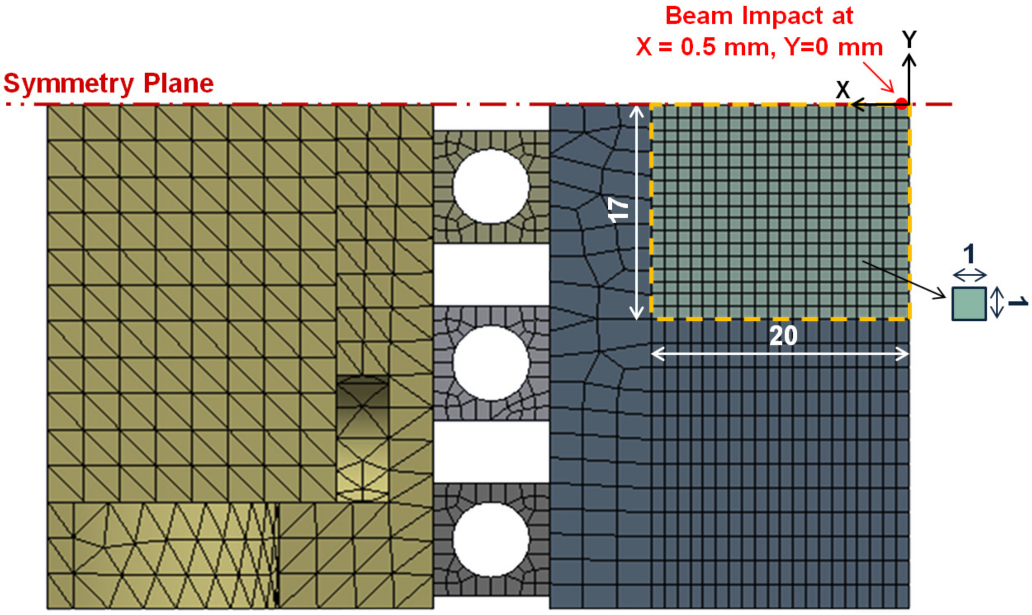

Figure 3.10: A cross-sectional (x-y) view of the discretised model of the collimator jaw assembly as used for the structural analyses. All dimensions are in mm. The only difference between the thermal and structural meshes is the mesh of the collimator jaw inserts (enclosed within the dashed yellow line), with a coarser mesh used for the structural analyses. The total number of elements used for the whole model during the structural analyses was 368,335.

3.3.3 Material modelling

Material modelling is considered a very important step in any FEA as it essentially drives the behaviour of the model and thus greatly influences the results. In FEM calculations with large temperature variations, such as in cases of shock beam impact, temperature-dependent thermal and structural properties are required in order to correctly evaluate the thermo-mechanical response of the structure. The materials of all the components making up the jaw assembly were modelled as isotropic and homogeneous, meaning that the material properties were not dependent on the direction and that each material had uniform composition throughout the component, respectively.

Temperature-dependent thermo-physical properties were initially defined for the thermal analyses. The Fourier's thermal conductivity equation (Equation 3.2) establishes the inter-relationship between the four basic thermo-physical properties - thermal conductivity

$k(T)$, specific heat capacity $c_\mathrm{p}(T)$, density $\rho(T)$ and thermal diffusivity $\kappa_\mathrm{cc}(T)$ - under the assumptions of a conservative system, of homogeneity of the thermally conducting medium (no spatial dependence of the material properties $k(T)$, $c_\mathrm{p}(T)$ and $\rho(T)$) and of the neglect of any non-linearity. In general, $\kappa_\mathrm{cc}(T)$ describes the so-called transport coefficient of the thermal conductivity problem. Equation 3.2 [107, p. 72] is given by:

$$\frac{\partial T(\vec{x},t)}{\partial t} = \left[\frac{k(T)}{\rho(T)\cdot c_\mathrm{p}(T)}\right]\cdot \Delta T(\vec{x},t) := \kappa_\mathrm{cc}(T)\cdot \Delta T(\vec{x},t), \tag{3.2}$$

Moreover, when an object is heated or cooled, its length $L(T)$ changes by an amount proportional both to the original length L_0 and the change in temperature $\Delta T(T)$. The relation between the linear thermal expansion of an object, $\Delta L(T)/L_0$, and the change in temperature, $\Delta T(T)$, is given by the coefficient of linear thermal expansion, $\alpha(T)$, as expressed by Equation 3.3 [108, p. 70-71]:

$$\alpha(T) = \frac{1}{\Delta T(T)}\cdot\frac{\Delta L(T)}{L_0}, \tag{3.3}$$

These thermo-physical properties ($k(T)$, $c_\mathrm{p}(T)$, $\rho(T)$ and $\alpha(T)$) were input in ANSYS® in the form of tabular data as a function of temperature. For property evaluation at element temperatures beyond the supplied tabular range, ANSYS® assumes a constant property at the extreme range value [68].

Temperature-dependent structural properties were subsequently defined for the structural analyses. In the 1-dimensional (1D) (uniaxial test) case, a specimen deforms up to yield and then generally undergoes hardening (Figure 3.11). Such behaviour depends on the temperature and strain-rate conditions. For high-temperature applications, significant recovery occurs and the material displays a rigid plastic deformation. Moreover, high strain-rates have the same effect as lowering the temperature, limiting material recovery in both cases and increasing the flow stress. For linear structural analyses, linear elastic material properties, namely the Young's Modulus $E(T)$ and the Poisson's Ratio $\nu(T)$, must be defined. The elastic behaviour of metals is most commonly described by the stress-strain (σ-ϵ) relationship of Hooke's Law, given by Equation 3.4 [108, p. 68]:

$$\sigma = E \cdot \epsilon, \tag{3.4}$$

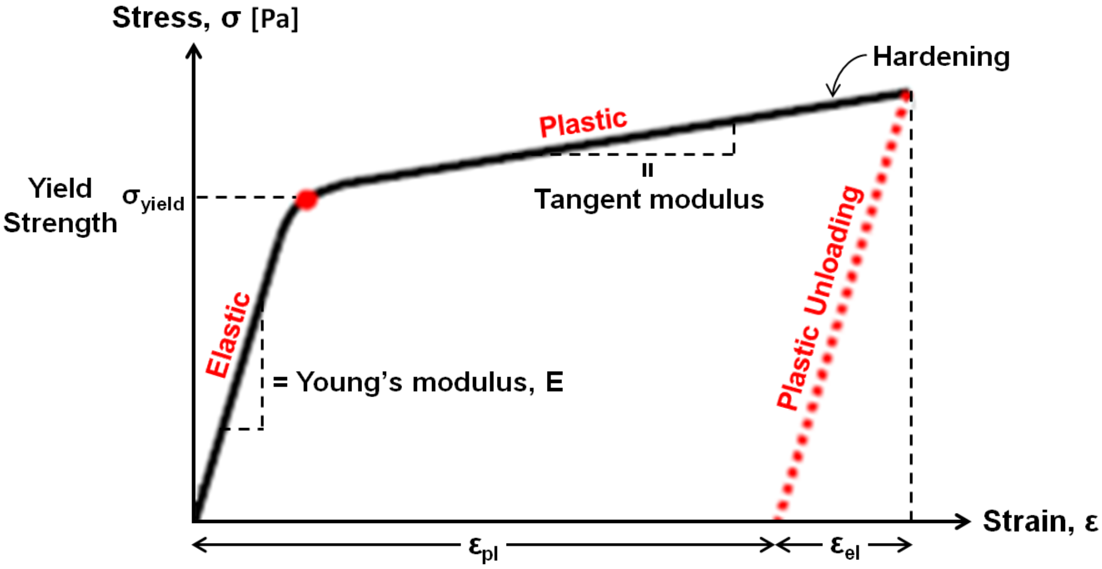

Figure 3.11: The uniaxial stress-strain curve (for a typical metal). The linear elastic part satisfies the stress-strain relationship of Hooke's Law given by Equation 3.4.

During elastic response, if the induced stresses are below the material's yield strength $\sigma_{\text{yield}}(T)$, the material can fully recover to its original shape upon unloading - this is called elastic unloading. On the other hand, when a ductile material experiences stresses beyond the elastic limit, it will yield with resulting permanent deformations upon unloading - this is referred to as plastic unloading (Figure 3.11). In this case, the total strain, ϵ, is composed of the elastic strain, ϵ_{el}, and the plastic strain, ϵ_{pl}. The portion of the overall strain that is recovered when an applied load causing the strain is removed is ϵ_{el}, while ϵ_{pl} represents the non-recoverable strain upon unloading that results in permanent deformations.

Plasticity is available as a non-linear material model in ANSYS® [68]. If the tangent modulus is zero, the model represents the perfectly plastic idealisation. For a perfectly plastic model, the stress will be kept at σ_{yield} for all higher strain values. If the stress is reduced, elastic unloading occurs. In the hardening case, once yield occurs, the stress needs to be continually increased in order to drive the plastic deformation.

Elastic-perfectly plastic materials exhibit no hardening and the yield surface remains unchanged. In the more general case, the evolution of the yield surface, in terms of size, shape and position during plastic deformation, is determined by hardening parameters. The description of how the yield surface changes with plastic deformation is called the hardening rule. In this work, the kinematic hardening rule is used in which the yield surface is defined to remain constant in size and translate in the direction of yielding [109].

Two different types of stress-strain curve representations - the bilinear model and the multilinear model - are possible for material data input in ANSYS® (Figure 3.12). Moreover, temperature-dependent values can be defined for both models via tabular input. The Bilinear Kinematic Hardening model can be introduced just by defining the yield strength and the tangent modulus in addition to the linear elastic modulus. The initial slope of the curve is in fact taken as the Young's Modulus of the material. At the specified σ_{yield}, the curve continues along the second slope defined by the tangent modulus. The tangent modulus cannot be less than zero nor greater than the Young's Modulus. The case of a tangent modulus equal to zero represents the elastic-perfectly plastic material model [68].

In a similar procedure, the Multilinear Kinematic Hardening model is described by a piecewise linear curve that is continuous from the origin and is defined by a number of stress and corresponding plastic strain points. The slope of the first segment of the curve must correspond to the Young's Modulus of the material and no segment slope should be larger. Moreover, for stress-strain curves at different temperatures, each stress-strain curve must have the same set of strain values. The slope of each stress-strain curve is assumed to be zero beyond the last user-defined stress-strain data point [68].

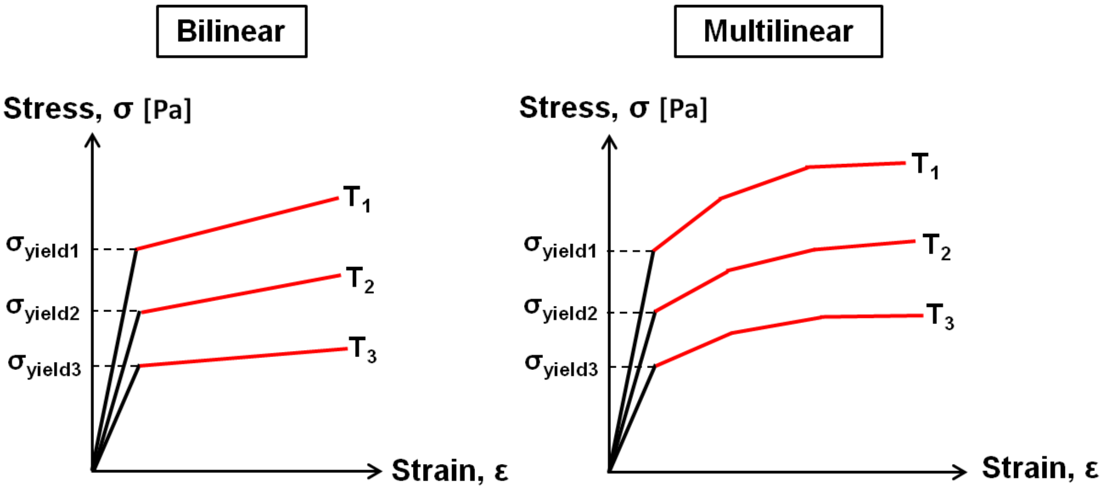

Figure 3.12: Two different types of stress-strain curve representations - the bilinear model (left) and the multilinear model (right). While the bilinear model consists of one constant slope (equivalent to the tangent modulus) after yielding, the multilinear model is composed of a series of straight lines upon yielding. Temperature-dependent stress-strain curves can be defined for both models via tabular input in ANSYS®.

3.3.4 Loading and boundary conditions

Accident cases entail rapid energy deposition on the hit structure. The thermal shock typically lasts from a few nanoseconds to some microseconds, depending on the bunch structure of the incoming beam. In the case of the asynchronous beam dump considered in this study, the thermal shock duration, τ_{shock}, is equal to the length of one bunch (1 ns), as will be explained in Section 4.2.1. In ANSYS®, the thermal load from the beam impact, as calculated by FLUKA, was applied as an instantaneous source of heat within the body of the collimator jaw. Transient thermal analyses were then performed for the whole collimator structure.

Thermal boundary conditions (BCs) included the convection on the internal surface of the cooling pipes and the thermal fluxes between the component interfaces. The heat convection coefficient of the inner wet surface of the cooling pipes was analytically calculated as a function of hydraulic parameters (thermal conductivity, kinematic viscosity) at the water temperature, water flow rate and inner diameter of the pipes, leading to a film coefficient of 13,500 W/m^{2}K on each pipe. Due to the very short duration of the beam impact, the cooling system does not exchange any heat with the jaw during this time so that the total deposited energy is equal to that of the beam. Moreover, thermal fluxes between the component interfaces were calculated based on the thermal conductance values provided for the contact interfaces as explained in Section 3.3.1.

With regard to structural constraints, the collimator jaw assembly was simply supported at its extremities (Figure 3.13), meaning that while the two ends could not move transversely (toward or away from the beam), one end could elongate (along the beam). The motion in the remaining degree of freedom (DOF) was zero by the symmetry condition. The effect of inner pressure due to the water flow on the cooling pipes was also considered. A pressure of 15 bar was experimentally measured [72] and an equivalent load was applied to the inner surface of the cooling pipes in the FE model.

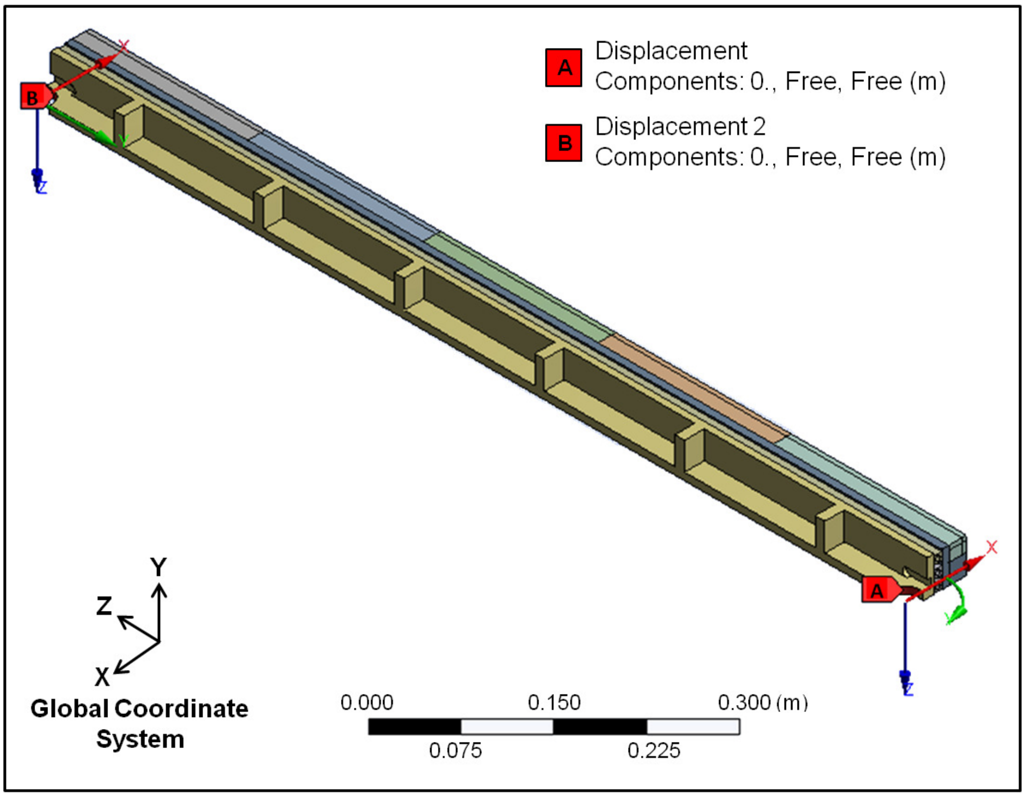

Figure 3.13: Back view of the collimator jaw assembly simply supported at its extremities. The coordinate systems at A and B are cylindrical and cartesian respectively.

The temperature $\{T\}$ and the displacement $\{u\}$ DOFs must be evaluated by solving both the thermal and structural problems, which are given in matrix form by Equations 3.5 and 3.6 respectively:

$$[C_{\text{thermal}}]\{\dot{T}\} + [k_{\text{thermal}}]\{T\} = \{Q_{\text{heatgen}}\} + \{Q_{\text{convection}}\} + \{Q_{\text{flux}}\} \tag{3.5}$$

$$[M]\{\ddot{u}\} + [C]\{\dot{u}\} + [K]\{u\} = \{F_{\text{thermal}}\} + \{F_{\text{pressure}}\}, \tag{3.6}$$

where $[C_{\text{thermal}}]$ is the thermal specific heat matrix, $[k_{\text{thermal}}]$ is the thermal conductivity matrix, $\{T\}$ is the temperature DOF vector, $\{\dot{T}\}$ is the time derivative of the temperature DOF vector, $\{Q_{\text{heatgen}}\}$ is the heat generation rate nodal load vector, $\{Q_{\text{convection}}\}$ is the convection nodal load vector, $\{Q_{\text{flux}}\}$ is the heat flux nodal load vector, $[M]$ is the mass matrix, $[C]$ is the damping matrix, $[K]$ is the structural stiffness matrix, $\{u\}$ is the displacement DOF vector, $\{\dot{u}\}$ and $\{\ddot{u}\}$ are the first and second time derivatives of the displacement DOF vector respectively, and finally $\{F_{\text{thermal}}\}$ and $\{F_{\text{pressure}}\}$ are the thermal strain and pressure nodal load vectors respectively.

The characteristic thermal diffusion time, $\tau_{\text{diffusion}}$, is the typical time it takes for heat energy to diffuse along distance l within the considered structure. One important term of comparison is the diffusion time with respect to the typical dimension of the beam or a fraction of this value. The $\tau_{\text{diffusion}}$ is calculated by Equations 3.7 [72, p. 117] and 3.8 [107, p. 68]:

$$\tau_{\text{diffusion}} = \frac{l^2}{\kappa_{\text{cc}}}, \tag{3.7}$$

$$\kappa_{\text{cc}} = \frac{k}{\rho c_{\text{p}}}, \tag{3.8}$$

where l [m] is the typical dimension of the structure along which heat diffusion is computed, κ_{cc} is the thermal diffusivity [m^2/s], k is the thermal conductivity [W/mK], ρ is the density [kg/m^3] and c_{p} [J/kgK] is the specific heat capacity at constant pressure.

As shown by Kalbreier et al. [110], it is possible to assume that no heat diffusion occurs during τ_{shock} because $\tau_{\mathrm{diffusion}}$ is generally much longer than τ_{shock}. This means that heat would not significantly diffuse across l during the shock duration. This is in fact the case for the studied accident scenarios as will be shown in Sections 4.3.2, 6.5.3 and 7.3.2.

Thus, given the rapidity of the phenomenon (τ_{shock}) when compared to the typical $\tau_{\mathrm{diffusion}}$, heat conduction plays a minor role on the short time scale. In this case, the thermal deformations are too small to affect the overall structural response. It is thus possible to consider such cases as weakly-coupled thermo-elastic problems where the elastic strains are influenced by the temperature distribution, but not the inverse. The non-linear transient thermal and structural analyses could be consequently decoupled and sequentially solved, with the calculated temperature field initially obtained used as an input for the evaluation of thermally induced stresses (Figure 3.14). Such an adopted approach means that very short time steps must be used to perform the analysis in order to maintain the validity of the short time scale and weakly-coupled thermo-elastic assumptions. The choice of the used time steps will be explained later by Equation 3.10.

The integration time steps (ITSs) and the mesh size need to be carefully chosen in order to capture the correct thermo-structural behaviour of the collimator jaw assembly. The rapid temperature increase provokes a dynamic response of the structure in terms of longitudinal and flexural vibrations, as well as propagation of thermal stress waves. The frequency range of these phenomena starts from a certain value, which corresponds to the first period of flexural oscillation of the jaw assembly, as calculated by Equation 3.9. Higher modes of longitudinal and transverse vibrations can reach a higher frequency range. Thus, this wide range of interest entails that simulations should have the correct time durations and ITSs to ensure that all the phenomena are correctly captured. Equation 3.9 [72, p. 117] is given by:

$$t_{\mathrm{flex}} = \frac{2}{\pi}\sqrt{\frac{ML^3}{EI}}, \tag{3.9}$$

where M, L and I are the mass [kg], length [m] and cross-sectional inertia [m^4] of the collimator jaw assembly respectively, and E is an equivalent Young's Modulus obtained as an average value between the various materials of the jaw assembly.

Moreover, the ITS also depends on the mesh size as given by Δt in Equation 3.10 [72, p. 124] that represents the Courant criterion [111] for the solution of dynamic structural problems:

$$\Delta t \leq \frac{0.9 L_{\mathrm{mesh}}}{c_{\mathrm{sound}}}, \tag{3.10}$$

where L_{mesh} [m] is a typical mesh size in the structural solution (0.001 m) and c_{sound} [m/s] is the speed of sound in the jaw insert material.

Although the implicit method is intrinsically stable, the Courant principle of stability should be applied to avoid numerical damping, which is typical of implicit codes. In ANSYS®, Equation 3.6 is solved implicitly, which means that $\{u\}$ is determined by computing the inversion matrix of $[K]$ while neglecting the mass and damping matrices in the process. The implementation of temperature-dependent material properties in the FE model introduces a non-linearity in the system. The matrix $[K]$ becomes a function of the displacement vector $\{u\}$ and hence, methods such as the Newton-Raphson method are used for the solution of non-linear equations. Meanwhile, each iteration carried out by an implicit solver is relatively computationally intensive due to the stiffness matrix inversion operation involved. In this study, the numerical simulations were performed using ANSYS® Academic Research licenses on a 32 GB RAM 4-core machine with a processor speed of 4.0 GHz.

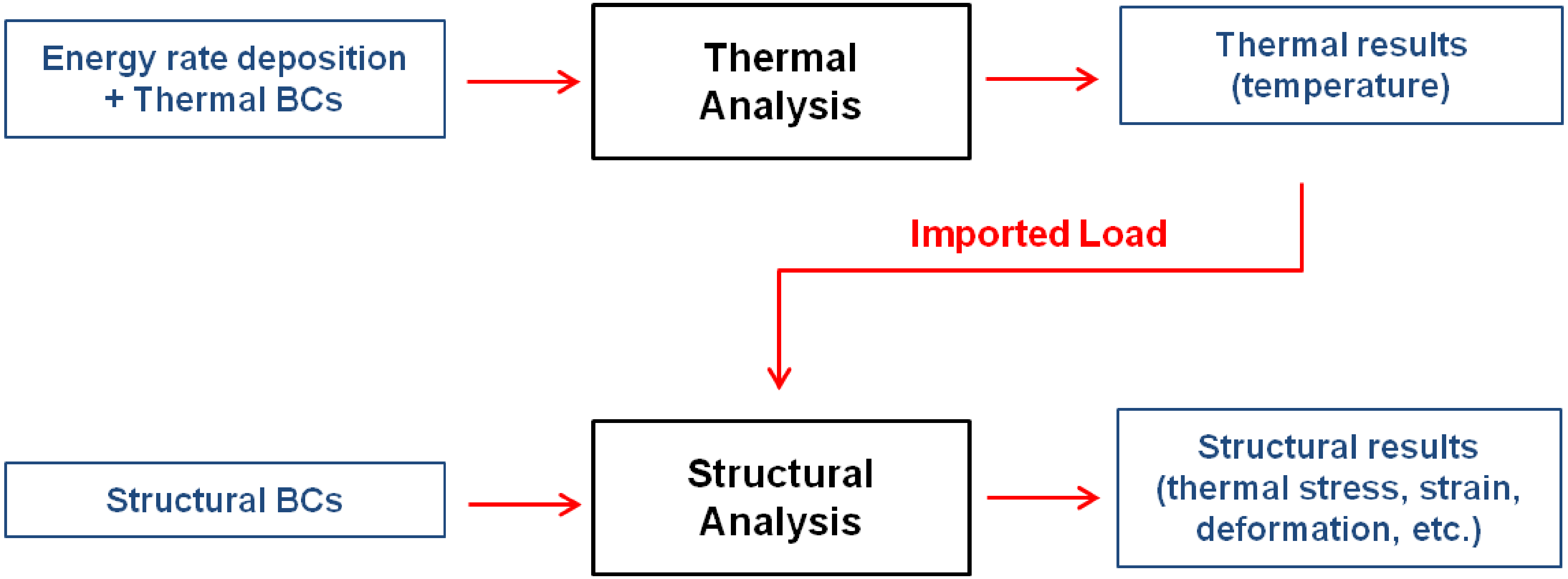

Figure 3.14: The data flow for a typical sequentially-coupled thermo-structural analysis. Inputs for the thermal analysis include the energy deposition maps provided from FLUKA and the applied thermal BCs (cooling convection and thermal conductance at the contact interfaces). Temperatures output from the thermal analysis are then applied as loads at different time steps in the structural analysis. Structural BCs (simply supported conditions and pressure on the inner surface of the cooling pipes) are defined and the structural analysis is then performed to give the resulting thermally induced effects such as thermal stresses and deformations.

The transient thermal and structural load cases were implemented as a sequence of load steps, as will be shown in Sections 4.3.2 and 7.3.2. The temperature distributions, obtained from the thermal analysis, were applied as a load at different time steps, in the structural analysis. ANSYS® linearly interpolates between load time steps, therefore closely following the actual temperature evolution to calculate deformations and other thermally induced effects (Figure 3.15).

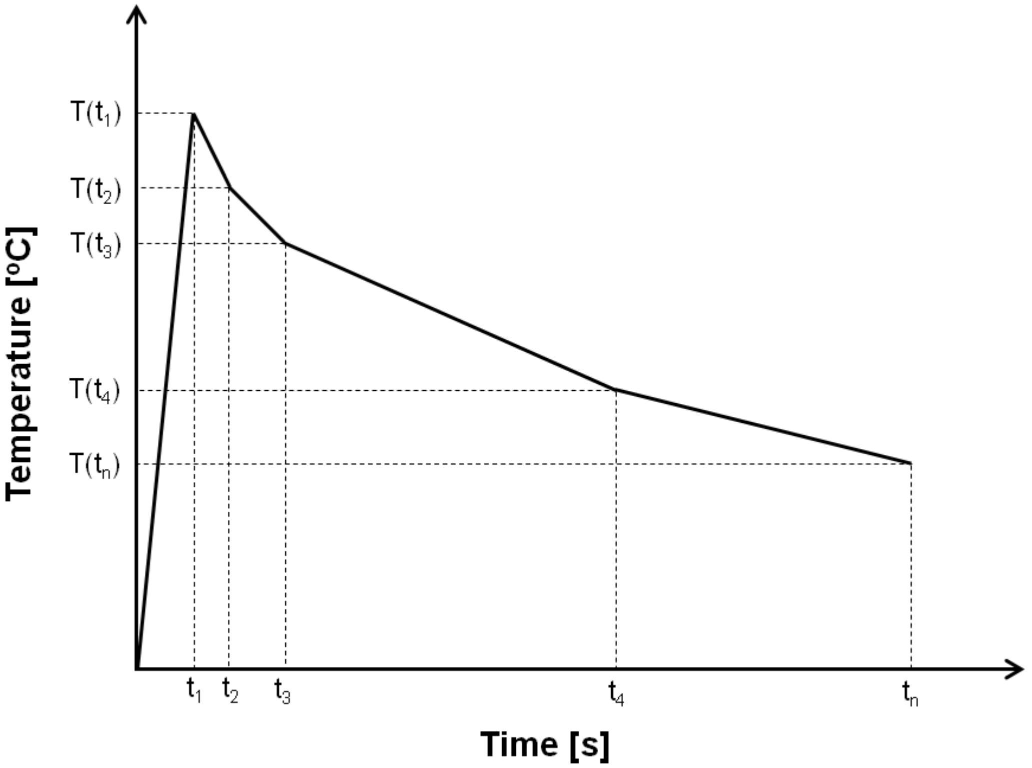

Figure 3.15: Temperature distribution as a function of time as applied from the thermal to the structural analysis. ANSYS® linearly interpolates between the load time steps, thus closely following the actual temperature evolution.

The thermo-mechanical solution was based on three sequential steps:

1. Once the heat load was known, the thermal problem could be solved and the temperature distribution could be calculated as a function of space and time.
2. The results of the temperature analysis were used as body loads in the structural analysis so that the dynamic thermal stresses and displacements could be evaluated.

3. A final quasi-static step was necessary in order to calculate any potential permanent deformations of the structure once the dynamic response had vanished.

This approach, generally valid for structures submitted to rapid heat loads, has already been successfully applied to the study of the LHC collimators [72]. It will be shown that the case studies presented in this work are characterised by the development of stress waves in the plastic domain due to the absence of material melting for cases studied within the structural domain, and as explained in Section 2.3.2, such cases can still be reasonably well-treated with FE codes using an implicit scheme of integration such as ANSYS®. Moreover, the use of an implicit code allows the evaluation of any potential plastic deformations through the performance of a static structural analysis after the dynamic effects have disappeared. Thus, the thermo-mechanical problem in this study was completely solved exploiting the implicit code ANSYS®, thereby avoiding the use of different codes for dynamic and static analyses.

3.4 Conclusions

The LHC collimators should withstand accident scenarios entailing large amounts of very rapidly deposited energy. Numerical methods have found an important application in the study of LHC collimators as has been presented in this chapter. An FE model, based on an implicit algorithm of integration, was thus developed in this study in order to evaluate both thermally induced vibrations on the short time scale as well as permanent plastic deformations on the long time scale resulting from a beam impact.

This chapter has given an overview of the FLUKA-ANSYS® simulation framework, with a focus on the numerical FE model developed in ANSYS®. The component setup, FE discretisation, material modelling, loading and boundary conditions were described in detail. This numerical model will be used in Chapter 4 and Chapter 7 in order to investigate the thermo-mechanical response of a TCT in defined novel jaw error cases based on an asynchronous beam dump. Moreover, the validity of the developed numerical model will be provided in Chapter 6 through a comparison between simulations and experimental measurements on a TCT at the CERN HiRadMat facility.

Chapter 4

Jaw-Beam Angle Case Studies

4.1 Introduction

Accident scenarios must be well studied in order to assess if the collimator design is robust against possible error scenarios in operation. One of the serious accident scenarios identified within the LHC is an asynchronous beam dump. This chapter presents a number of novel jaw error cases that are derived based on conservative assumptions of this accident scenario and also take into account angular misalignment errors of the collimator jaw. The numerical FEM approach presented in Chapter 3 is implemented and sequential fast-transient thermo-structural analyses are performed in the elastic-plastic domain. The thermo-mechanical response of TCTs to beam impact in these realistic scenarios is evaluated. Relevant collimator damage limits are taken into account, with the aim to identify optimal operational conditions of the LHC.

4.2 Studied accident scenario

4.2.1 Asynchronous beam dump

One of the worst accident scenarios in the LHC corresponds to an asynchronous trigger of the beam dumping system [45]. The LHC beam dumping system is located at Point 6 of the LHC (Figure 1.11) and it is shown schematically in Figure 4.1. Its function is to fast-extract the beam in a loss-free way from each LHC ring and to transport it to an external absorber.

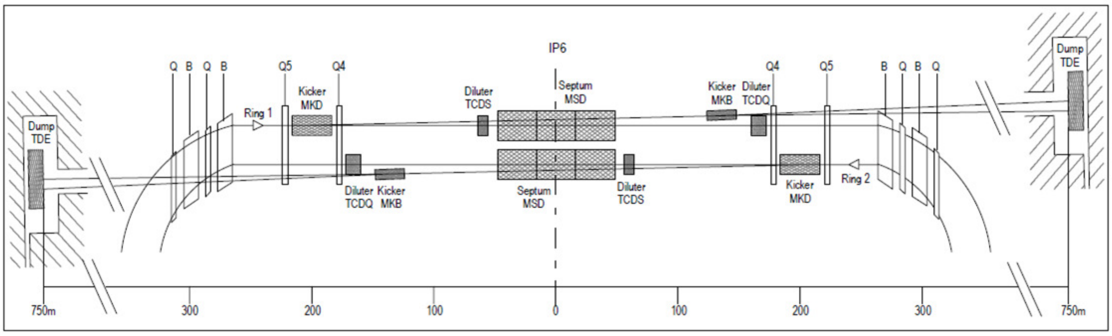

Figure 4.1: Schematic layout of the beam dumping system elements around Point 6 of the LHC [112].

A loss-free extraction requires a particle-free abort gap in the circulating beam, during which the field of the ejection dump kicker (MKD) magnets can rise to its nominal value. In order to achieve this, the beam dumping system is composed of the following for each ring of the collider:

1. Horizontally deflecting MKD magnets
2. Vertically deflecting steel ejection dump septum (MSD) magnets
3. Diluter dump kicker (MKB) magnets
4. An external graphite dump absorber block known as the dump for ejected beam (TDE)

The MKD system, which consists of 15 fast-pulsed extraction magnets and their generators, horizontally deflects the beam into the MSD magnets that then deflect the beam vertically out of the LHC machine into the beam-line. The extracted beam is then swept in a quasi-circular figure by two sets of orthogonally deflecting MKBs. The beam size is increased in both planes and ultimately, the beam is deposited 600 m further downstream onto the TDE (Figure 4.1) [112, 113].

An asynchronous beam dump refers to a situation where one (or more) of the 15 pre-charged MKD circuits spontaneously fires out of time with the particle-free abort gap. The result of this accident scenario is that the beam is partially horizontally deflected. Consequently, spraying of beam pulses onto LHC machine elements occurs before the MPS can fire the remaining kicker circuits and bring the beam to the dump. Such unsynchronised beam aborts cannot be excluded. Moreover, if they occur, they can seriously damage downstream accelerator components as they might result in one or more high energy density bunches directly impacting the MSD magnets, the experimental low-β triplet magnet apertures and the horizontal collimators.

A system of protection devices is however in place in order to prevent the mis-directed bunches from causing local equipment damage. Such dilution devices include a dedicated fixed dump septum collimator (TCDS) and a movable TCDQ. These are placed in front of the MSD magnets and the SC quadrupole Q4 respectively (Figure 4.2). Such devices also prevent bunches with large excursions from causing damage where aperture is restricted (notably the arcs at 450 GeV and the low-β insertions around the LHC experiments at 7 TeV) as well as reduce the number of bunches deposited on the collimator jaws. If the collimators are set up correctly, sensitive equipment, such as the SC magnets, is in the shadow of the TCDQ block and is thus protected from the mis-directed bunches in case of such a failure. While the TCDQ, and the robust TCP and TCS system, are designed to withstand full bunch beam impacts and to protect the cold regions of the LHC and the experiments, there may however be machine conditions [48, 49] that expose the TCTs and thus put them at risk of damage. This is for example the case during the setup of the collimation system.

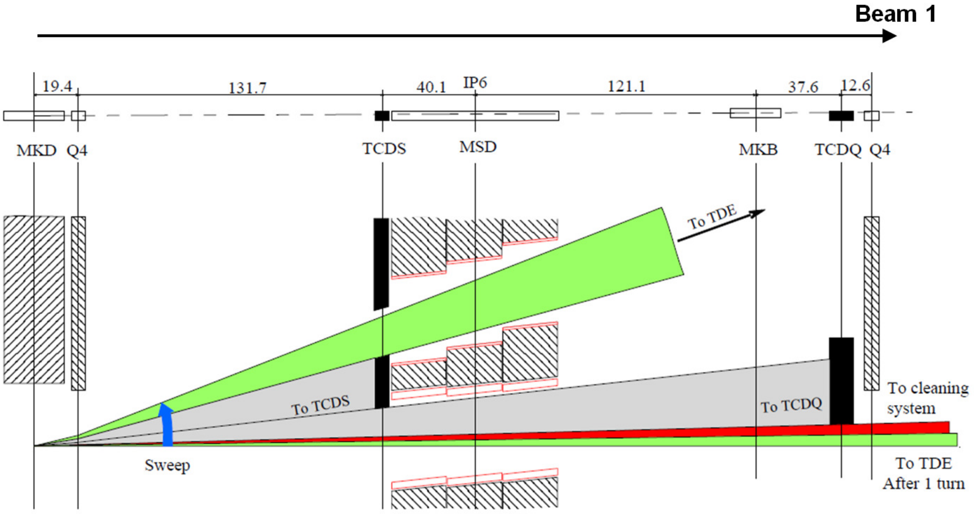

Figure 4.2: Schematic and functional layout of the TCDS and the TCDQ diluter elements for Beam 1 [113].

The probability that an asynchronous beam dump event occurs was originally estimated to be once per year [45]. However, the probability that a TCT is hit directly by a full intensity bunch is lower as other conditions must be simultaneously present for this to happen. When an asynchronous abort is detected, the remaining MKDs are re-triggered within 0.9 μs and only one bunch should escape the beam dump system. This results in a thermal shock duration of 1 ns in case of a beam impact on a collimator involving one bunch. In this context, a scenario with such combined errors [49] was considered in this thesis as a conservative case study in order to understand the consequences of a potentially severe beam impact event on a tungsten-based collimator.

4.2.2 Studied jaw error cases

Different jaw error cases were identified based on the worst case scenario described in Section 4.2.1. These novel jaw error cases take into account conditions when the planar collimating surface of the horizontal TCT jaw is either exactly parallel to the beam or has a slight inclination of a few milliradians due to misalignment errors of the collimator installation at the beam-line (Figures 4.3 and 4.4).

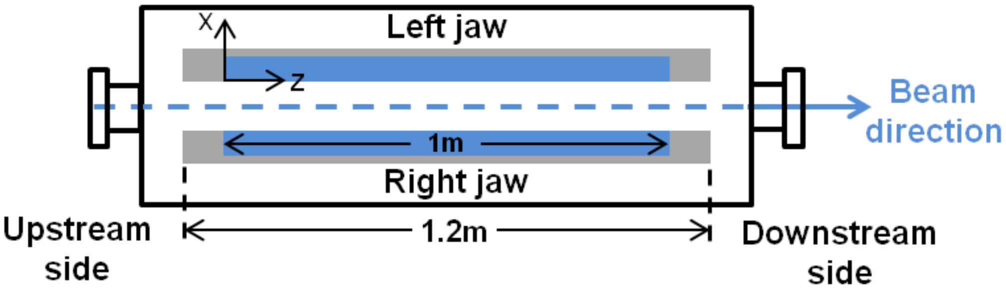

Figure 4.3: Top schematic view of a horizontal TCT (not to scale). The blue bars represent the five tungsten jaw inserts (total length = 0.2 m × 5 = 1 m) that are screwed to the copper housing (grey).

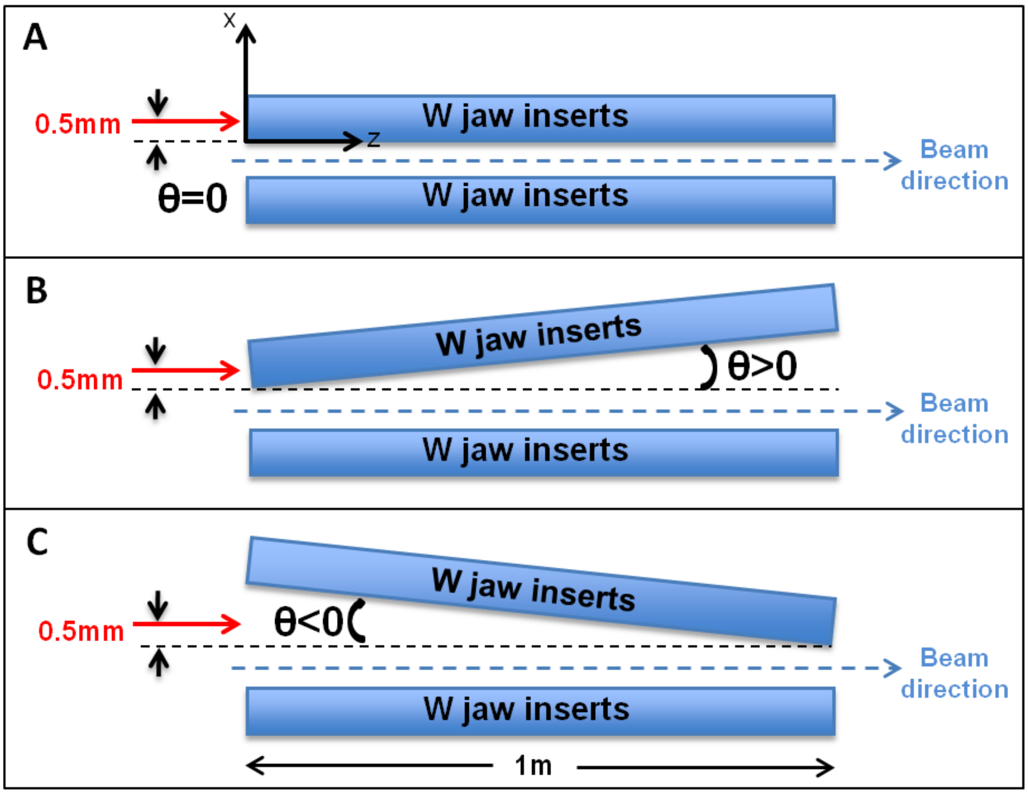

Figure 4.4: Schematic diagrams (not to scale) of the studied jaw error cases: an ideal case that constitutes perfect alignment of the collimator jaws with respect to the beam direction (A), and cases with a tilt (θ) of one collimator jaw due to misalignment errors (B, C). Each blue bar comprises the five jaw inserts, where the dimensions of each insert are 20 mm (x) × 34 mm (y) × 200 mm (z), while the considered beam impact parameter is 0.5 mm in the x-direction. The sign of the tilt angle is shown and the dashed black line refers to the collimator position in design orbit.

The studied jaw error cases used a beam bunch of 1.30 × 10^{11} protons with a Gaussian transverse profile of 0.30 mm (σ_{x}) × 0.30 mm (σ_{y}) RMS beam size. A charge of 1.30 × 10^{11} protons per bunch constitutes a conservative but realistic approach with respect to the nominal bunch intensity (1.15 × 10^{11} protons per bunch) [47]. This choice also serves as a good representation of the LHC Run 1 operational conditions, during which the design bunch intensity was surpassed and the average bunch intensities in 2011 and 2012 operation were 1.20 × 10^{11} and 1.40 × 10^{11} protons per bunch respectively (Table 1.1).

The beam impact parameter, which is the transverse depth at which the beam first makes contact with the jaw material, was assumed to be 0.5 mm. Studies with an impact parameter of 2 mm have been carried out in [47, 114], which investigated the impact of the full mis-directed bunch on the bulk material of the jaw inserts. By using an impact parameter of 0.5 mm in this study, the effects of grazing of the mis-directed bunch on the TCT's planar collimating surface were investigated. In this way, this study complements the other studies in analysing a range of reasonable impact parameter values for an asynchronous beam dump scenario [27].

As will be described in Section 4.3.1, a FLUKA study was carried out for different jaw-beam angles and beam energies in order to provide the required inputs for the thermo-mechanical analyses. The tilt of one collimator jaw was changed from θ = -5 mrad to θ = +5 mrad in steps of 1 mrad where the tilts of ±5 mrad were studied as limiting cases. Thus, this study presents the cases of $\theta = 0$ mrad and $\theta = \pm5$ mrad to represent the studied angle range as well as the case of θ = -1 mrad due to the indications that such a tilt can actually reduce the damage caused by an asynchronous beam dump on a hit collimator.

Table 4.1 summarises the studied cases. The lower values of deposited energy for the tilted jaw cases when compared to the perfectly aligned ones indicate more shower leakage from the faces of the collimator jaw. As shown schematically in Figure 4.4, when the tilt angle is +5 mrad, the beam strikes the upstream face and the nominal exit point is 10 cm away; when the tilt angle is -5 mrad (-1 mrad), the beam strikes the inner jaw surface 10 cm (50 cm) from its downstream end.

Table 4.1: List of studied jaw error cases. The convention for the positive and negative values of the angle is as depicted in Figure 4.4. The LHC operation started at a lower-than-design energy of 3.5 TeV in 2010, with the goal to reach the design parameters of 7 TeV per beam in the future.

Case	**Energy** [TeV]	**Angle, θ** [mrad]	**Deposited energy on 1 jaw** [kJ]	**TNT equivalent** [g]
1	7	0	48.50	11.56
2	7	+5	12.11	2.89
3	7	-5	10.32	2.46
4	3.5	0	23.08	5.50
5	3.5	+5	6.39	1.52
6	3.5	-5	5.22	1.24
7	7	-1	29.73	7.09
8	3.5	-1	14.18	3.38

4.3 Numerical analysis

4.3.1 FLUKA energy deposition maps

A FLUKA jaw-beam angle scanning study was carried out in order to provide inputs for the ANSYS® calculation (Figure 4.5). The general inputs of beam size, intensity and impact parameter given in Section 4.2.2 were used in a simplified impact model in FLUKA in order to investigate what happens to the collimator structure in case of different jaw-beam angles and beam energies.

4.3.2 Finite element modelling

The developed numerical FEM approach described in Chapter 3 was implemented. The detailed modelling approach, specific to the jaw-beam angle case studies considered in this chapter, is described below.

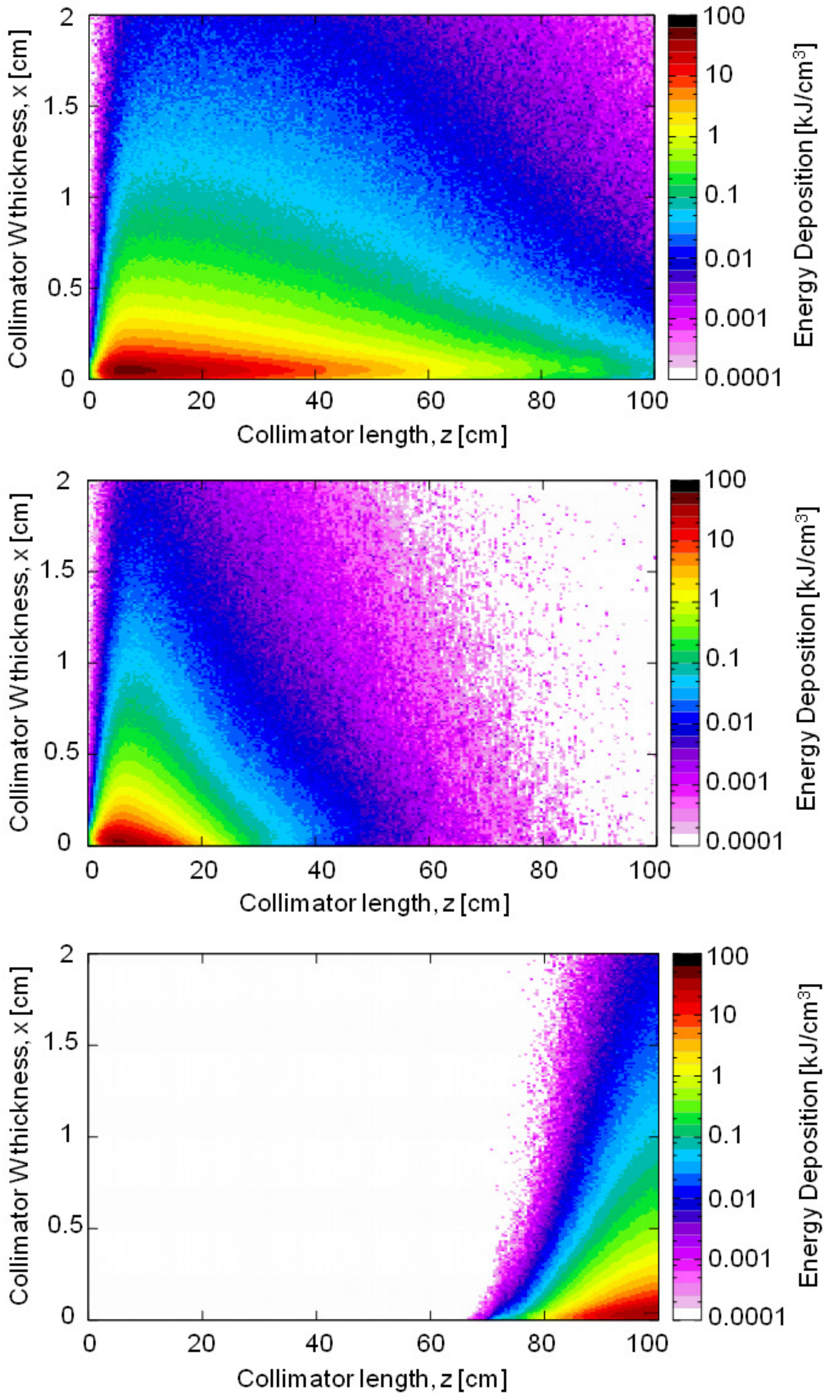

Figure 4.5: Comparison of the FLUKA energy deposition maps of the tungsten collimator jaw inserts for the different jaw-beam angle case studies. All cases consider 1 LHC bunch with 1.30×10^{11} protons, a beam size of 0.30 mm × 0.30 mm and an impact parameter of 0.5 mm. These maps show energy deposition x-z distributions (in kJ/cm^3) along the symmetry plane (y=0) for a 7 TeV particle beam impact case at $\theta = 0$ mrad (top), $\theta = +5$ mrad (middle) and $\theta = -5$ mrad (bottom) angles (results obtained in collaboration with L. Lari, CERN).

Geometry, component setup and FE discretisation

The jaw-beam angle case studies evaluated beam impacts on the left collimator jaw assembly, whose geometry and component setup were described in Section 3.3.1. Moreover, the 3D model of the lower symmetrical half of the left jaw assembly was discretised as shown in Section 3.3.2.

Material modelling

As described in Section 2.2.3, the material of the TCT jaw inserts is a commercial alloy of tungsten, known as INERMET® 180, and composed of W (95 wt.%), Ni (3.5 wt.%) and Cu (1.5 wt.%) [59]. Data providing properties of such a metal alloy under extreme conditions is not easily available. Thus, in this study, it was decided to use the more defined temperature-dependent thermal and structural material properties of pure tungsten for the jaw inserts (Figures 4.6, 4.7 and 4.8).

Figure 4.9 shows that a bilinear kinematic hardening model at different temperatures was defined for the jaw inserts. The values of $E(T)$ and σ_{yield} were extracted from Figure 4.7 resulting in an elastic-perfectly plastic idealisation as described in Section 3.3.3. Given the complexity of the simulations involved, a 5% modelling error (resulting from using pure tungsten instead of INERMET® 180) is still considered reasonable as highlighted in [47] where a similar approach was adopted.

The OFE-Cu of the block housing, the Cu-Ni alloy of the cooling pipes and the GlidCop® AL-15 of the back stiffener were modelled with the thermo-physical and structural properties given in Tables 4.2, 4.3 and 4.4 respectively.

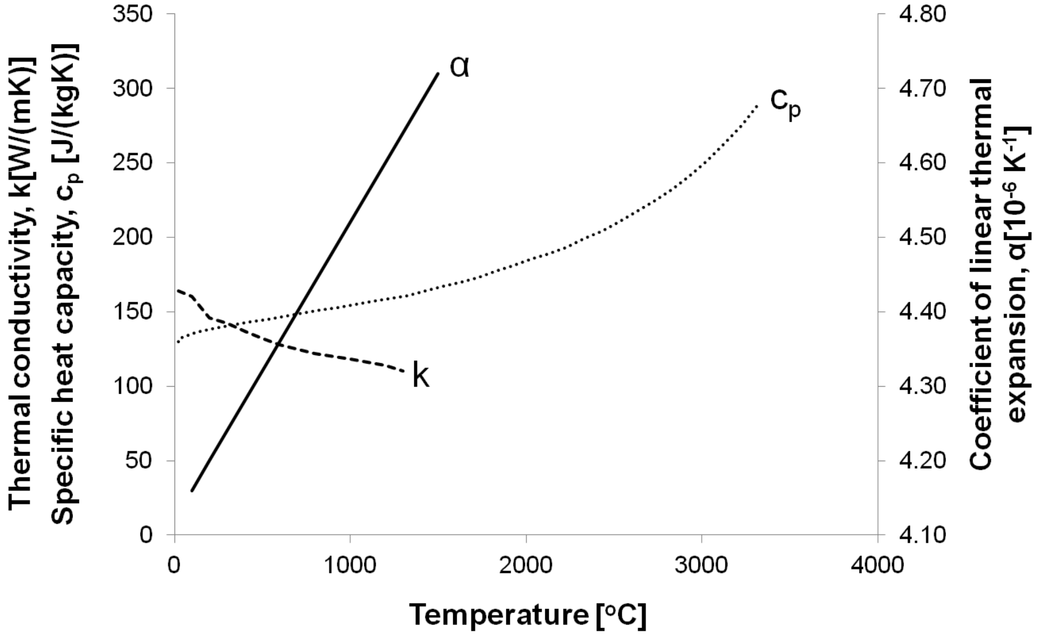

Figure 4.6: Temperature-dependent thermal properties of tungsten used for the material model of the collimator jaw inserts. The density was assumed constant at $\rho = 19{,}300$ kg/m^3 [115].

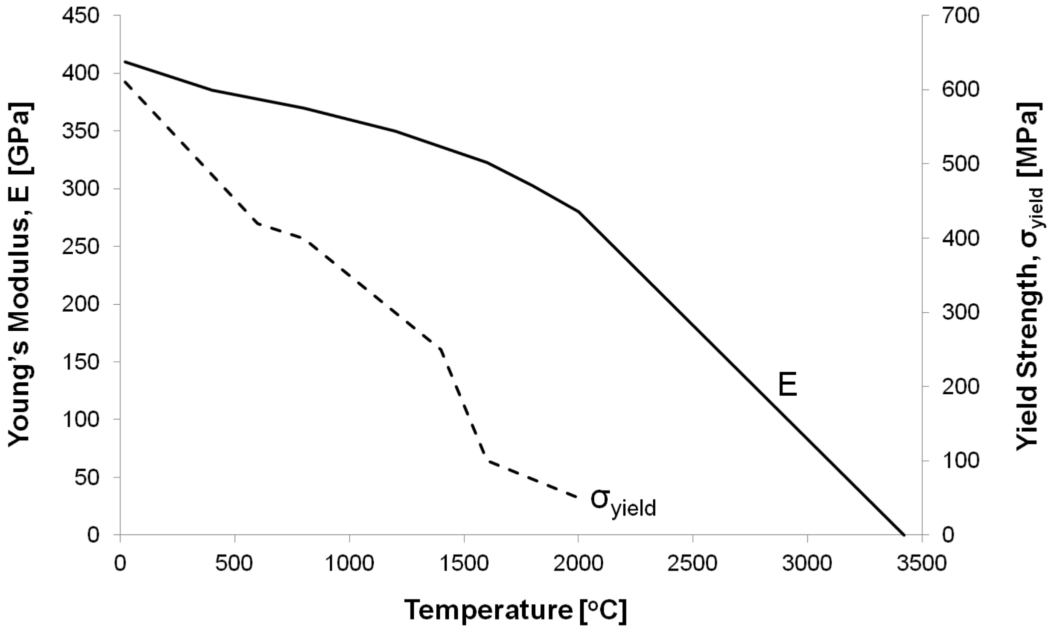

Figure 4.7: Temperature-dependent structural properties of tungsten used for the material model of the collimator jaw inserts. The very small values of E on nearing the melting temperature of the material are due to the fact that the material loses its shear strength at such high temperatures and starts to behave like a fluid [115].

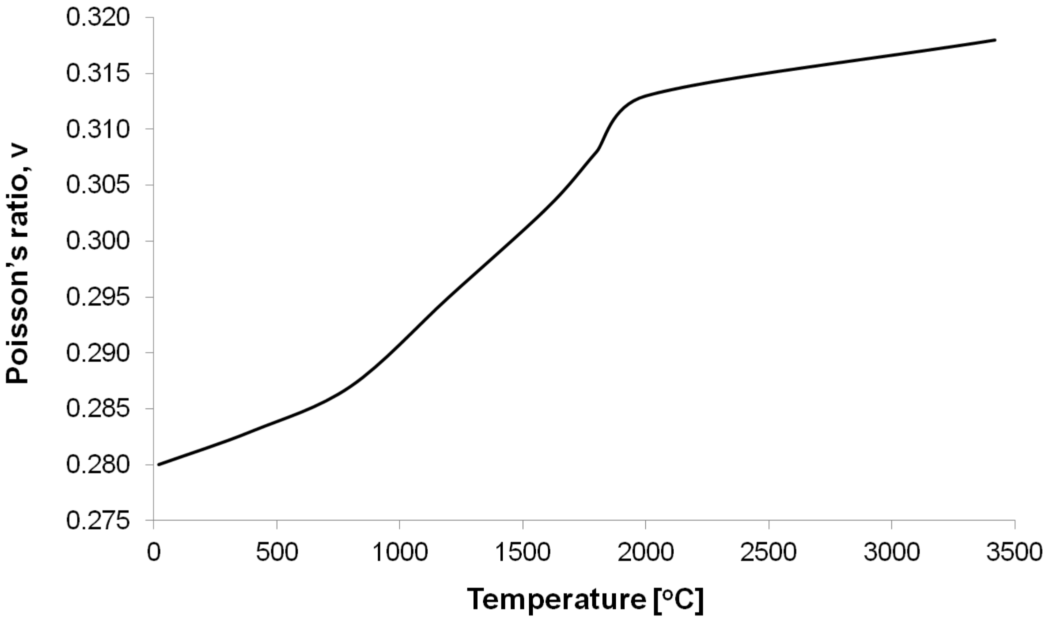

Figure 4.8: The temperature-dependent Poisson's ratio ν of tungsten used for the material model of the collimator jaw inserts [115].

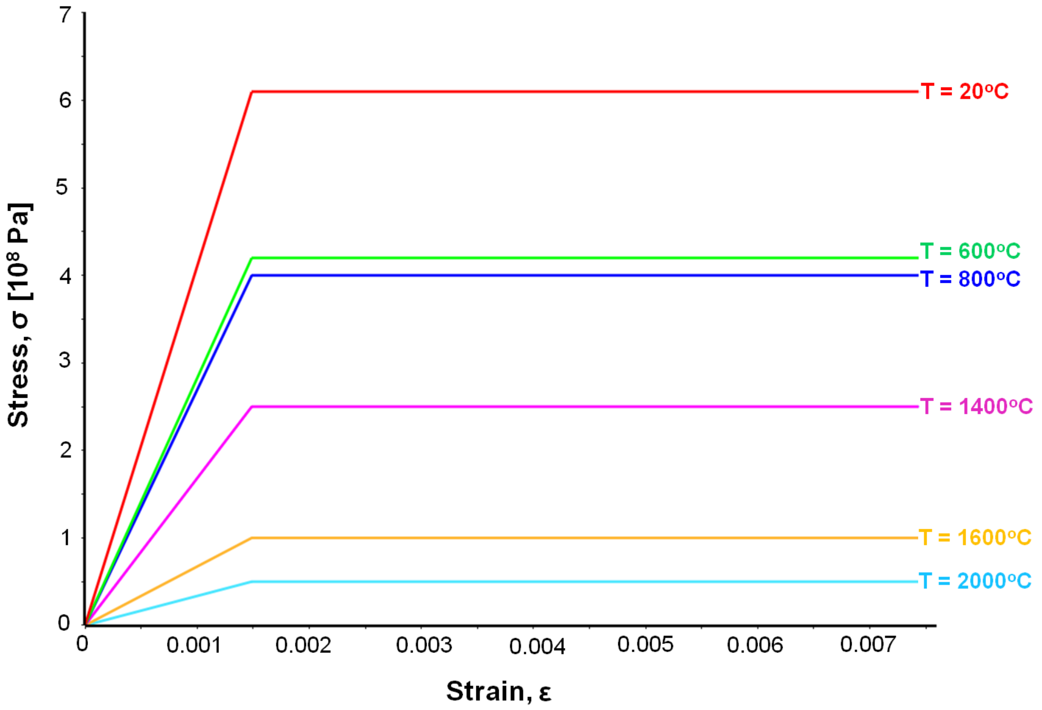

Figure 4.9: Elastic-perfectly plastic material models used for the collimator jaw inserts (material: pure tungsten). The temperature-dependent structural properties (elastic E and σ_{yield}) of tungsten are extracted from Figure 4.7.

Table 4.2: Thermo-physical and mechanical properties of OFE-Cu at ambient temperature used for the material model of the block housing.

Property	**Value**
Density, ρ [kg/m^3]	8940
Specific heat capacity, c_p [J/kgK]	383.46
Thermal conductivity, k [W/mK]	400.68
Coefficient of linear thermal expansion, α [K^{-1}]	1.52×10^{-5}
Young's Modulus, E [GPa]	105
Poisson's ratio, ν	0.343

Table 4.3: Thermo-physical and mechanical properties of the Cu-Ni alloy at ambient temperature used for the material model of the cooling pipes.

Property	**Value**
Density, ρ [kg/m^3]	8900
Specific heat capacity, c_p [J/kgK]	380
Thermal conductivity, k [W/mK]	50
Coefficient of linear thermal expansion, α [K^{-1}]	1.71×10^{-5}
Young's Modulus, E [GPa]	130
Poisson's ratio, ν	0.345

Table 4.4: Thermo-physical and mechanical properties of GlidCop® AL-15 at ambient temperature used for the material model of the back stiffener.

Property	**Value**
Density, ρ [kg/m^3]	8900
Specific heat capacity, c_p [J/kgK]	250
Thermal conductivity, k [W/mK]	320
Coefficient of linear thermal expansion, α [K^{-1}]	1.65×10^{-5}
Young's Modulus, E [GPa]	130
Poisson's ratio, ν	0.300

Loading and boundary conditions

As explained in Section 3.3.4, the $\tau_{\text{diffusion}}$ for the jaw inserts must be calculated using Equations 3.7 and 3.8. The transverse edge length of one mesh element in the thermal solution (0.10 mm) was considered as the typical dimension of the structure along which heat diffusion is computed; this characteristic dimension is also representative of a fraction of the beam dimension (0.30 mm) as specified in Section 3.3.4. Therefore, considering l = 0.10 mm and pure tungsten as the material of the jaw inserts, $\tau_{\text{diffusion}}$ was found to be approximately 153 μs for the studied jaw error cases. Since τ_{shock} was equal to the length of 1 bunch, i.e. $\tau_{\text{shock}} = 1$ ns, this confirmed that $\tau_{\text{diffusion}} >> \tau_{\text{shock}}$. Thus, it was possible to assume that no heat diffusion occurred during τ_{shock} and that the thermal and structural analyses could be decoupled and sequentially solved, provided very short time steps were used.

The first period of flexural oscillation of the jaw assembly was approximately 100 Hz (Equation 3.9). Since higher modes of vibrations could reach a frequency range on the order of kHz, the duration of the simulations was chosen to be, at least, of the order of 100 ms compared with an ITS of the order of 1 μs for the cooling time after the beam impact. In this way, all the phenomena could be correctly captured. Temperature evolution was simulated until 120 ms according to the typical response time of the structure (t_{flex} = 10 ms as calculated by Equation 3.9).

A more accurate value of the ITS can be calculated using the analytical estimation of the Courant criterion given by Equation 3.10. Using $L_{\text{mesh}} = 1 \times 10^{-3}$ m and $c_{\text{sound}} \approx$ 5180 m/s [115], the minimum step size was fixed to 0.1 μs for the structural analysis after the beam impact in order to ensure the capture of all dynamic phenomena. Due to the unconditional stability of implicit integration schemes, the ITS could be progressively incremented (Table 4.5). In this way, excessive CPU time of calculation was avoided while still ensuring that the higher frequency phenomena were correctly captured on the very short time-scale. Moreover, temperature distributions were applied as a load at different time steps in the structural calculation (Table 4.5).

Table 4.5: Load step sequences used for the FEM transient thermal and structural analyses in the jaw-beam angle case studies. The first load step represents the beam impact while the remaining load steps represent the cooling time after the beam impact. The computational time needed to achieve the given structural ITSs is very significant (∼3 weeks per simulation on a 32 GB RAM 4-core machine with a processor speed of 4.0 GHz).

Load Step Number	**Load Step End Time** [s]	**Thermal ITS,** $\Delta t_{\mathbf{thermal}}$ [μs]	**Structural ITS,** $\Delta t_{\mathbf{structural}}$ [μs]	**Imported Temperature Load Time Step** [s]
1	1.00×10^{-9}	1.25×10^{-4}	1.25×10^{-4}	1.00×10^{-9}
2	1.00×10^{-6}	0.10	0.10	1.00×10^{-6}
3	1.00×10^{-4}	2.50	1.00	1.00×10^{-4}
4	2.00×10^{-3}	20.00	10.00	2.00×10^{-3}
5	0.02	200.00	100.00	0.02
6	0.06	500.00	250.00	0.06
7	0.12	500.00	250.00	0.12

4.4 Results and evaluation

4.4.1 Thermal analyses

A preliminary assessment of the extent of beam-induced damage was done by evaluating the maximum temperatures reached and consequently, the dimension of the molten region on the jaw inserts. The first step of solution was a transient thermal analysis, where given the energy deposition map, it was possible to calculate the temperature distribution and its evolution over time. During the 1 ns beam impact duration, the system received all the energy and reached the maximum temperature on the collimator jaw inserts.

The studied jaw error cases (Table 4.1) led to different results, both in terms of peak temperature value as well as its location (Figure 4.10). The temperature computation was done starting from the internal energy value and using the heat capacity and density of the solid material. For this reason, the simulated temperature values are realistic only in the solid material part of the component and temperatures exceeding the melting temperature are thus shown in dashed lines.

On analysing the temperature distribution results (Figure 4.10), it is clear that in most of the cases, the melting temperature of the jaw insert material was exceeded in certain regions. The molten region caused by the beam impact signifies the formation of a groove on the jaw surface. The high temperatures reached and the extent of the molten region prove the highly destructive nature of the LHC beams.

The impact of the beam at different jaw-beam angles also influenced the spread in the energy deposition and thus, the cross-sectional temperature distribution on the collimator jaw inserts. The differences in the extent of the molten region at 7 TeV, in particular between the most loaded case (‘7 TeV, 0 mrad’) and the least loaded case (‘7 TeV, -1 mrad’), is evident (Figure 4.11).

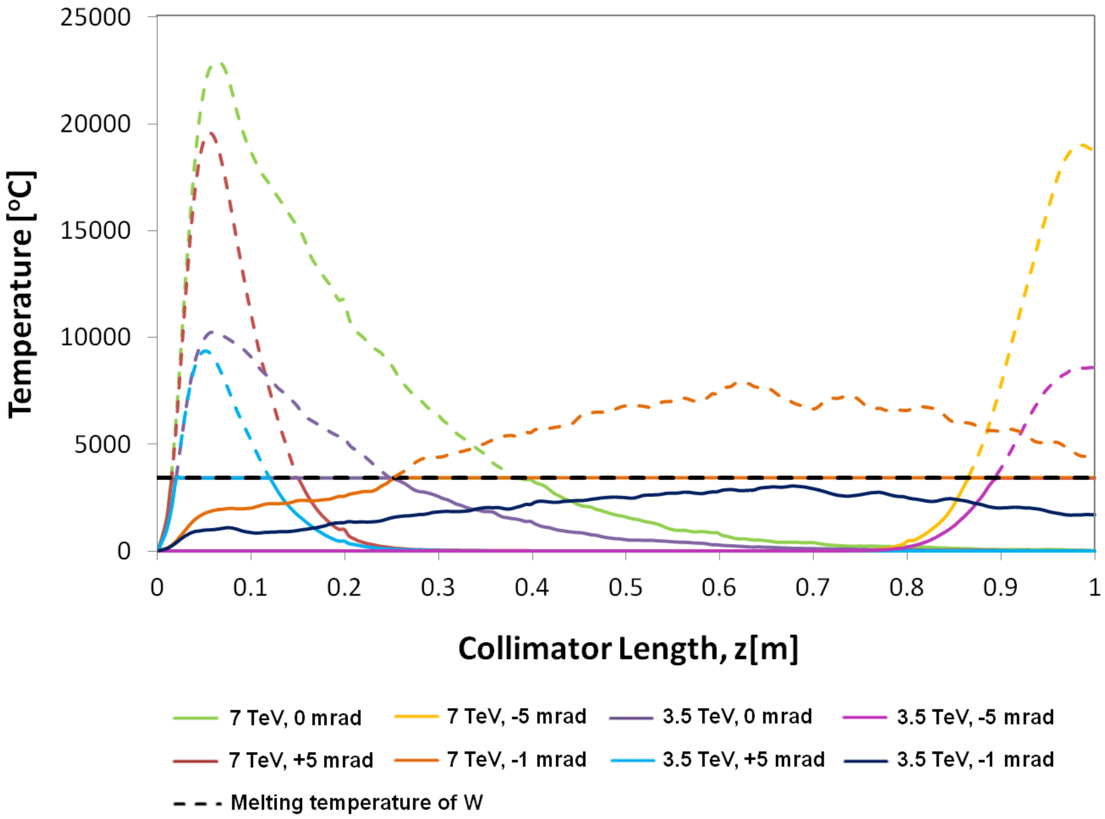

Figure 4.10: Temperature peak profiles along the beam direction for the different jaw-beam angle error cases. The melting temperature of the jaw inserts is marked at 3420 °C, assuming pure tungsten as the jaw insert material. The reason for the dashed graph lines above the melting temperature is that the simulated temperature values are realistic only in the solid material part of the component.

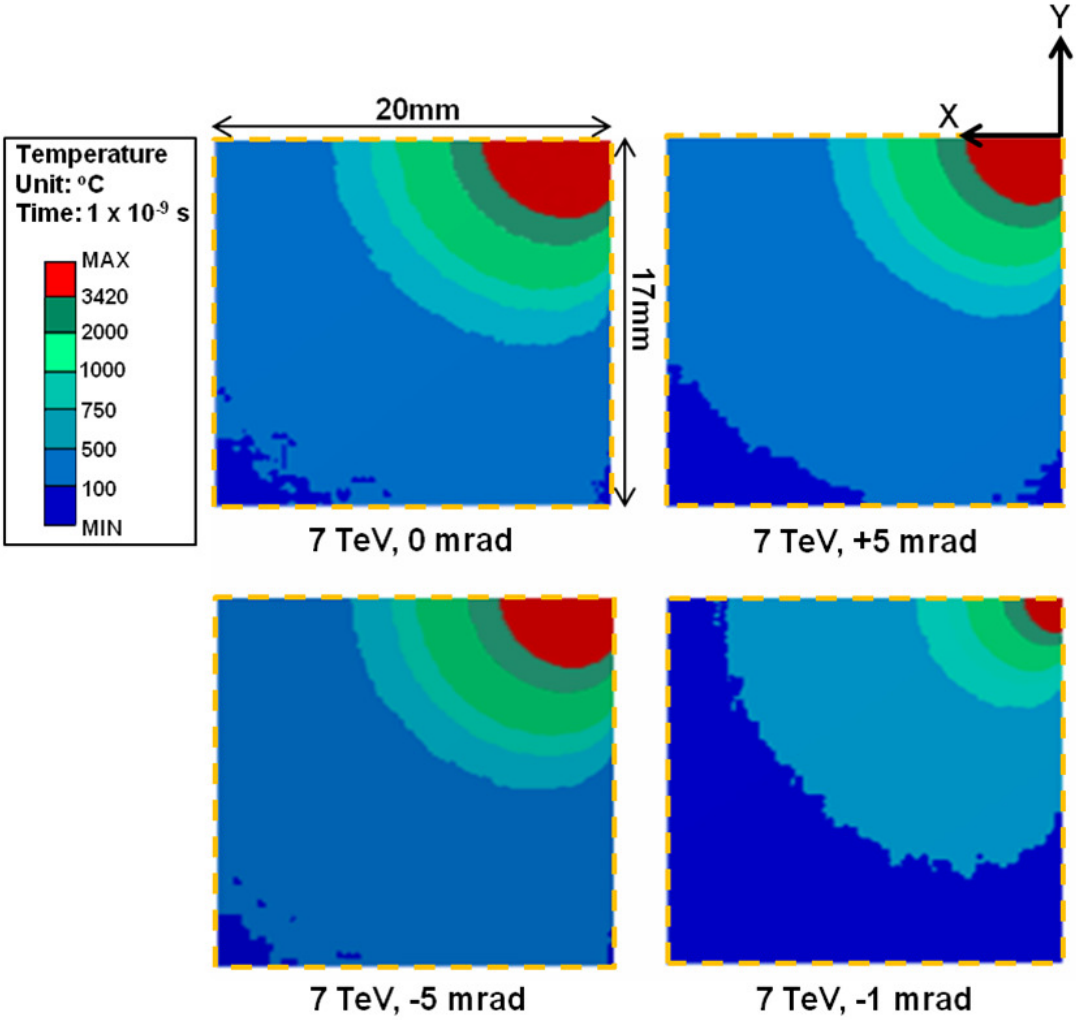

Figure 4.11: Comparison of the cross-sectional temperature distributions at $T_{\max}$-section for the different jaw-beam angle error cases after the beam impact at 7 TeV. The red region represents temperatures exceeding the melting temperature of pure tungsten (3420 °C). The enclosed area is the same as that shown enclosed within the dashed yellow line in Figures 3.6 and 3.7.

An analysis of the temperature peak profiles in Figure 4.10 also shows that the '7 TeV, -1 mrad' and '3.5 TeV, -1 mrad' cases exhibit different behaviour when compared to the other scenarios. The 0.5 mm impact parameter and -1 mrad jaw tilt mean that the first point of impact of the central 1σ of the beam (assumed 0.30 mm wide RMS) was spread between z = 0.2 m and z = 0.8 m along the collimator length, thus reducing the peak thermal load. As a comparison, at θ = -5 mrad, the same first point of impact of the 0.30 mm RMS beam was only spread between z = 0.84 m and z = 0.96 m.

Although the '3.5 TeV, -1 mrad' case involved a larger energy deposition than the '3.5 TeV, ±5 mrad' cases (Table 4.1), the former case has a better temperature distribution along the jaw as shown in Figures 4.10, 4.12 and 4.13. This was a very interesting observation; hence it was decided to focus on the '3.5 TeV, -1 mrad' case in Section 4.4.2 for further detailed structural analyses.

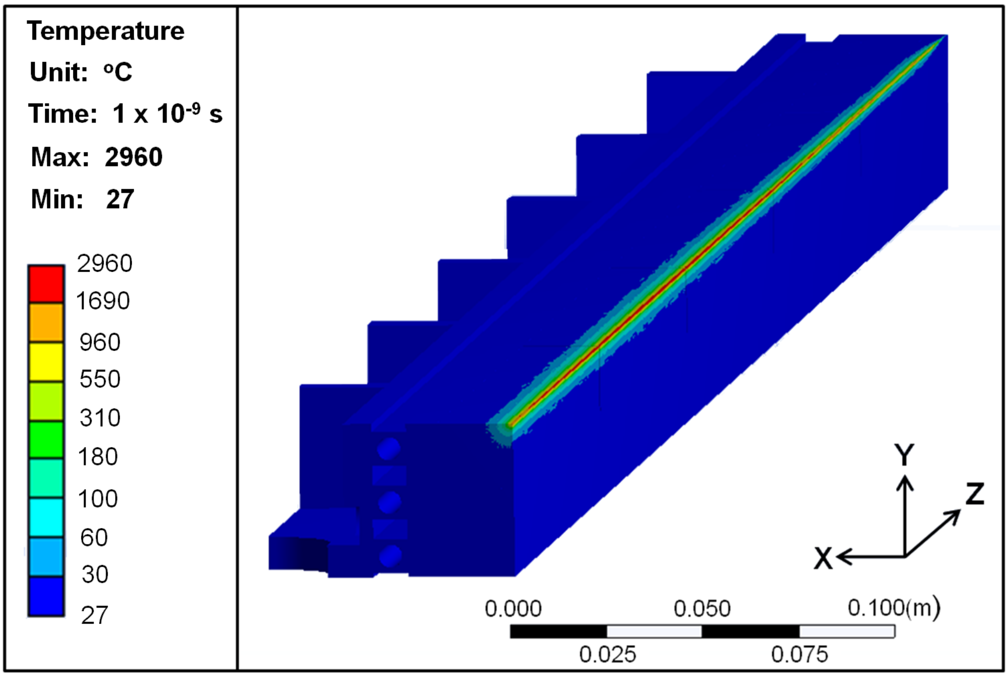

Figure 4.12: Logarithmic temperature distribution on the collimator jaw model for the '3.5 TeV, -1 mrad' case as provoked by the beam impact at 1 ns.

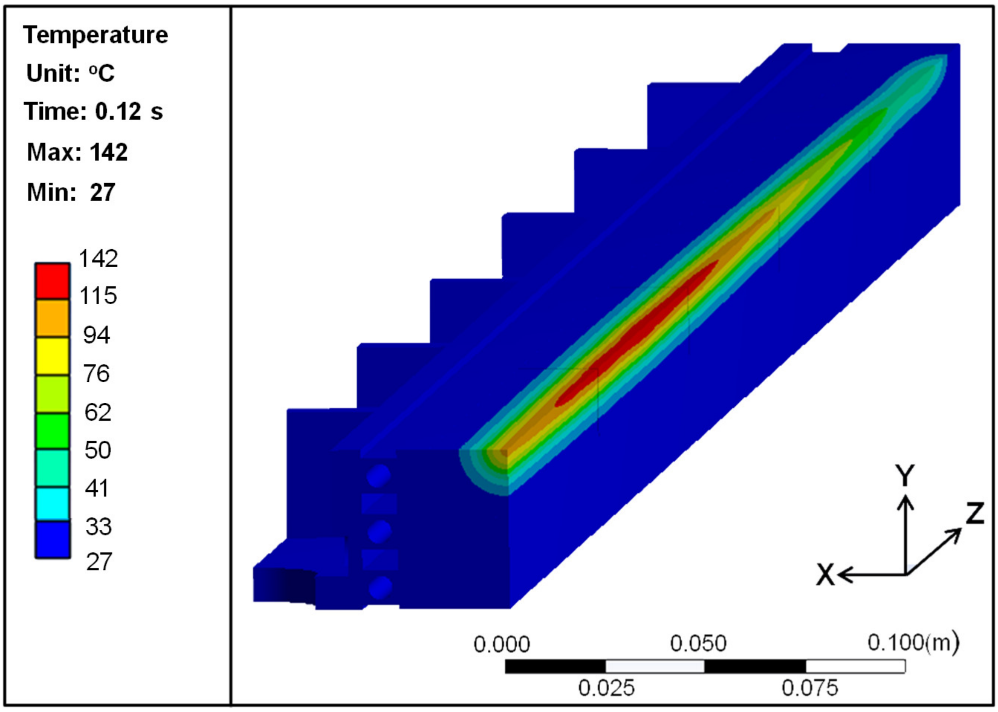

Figure 4.13: Logarithmic temperature distribution on the collimator jaw model for the '3.5 TeV, -1 mrad' case as provoked by the beam impact at 120 ms.

Since the jaw insert material was assumed to be pure tungsten for the purpose of these simulations, the melting temperature (T_{melt} = 3420 °C for tungsten) was not exceeded in any part of the collimator jaw for the '3.5 TeV, -1 mrad' case. This meant that there was no change of state in the material, resulting in the formation of stress waves in the plastic domain as explained in Section 2.3.2. Consequently, the use of an FE model with an implicit scheme of integration was sufficient for this study and it was in fact used for the structural analyses presented in Section 4.4.2.

Given that in reality the material of the jaw inserts is INERMET$^{®}$ 180 and not pure tungsten, the copper-nickel matrix melts before the tungsten grains, thus lowering the operating temperature of the whole material. Taking into account this lower melting temperature limit, the molten region in the '3.5 TeV, -1 mrad' case will still be limited to a small region when compared to the other jaw error cases. Thus, a jaw tilt of -1 mrad will still classify as an optimised jaw-beam orientation for an asynchronous beam dump accident.

4.4.2 Structural analyses

This section will present the structural analyses of the collimator structure in the elastic-plastic domain of its constituent materials for the '3.5 TeV, -1 mrad' case. This includes the evaluation of both the dynamic response and the potential permanent damage of the jaw assembly as calculated with ANSYS®.

Once the expected temperature increase was known, simple formulae could be applied to estimate the range of compressive stresses as well as to predict the plasticisation provoked by the thermal shock. Assuming that no longitudinal expansion occurs (plane-strain case), compressive strains, ϵ, and linear elastic stresses, σ^{linear}, can be estimated analytically using Equations 4.1 [108, p. 70-71] and 4.2 [108, p. 71-74] respectively:

$$\epsilon_{z_{\max}} = -\alpha \Delta T_{\max}, \tag{4.1}$$

$$\sigma_{z_{\max}}^{\text{linear}} = -\frac{E\alpha\Delta T_{\max}}{1-2\nu}, \tag{4.2}$$

where E, α and ν are the Young's Modulus, coefficient of thermal expansion and Poisson's ratio of the jaw insert material respectively, and $\Delta T_{\max} = T_{\max}$ - T_{ref}.

The analytical and FEM approaches to find the compressive strains and stresses that develop within the jaw inserts during the beam impact are compared (Figure 4.14). The compressive strains show good agreement, with both methods giving a maximum compressive longitudinal strain of approximately 0.012 at the end of the impact duration. Both approaches also give compressive thermal stresses on the order of GPa. Moreover, the longitudinal deformation of the collimator jaw assembly due to the particle beam impact does not exceed 0.1 mm (Figure 4.15), thus justifying the modelling approach of the contact interface between the jaw inserts as described in Section 3.3.1.

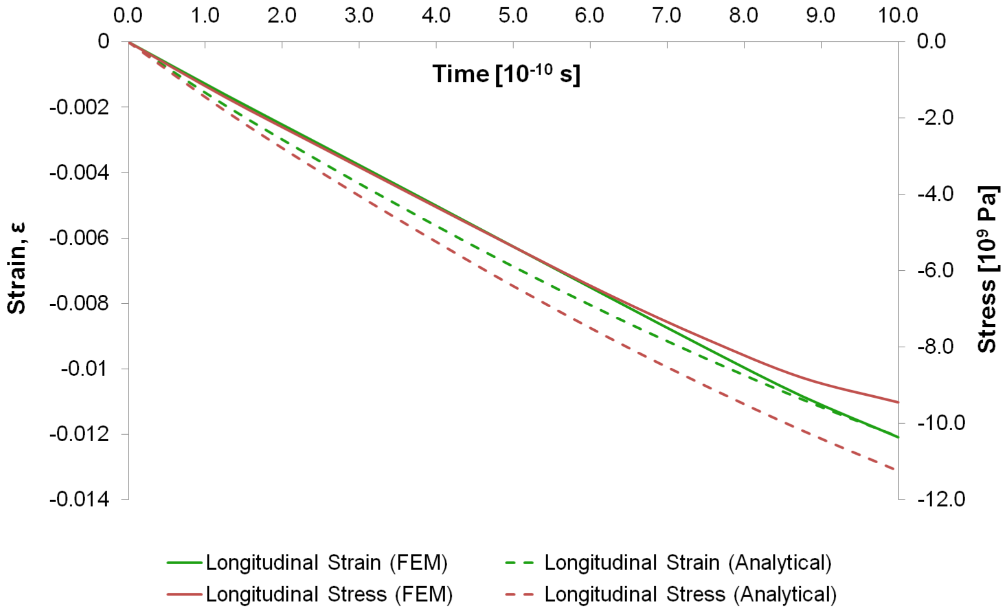

Figure 4.14: Maximum compressive longitudinal stresses and strains that developed within the jaw inserts over the duration of the beam impact ($\tau_{\text{shock}} = 1$ ns). Values obtained as a result of FEM simulations, as well as analytically using Equations 4.1 and 4.2, are compared.

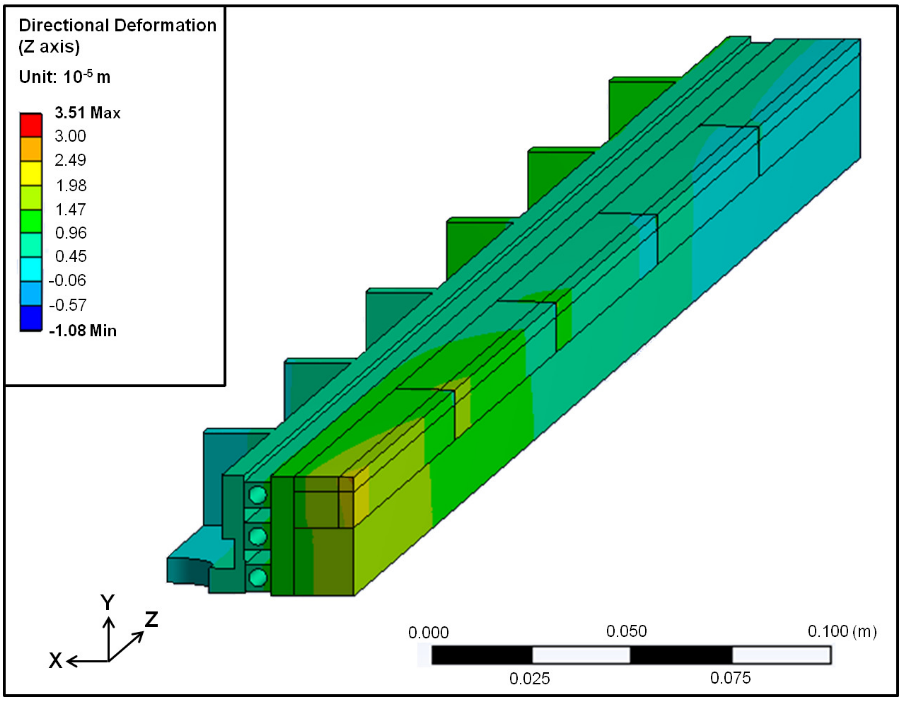

Figure 4.15: Longitudinal deformation (z-direction) of the collimator jaw assembly due to the studied particle beam impact. The maximum longitudinal deformation is ∼35 μm.

On comparing the temperature distribution (Figure 4.12) to the stress distribution (Figure 4.16), it can be observed that the region of maximum compressive stresses is the same as the region of maximum temperatures induced during the beam impact. The high temperatures cause the expansion of this region of material. However, due to the very fast temperature change occurring within the collimator jaw, thermal expansion is prevented by the inertia of the surrounding material, thereby establishing a coupling between thermally originated elastic forces and inertia forces.

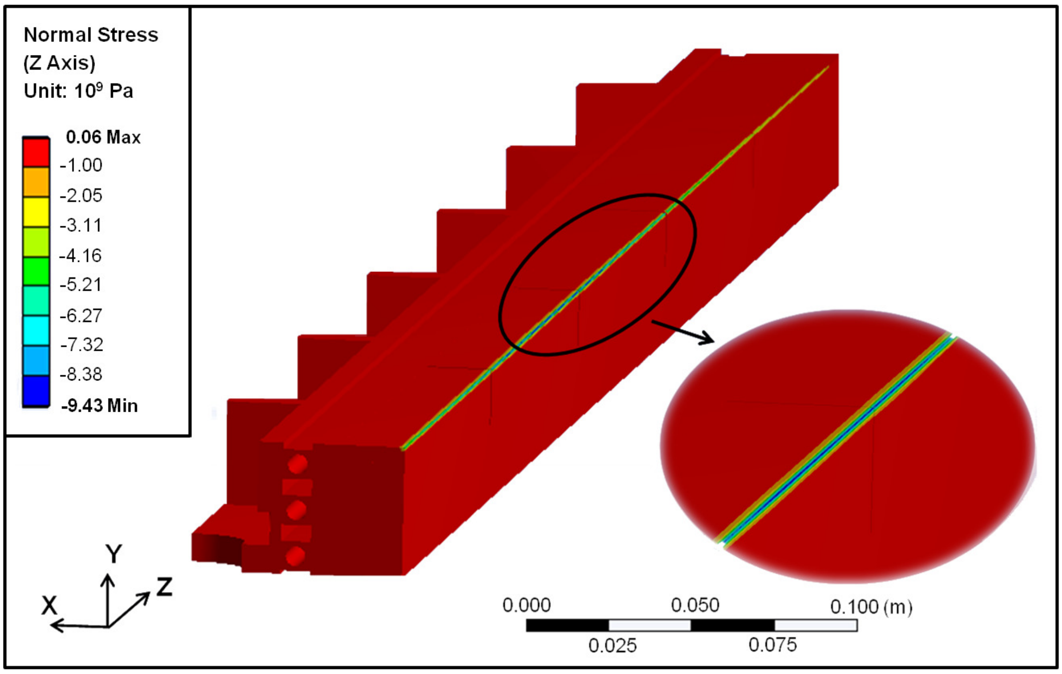

Figure 4.16: Longitudinal stresses (z-direction) on the collimator jaw assembly due to the particle beam impact. High compressive stresses dominate the region of the maximum energy deposition. A detailed view is shown in the inset.

In the case of a simply supported beam, which is the case of the collimator jaw, this effect gives rise to dynamic stresses propagating along the beam axis. Assuming a very short τ_{shock} from the beam impact, at $t = \tau_{\text{shock}}$, the system would still be in a compressive state. The stress relaxation due to the elastic forces starts from the extremities of the beam - two stress waves appear travelling from the extremities, superimposing at the centre and reflecting at the other ends [70].

The structural dynamic effects provoked by the thermal shock can be studied as the response of the system to two dynamic thermal loads acting at the extremities of the beam - axial force and bending moment. These loads are superimposed to the quasi-static field and are necessary to ensure the dynamic equilibrium. Since no heat diffusion is assumed to occur during τ_{shock}, these two loads grow linearly from zero to the maximum value at the end of the energy deposition. From this time onwards, the force remains constant since it is proportional to the deposited energy while the bending moment decreases as the temperature distribution tends to become more uniform because of thermal diffusion [70].

The main frequency of flexural oscillation, approximately 100 Hz as calculated in Section 4.3.2 using Equation 3.9, was correctly predicted by the transient structural simulations. The jaw assembly, hit by the high-energy particle beam, showed a dynamic flexural response with a main frequency of approximately 95 Hz (Figure 4.17). Furthermore, the jaw assembly vibrated with an underdamped response around its quasi-static deflected position.

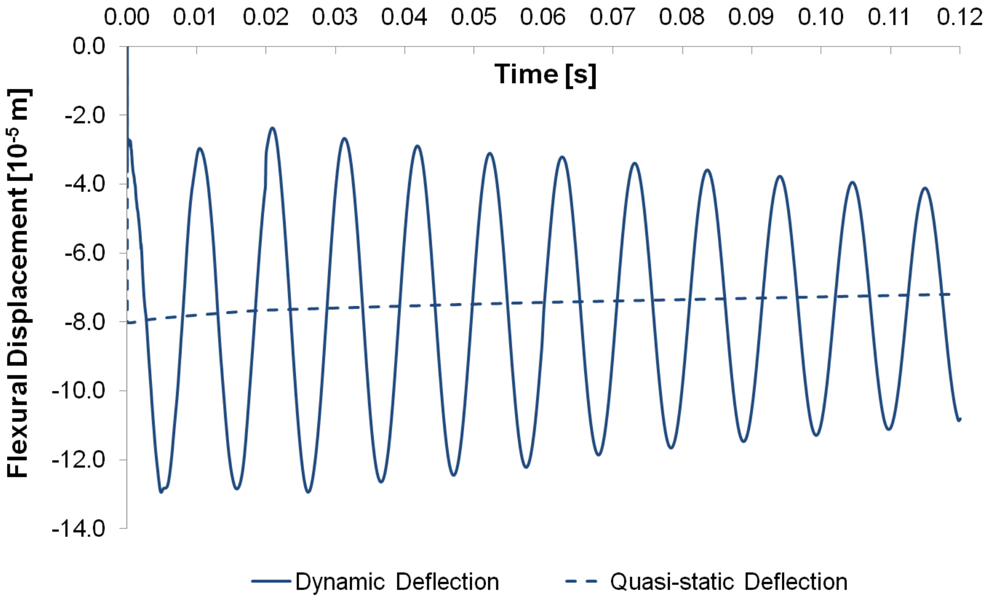

Figure 4.17: Dynamic flexural displacement (x-direction) of the collimator jaw assembly at z = 0.430 m, as provoked by the particle beam impact. The quasi-static deflection due to the thermal bending moment is also shown.

The interpretation of the structural dynamic effects provoked by the beam impact as two dynamic thermal loads helps to explain the development of the longitudinal and flexural vibrations, as well as of the dynamic thermal stresses. Figures 4.18 and 4.19 show the longitudinal and flexural response of the collimator structure to the beam impact as obtained from the numerical FEM analysis.

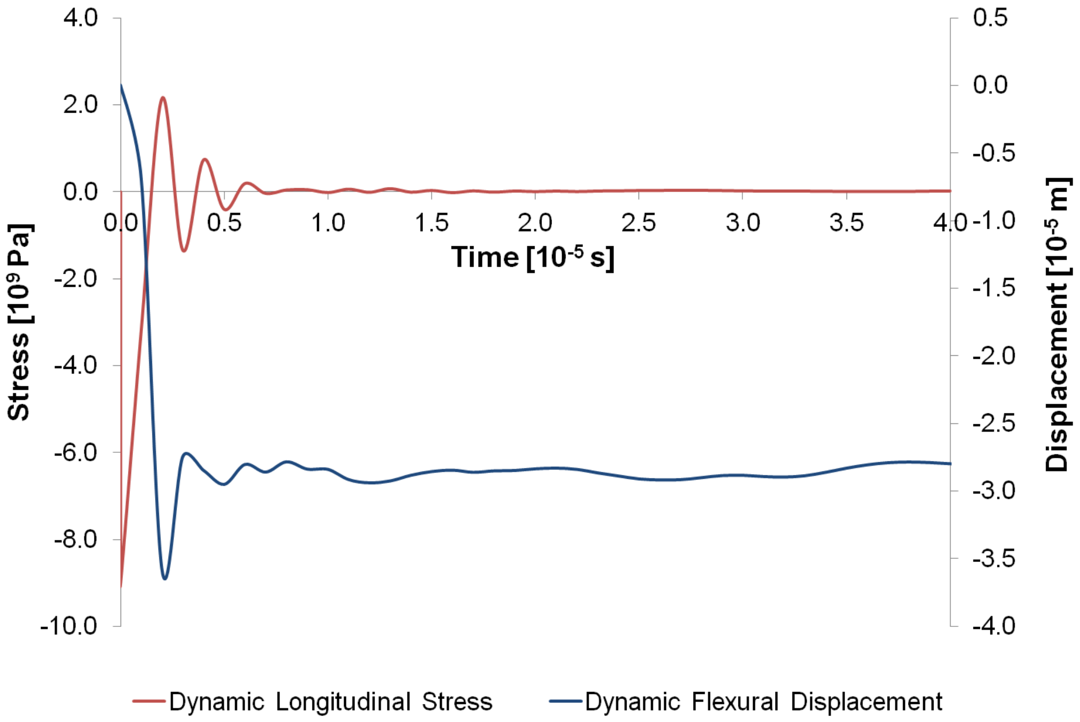

Figure 4.18: Dynamic flexural displacement (x-direction) and dynamic longitudinal stress (z-direction) on the collimator jaw assembly at z = 0.430 m, as provoked by the particle beam impact during the first few microseconds. It can be observed that oscillations start at a frequency range on the order of kHz.

A typical mode of material failure during high velocity impact is spallation. As described in Section 2.3.3, the maximum principal stress model can be used to detect if spallation occurs. The dependence of the UTS of pure tungsten on temperature is given in Figure 4.20. It can be noticed that the highest temperature developed in Figure 4.12 exceeds the temperature at which the UTS data of pure tungsten is available (Figure 4.20). It can however be concluded from the contour plot of the maximum principal stress on the collimator jaw (Figure 4.21) that the highest tensile stresses are concentrated over a small region resulting in limited crack formation and consequent damage.

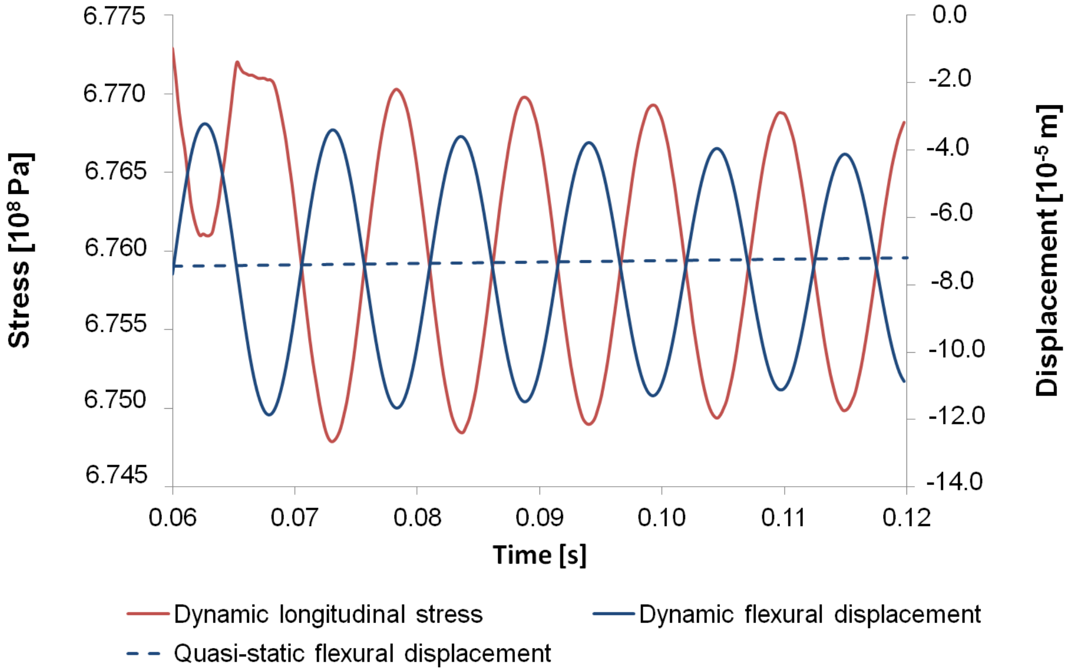

Figure 4.19: Dynamic flexural displacement (x-direction) and dynamic longitudinal stress (z-direction) detected on the collimator jaw assembly at z = 0.430 m between t = 0.06 s and t = 0.12 s after the particle beam impact. It can be observed that oscillations settle at a main frequency of approximately 95 Hz, which is equivalent to the first period of flexural oscillation of the jaw assembly.

A quasi-static structural analysis was finally performed after the dynamic response had disappeared to investigate if the collimator jaw assembly would remain permanently deformed due to the particle beam impact. Figure 4.22 shows the residual plastic strains on the collimator jaw inserts. As expected, the region of the jaw inserts that is subject to the high temperature distribution (Figure 4.12) expands outwards resulting in a permanent deformation of approximately 82 μm of the collimator jaw assembly as shown in Figure 4.23.

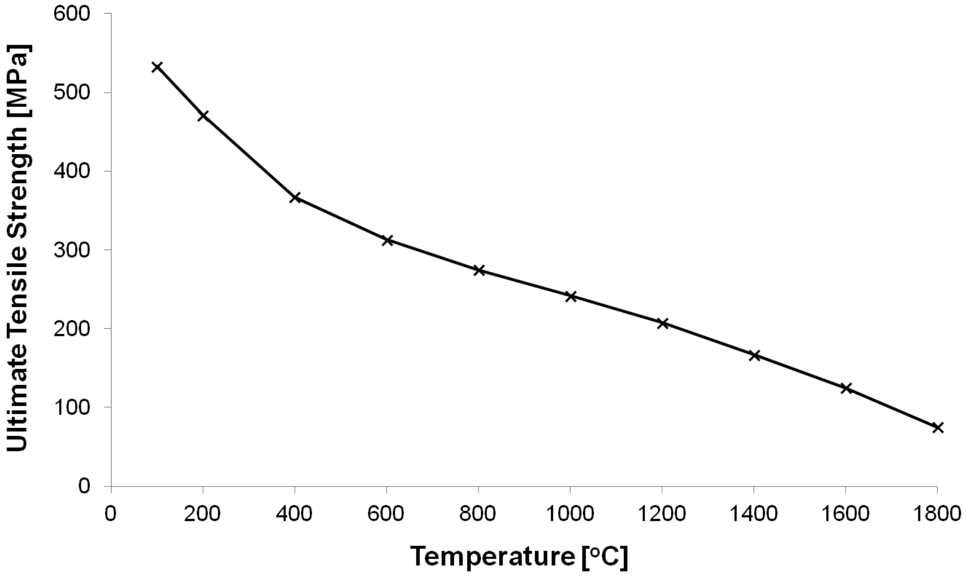

Figure 4.20: The ultimate tensile strength (UTS) of tungsten as a function of temperature [116].

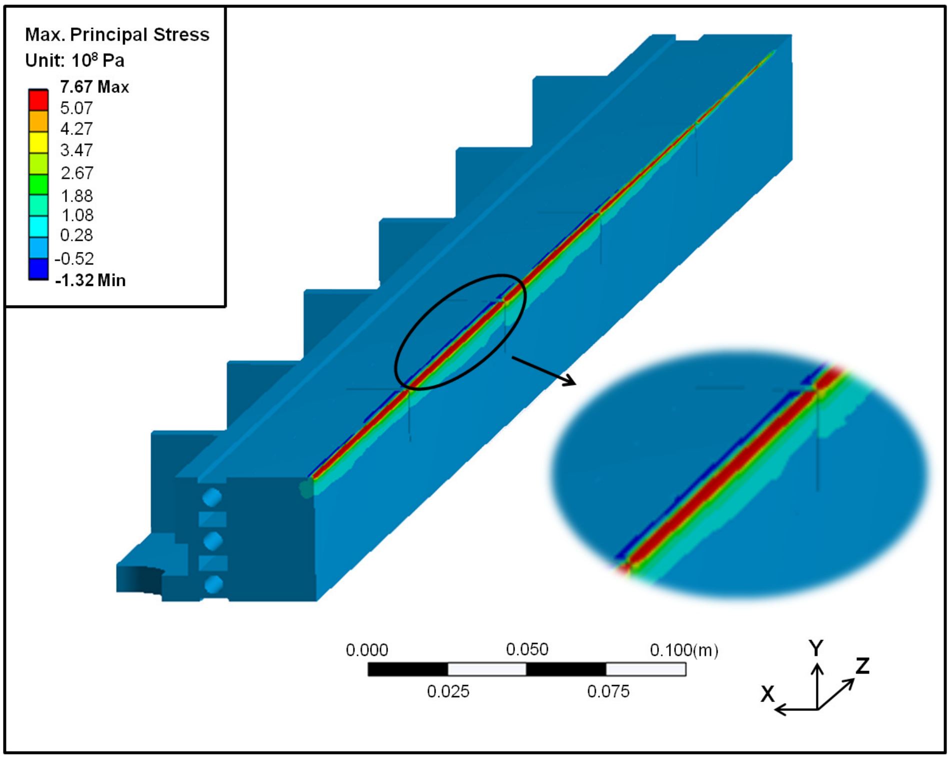

Figure 4.21: Contour plot of the maximum principal stress on the collimator jaw assembly at the end of the dynamic response. The region with the highest tensile stresses is subject to the formation of micro-cracks and ultimately, spallation. A detailed view is shown in the inset.

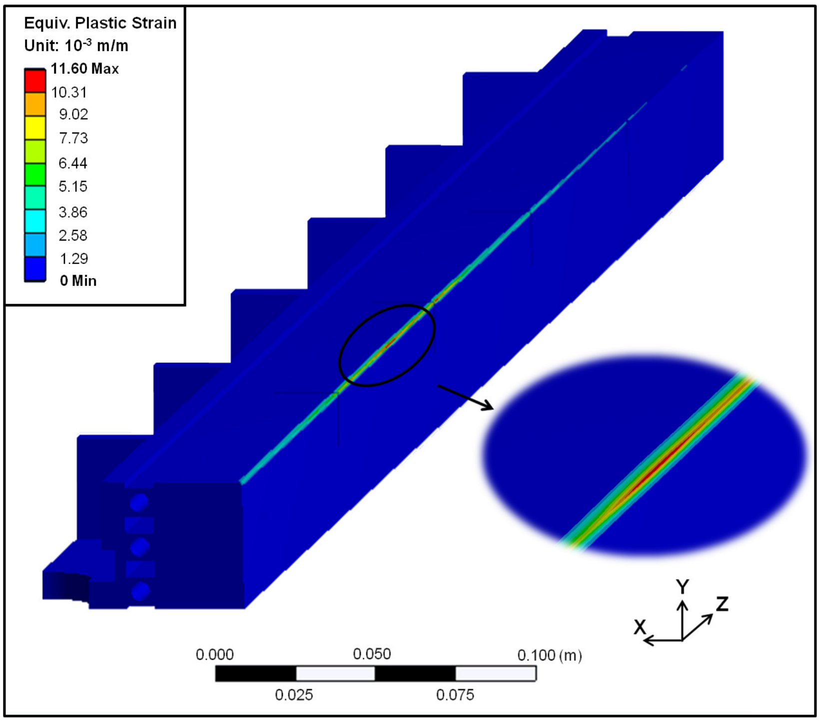

Figure 4.22: Equivalent plastic strains on the collimator jaw assembly due to the beam impact. A detailed view is shown in the inset.

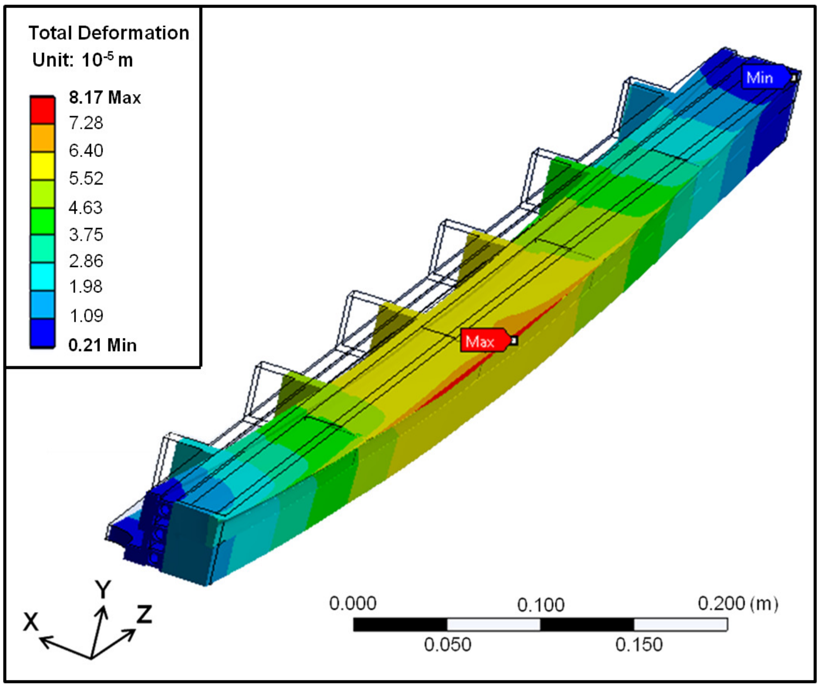

Figure 4.23: Total deformation of the collimator jaw assembly resulting from the beam impact. The deformation scale factor is 310.

4.5 Conclusions

This work focuses on the study of a conservative accident scenario involving the direct impact of 1 LHC bunch on a TCT jaw as a result of an asynchronous beam dump. This study is important because if such an accident happens during physics or collimation beam-based alignment setups, it can have catastrophic consequences which must be understood a priori.

In this chapter, the thermo-mechanical response of TCTs in novel jaw error cases was evaluated and the most interesting load cases were identified for further detailed analyses. A thermal evaluation of the extent of beam-induced damage was performed. Comparison of the peak temperatures reached and of the extent of the molten region indicated that the most loaded case was when the beam impact occurred on jaw inserts that were perfectly aligned with the beam direction ($\theta = 0$ mrad). Significant peak temperatures were also observed when the collimator jaws were slightly inclined.

However, it was found that in the case of a jaw inclination of -1 mrad, no region with very focused energy deposition resulted from the beam impact, leading to an overall lower peak temperature. Such a tilt, together with an impact parameter of 0.5 mm, meant that the 0.30 mm RMS beam hit the jaw surface 50 cm from its downstream end and that the first point of impact was spread from z = 0.20 m to z = 0.80 m.

Subsequently, the thermally induced dynamic response of the collimator structure was studied for the ‘3.5 TeV, -1 mrad’ asynchronous beam dump case. This was followed by a quasi-static analysis to calculate potential permanent deformations of the structure once the dynamic response had disappeared. A permanent deformation of approximately 82 μm was observed on the collimator jaw assembly for the ‘3.5 TeV, -1 mrad’ jaw error case, which damage is much lower than what is expected of the perfectly aligned case. In conclusion, it was shown that a tilt of the jaw can actually mitigate the effect of the beam-induced damage caused by an asynchronous beam dump on TCTs.

Chapter 5

Material Characterisation Tests

5.1 Introduction

Reliable FEM simulations are strongly dependent on a correct material model. When the high-energy particle beam impacts the collimator structure during an asynchronous beam dump, a great percentage of the energy is deposited within the collimator jaw inserts. This makes the material modelling of the jaw inserts extremely critical in order to be able to numerically simulate beam impact events with a high level of confidence. Research in tungsten heavy alloys is mostly boosted by their ballistic applications as anti-armour kinetic energy penetrators, and as explained in Section 4.3.2, data providing properties of such materials under extreme conditions is very scarce. For this reason, full thermal and structural material characterisation campaigns were commissioned for INERMET® 180 in different test laboratories, as will be explained in this chapter.

5.2 INERMET® 180

5.2.1 Composition

The outstanding thermal properties of tungsten metal make it suitable for a wide range of applications. However, some of the properties of tungsten metal, such as the electrical and thermal conductivities, the sensitivity towards oxidation and the poor workability, are unsatisfactory for certain applications and thus restrict its use. Such limitations have led to the development of two-phase alloys that combine the useful properties of tungsten with those of the additive [116]. Two important alloy systems include:

- **Tungsten heavy metal alloys**: this term refers to a group of two-phase alloys based on W-Ni-Fe and W-Ni-Cu-(Fe). Such alloys are characterised by a high density and a unique combination of strength and ductility. They are therefore used wherever high density, excellent mechanical properties and good workability are necessary.
- **W-Cu and W-Ag alloys**: such alloys combine the high electrical and thermal conductivities of copper, or silver, with the high hardness and wear resistance of tungsten.

INERMET® 180 is a tungsten heavy metal alloy with a composition of 95 wt.% W - 3.5 wt.% Ni - 1.5 wt.% Cu. A typical microstructure (Figure 5.1) consists of spherical tungsten grains (20 to 60 μm in diameter) embedded in a tough metallic copper-nickel matrix that also provides the necessary thermal and electrical continuity to the material. The elemental composition is shown in Figure 5.2.

While the tungsten grains show the typical body-centred cubic (BCC) structure with a very high Young's Modulus, the structure of the binder phase that contains around 20 wt.% W in solid solution is commonly face-centred cubic (FCC) [116]. Moreover, INERMET® 180 does not have a unique melting temperature due to its composition of W and Cu-Ni phases. The melting temperature of pure tungsten is around 3420 °C. However, a conservative value for the melting temperature of INERMET® 180 is taken as 1343 °C; this is equivalent to the melting temperature of the Cu-Ni phase of the alloy which corresponds to loss of shear strength and if exceeded, might create instability in the material.

During a beam impact on INERMET® 180 which causes the melting of the Cu-Ni phase, there is no sufficient time for the molten phase to flow out of the pores of the material. The expansion of the Cu-Ni phase thus results in a large internal pressure that can provoke degradation of the thermo-mechanical properties as well as create zones with different porosities and composition. The mechanical properties of the final alloy are therefore mainly related to the properties of the individual phases as well as the complex interaction between them.

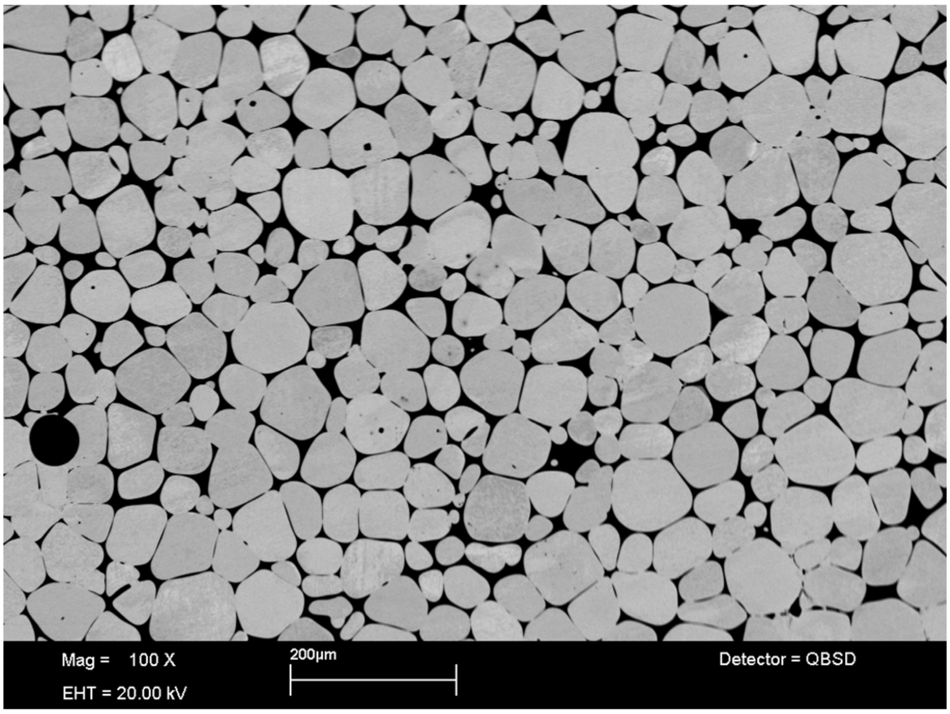

Figure 5.1: Scanning electron microscope image at low magnification (100×) showing the typical microstructure of INERMET® 180 by means of a quadrant back scattering detector. The tungsten grains are clear while the binder phase appears black.

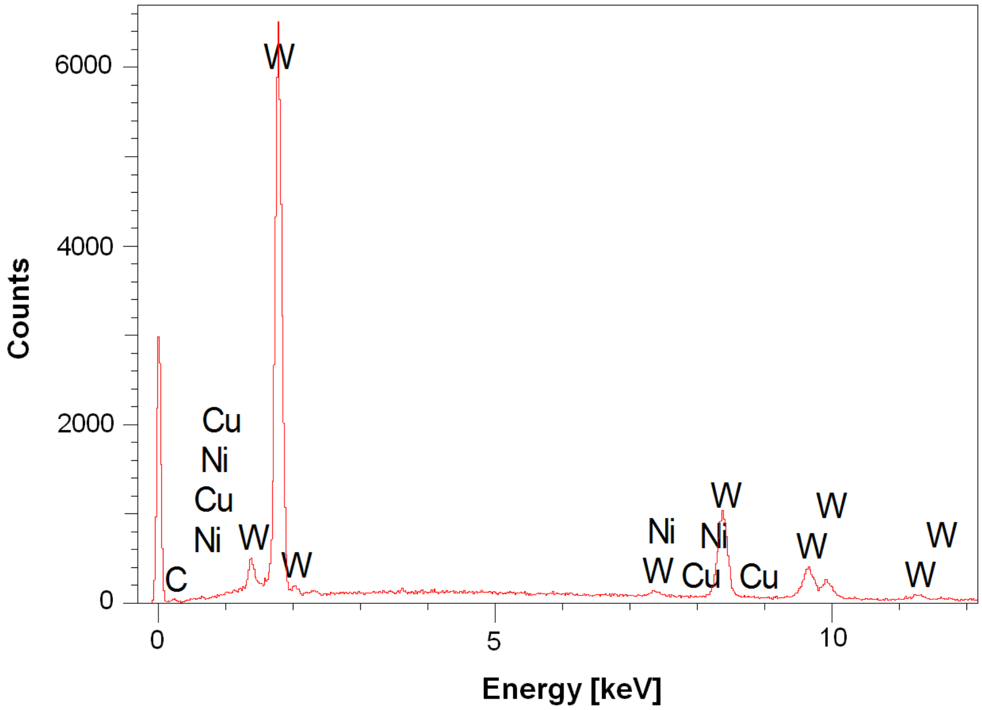

Figure 5.2: Elemental composition of INERMET® 180 obtained through the production of characteristic X-rays with the scanning electron microscope. As expected, the main chemical elements are W, Ni and Cu. The carbon peak represents the presence of a surface contamination; this in fact appears as a large black circle on the left hand side of the microstructure in Figure 5.1.

5.2.2 Manufacture and Fabrication

Conventional manufacturing techniques such as melting and casting in a mold are commonly applied for most metals. However, due to the high melting temperature of pure tungsten, such techniques cannot be used for the manufacture of tungsten heavy alloys. In such cases, a powder metallurgy technique (Figure 5.3) is alternatively used for the material production.

In the case of INERMET® 180, the tungsten powders are mixed with the low melting elements (copper and nickel) in the desired ratio. The liquid phase sintering process implies that the mixed powders are first compacted to form a green body and then subjected to heat treatment below the melting temperature of tungsten. In this way, the lower melting elements undergo melting and form the matrix that bonds the unmolten tungsten particles

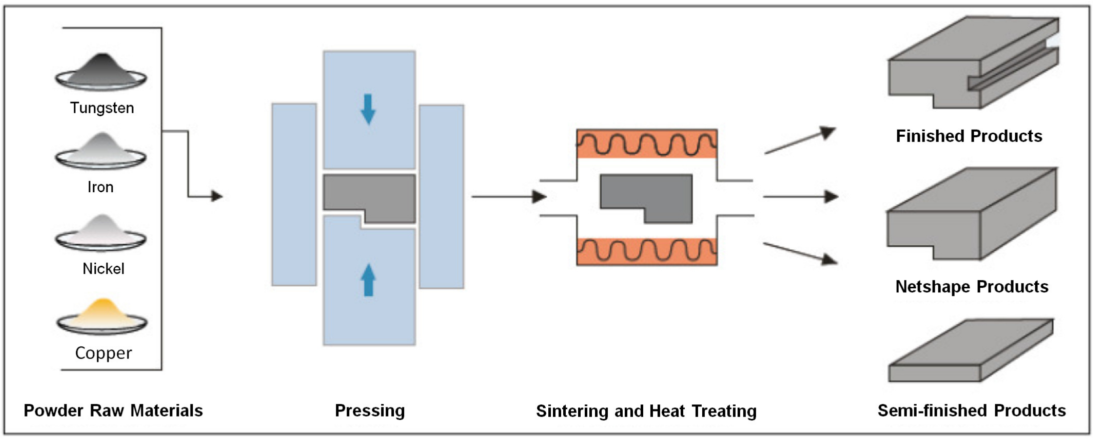

Figure 5.3: Powder metallurgy process used for the manufacturing of INERMET® products [59].

together. As a matter of fact, the spheroidised microstructure shown in Figure 5.1 is the result of the sintering process in which the rounded phase is pure tungsten surrounded by a metallic binder phase also containing dissolved tungsten in solid solution. Both die pressing and isostatic pressing (dry- and wet-bag pressing) can be used during the manufacturing process. Since the green strength is high enough to handle the compacts, no lubricant is commonly added. Powder injection moulding (PIM) is used where net shaping is desired and large quantities of complex parts are produced [59].

5.2.3 Properties

As is the general case for most materials, mechanical properties are very sensitive to processing conditions, impurities and microstructure. Thus, problems with controlling porosity, impurities and microstructural homogeneity are commonly found in heavy alloy fabrication. Residual sinter porosity and the formation of interface precipitates must be avoided as they are the main reason for inferior material properties.

Besides the high density and the unique combination of high strength and ductility, other attributes [59] that make heavy metal alloys, such as INERMET® 180, a versatile product are:

- High modulus of elasticity
- Excellent vibration damping characteristics
- Good machinability
- High absorption ability for X-rays and gamma-rays
- Good thermal and electrical conductivities
- Low coefficient of thermal expansion
- Low electrical erosion and welding tendency
- Good resistance to corrosion
- Inexpensive manufacturing of complex products and components
- Harmless to the health and environment

Additionally, a clear advantage of W-Ni-Cu alloys lies in their non-magnetic characteristics. Members of the W-Ni-Cu group also exhibit a higher electrical conductivity when compared to W-Ni-Fe alloys. The nickel-to-copper ratio in W-Ni-Cu alloys ranges from 3:2 to 4:1; for the case of INERMET® 180, this ratio is 3.5:1.5. On the other hand, W-Ni-Cu alloys exhibit lower strength and ductility at room temperature when compared to W-Ni-Fe alloys. This effect is caused by the amount and the dimension of the tungsten particles, both of which influence the fracture mode of the material [117].

A microstructure and fractographic analysis [118] of both W-Ni-Cu and W-Ni-Fe alloys demonstrated that the W-Ni-Fe alloy has smaller tungsten grains and a smaller amount of tungsten-tungsten interfaces when compared to the W-Ni-Cu alloy. The dimension of the tungsten grains depends on the sintering temperature and since the W-Ni-Cu alloys require a higher temperature, this results in the formation of bigger grains [117]. This in turn implies a lower amount of binder phase and an increase in the tungsten-tungsten interfacial area. As described in Section 2.3.3, the tungsten-tungsten interfaces act as the weak link in the microstructure and thus a larger amount of such interfaces for the W-Ni-Cu alloy compromises the material strength and ductility.

5.2.4 Applications

Heavy metals are used in applications where the high specific weight of the material plays an important role. Such applications include counterweights, rotating inertia members, X-ray and gamma-radiation shields, rigid tools for machining as well as mechanisms for defence purposes (such as kinetic energy penetrators and fragmentation devices).

With a density of around 18,000 kg/m^3 and a high X-ray and gamma-ray absorption capacity, such tungsten heavy metal alloys are the ideal materials for collimators and shielding components in radiotherapy. In comparison to other materials, these alloys have exceptional stability and freedom from distortion. Apart from the applications in high-energy physics, collimators are also used in medical technology where they serve as channels for filtering radiation, concentrating the beam directly onto the treatment site while protecting the surrounding healthy tissue. Shielding components are also built into linear accelerators to ensure the protection of the surrounding area right up to the end collimator. In addition, the good machinability of such alloys makes them appropriate for a broad range of applications in the aerospace, automotive and construction industries [59].

5.3 Thermal characterisation

5.3.1 Thermo-physical deliverables

Due to the use of INERMET® 180 as a collimator jaw insert material, knowledge of its temperature-dependent thermo-physical properties is of paramount importance for the correct modelling of collimators in such a high-temperature application. A thermo-physical analysis of INERMET® 180 was thus commissioned at the Austrian Institute of Technology.

This test campaign involved the solid state measurements of the basic thermo-physical properties, as described in Section 3.3.3, of INERMET® 180 between room temperature and 1450 °C. The aim was to obtain the thermo-physical properties over the widest possible range of temperatures, however taking care not to induce significant melting of the material due to potential damage to the testing equipment.

The methodologies used for the different thermal characterisation tests as well as the results of the measurement campaign are presented in the next sections as indicated for each thermo-physical property listed below:

- Coefficient of linear thermal expansion, $\alpha(T)$ (Section 5.3.3)
- Density, $\rho(T)$ (Section 5.3.3)
- Specific heat capacity, $c_\mathrm{p}(T)$ (Section 5.3.4)
- Thermal diffusivity, $\kappa_\mathrm{cc}(T)$ (Section 5.3.5)
- Thermal conductivity, $k(T)$ (Section 5.3.6) - calculated out of the measurement data of $\rho(T)$, $c_\mathrm{p}(T)$ and $\kappa_\mathrm{cc}(T)$

5.3.2 Overview of thermal characterisation tests

All adopted methods were used in accordance with the relevant standards. The statement of a measurement result is only complete if it contains both the value attributed to the measurement as well as the uncertainty associated with the measurement result. A statistical analysis [119] was thus carried out according to DIN V ENV 13005 [120] as explained below.

When a physical quantity X_i is measured repeatedly, the best estimate of X_i is the arithmetic mean q_i of the n individual measurements $q_{i,1}, q_{i,2}, \ldots q_{i,k}, \ldots q_{i,n}$ (Equation 5.1). The best estimate of the uncertainty of an individual $q_{i,k}$ is the standard deviation of the individual measurements, $s(q_{i,k})$ (Equation 5.2). The uncertainty of the arithmetic mean of the full set of $\{q_{i,k}\}$ is $u(q_i)$ (Equation 5.3). The best output estimate y is calculated with Equation 5.4, using the best input estimates q_i as shown in Equation 5.1. Finally, the uncertainty of the output estimate $u_\mathrm{c}(y)$ is calculated by Equation 5.5, and it is called the *standard uncertainty of the output estimate*, well known as the Gaussian Error Propagation Law.

$$q_i = \frac{1}{n} \cdot \sum_{k=1}^{n} q_{i,k}, \tag{5.1}$$

$$s(q_{i,k}) = \sqrt{\frac{1}{n-1} \cdot \sum_{k=1}^{n} (q_{i,k} - q_i)^2}, \tag{5.2}$$

$$u(q_i) = \frac{1}{\sqrt{n}} \cdot s(q_{i,k}) := u(x_i), \tag{5.3}$$

$$y = f(q_1, q_2, ...q_i, ...q_n), \tag{5.4}$$

$$u_{\mathrm{c}}^2(y) = \sum_{i=1}^{n} \left(\frac{\partial f}{\partial x_i} \right)^2 \cdot u^2(x_i), \tag{5.5}$$

Equation 5.5 calculates the standard uncertainty of the output estimate with respect to a 66% confidence interval. Measurement results of technical data are usually attributed with uncertainties of a 95% confidence interval, which is achieved by multiplying Equation 5.5 with a coverage factor of 2 as shown in Equation 5.6.

$$u_{\mathrm{c};95\%}^2(y) = 2 \cdot \sum_{i=1}^{n} \left(\frac{\partial f}{\partial x_i} \right)^2 \cdot u^2(x_i), \tag{5.6}$$

Each thermo-physical method has specific reference materials as will be given in Sections 5.3.3, 5.3.4 and 5.3.5 for each respective method. Measurements performed with such reference materials show that the uncertainties of measurement results should typically be around 1% of the measured values, provided that tests are performed on a suitable specimen. The use of a suitable specimen is important to eliminate any possible influences caused by the material or the specimens themselves. The calculated thermal conductivity can then be obtained with an uncertainty of less than 5%.

Schematic diagrams of the sample geometries used for the thermal characterisation tests are shown in Figure 5.4. All types of measurements had to be repeated a number of times for statistical reasons and thus three samples were respectively provided for each measurement of $\alpha(T)$, $c_{\mathrm{p}}(T)$ and $\kappa_{\mathrm{cc}}(T)$.

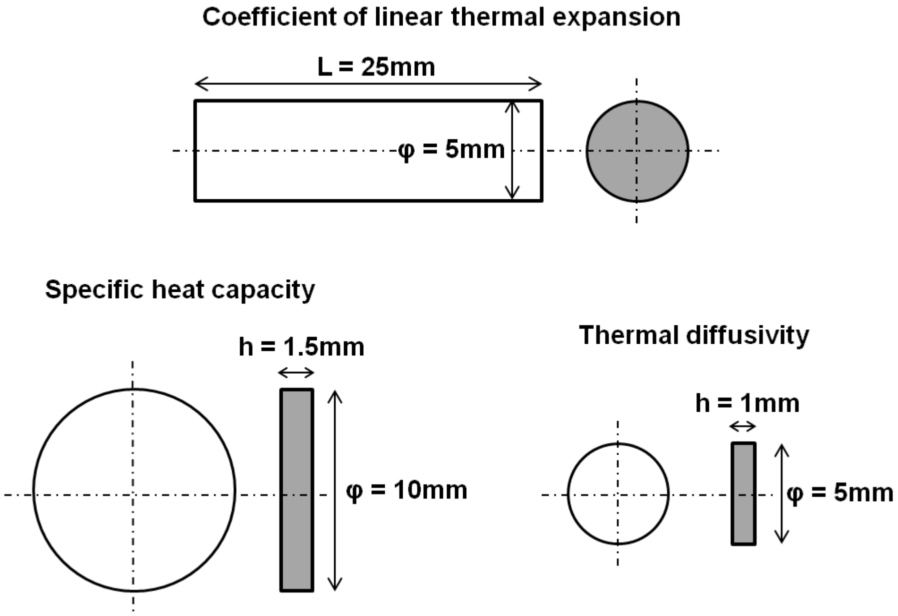

Figure 5.4: Schematic diagrams of the sample geometries used for the thermal characterisation tests.

5.3.3 Coefficient of linear thermal expansion

The *linear thermal expansion* of INERMET® 180 was measured using the pushrod dilatometry method. A high temperature dilatometer, NETZSCH DIL 402C (Figure 5.5), was used for the specific temperature range of [+25 °C, +1450 °C] and measurements were performed according to the standards DIN 51909, DIN 51045, DIN EN 821-1 and DIN V ENV 1159-1.

A dilatometric analysis is used to determine dimensional changes versus temperature or time while a sample undergoes a controlled temperature program. It is performed by inserting the sample into a special holder within a movable furnace. A pushrod is positioned directly against the sample and transmits the length change to an LVDT (Figure 5.6). As the sample length changes during the temperature program, the LVDT core is moved and an output signal proportional to the displacement is recorded. The temperature program is controlled using a thermocouple located in direct proximity to the sample, thus yielding reproducible temperature measurements. Moreover, a thermostat ensures that neither variation in air temperature nor heat radiation from the furnace affect the measurement result.

Since the sample holder and the front part of the pushrod are being exposed to the same temperature program as the sample, they are also expanding. The resulting dilatometer signal is therefore the sum of the length changes of the sample, the sample holder and the pushrod. It is thus necessary to correct the raw dilatometer data in order to obtain a true view of the sample behaviour. The measuring process is consequently done in two sequential steps:

1. The determination of the expansion behaviour of the dilatometer itself (using a reference material R)
2. The measurement of the specimen S

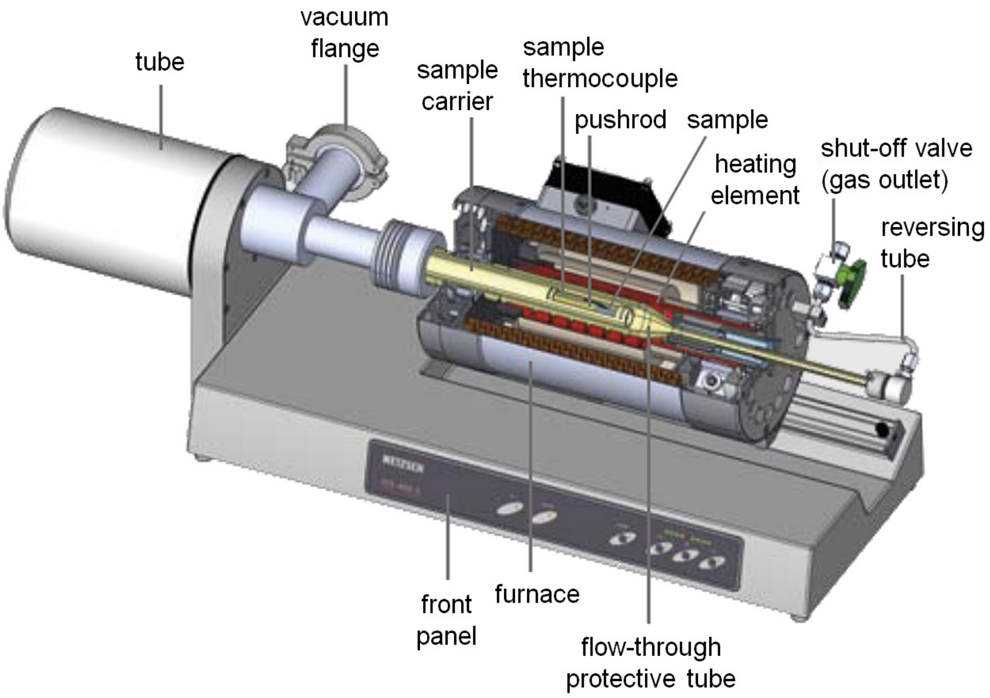

Figure 5.5: 3D sectional view of a high temperature pushrod dilatometer NETZSCH DIL 402C [121].

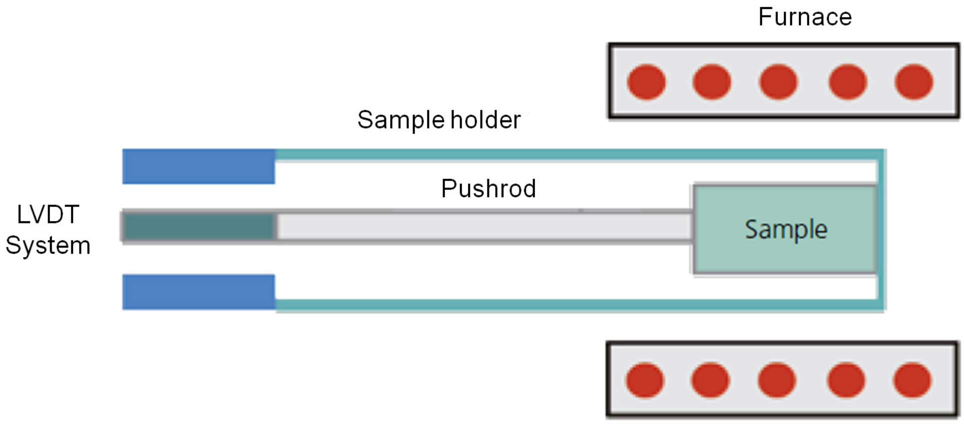

Figure 5.6: Functional diagram of a pushrod dilatometer [121].

The highly vacuum-tight construction of the pushrod dilatometer DIL 402C (Figure 5.5) allows measurements to be carried out both in a pure gas atmosphere or in a vacuum in order to avoid corrosion at high temperature. In this measurement campaign, the high temperature dilatometer was operated under helium conditions with a gas flow rate of 50 ml/min. Furthermore, a heating rate of 2 K/min was used in accordance with the relevant standards, leading to sufficiently low uncertainties.

The physical definition of the linear thermal expansion $\Delta L(T)/L_0$, and the knowledge of the thermal expansion behaviour of a reference material, enable to derive the equation for the correction function $K_\mathrm{R}(T)$ to eliminate systematic errors in the measurement process (Equation 5.7). This allows the calculation of the values of the linear thermal expansion of an unknown material (sample: S) with Equation 5.8 when the curve of the temperature-dependent position $P_\mathrm{S}(T)$ is known. Equations 5.7 [119, p. 8] and 5.8 [119, p. 8] are given here, where the subscriptions *R*, *Lit* and *S* indicate measurements done with a reference material *R* (typically sapphire, fused silica, alumina or platinum) or with a specimen *S*, or else refer to reference data from *Literature* respectively:

$$K_\mathrm{R}(T) = \left[\left.\frac{\Delta L_\mathrm{R}(T)}{L_{0;\mathrm{R}}}\right|_\mathrm{Lit} - \frac{P_\mathrm{R}(T)}{L_{0;\mathrm{R}}} \right], \tag{5.7}$$

$$\frac{\Delta L_\mathrm{S}(T)}{L_{0;\mathrm{S}}} = \frac{P_\mathrm{S}(T)}{L_{0;\mathrm{S}}} + K_\mathrm{R}(T) = \frac{P_\mathrm{S}(T)}{L_{0;\mathrm{S}}} + \left[\left.\frac{\Delta L_\mathrm{R}(T)}{L_{0;\mathrm{R}}}\right|_\mathrm{Lit} - \frac{P_\mathrm{R}(T)}{L_{0;\mathrm{R}}} \right], \tag{5.8}$$

The uncertainty of $\Delta L_\mathrm{S}(T)/L_{0;\mathrm{S}}$, and the equipment specific uncertainty (ESU) of the dilatometer, $ESU\ |_{\Delta L/L_0}$, are respectively given by Equations 5.9 [119, p. 10] and 5.10 [119, p. 10] below:

$${u_\mathrm{c}}^2 \left(\frac{\Delta L_\mathrm{S}}{L_{0;\mathrm{S}}} \right) = 1^2.u^2 \left(\frac{P_\mathrm{S}}{L_{0;\mathrm{S}}} \right) + 1^2.u^2 \left(\left.\frac{\Delta L_\mathrm{R}}{L_{0;\mathrm{R}}}\right|_\mathrm{Lit} \right) + 1^2.u^2 \left(\frac{P_\mathrm{R}}{L_{0;\mathrm{R}}} \right), \tag{5.9}$$

$$ESU^2\big|_{\Delta L/L_0} = u^2\left(\frac{P_\mathrm{R}}{L_{0;\mathrm{R}}}\right) + u^2\left(\left.\frac{\Delta L_\mathrm{R}}{L_{0;\mathrm{R}}}\right|_\mathrm{Lit}\right), \tag{5.10}$$

The *coefficient of linear thermal expansion*, $\alpha(T)$, and $ESU^2\big|_\alpha$ are then given by Equations 5.11 [119, p. 8] and 5.12 [119, p. 10] respectively:

$$\alpha_\mathrm{S}(T) := \frac{1}{\Delta T(T)}.\frac{\Delta L_\mathrm{S}(T)}{L_{0;\mathrm{S}}}, \tag{5.11}$$

$$ESU^2\big|_\alpha = \frac{1}{\Delta T^2}\cdot ESU^2\big|_{\Delta L/L_0}, \tag{5.12}$$

The variation of $\Delta L(T)/L_0$ and $\alpha(T)$ are presented in Figures 5.7 and 5.8 respectively. The drop in the measurement values of $\Delta L(T)/L_0$ and $\alpha(T)$ observed at high temperature is the result of the initiation of melting of the Cu-Ni binder phase. The variation with temperature of the relative thermal density, ρ/ρ_0, and the relative volume, V/V_0, were also extracted from the measurements of $\Delta L(T)/L_0$ and are given in Figure 5.9.

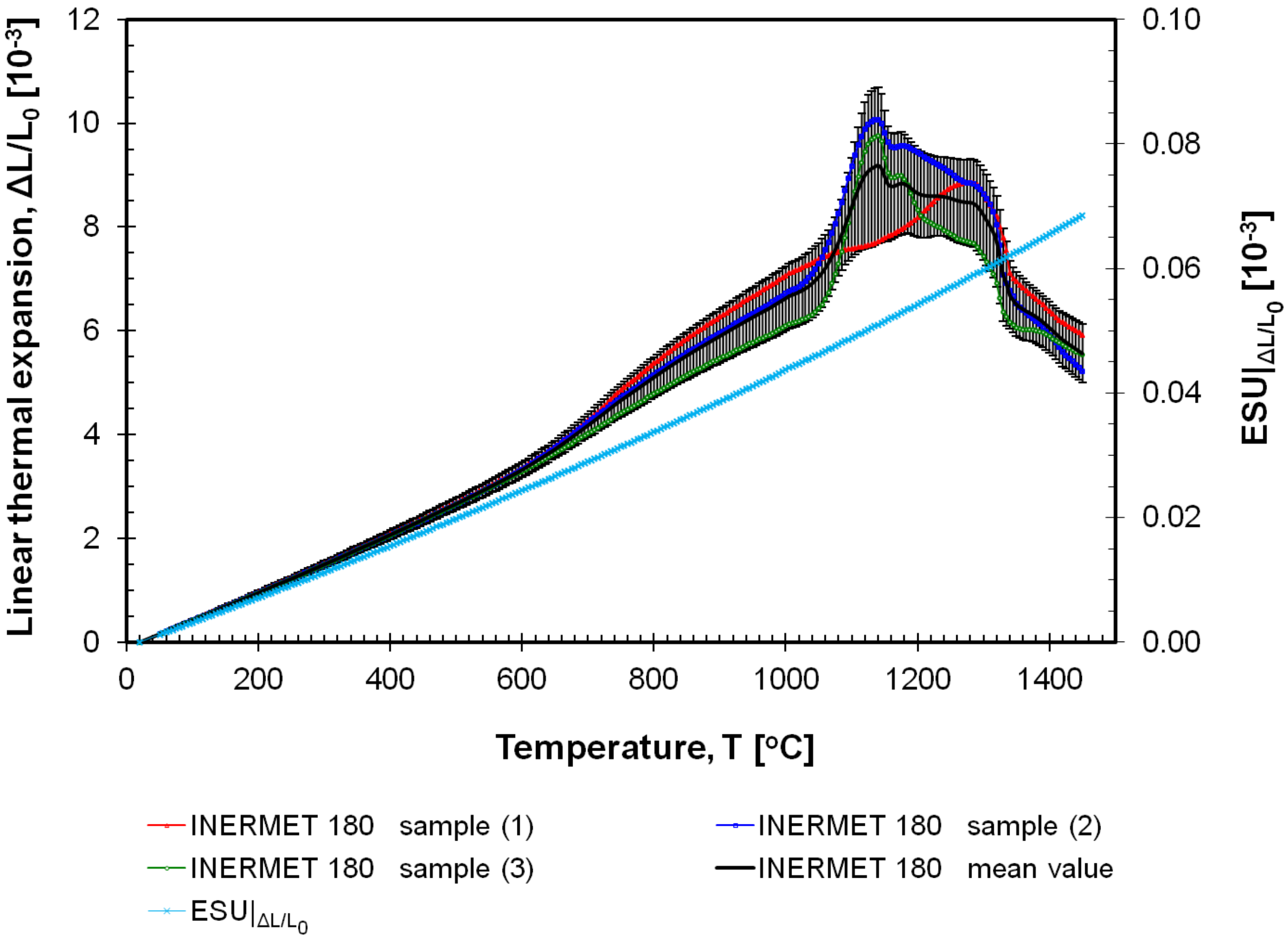

Figure 5.7: Linear thermal expansion of INERMET® 180 as a function of temperature.

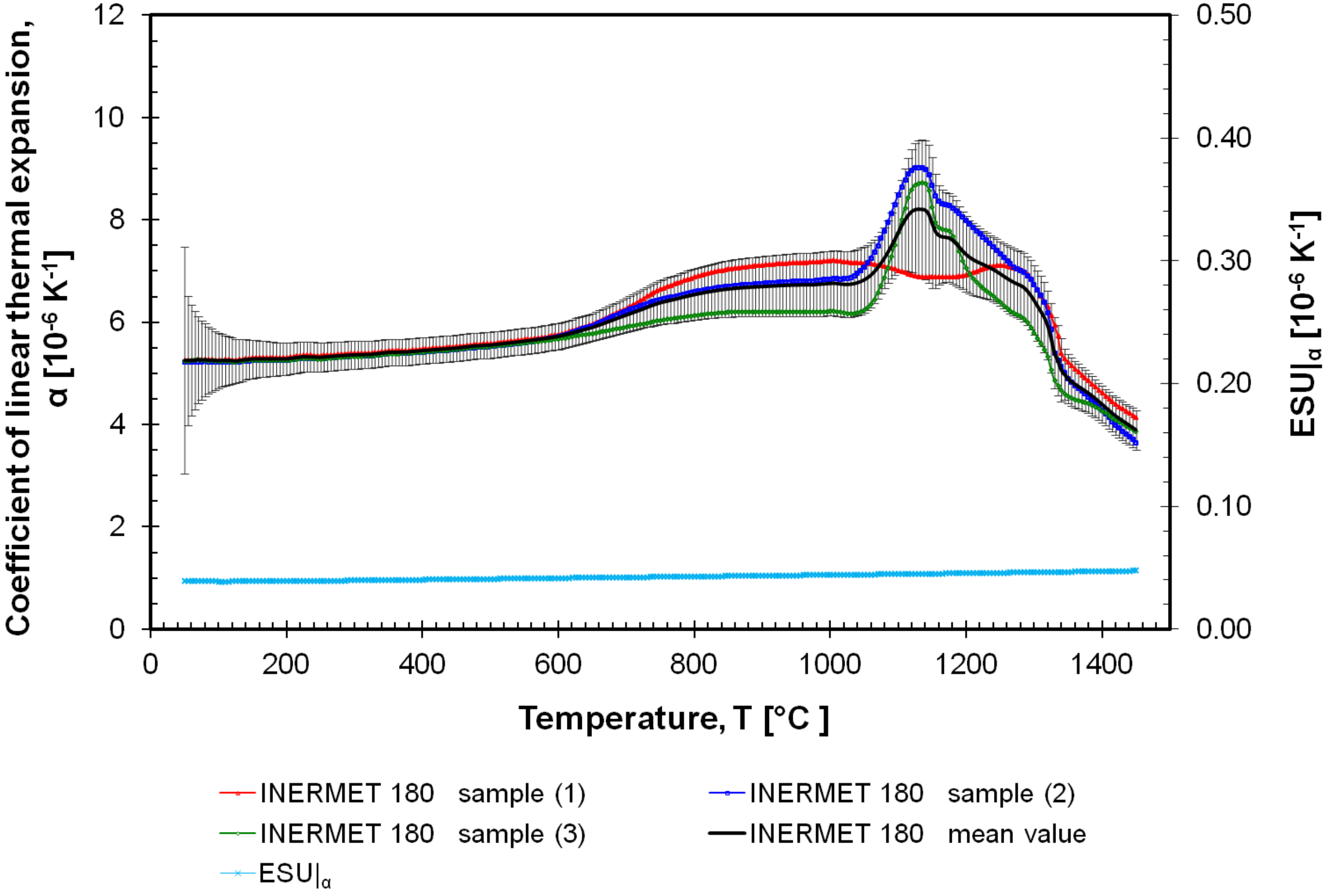

Figure 5.8: Coefficient of linear thermal expansion of INERMET® 180 as a function of temperature.

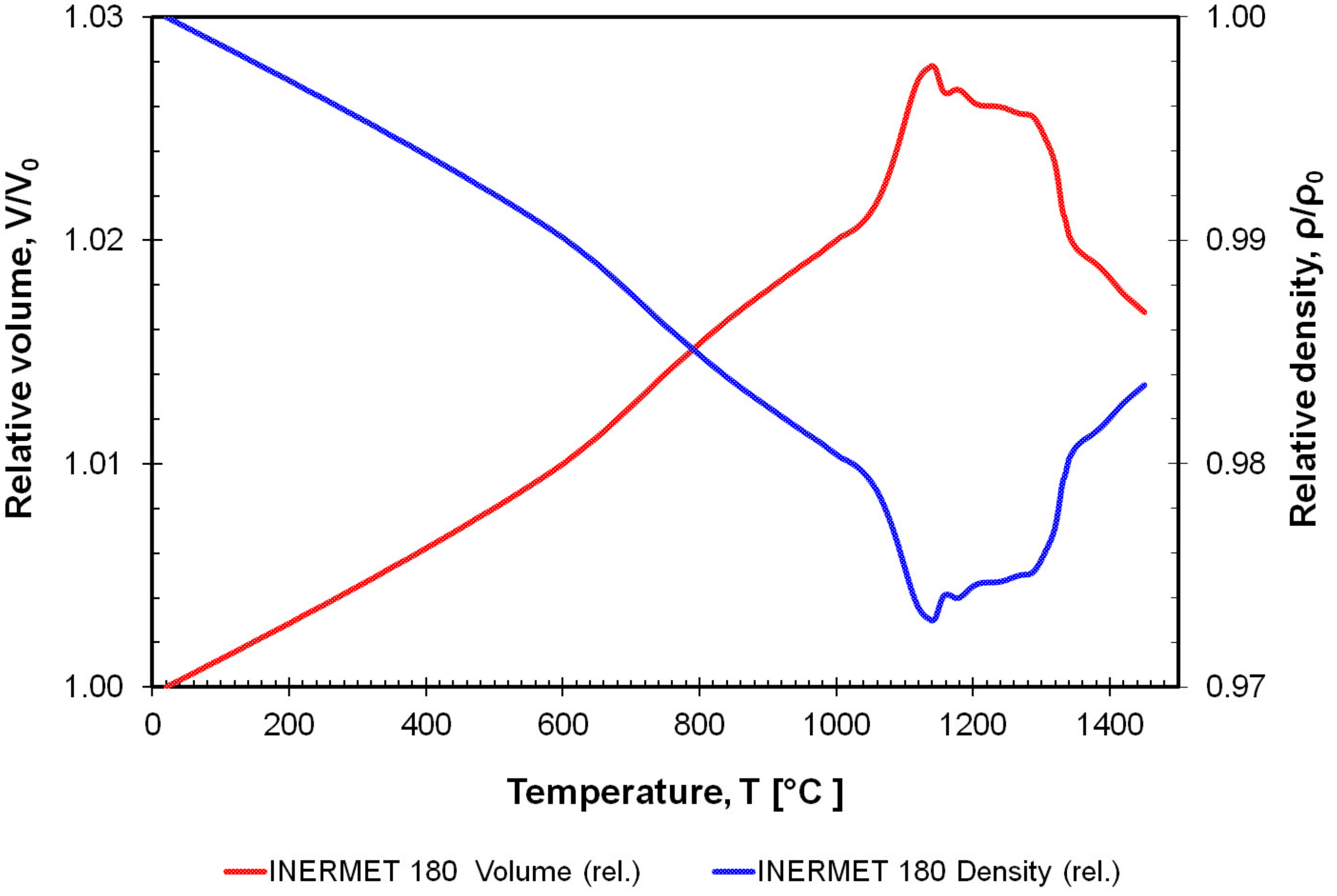

Figure 5.9: Relative thermal density and volume of INERMET® 180 as a function of temperature.

5.3.4 Specific heat capacity

The value of the *specific heat capacity* of INERMET® 180 was measured using the differential scanning calorimetry (DSC) method in accordance with the standards DIN V ENV 1159-3 and DIN ENV 821-3. The DSC method is an experimental technique for measuring the energy necessary to establish a nearly zero temperature difference between a test specimen S and an inert reference material R while the two samples are subjected to an identical temperature program.

A high temperature calorimeter, NETZSCH DSC 404C (Figure 5.10), was used for the specific temperature measurement range of [+25 °C, +1450 °C]. This calorimeter was operated dynamically under argon conditions with a gas flow rate of 50 ml/min in order to avoid corrosion at high temperature. A heating rate of 20 K/min was used in accordance with the relevant standards, leading to sufficiently low uncertainties.

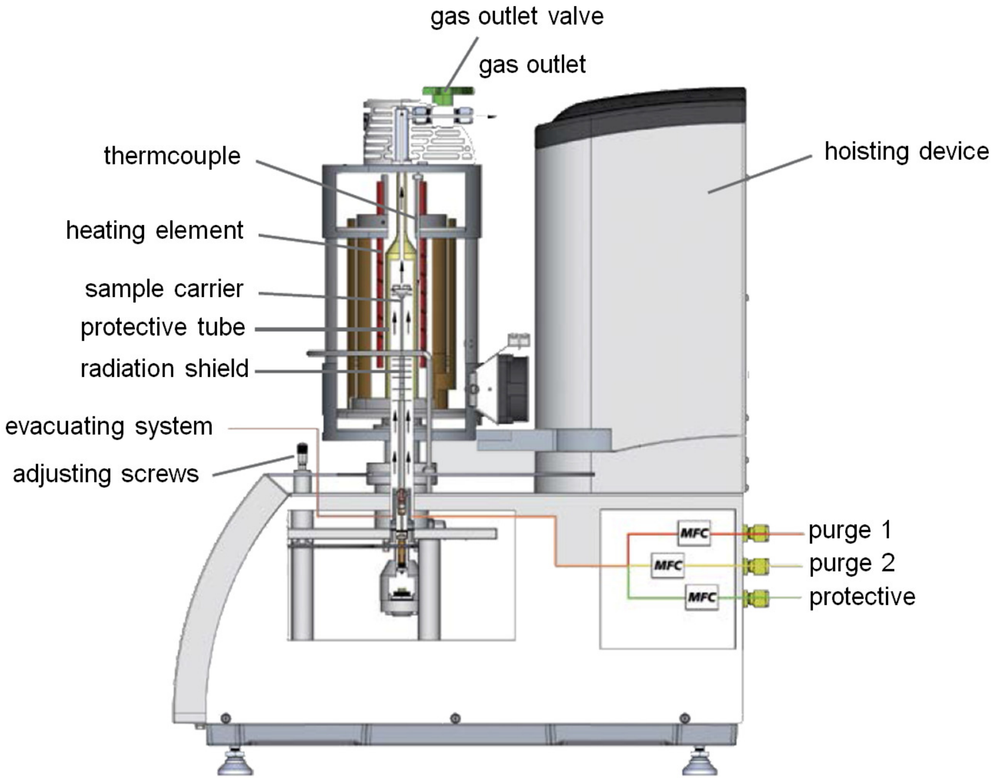

Figure 5.10: Sectional view of a high temperature calorimeter NETZSCH DSC 404C [122].

The DSC 404C system operates according to the heat flux principle (Figure 5.11). With this method, a sample and a reference material are subjected to a controlled temperature program (heating, cooling or isothermal). The measuring process consists of three sequential steps:

1. The determination of the behaviour of the empty calorimeter (base-line: B)
2. The measurement of a reference material R (typically sapphire)
3. The measurement of the sample S

The actual measured properties are the temperature of the sample and the temperature difference between the sample and the reference material measured with a thermocouple. From the raw data signals, the heat flow difference between the sample and the reference material can be determined, from which the specific heat capacity of the sample can then be calculated as will be shown by Equation 5.15. To ensure an optimum representation of the occurring heat consumptions, base-line corrected DSC signals are used.

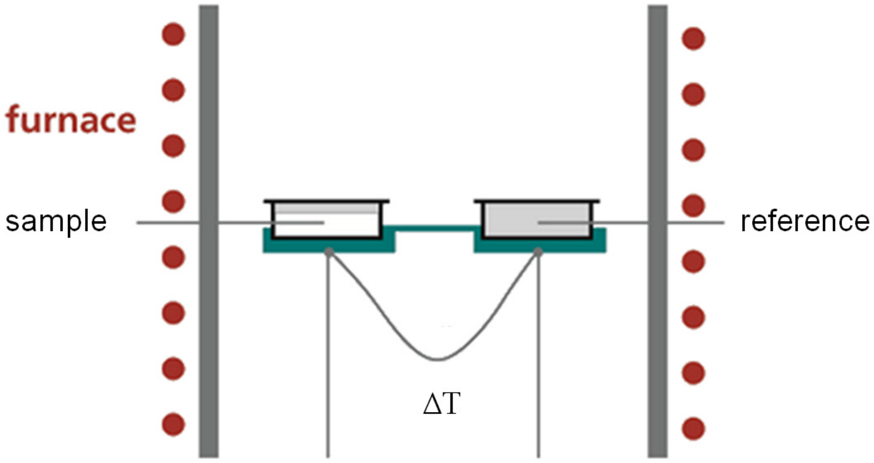

Figure 5.11: Functional principle of a heat-flux DSC [122].

The physical definition of the specific heat capacity $c_{\mathrm{p}}(T)$ (Equation 5.13), together with the mathematical description of the heat content of a material as a function of temperature (Equation 5.14), lead to the derivation of the dynamic calorimeter equation (Equation 5.15). The specific heat capacity can then be calculated based on the measured DSC data from

Equation 5.15. Equations 5.13 [119, p. 13], 5.14 [119, p. 13] and 5.15 [119, p. 13] are given below, where V means the volume of the sample, ρ is the density and DSC refers to the sensor signal:

$$\Delta Q = c_{\mathrm{p}} \cdot m \cdot \Delta T \leftrightarrow c_{\mathrm{p}} = \frac{\Delta Q}{m \cdot \Delta T} = \frac{Q \mid_T^{T+dT}}{m.dT}; [c_{\mathrm{p}}] = 1\frac{J}{g \cdot K}, \tag{5.13}$$

$$Q(t) = \oint_V dV \cdot \rho(\vec{x}, T) \cdot \int_0^{T(\vec{x},t)} c_{\mathrm{p}}(\vec{x}, T) \cdot dT, \tag{5.14}$$

$$c_{\mathrm{p}}{}^{(S)}(T) = \frac{DSC^{(S)}(T) - DSC^{(B)}(T)}{DSC^{(R)}(T) - DSC^{(B)}(T)} \cdot \frac{m^{(R)}}{m^{(S)}} \cdot c_{\mathrm{p}}{}^{(R)}(T), \tag{5.15}$$

where $\frac{m^{(R)}}{m^{(S)}} \cdot c_{\mathrm{p}}{}^{(R)}(T) = f_{\mathrm{e}}(T)$ and $\frac{DSC^{(S)}(T)-DSC^{(B)}(T)}{DSC^{(R)}(T)-DSC^{(B)}(T)} = DSC(T)$

The $ESU \mid_{c_{\mathrm{p}}}$ and the combined standard uncertainty of the measured c_{p} results are given by Equations 5.16 [119, p. 14] and 5.17 [119, p. 14] respectively:

$$\begin{aligned} ESU^2\Big|_{c_{\mathrm{p}}} \cong{} & f_{\mathrm{e}}^2 \cdot \left[\frac{(DSC^{(S)} - DSC^{(B)})^2}{(DSC^{(R)} - DSC^{(B)})^4} \cdot u^2(DSC^{(R)})\right] \\ & + f_{\mathrm{e}}^2 \cdot \left[\frac{(DSC^{(S)} - DSC^{(R)})^2}{(DSC^{(R)} - DSC^{(B)})^4} \cdot u^2(DSC^{(B)})\right] + \left(\frac{m^{(R)}}{m^{(S)}}\right)^2 \cdot DSC^2(T) \cdot u^2(c_{\mathrm{p}}), \end{aligned} \tag{5.16}$$

$$u_{\mathrm{c}}^2(c_{\mathrm{p}}{}^{(S)}(T)) = ESU^2 + f_{\mathrm{e}}^2 \cdot \frac{u^2 DSC^{(S)}}{(DSC^{(R)} - DSC^{(B)})^2}, \tag{5.17}$$

The measured variation of the specific heat capacity with temperature is shown in Figure 5.12. The curves obtained from the measured c_{p} values of the three INERMET® 180 samples indicate the enthalpy effect. This effect cannot be separated from c_{p} effects using standard DSC methods. Thus, the recommended specific heat capacity is calculated using extrapolated values which then give the correct inner transformation intervals.

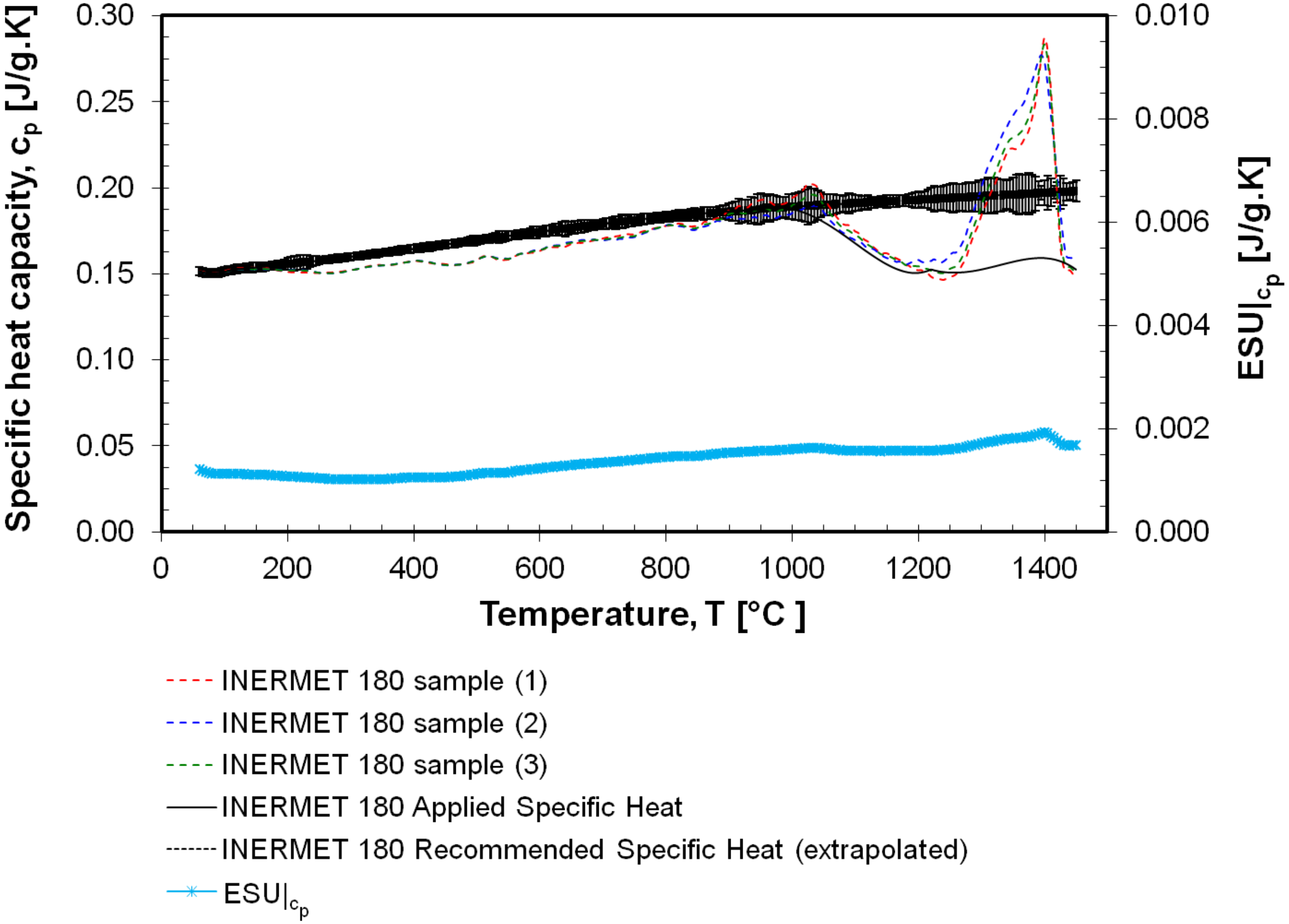

Figure 5.12: Specific heat capacity of INERMET® 180 as a function of temperature.

5.3.5 Thermal diffusivity

The *thermal diffusivity* of INERMET® 180 was measured using the laser flash analysis (LFA) method. This method replaces the measurements of the absolute quantity of laser energy absorbed by the sample, and of the resulting absolute temperature increase, with a more accurate and direct measurement of the time and relative temperature increase. A high temperature NETZSCH LFA 427 (Figure 5.13) was used for the specific temperature range of [+25 °C, +1450 °C]. The measurement procedure was carried out conforming to the standards DIN 51936, DIN V ENV 1159-2, DIN EN 821-2 and ASTM E1461-01.

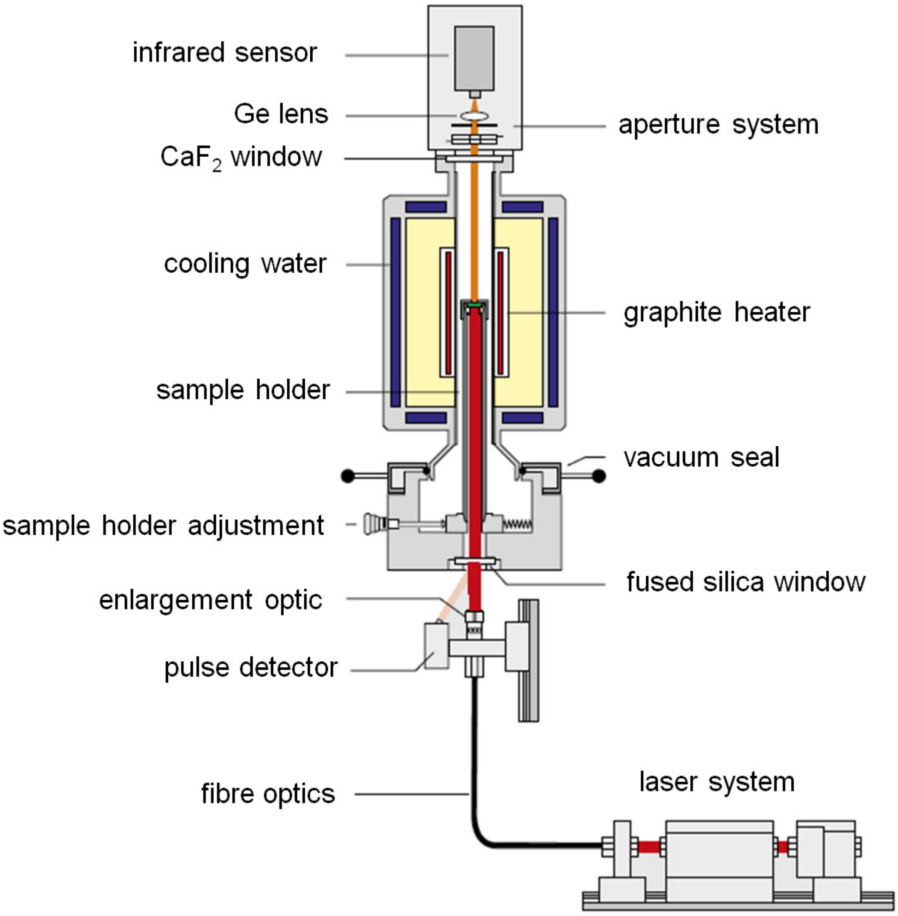

Figure 5.13: Schematic sectional view of the hardware of a NETZSCH LFA 427 [123].

The laser flash apparatus (Figure 5.14) consists of four essential components:

- Measuring unit with furnace, sample carried and infrared detector
- Controller for measuring unit
- Laser system connected via fibre optics
- Data acquisition (DAQ) system and computer

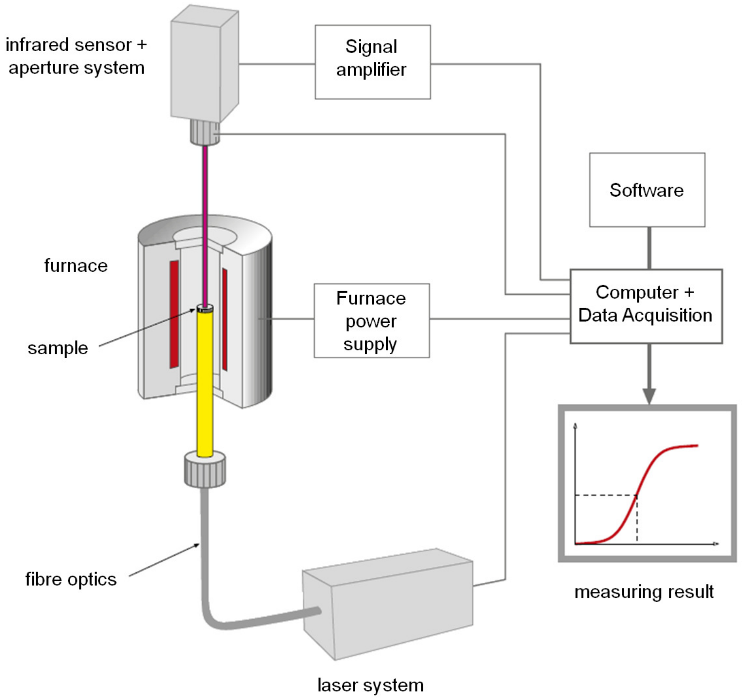

Figure 5.14: Functional principle of the laser flash apparatus [123].

The LFA was operated under isothermal ($\delta T/\delta t < 0.1$ K/min) and helium conditions with a gas flow rate of 50 ml/min. Similar to the other methods, operation with a pure gas is chosen to reduce the possibility of corrosion at high temperature. In general, coplanar discoid samples of a height h are used for the LFA method. Each sample is mounted on a carrier system which is located in a furnace. After the sample reaches a pre-determined temperature, a burst of energy emanating from a pulsed laser is absorbed on the front face of the sample, resulting in homogeneous heating. Reference materials for this method typically include steel 4970, graphite and silicon carbide.

The measuring process is then done in one step and is based on the detection of the time-dependent temperature curve at the rear side of the specimen (away from the laser heated top side of the specimen). The relative temperature increase on the rear face of the sample is measured as a function of time by an infrared detector. The relevant data used to determine the thermal diffusivity are the maximum temperature increase on the rear side $\Delta T_{\max}$, and the time till half of this temperature increase occurs, $t_{1/2}$, where $0.5\Delta T_{\max} = \Delta T(t_{1/2})$.

In case of flash experiments, adiabatic boundaries are applied, meaning that an ideal thermal insulation of the considered volume is assumed. After the initial heat impact applied by the laser pulse, no further heat exchange between the specimen and the thermal environment occurs. The thermal diffusivity is computed by the DAQ software using the time/relative temperature increase data. For adiabatic conditions and under the basic assumptions of Parker's description of a flash technique, the thermal diffusivity κ_{cc} is determined by the Equation 5.18 [119, p. 17]:

$$\kappa_{\mathrm{cc}}(T) = -\frac{ln(\frac{1}{4})}{\pi^2} \cdot \frac{h^2(T)}{t_{1/2}}, \tag{5.18}$$

The ESU of the flash setup and the standard uncertainty of κ_{cc} are given by Equationn 5.19 [119, p. 17] and 5.20 [119, p. 17] respectively:

$$ESU^2(\kappa_{\mathrm{cc}}) = {\kappa_{\mathrm{cc}}}^2 \cdot \left[\frac{4 \cdot u^2(h)}{h^2} + \left(\frac{a \cdot \pi^2}{ln(1/4) \cdot h^2)}\right)^2 \cdot u^2(t_{1/2})\right], \tag{5.19}$$

$$u_c^2(\kappa_{\mathrm{cc}}) = SDV^2(\kappa_{\mathrm{cc}}) + ESU^2(\kappa_{\mathrm{cc}}), \tag{5.20}$$

The measured variation of the thermal diffusivity with temperature is given in Figure 5.15. The phenomenon of the onset of densification is marked on Figure 5.15 and it refers to when the process of sintering occurs, resulting in a decrease in the sample thickness. Thickness relevant data (such as thermal diffusivity) become highly uncertain at temperatures higher than onsets like this and thus such measurement values were not used for the material model in ANSYS®.

5.3.6 Thermal conductivity

One of the most widely used methods for determining the *thermal conductivity* $k(T)$ is to measure the density ρ, the thermal diffusivity κ_{cc} and the specific heat capacity c_{p} as a function of temperature using the methods explained above. In this case, the computation of $k(T)$ as a product of these data was performed for the temperature range [+25 °C, +1450 °C] using Equation 5.21 [107, p. 68]:

$$k(T) = \rho(T) \cdot \kappa_{\mathrm{cc}}(T) \cdot c_{\mathrm{p}}(T), \tag{5.21}$$

The calculated variation of the thermal conductivity with temperature is given in Figure 5.16. The phenomenon of the onset of densification comes from the thermal diffusivity measurements as explained in Section 5.3.5.

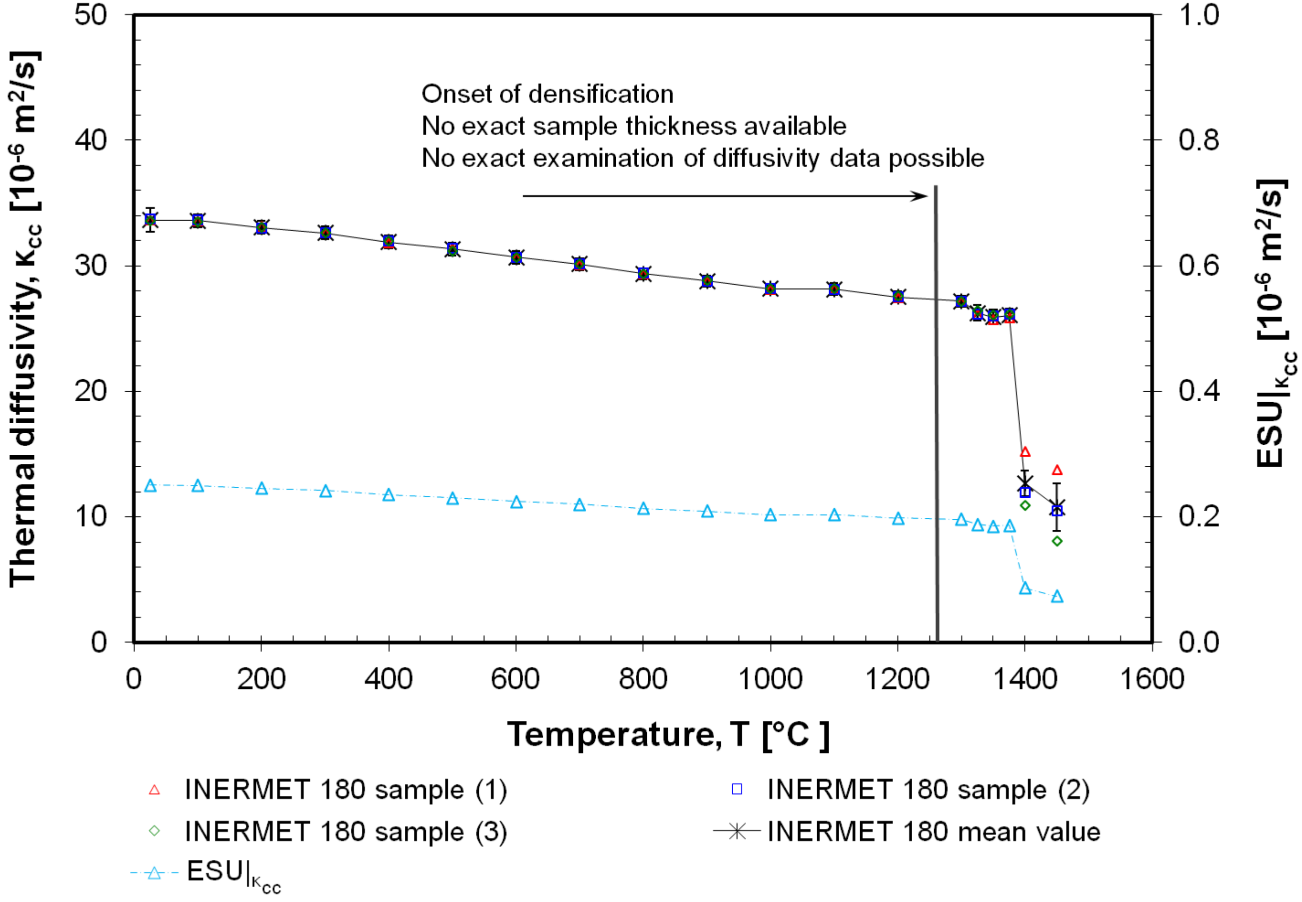

Figure 5.15: Thermal diffusivity of INERMET® 180 as a function of temperature.

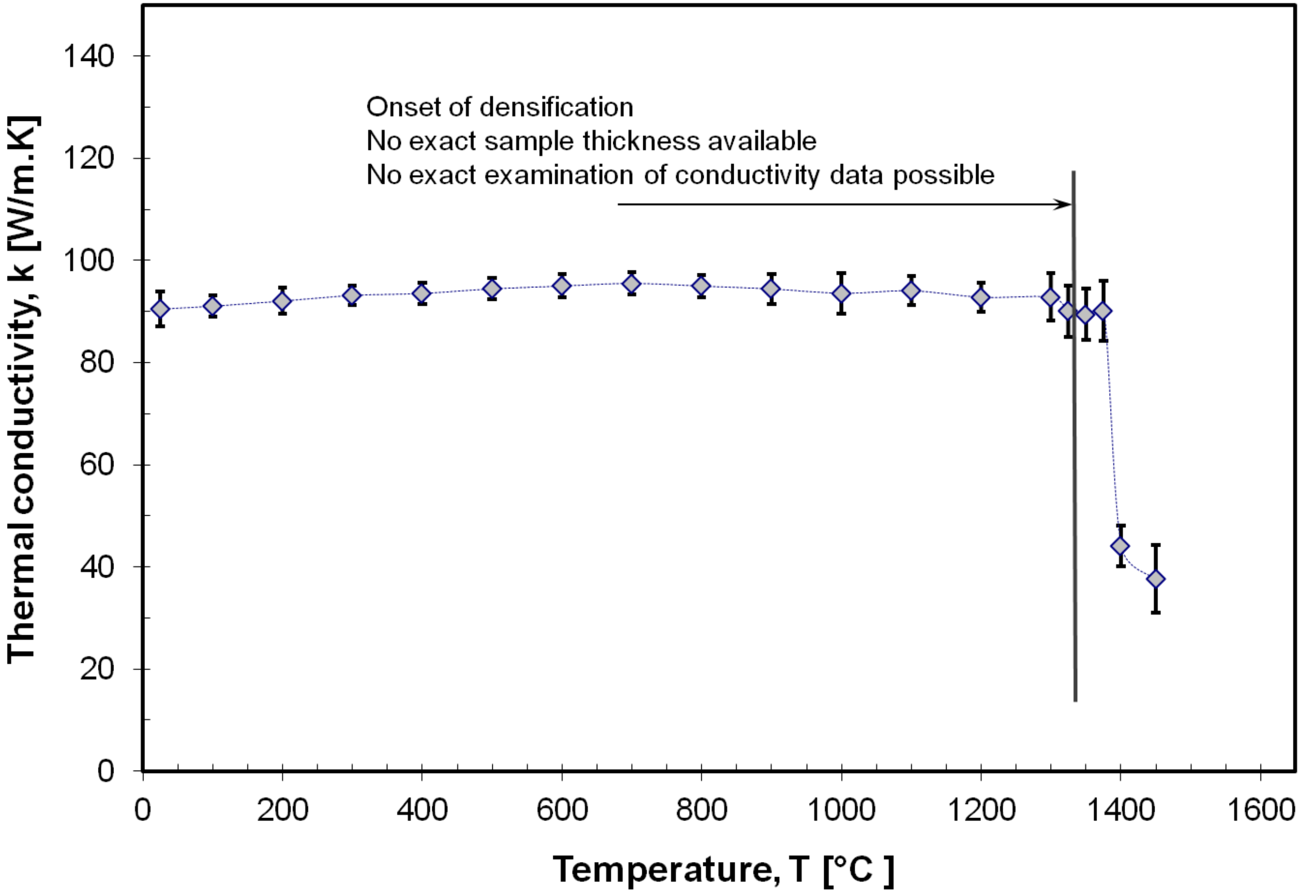

Figure 5.16: Thermal conductivity of INERMET® 180 as a function of temperature.

5.4 Structural characterisation

5.4.1 Structural deliverables

In addition to the thermo-physical characterisation presented in Section 5.3, a structural test campaign was also necessary in order to completely characterise the material behaviour of INERMET® 180. A suitable strength material model for INERMET® 180 was needed to be able to correctly reproduce the mechanical behaviour over a wide strain-rate and temperature range as required for the cases studied in this thesis.

For this reason, a structural characterisation campaign was commissioned and performed at the DYNLab at Politecnico di Torino. This test campaign involved the investigation of the mechanical behaviour of INERMET® 180 under static and dynamic loading conditions at different temperatures. This was achieved through a series of tests consisting of:

- Tests at different strain-rates ($\dot{\epsilon} = 10^{-3}$ s^{-1}, 10^{-1} s^{-1}, 10^{1} s^{-1}, 10^{3} s^{-1}) at a fixed temperature ($T = 25$ °C) to characterise the strain-rate sensitivity of the material (Section 5.4.3)
- Tests at different temperatures ($T = 25$ °C, 100 °C, 200 °C, 400 °C, 600 °C) at two fixed strain-rates to characterise the thermal softening of the material in static ($\dot{\epsilon} = 10^{-3}$ s^{-1}) and dynamic ($\dot{\epsilon} = 10^{3}$ s^{-1}) loading conditions (Section 5.4.4)

The experimental setup and methodologies used to obtain the temperature and strain-rate behaviour of INERMET® 180 are presented in the following sections as indicated for each set of tests above. The results of the test campaign are then presented in Sections 5.4.5 and 5.4.6.

5.4.2 Overview of structural characterisation tests

Temperature and strain-rate are two variables of fundamental importance for the description of the mechanical behaviour of materials. In some elastic-plastic models, the effects, resulting from these two variables, are considered to act independently. Such an approach allows the simplification of the experimental setup corresponding to the parameter identification of the material model. This is because while the parameters for the strain-rate sensitivity can be extracted from tests at different strain-rates at a fixed temperature, the parameters for the temperature sensitivity can be extracted from tests at different temperatures at a fixed strain-rate.

However, in applications such as high energy deposition on metals where the materials are deformed at very high speed (which implies self-heating due to the adiabatic process) in high-temperature conditions, it is not acceptable to decouple the effects of strain-rate and temperature. In such cases, the stress-strain behaviour of the material is the result of the mutual effects of both hardening (due to strain and strain-rate) and thermal softening. Thus, in this perspective, a methodology for testing materials by varying both strain-rate and temperature was applied for the commissioning of the structural characterisation tests of INERMET® 180.

The experimental tests were performed in tensile loading condition on standard dumbbell (dog-bone) shaped specimens. Such specimens consist of a central zone with a constant cross-section and two transition zones in which the cross-section gradually increases (Figure 5.17). Unique specimen geometry was used for all the performed tests in order to avoid the influence of geometry and dimensions on the results, as well as to have the possibility to directly compare the results coming from the different loading conditions.

An effective structural characterisation campaign is normally composed of three main steps [124], which in this case were carried out and provided by the research group at Politecnico di Torino:

1. The completion of experimental tests performed at different strain-rates (from quasi-static loading to high strain-rate) and different temperatures (from 25 °C to 600 °C) (Sections 5.4.3, 5.4.4 and 5.4.5).
2. The fitting of the obtained experimental results with analytical models that can be used in numerical FEM simulations in order to obtain reference material strength parameters. Such parameters serve as starting trial points in the inverse method optimisation procedure (Section 5.4.6).
3. The optimisation of the material strength parameters via a numerical inverse method in order to obtain a reliable strength material model (Section 5.4.6).

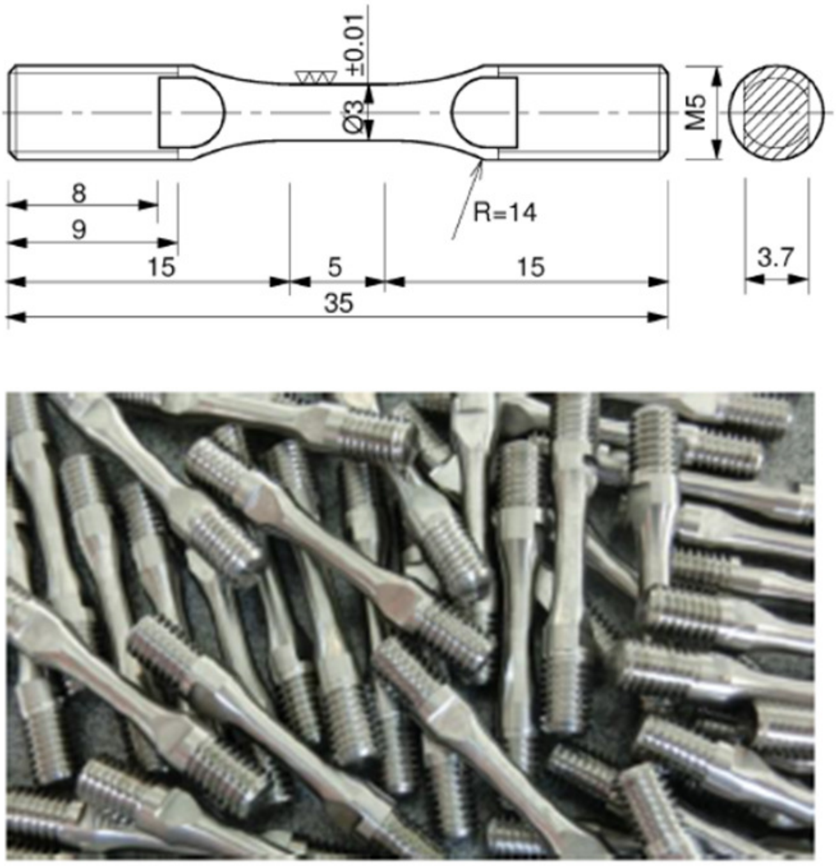

Figure 5.17: Specimens of INERMET$^{®}$ 180 used for the structural characterisation tests: schematic diagram of the standard dumbbell (dog-bone) shaped specimen used for the tensile tests ($\phi = 3$ mm, $L = 5$ mm) (top), and 60 samples of INERMET$^{®}$ 180 used for the experimental test campaign (bottom).

5.4.3 Tests varying the strain-rate

The strain-rate behaviour of INERMET® 180 and the effects of hardening (strain and strain-rate) on the material strength were obtained through experimental tests with strain-rate variation. A series of tests were thus performed at different strain-rates and at room temperature in order to obtain information about the strain-rate sensitivity of the material. The nominal strain-rates ($\dot{\epsilon}$) of the tests were 10^{-3} s^{-1}, 10^{-1} s^{-1}, 10^{1} s^{-1} and 10^{3} s^{-1}. The choice of such values was to provide a good overview of the strain-rate behaviour of the material over a wide range of strain-rates while at the same time taking into account testing machine limits.

While the low strain-rate tests were performed on a standard electro-mechanical testing machine - the Zwick Z-100 (maximum load = 100 kN, maximum travel speed = 5 mm/s), the medium strain-rate tests were achieved using a standard servo-hydraulic testing machine - the Dartec HA100 (maximum load = 100 kN, maximum speed = 100 mm/s). The experimental setup used for the quasi-static ($\dot{\epsilon} = 10^{-3}$ s^{-1}), low ($\dot{\epsilon} = 10^{-1}$ s^{-1}) and medium ($\dot{\epsilon} = 10^{1}$ s^{-1}) strain-rate tests at room temperature (25 °C) is shown in Figure 5.18.

The Split Hopkinson tensile bar setup (Figure 5.19) was then used to perform the high strain-rate ($\dot{\epsilon} = 10^{3}$ s^{-1}) tests. The setup consists of a gas-gun, an impactor, and incident and transmitter bars. The specimen is fixed to the incident and transmitter bars. The gas-gun is 1.5 m long and uses compressed air. The striker bar is a 750 mm long tube made of glass reinforced nylon. The incident and the transmitter bars are made of martensitic high strength precipitation-hardening stainless steel (17-4 PH) with a diameter of 10 mm and they have a length of 6.8 m and 3.4 m respectively.

The outer end of the incident bar is hit by the striker, which is pneumatically accelerated. An initial compression wave, which propagates along the incident bar towards the specimen, is generated. When this compression wave (incident wave) reaches the specimen, it is partly reflected back off the free end of the incident bar as a tensile wave (reflected wave) and partly transmitted to the transmitter bar (transmitted wave). As a result, the specimen

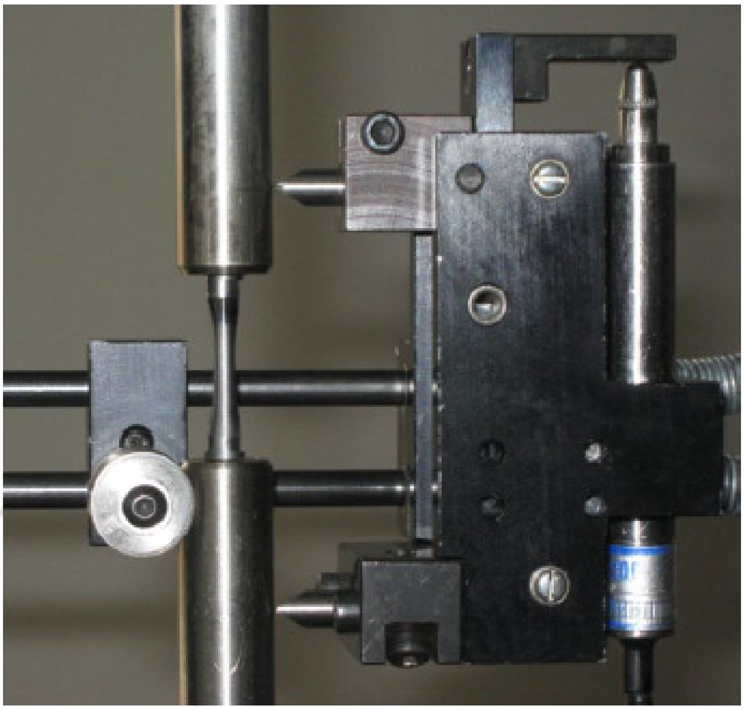

Figure 5.18: The experimental setup used for the quasi-static up to medium strain-rate tests at room temperature using the Zwick Z-100 and the Dartec HA100 machines respectively.

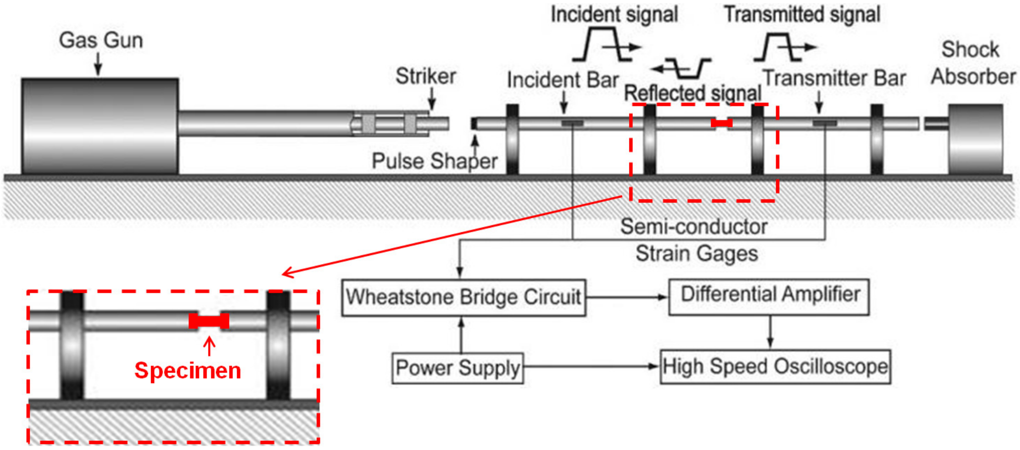

Figure 5.19: Schematic diagram of the Split Hopkinson tensile bar setup used for the dynamic tensile tests (direct tension up to a strain-rate of 10^3 s^{-1}). A detailed view of the dog-bone-shaped test specimen fixed into the incident and transmitter bars is shown in the inset (adapted from [125]).

is subjected to a high strain-rate tensile load through its interaction with the reflected tensile wave.

The strain histories corresponding to the incident, reflected and transmitted waves are measured by means of semiconductor strain gauges located on both the incident and transmitter bars (Figure 5.20). Such strain gauges surpass traditional resistance strain gauges in that they are able to obtain a signal with a very low level of noise. Moreover, due to their higher gauge factor, they do not require the use of a dedicated amplifier but can be directly connected to the DAQ system.

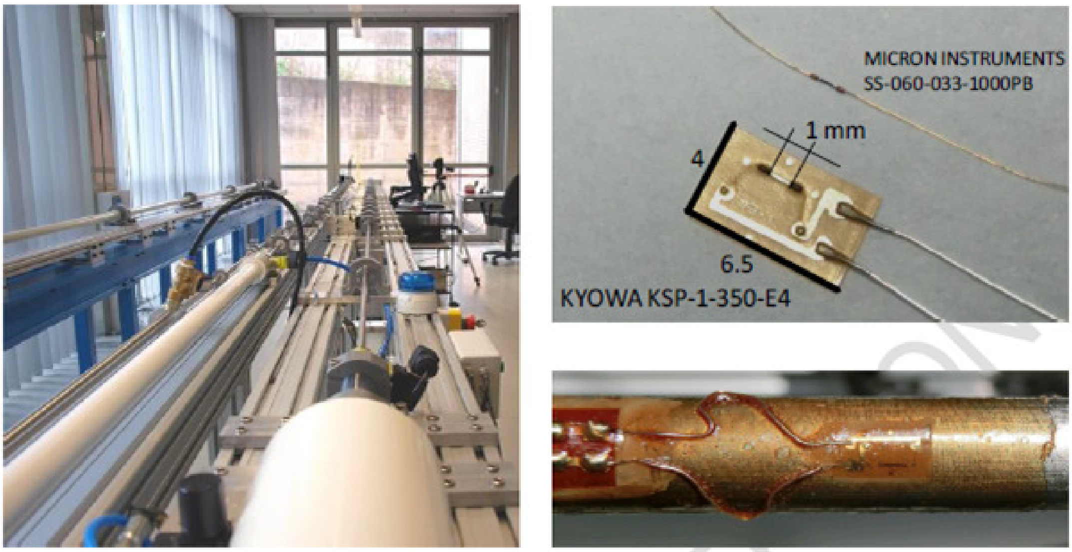

Figure 5.20: The Split Hopkinson bar experimental setup used for the high strain-rate tests: experimental setup in DYNLab of Politecnico di Torino (left), and two types of strain gauges used for the strain measurements (right).

5.4.4 Tests varying the temperature

The mechanical behaviour of INERMET® 180 was fully characterised by performing tests varying the temperature in order to be able to describe the thermal softening effects on the material strength. Thus, a series of tests at different temperatures were carried out both in quasi-static and in high dynamic loading conditions. In both cases, the specimen was heated using an induction coil system, properly designed in order to concentrate the heat flux in the gauge length of the specimen (Figure 5.21).

In the case of quasi-static tests ($\dot{\epsilon} = 10^{-3}$ s^{-1}), the nominal temperatures (T) of the tests were 25 °C, 100 °C, 200 °C, 400 °C and 600 °C. Quasi-static tests at higher temperatures could not be performed because of the high test duration in these cases and the limitation that the testing equipment could not tolerate to remain at such a high temperature for a long time. In high dynamic loading conditions ($\dot{\epsilon} = 10^{3}$ s^{-1}), the temperatures (T) investigated were 25 °C, 200 °C, 400 °C and 600 °C. In this case, the maximum temperature was fixed to that attainable during the quasi-static tests.

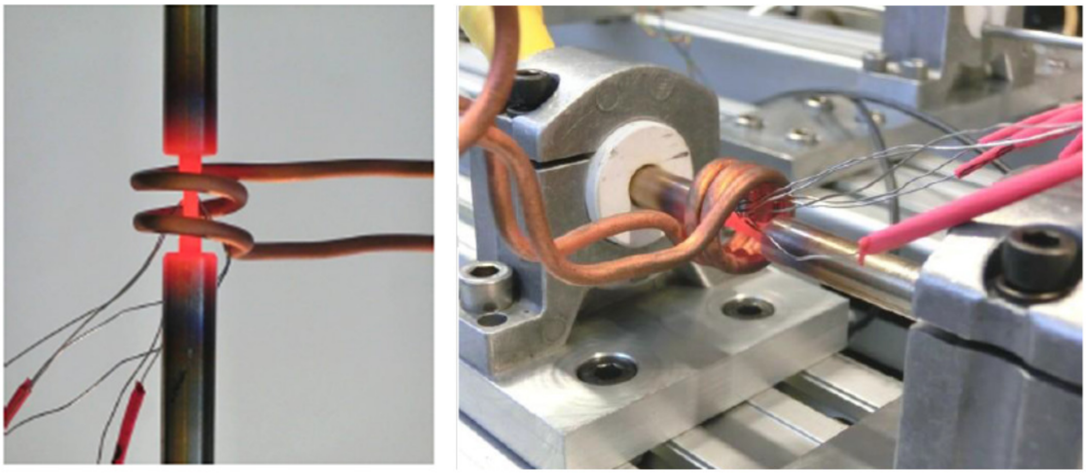

Figure 5.21: The experimental setup for the quasi-static and dynamic tests at high temperature: photo of the setup for the quasi-static test (strain-rate: 10^{-3} s^{-1}) at 600 °C (left), and photo of the heating and cooling system for the Hopkinson test (strain-rate: 10^{3} s^{-1}) at 600 °C (right).

The temperature was controlled by a proportional-integral derivative (PID) controller that provided feedback on the basis of the thermocouple measurements. The thermocouples were welded directly on the specimen surface, far from the gauge length in order to avoid inducing any changes or altering the area of necking. Each specimen was kept for about 5 minutes at the desired temperature before the test was performed in order to reach uniformity.

A calibration procedure was performed on the specimen before the experimental tests were performed. The specimen was mounted in the machine to replicate the testing condition. Three thermocouples were used in order to correlate the temperature in the middle of the gauge length of the specimen, T_2, with the temperature where the thermocouples were welded (T_1, T_3), and to monitor the uniformity of the heating (Figure 5.22). Two different calibrations were performed for the quasi-static and the dynamic tests. Due to the small dimension of the specimen and the high power of the heating induction system, the difference in temperature between T_2 and T_3 was on the order of 2%, while that between the control thermocouple T_1 and the other thermocouple T_3 was less than 1%.

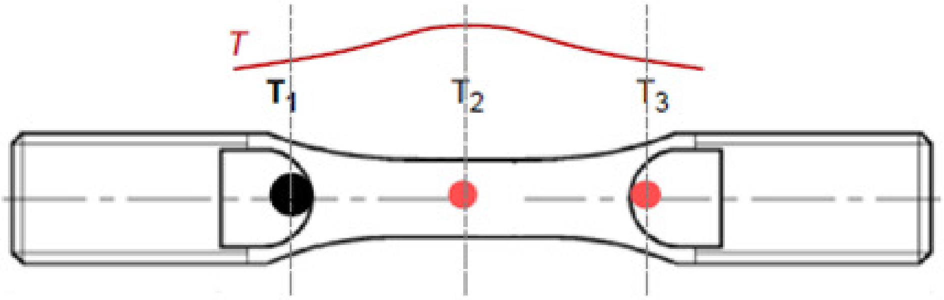

Figure 5.22: Schematic diagram of the calibration procedure used for the temperature control in the tests varying the temperature.

5.4.5 Experimental results

For each test, the load (F) applied by the testing equipment and the change in length (ΔL) of the specimen were recorded. From these values, and considering the nominal cross-sectional area (A_0 with a diameter of 3 mm) and the nominal gauge length ($L_0 = 5$ mm) of the specimens, it was possible to evaluate the engineering stress-strain curves of the material using Equations 5.22 [126, p. 134]) and 5.23 [126, p. 135] given by:

$$\sigma_{\text{eng}} = \frac{F}{A_0}, \tag{5.22}$$

$$\epsilon_{\text{eng}} = \frac{\Delta L}{L_0}, \tag{5.23}$$

Three repetitions were at least performed for each testing condition in order to ensure control over the data scattering; however, for the sake of clarity, Figures 5.23, 5.24 and 5.25 only show the experimental results obtained from two different samples per test condition. It can be observed that, as expected, the material behaviour is both temperature and strain-rate sensitive [127].

Figure 5.23 shows that the material behaviour at room temperature becomes quite brittle on increasing the strain-rate, with a consequent reduction in the ductility. In fact, the maximum strain at failure for a specimen under high strain-rate at room temperature is only about 1%. On the other hand, on increasing the temperature at high strain-rate, the material becomes more ductile and reaches strains greater than 10% (Figure 5.25).

Moreover, it can be observed from Figure 5.23 that the flow stress increases on increasing the strain-rate. This effect is also evident on comparing Figures 5.24 and 5.25 and it is due to the fact that there is less time for material recovery in high strain-rate conditions. The presence of initial oscillations in the dynamic tests is not related to the material yield stress but it is due to inertia or misalignment factors in the experimental setup. Both in the quasi-static and dynamic regimes, the strain to failure grows on increasing the temperature until it reaches a maximum after which it decreases again for very high temperatures (Figures 5.24 and 5.25).

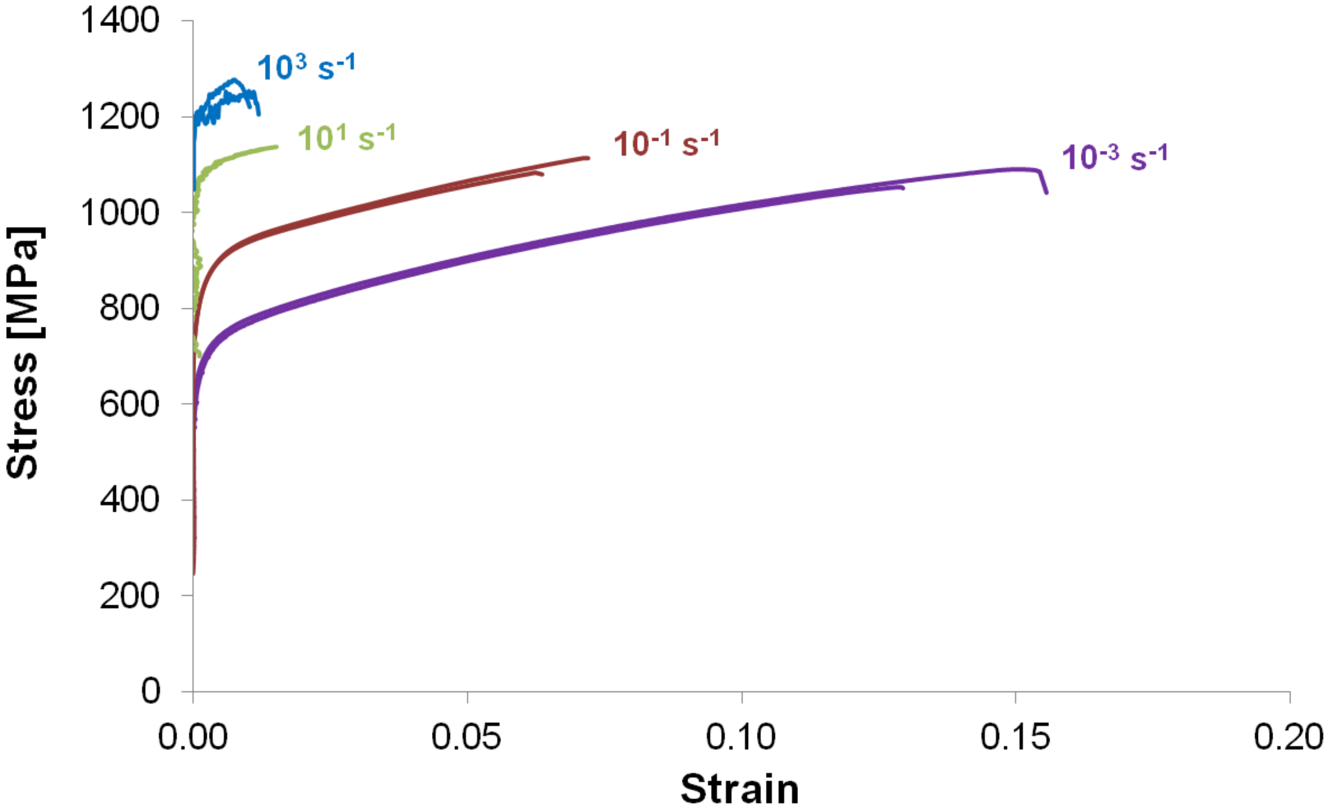

Figure 5.23: Experimental results of INERMET® 180 in terms of engineering stress versus engineering strain for dynamic tests at different strain-rates at room temperature (T = 25 °C).

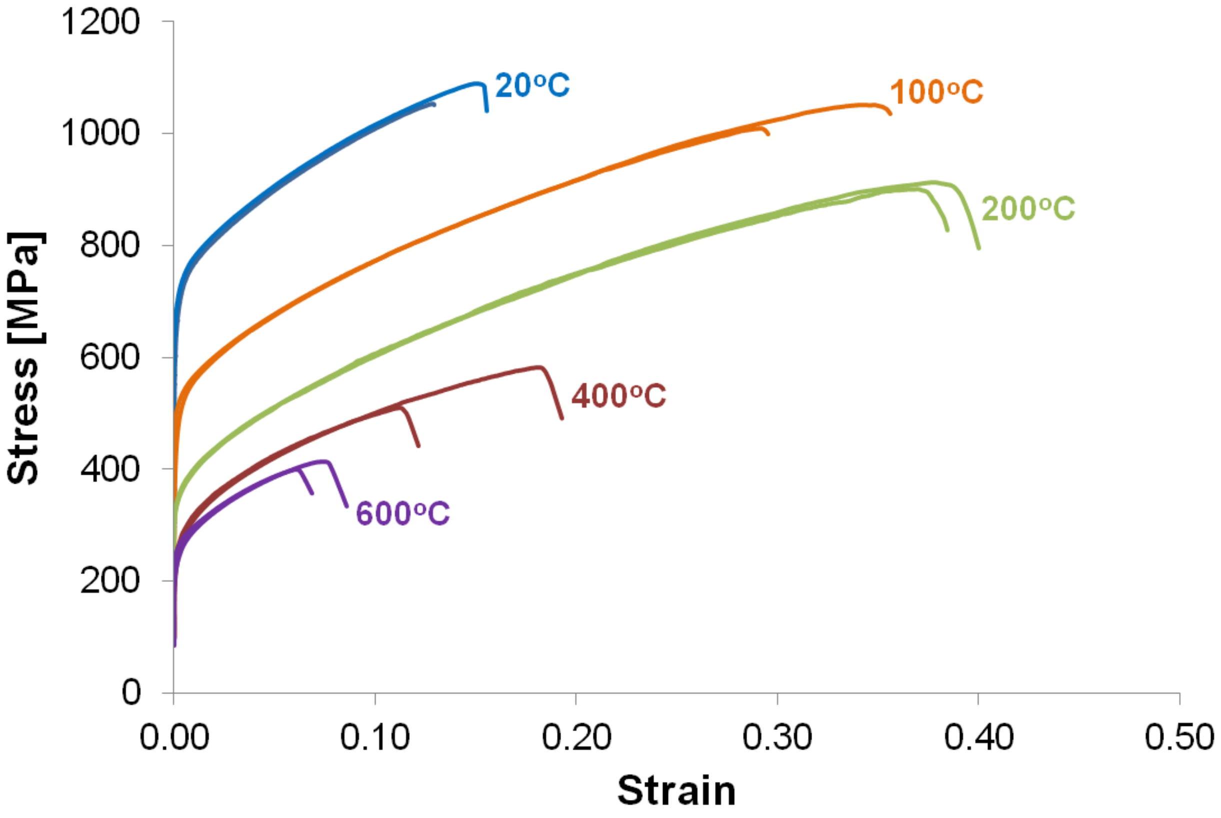

Figure 5.24: Experimental results of INERMET® 180 in terms of engineering stress versus engineering strain for quasi-static tests ($\dot{\epsilon} = 10^{-3}$ s^{-1}) at different temperatures.

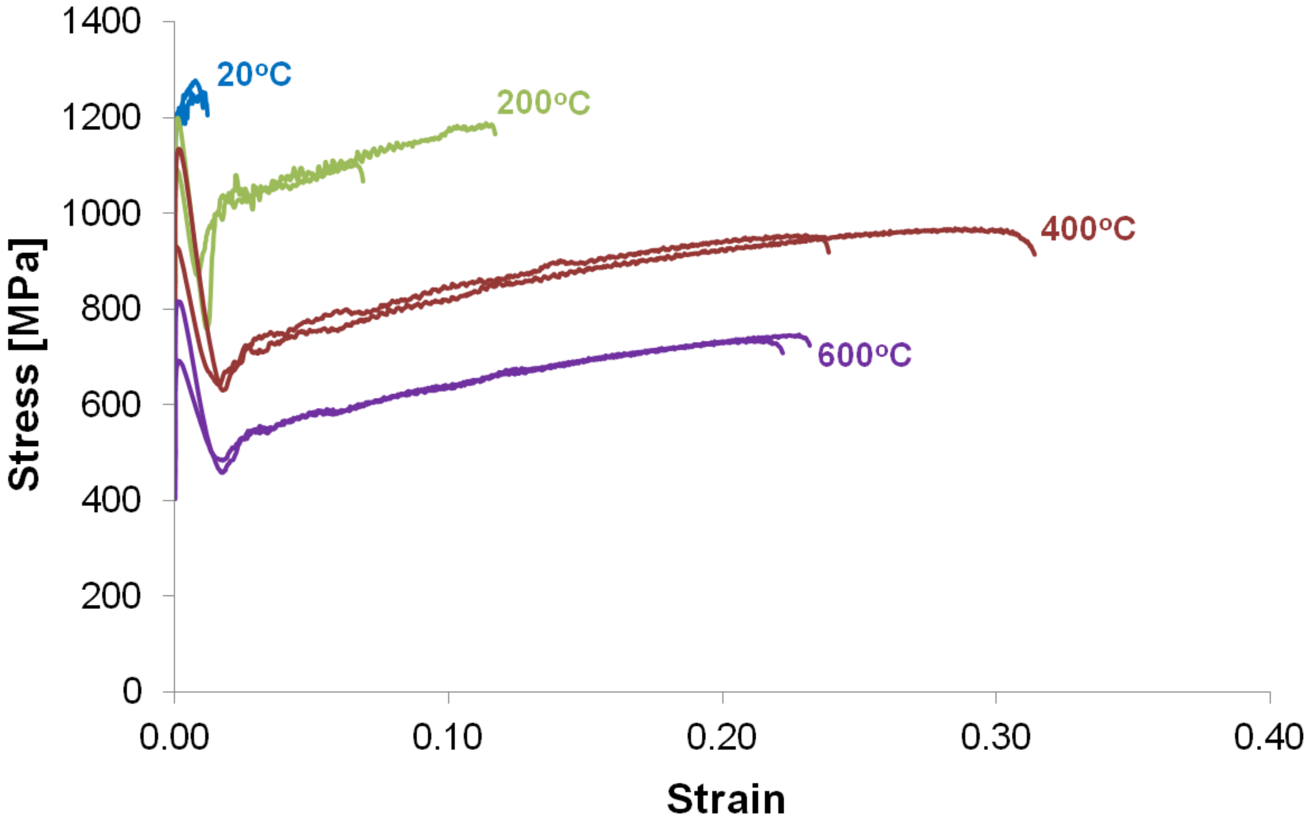

Figure 5.25: Experimental results of INERMET® 180 in terms of engineering stress versus engineering strain for high strain-rate tests ($\dot{\epsilon} = 10^3\ \mathrm{s}^{-1}$) at different temperatures.

In general, the stress-strain curve results in Figures 5.23, 5.24 and 5.25 indicate repeatability with a low level of scattering. This is summarised in Table 5.1 that gives an estimate of the data scatter by means of the normalised root mean square error (NRMSE) value.

Table 5.1: Data scatter evaluation in terms of NRMSE (%) for tests at different temperature (T) and strain-rate ($\dot{\epsilon}$) loading conditions.

$\dot{\epsilon} \setminus T$	**25 °C**	**100 °C**	**200 °C**	**400 °C**	**600 °C**
$\mathbf{10^{-3}\ s^{-1}}$	0.93	0.15	0.39	1.94	0.96
$\mathbf{10^{3}\ s^{-1}}$	1.98	...	1.39	8.36	0.39

5.4.6 Modelling and numerical inverse method

The experimental results presented in Section 5.4.5 were finally used to identify a suitable strength material model for the mechanical behaviour description of INERMET® 180. The engineering stress-strain results given in Figures 5.23, 5.24 and 5.25 were analytically converted into true stress-strain results under the hypothesis of volume conservation (Equations 5.24 and 5.25). Finally, the true (or effective) plastic strain, ϵ_{pl}, was obtained by subtracting the elastic part of the deformation (Equation 5.26). Equations 5.24, 5.25 and 5.26 [126, p. 151] are given by:

$$\sigma_{\mathrm{true}} = \sigma_{\mathrm{eng}} \left(1 + \epsilon_{\mathrm{eng}}\right), \tag{5.24}$$

$$\epsilon_{\mathrm{true}} = ln \left(1 + \epsilon_{\mathrm{eng}}\right), \tag{5.25}$$

$$\epsilon_{\mathrm{pl}} = \epsilon_{\mathrm{true}} - \frac{\sigma_{\mathrm{true}}}{E}, \tag{5.26}$$

The reference material strength parameters of INERMET® 180 were initially obtained by fitting the experimental curves with an analytical Johnson-Cook (J-C) model [128]. These parameters were then implemented into the commercial FE code LS-DYNA in order to numerically simulate the performed experimental tests and ultimately correlate the resulting model parameters with the experimental data. In order to reduce the CPU time of calculation and to correctly reproduce the experimental tests, FE models consisted only of the specimen with the applied load history directly registered from the testing equipment.

It was however observed that the model parameters obtained as an outcome of these numerical simulations did not fit the experimental data of INERMET® 180. In fact, the reference material parameters obtained from a standard analytical fit of the experimental data and used for the numerical simulations were based on a number of assumptions including:

- Uniaxial stress-strain fields are assumed inside the specimen. However, three-axial stress-strain fields are in fact provoked by the necking of the specimen during the tensile tests.
- A constant strain-rate is assumed inside the specimen. This is not the case during the dynamic tests and thereby such a choice influences the stain-rate sensitivity parameters.
- A uniform temperature is assumed inside the specimen. Once again, the temperature has a certain distribution proportional to the distribution of plastic deformation inside the specimen, and this effect is even more pronounced for dynamic tests. Consequently, this assumption influences the identification of the thermal softening parameters.

A numerical optimisation procedure of the reference material parameters was thus deemed necessary in order to cater for these assumptions and to determine a selected set of unknown parameters in the numerical model, which would correctly reproduce experimental tests with

FEM calculations. The main advantage of this numerical inverse optimisation procedure is that no hypothesis about the internal specimen stress-strain, temperature or strain-rate fields is made. As a matter of fact, the comparison is made in terms of macroscopic quantities that are usually force and displacement. Moreover, the adiabatic self-heating can be taken into account for dynamic tests. On the other hand, the main disadvantage of the inverse method is the high computational times that the optimisation algorithms need as the latter must iteratively perform a certain number of FEM simulations. The number of iterations also dramatically increases when the DOFs of the problem increase or when the trial parameters are far from the optimum ones.

The procedure consists of iteratively solving numerical simulations, having the experimental curves as objective functions and starting from trial values of the parameters obtained from a standard analytical optimisation method. For each experimental curve, the normalised distance between the experimental data and the model prediction was minimised, varying all model parameters. Optimisation of the parameter identification has been performed with a dedicated algorithm included in the software LS-OPT. The optimisation algorithm consisted of a multi-objective procedure, in which at the same time the true stress versus true plastic strain curves of all the experimental tests were used as target functions. All the simulations were then run simultaneously relative to a specific set of parameters that had to be optimised.

The most popular strength material models are the J-C model, the Zerilli-Armstrong (Z-A) model or other models in which strain-rate and temperature are mutually related. The J-C model was implemented as a first optimisation procedure. However, the J-C model is a multiplicative model in which the effects of plastic strain, strain-rate and temperature are assumed to act independently. It is shown by Equation 5.27 that a strain-rate or temperature variation only implies a scaling, and not a modification in the shape of the strain hardening curve. Equation 5.27 [128] describes the flow stress as follows:

$$\sigma = (A + B\epsilon_{\mathrm{pl}}^{n}) \left(1 + Cln\frac{\dot{\epsilon}_{\mathrm{pl}}}{\dot{\epsilon}_0}\right) \left(1 - \left(\frac{T - T_{\mathrm{ref}}}{T_{\mathrm{melt}} - T_{\mathrm{ref}}}\right)^{m}\right), \tag{5.27}$$

where A is the yield strength, and B and n are the work hardening parameters that influence the slope of the flow stress in the plastic domain. The parameter n usually assumes values between 0 (for a perfectly plastic model) and 1 (for a piecewise linear model). C is the strain-rate sensitivity coefficient and m describes the thermal softening. The thermal effects are also described as a function of the reference temperature T_{ref} at which there are no thermal effects, and the melting temperature T_{melt} at which the material mechanical strength drops down to zero, and the material loses its shear strength and starts to behave like a fluid.

The Z-A model was subsequently chosen as a constitutive model for the visco-plastic flow behaviour as it is able to couple the effects of temperature and strain-rate with a sufficient level of accuracy. The Z-A material model is partially physically based on simplified dislocation mechanics and in fact, it is able to differentiate between BCC and FCC materials. The Z-A model expresses the flow stress for BCC metals as given by Equation 5.28 [129]:

$$\sigma = C_1 + C_2 e^{[-C_3 + C_4 ln(\dot{\epsilon}_{\mathrm{pl}})]T} + C_5 \epsilon_{\mathrm{pl}}^n, \tag{5.28}$$

where T is the temperature, ϵ_{pl} and $\dot{\epsilon}_{\mathrm{pl}}$ are the effective plastic strain and strain-rate, while C_1, C_2, C_3, C_4, C_5 and n are experimental constants used as the variables of optimisation.

A modified version of the Z-A model as proposed in [130] was used by the team at the Politecnico di Torino for this study, resulting in a more suitable constitutive equation for the flow stress. This is given by Equation 5.29 that takes into account the coupling between strain and temperature in addition to that between temperature and strain-rate:

$$\sigma = (C_1 + C_2 \epsilon_{\mathrm{pl}}^n) e^{-(C_3 + C_4 \epsilon_{\mathrm{pl}})T^* + (C_5 + C_6 T^*) ln \dot{\epsilon}_{\mathrm{pl}}^*}, \tag{5.29}$$

where T^* is the temperature increment with respect to the reference condition and $\dot{\epsilon}^*_{\mathrm{pl}}$ is the ratio between the actual and reference strain-rates. The model parameters C_1, C_2, C_3, C_4, C_5, C_6 and n are the variables of optimisation.

Although all investigated material models were able to partially reproduce the material response at different loading conditions, the modified Z-A formulation presented the best solution as it entailed a reduction in the error for all loading conditions. The comparison between the experimental data and the modified Z-A model prediction for different loading conditions is shown in Figures 5.26, 5.27 and 5.28. It can be observed that for most cases, the error is around or less than 5% except for some quasi-static cases in which the error is between 10 - 20%.

In conclusion, the modified Z-A model is able to correctly reproduce the material behaviour at high strain-rates over a wide range of temperatures as well as the material response at different strain-rates at room temperature. The model is slightly less accurate in the prediction of the behaviour at different temperatures in the quasi-static regime, especially over 400 °C.

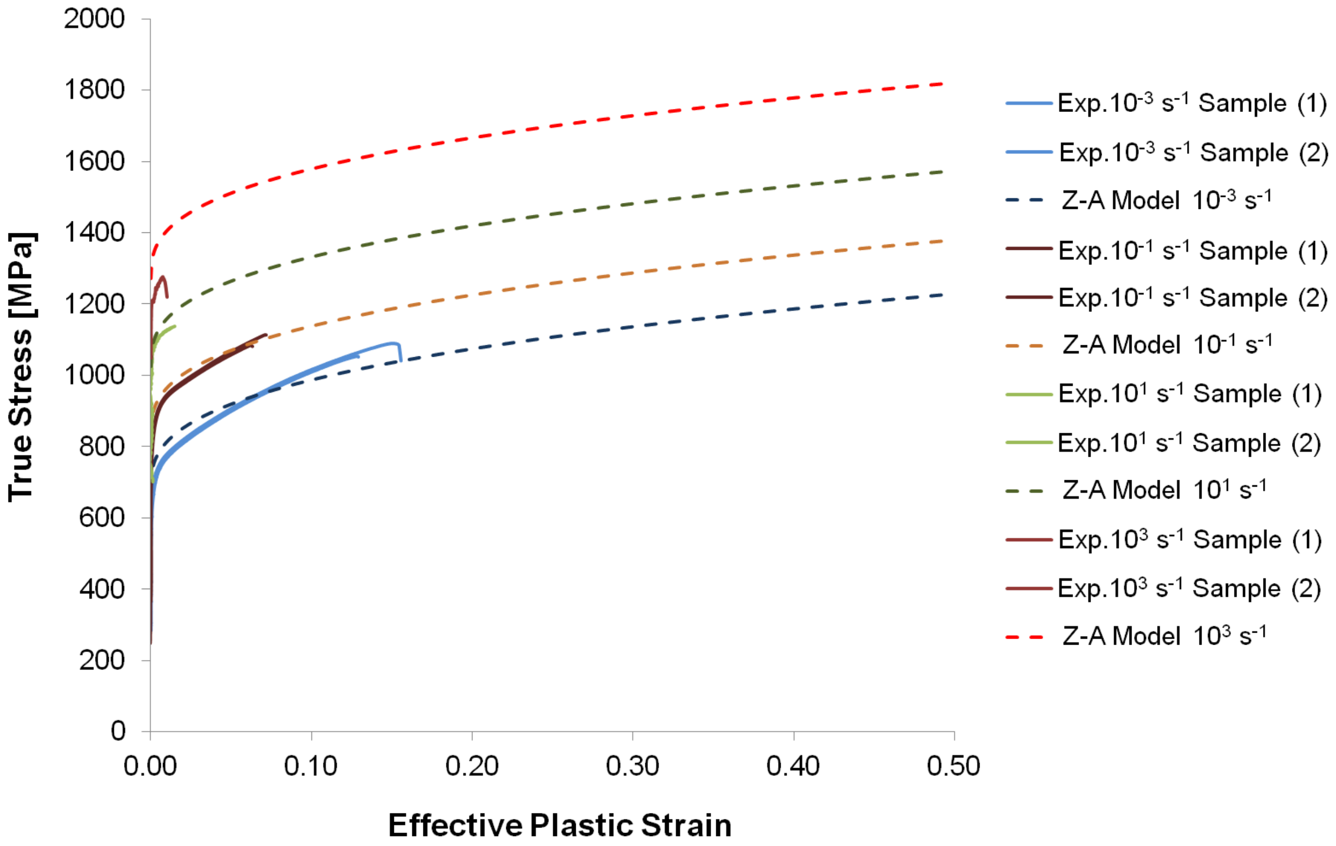

Figure 5.26: Comparison between experimental and numerical results in terms of true stress versus effective plastic strain for dynamic tests (different $\dot{\epsilon}$) at room temperature ($T = 25$ °C).

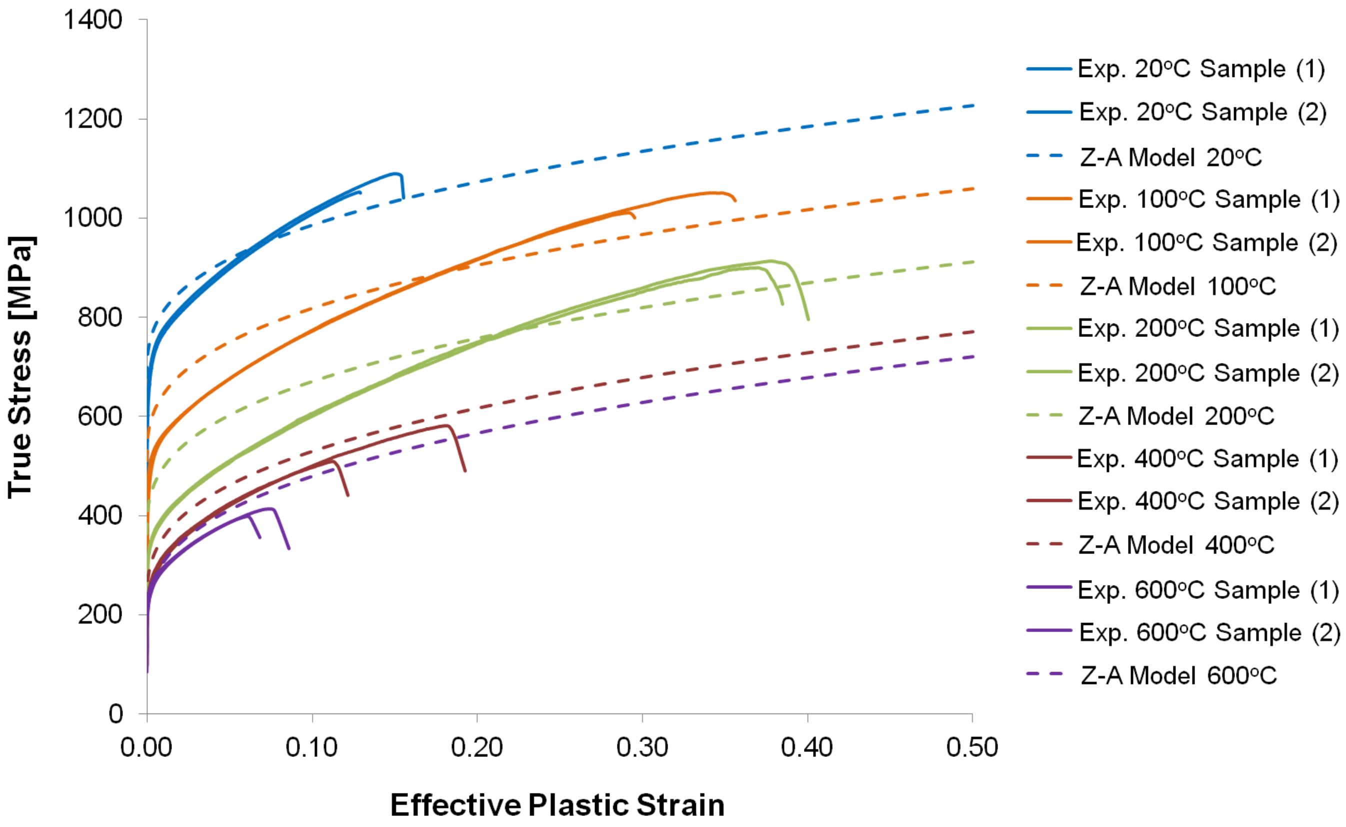

Figure 5.27: Comparison between experimental and numerical results in terms of true stress versus effective plastic strain for quasi-static tests ($\dot{\epsilon} = 10^{-3}\ \mathrm{s}^{-1}$) at different temperatures.

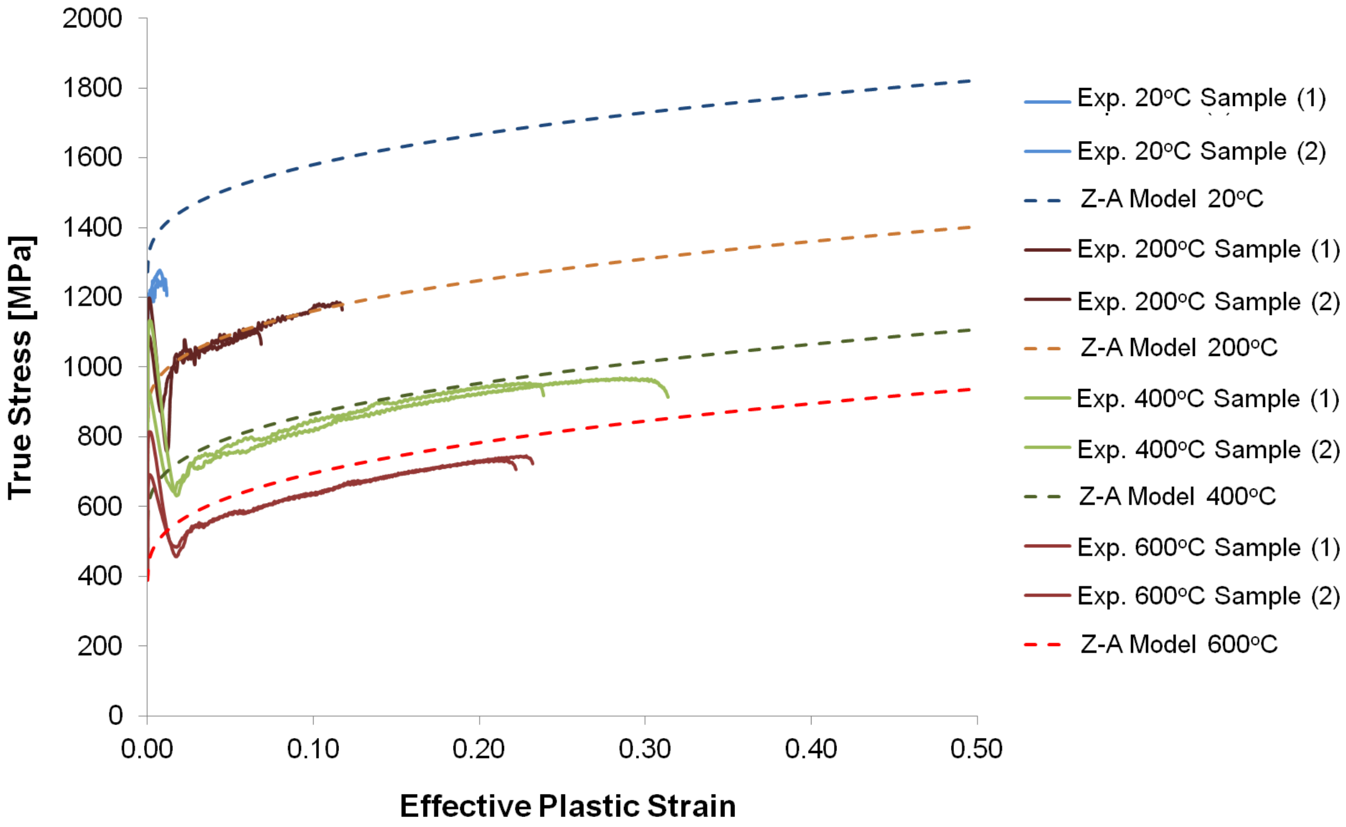

Figure 5.28: Comparison between experimental and numerical results in terms of true stress versus effective plastic strain for high strain-rate tests ($\dot{\epsilon} = 10^3$ s^{-1}) at different temperatures.

5.5 Conclusions

Rapid energy deposition during beam impact on a TCT causes a fast temperature increase on the jaw inserts. This makes the implementation of temperature-dependent thermal and structural material properties extremely important for a reliable FE model. In this regard, this chapter has introduced the microstructure and properties of the TCT jaw insert material, INERMET® 180, focusing on material characterisation tests. Such tests have been commissioned in order to obtain a full thermal and structural characterisation of this alloy over a wide range of temperatures and strain-rates. The material characterisation campaigns in such extreme conditions proved to be very challenging both in terms of cost and resources.

A thermo-physical analysis of INERMET® 180 was commissioned at the Austrian Institute of Technology. The main thermo-physical properties, including the coefficient of linear thermal expansion $\alpha(T)$, the density $\rho(T)$, the specific heat capacity $c_\mathrm{p}(T)$, the thermal diffusivity $\kappa_\mathrm{cc}(T)$ and the thermal conductivity $k(T)$, were defined between room temperature and 1450 °C.

The structural characterisation campaign was commissioned at the DYNLab at Politecnico di Torino in order to obtain a complete strength material model of INERMET® 180. This test campaign involved the investigation of the mechanical behaviour of INERMET® 180 under static and dynamic loading conditions, at different temperatures. These tests were performed to obtain information about the thermal softening and strain-rate sensitivity of the material.

The experimental stress-strain curve data was then processed via a numerical inverse method based on FEM numerical simulations. The best description of the flow stress was obtained with a modified version of the Z-A model that takes into account the coupling between both strain and temperature, as well as between strain-rate and temperature. The maximum correlation coefficient between the experimental and predicted flow stress was obtained with this strength model, which has in fact allowed the reproduction of the experimental data with the lowest error value over the entire range of temperatures and strain-rates.

Chapter 6

Experimental Validation at HiRadMat Facility

6.1 Introduction

A dedicated beam experiment (HRMT-09) was set up at the CERN HiRadMat facility in order to investigate better the effects of an asynchronous beam dump on a complete TCT, as well as to benchmark numerical simulations. This chapter gives an overview of the collimator robustness experiment. It first presents the experimental setup, and describes the installation layout and the used measurement sensors. This is followed by an overview of the experimental tests performed, and the main beam test results including some first outcomes from visual inspection. Finally, a comparison of these experimental results with numerical simulations, together with other direct outcomes of the tests, are discussed.

6.2 Experimental setup

The collimator robustness experiment (HRMT-09) was carried out in August 2012 at the CERN HiRadMat test facility [94], which is located in the TNC tunnel in the SPS

BA7 area. The HiRadMat facility was designed and recently commissioned to provide high-intensity pulsed beams to an irradiated test area where full assemblies can be tested. The facility uses an LHC-type particle beam that is extracted from the CERN SPS, and delivered to HiRadMat via the TT60 and TT66 transfer lines. Both protons and ions can be used for tests within the facility.

The collimator tests were performed at different intensities using 440 GeV proton beams. Table 6.1 gives the HiRadMat beam design parameters for proton operation. It should be noted that for a given emittance, the size of the proton beam is a function of the beam optics, which then depends on the quadrupole settings and on the longitudinal position in the region of the experimental area. The beam-line is capable of providing beam radii between $\sigma = 0.10$ mm and $\sigma = 2.00$ mm at the different focal point positions of the experimental area (σ values corresponding to the nominal emittance). Moreover, different beam spot sizes are then achievable at the different test stands, as further explained in [131].

Table 6.1: Key beam design parameters for the HiRadMat proton beam [94].

Paramaters	**Protons**
Energy	440 GeV
Bunch intensity (max)	1.70×10^{11}
Number of bunches (max)	288
Pulse intensity (max)	4.90×10^{13}
Pulse energy (max)	3.4 MJ
Bunch length	11.24 cm
Bunch spacing	25 ÷150 ns
Pulse length (max)	7.2 µs
Transverse normalised emittance (1σ)	2 ÷ 4 µm

A fully operational, series production horizontal TCT was mounted on a support frame, and the fully assembled table (Figure 6.1) was lowered to the experimental area. The collimator was installed a few metres upstream of a beam dump. An installation layout sketch is shown in Figure 6.2, and more details on the beam-line can be found in [94].

Figure 6.1: The collimator tank mounted on the fully assembled table to be lowered to the HiRadMat experimental area.

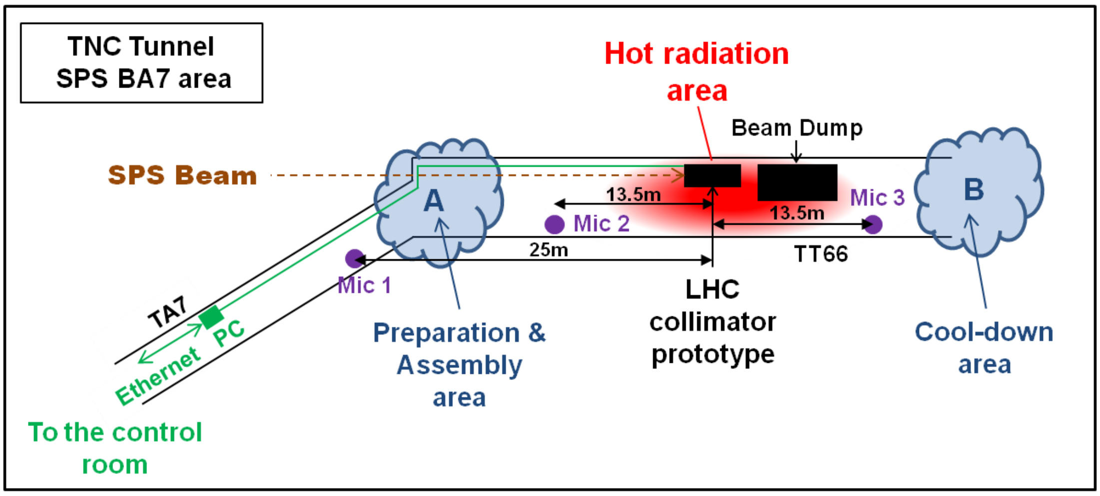

Figure 6.2: Installation layout for the collimator in the HiRadMat experimental area.

The response of the collimator to the different beam impacts was captured by relying on embarked instrumentation. During the experiment, movements of the jaws and of the whole collimator tank were done remotely via a control application. Furthermore, the water cooling pipes, that are an integral part of the collimator structure, were connected to the external cooling circuit provided in the HiRadMat experimental area. The total flow of the cooling water was adjusted according to the settings for standard LHC collimators (Section 2.2.2).

The collimator prototype was equipped with additional instrumentation compared to a standard LHC TCT. Standard LHC collimator instrumentation includes two stepper motors per jaw, position sensors as well as temperature sensors (Section 2.2.1 and Figure 2.5). A vacuum pump with external power connection, a fifth stepper motor allowing vertical movements of the whole collimator tank (20 mm full stroke), and some additional temperature and pressure sensors on various components of the collimator, were also installed, specifically for the HiRadMat experiment. All sensor read-outs were monitored online and stored for analysis. The main technical specifications of the various measurement sensors and other equipment are listed in Table 6.2.

To benchmark simulations, one of the most important physical entities to be acquired was the temperature developed within the jaws of the collimator. The four jaw temperature sensors were attached to the back of the copper housing at the left upstream (LU), left downstream (LD), right upstream (RU) and right downstream (RD) locations, in the same way as in a standard TCT unit (Figure 6.3). The location of the water temperature and water pressure sensors is given in Figure 6.4. In addition, three microphones (sensitivity = 4 mV/Pa) were installed in the tunnel area for sound DAQ (Figure 6.2) [132].

Table 6.2: Main characteristics of the DAQ system and other equipment used in the HiRadMat experiment. The number of standard LHC collimator equipment is represented by *. The rest is equipment added specifically for the experimental tests.

Sensor type / Equipment	**Specification**	**Quantity**	**Acquisition range/ Bandwidth**	**Sampling frequency**
Position sensor (LVDT)	HCA 2000	7*	± 50.8 mm	1 Hz
Jaw temperature sensor	PT100	4*	-200 °C ÷ 650 °C	1 Hz
Collimator tank temperature sensor	PT100 Model S100820	2	-50 °C ÷ 260 °C	1 Hz
Water temperature sensor	PT100	$1^* + 1$	-100 °C ÷ 200 °C	1 Hz
Water pressure sensor	CTE 9000 (signal 4 - 20 mA)	2	100 mbar ÷ 35 bar	1 Hz
Vacuum pressure sensor	Pirani gauge	2	10^{-4} mbar ÷ 1000 mbar	0.5 Hz
Microphone	B&K 4939	3	4 Hz - 100000 Hz	...
Stepper motor	Maccon SM 87.2.18M2N	$4^* + 1$	5 μm - ...	...
End-position switch	Saia Burgess V3FN	12*	...	...

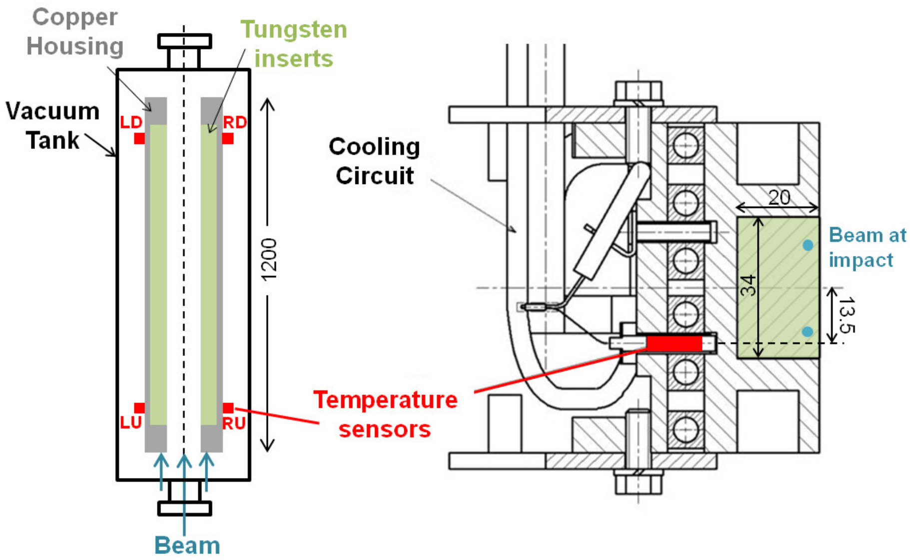

Figure 6.3: Schematic diagrams of a standard horizontal TCT. Top view (left) and front view (right) of the cross-section of the left jaw assembly. The positions of the jaw temperature sensors (LU, LD, RU and RD) are indicated. All dimensions are in mm.

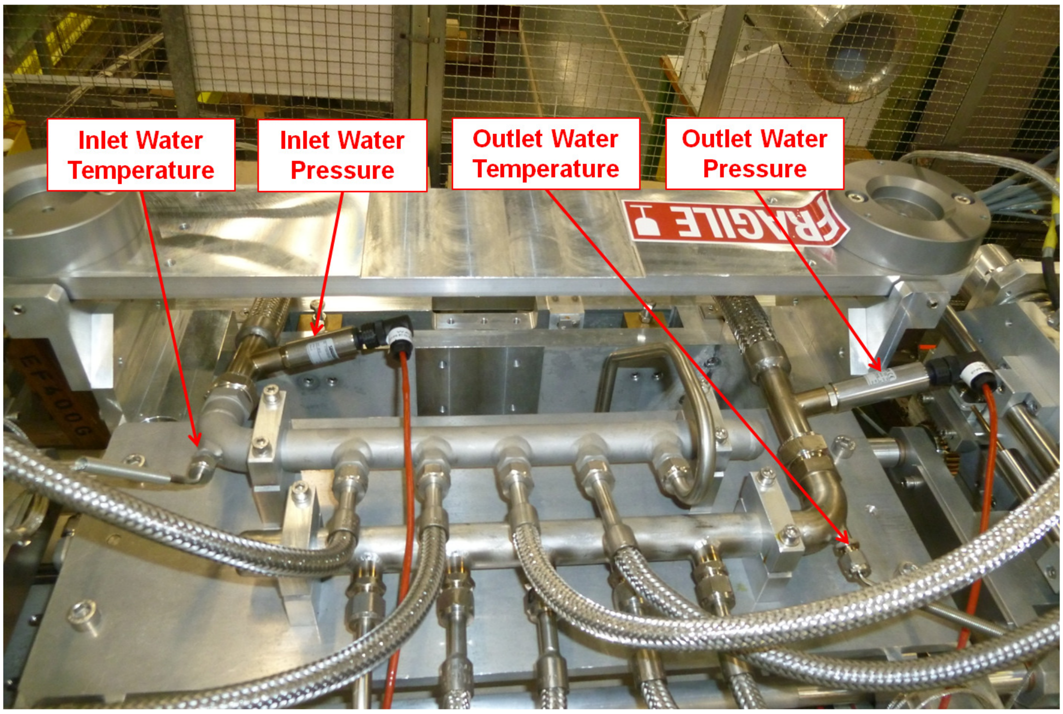

Figure 6.4: Top view of the collimator prototype, indicating the location of water temperature and water pressure sensors.

A remotely controlled computer was placed in the TA7 access tunnel for DAQ purposes (Figure 6.2). A TPG 300 controller was also installed in the electronics bunker outside the high radiation area. Moreover, BLMs, BPMs and BCTs were provided at the HiRadMat test facility in order to monitor the beam orbit, and to obtain values for beam intensity and beam losses.

6.3 Overview and goal of tests

The goal of the collimator tests was to investigate the robustness and performance integrity of a fully assembled TCT, following direct beam impact that reproduced realistic fast failure scenarios in the LHC. Such scenarios included an asynchronous beam dump at nominal 7 TeV conditions, and important accident scenarios at 5 TeV that had been considered during the LHC Run 1 [47]. Three high-intensity impacts were foreseen to test different equivalent damage levels for the considered cases.

Since the collimator robustness tests were performed using 440 GeV proton beams, it was essential to calculate the necessary beam intensity at 440 GeV to respectively obtain the equivalent damage levels of the 5 TeV and 7 TeV accident scenarios to be studied. Preliminary simulations were first completed with FLUKA to determine the equivalent intensity, I_{equiv}, based on the equivalence of the energy peak for each case. Since different energy particles were involved (440 GeV compared to 5 TeV/7 TeV), the damage zone in the target might have been different in the two cases, even if the peak values of the energy deposition for the SPS and LHC cases were made equal by adjusting the intensity.

Consequently, starting from the intensity determined by FLUKA, AUTODYN® simulations [133] were carried out to investigate what value of intensity at 440 GeV would give an equivalent level of jaw damage between the 440 GeV and 5 TeV/7 TeV cases. This meant that a realistic I_{equiv} was established for the tests, thus reproducing the studied cases more correctly. Table 6.3 compares the intensity and peak energy deposition values for the LHC and SPS cases.

Table 6.3: Comparison of the intensity and the peak energy deposition values for the LHC cases and the equivalent SPS cases to be studied in Tests 1 and 3. I_{equiv} from FLUKA is based on the equivalent energy peak, while I_{equiv} from AUTODYN® is based on the equivalent jaw damage level. The peak energy deposition for the SPS cases is calculated based on I_{equiv} from AUTODYN®.

	Test	**Test 1**	**Test 3**
LHC Cases	Beam energy [TeV]	7	5
	Intensity, I [protons]	1.50×10^{11}	5.20×10^{11}
	Peak energy deposition [J/kg]	2.237×10^{6}	5.531×10^{6}
SPS Cases	Beam energy [GeV]	440	440
	I_{equiv} - FLUKA [protons]	3.00×10^{12}	7.50×10^{12}
	I_{equiv} - AUTODYN® [protons]	3.00×10^{12}	9.75×10^{12}
	Peak energy deposition [J/kg]	2.143×10^{6}	6.964×10^{6}

The equivalent jaw damage level was compared based on two direct effects of the beam impact:

1. The damage extension on the tungsten jaw in terms of the dimensions (i.e. the height or radius) of the formed groove.
2. The maximum plastic deformation of the cooling pipes.

An equivalent damage level provoked on the cooling pipes was not reproducible for all the tests in the HiRadMat facility due to a large number of required SPS bunches. It was thus concluded to use I_{equiv} based on the damage extension of the tungsten surface for the three high-intensity shots. It is important to point out that since the penetration depth of 5 TeV and 7 TeV protons is much longer than that of 440 GeV protons, the damage equivalence in the target was done in terms of the height of the groove only, and not of the length of the groove.

The tests performed on the TCT will now be explained. The details of the tests are given in Figure 6.5. The objective of Test 1 (7 TeV-equivalent intensity of 3.00×10^{12} protons) was to investigate the effect of an asynchronous beam dump, inducing the impact of one LHC bunch on the TCT jaw. On the other hand, Test 2 (7 TeV-equivalent intensity of 9.00×10^{11} protons) was intended to inspect the onset of damage caused by a beam impact on the TCT. Finally, Test 3 (5 TeV-equivalent intensity of 9.75×10^{12} protons) was designed to reproduce a disruptive scenario for asynchronous beam dump, involving the direct impact of 4 LHC bunches at 5 TeV as studied in [47].

As indicated in Figure 6.5, all tests were performed at an impact parameter of 2 mm from the outer surface. Such an impact parameter was chosen as a compromise in order to ensure that the bulk material of the jaw insert was hit during the experiment, while still being a reasonable value for an asynchronous beam dump scenario. Hitting jaws at different locations was possible thanks to the fifth axis vertical movement of the collimator tank (±10 mm). The choice of the locations for the tests was done in such a way as to minimise interference between the high-intensity shots in case of material projection. A beam size of 0.50 mm (σ_x)× 0.50 mm (σ_y) was specified for all the cases on the basis of HiRadMat output beam parameters [131].

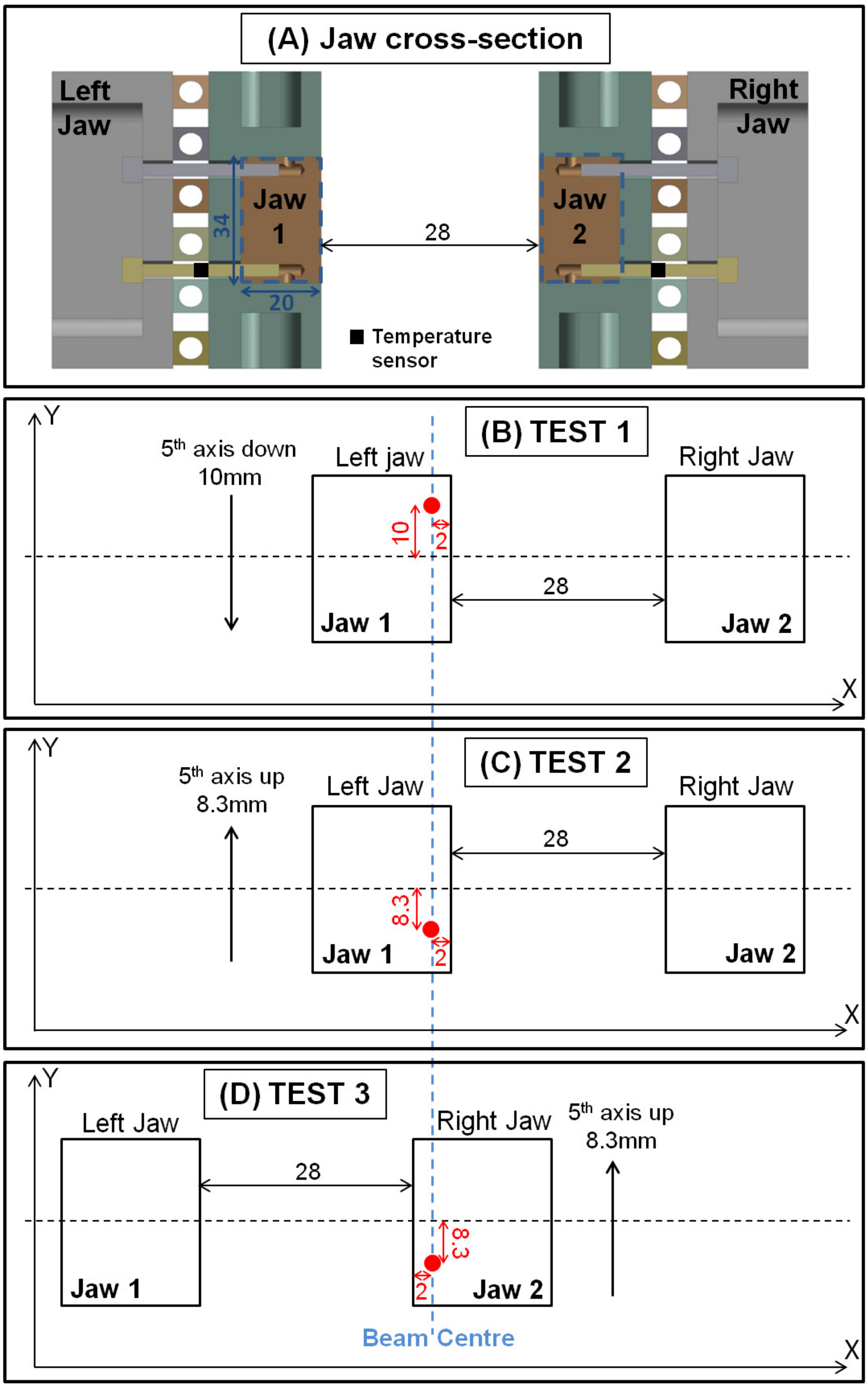

Figure 6.5: Schematic diagrams for Tests 1-3. The parts of the left and right collimator jaws enclosed within the dashed blue lines in (A) represent the schematic diagrams of Jaw 1 and Jaw 2 in (B), (C) and (D). A distance of 28 mm between the jaws is equivalent to the collimator gap when the jaws are in their parking positions, i.e. completely open with the maximum collimator gap. The beam impact location is shown in red and all dimensions are in mm.

6.4 Beam test results

6.4.1 Beam-based alignment (BBA)

In order to ensure a precise location of the beam impact, a BBA was required before each high-intensity shot. This was done with safe intensity (using pilot bunch) to avoid damage that could compromise the results. Prior to each high-intensity test, several low-intensity (on the order of 10^9 protons) beam extractions were used to correctly set up the beam-line and the experiment (Figure 6.6). This was essential in order to ensure an accurate setup for the tests with the correct impact parameter.

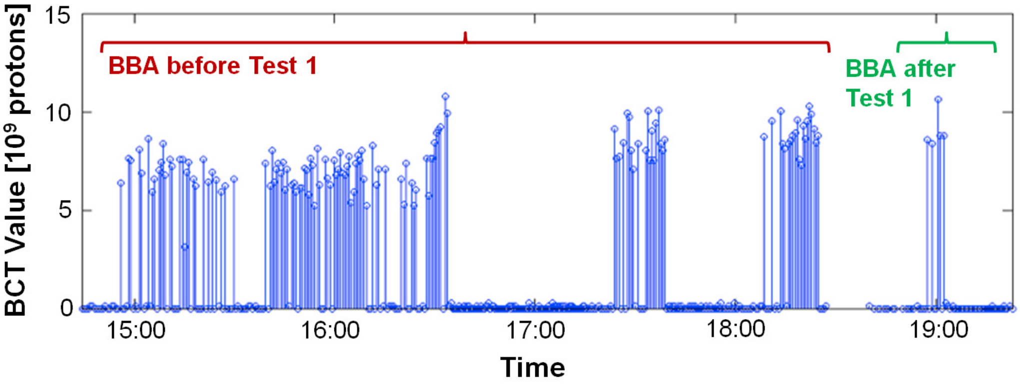

Figure 6.6: Low-intensity SPS pilot beam extraction intensities (on the order of 10^9 protons) used for the BBA before and after Test 1.

The same beam setup was performed for all measurement campaigns. In order to ensure reproducibility of orbit and beam size, the same SPS cycle, that is normally used in high-intensity operation, was used for these tests. The adopted procedure was then to scrape down these high-intensity beams in the SPS to the required pilot intensity.

The left and the right jaws were respectively moved in steps (step sizes ranging from 0.25 mm to 1 mm) and the developed losses, as measured from the BLMs installed in the beam-line, were recorded for each calibration shot. Alignment fits were generated for both jaws from which the beam centre was determined (Figure 6.7).

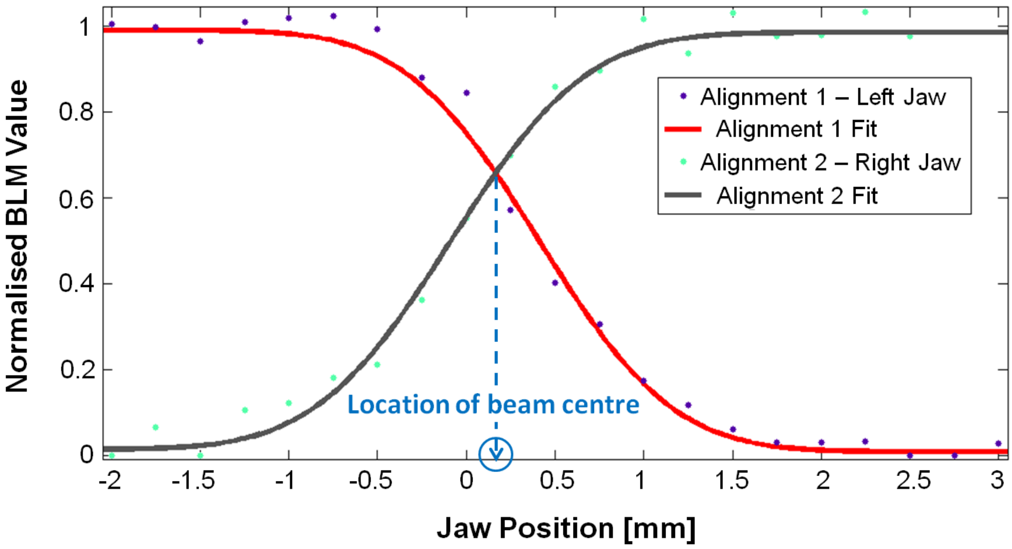

Figure 6.7: One example of the alignment fits generated for the beam-based setup, showing movements with the left and right jaws in order to determine the location of the beam centre.

Table 6.4 summarises the sequence of the beam-based alignments and the experimental tests, and gives the total intensity that the TCT has been subjected to during these tests. It can be seen that following the beam-based alignments, each respective test could be performed using a high-intensity shot (on the order of 10^{12} protons).

Table 6.4: Sequence of the tests. Tests 2 and 3 were carried out on a different day from Test 1. The intensity of pilot and high-intensity bunches is on the order of 10^9 and 10^{11} protons, respectively.

Test	**Intensity [10^{11} protons]**	**No. of bunches**
BBA before Test 1	5.67	79 pilot
Test 1	33.60	24 high-intensity
BBA after Test 1	1.51	18 pilot
BBA before Test 2	4.05	35 pilot
Test 2	10.36	6 high-intensity
BBA after Test 2/before Test 3	2.32	22 pilot
Test 3	93.40	72 high-intensity
TOTAL	**147.90**	

6.4.2 Experimental measurements

Beam parameters of high-intensity tests

The beam parameters used for each test, as well as their physical effect on the impacted jaw, are summarised in Table 6.5. Although a beam size of 0.50 mm (σ_{x}) × 0.50 mm (σ_{y}) was specified (Section 6.3), it was not easy to obtain the same precise beam optics for each test. However, it was shown by simulations [47] that small changes in beam size do not considerably affect the damage extension in case of highly disruptive tests at the chosen impact parameter. The precision on the beam size at impact, as given in Table 6.5, is in the order of 10%.

Table 6.5: Summary of the test parameters.

Test	**1**	**2**	**3**
SPS extraction intensity [10^{12} protons]	3.36	1.04	9.34
Number of bunches	24	6	72
Average bunch intensity [10^{11} protons]	1.40	1.73	1.30
Bunch spacing [ns]	50	50	50
Beam energy [GeV]	440	440	440
Beam size at impact ($\sigma_{\mathrm{x}} \times \sigma_{\mathrm{y}}$)[mm^2]	0.38 × 0.38	0.50 × 0.50	0.49 × 0.49
Energy on jaw [kJ]	87.89	27.72	249.87
TNT equivalent [g]	21.01	6.62	59.72

Surface integrity

A beam-based setup was performed after Test 1 and Test 2 as an attempt to check the surface integrity of the jaws and the collimator mechanics following the beam shots. Major damage of the jaw might result in different values in the results of the BBA procedure. As can be observed from Figure 6.8, there are no large variations between the beam positions before and after the shot, apparently indicating the absence of critical damage to the jaw surface. It is however difficult to conclude on errors in the range of 100 μm.

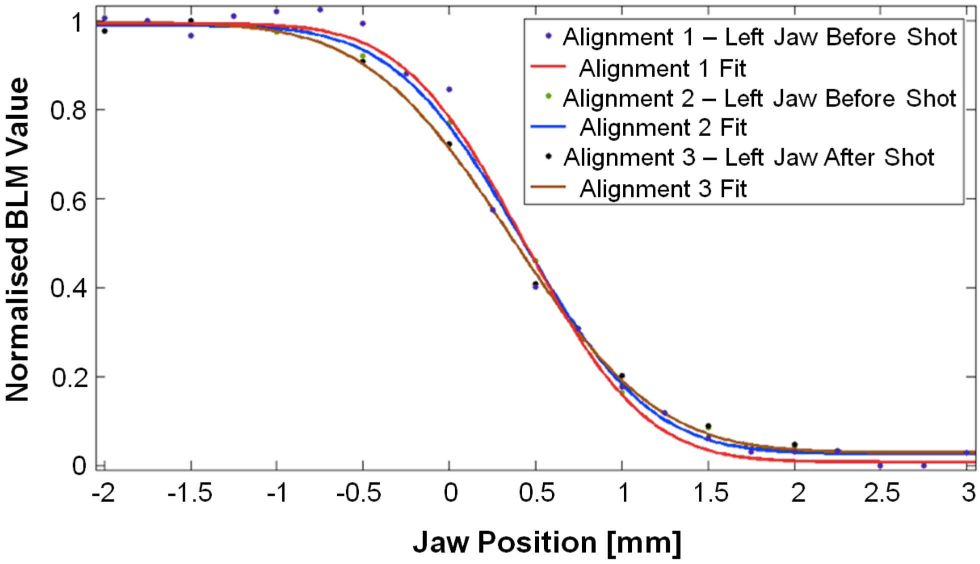

Figure 6.8: Beam-based alignment of the left jaw to check the surface integrity after Test 1. Alignment 1 and Alignment 2 are performed before Test 1, while Alignment 3 represents the check after Test 1.

As will be shown in the preliminary post-irradiation analysis (Section 6.4.3), it results that grooves from Test 1 and Test 3 can in fact be observed on the surface of the jaws. The reason why the alignment checks in Figure 6.8 did not indicate the presence of such grooves is because the grooves do not cover the full length of the jaw. In such cases, the unperturbed part at the end of the jaw still determines the closest point to the beam that in turn determines the alignment.

Temperature and pressure measurements

Temperature and pressure measurements were made during the three tests using the installed instrumentation. Some of the most significant temperature and vacuum pressure results obtained for Test 1 and Test 3 are presented in Figures 6.9 and 6.10 respectively. The recorded jaw temperature profiles show a temperature rise following the impact, which although clearly observable, is much lower than expected and is not really compatible with the post-irradiation observations presented later in this chapter.

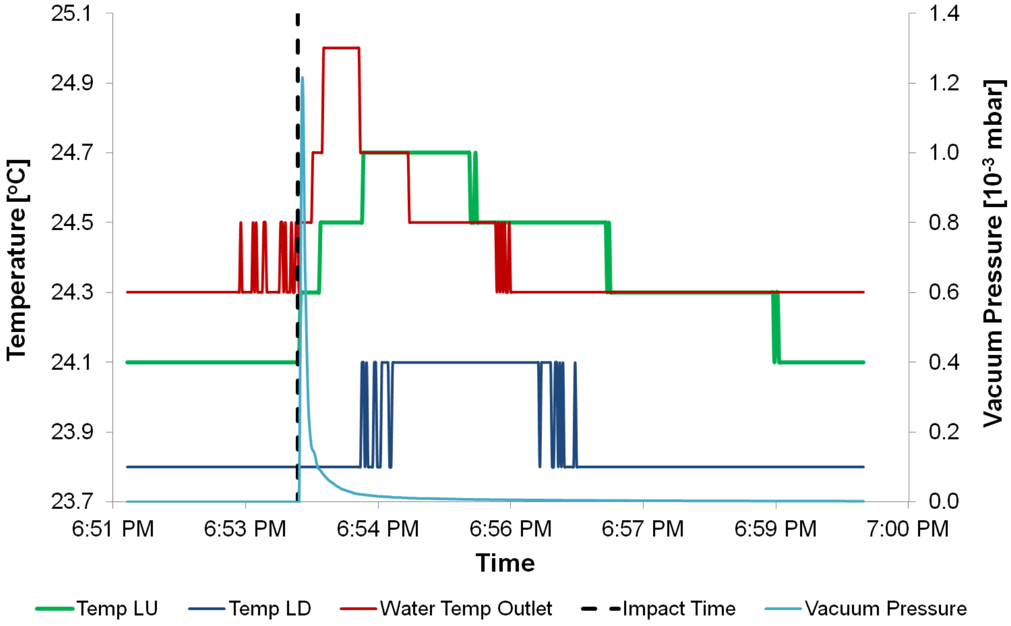

Figure 6.9: Test 1: temperature and pressure profiles captured by the LU and LD jaw temperature sensors, the water outlet temperature sensor, and the vacuum pressure sensor. A peak in vacuum pressure for Test 1 is observed at the moment of impact. Beam impact at 6:53:51 PM (corresponding to dashed vertical line).

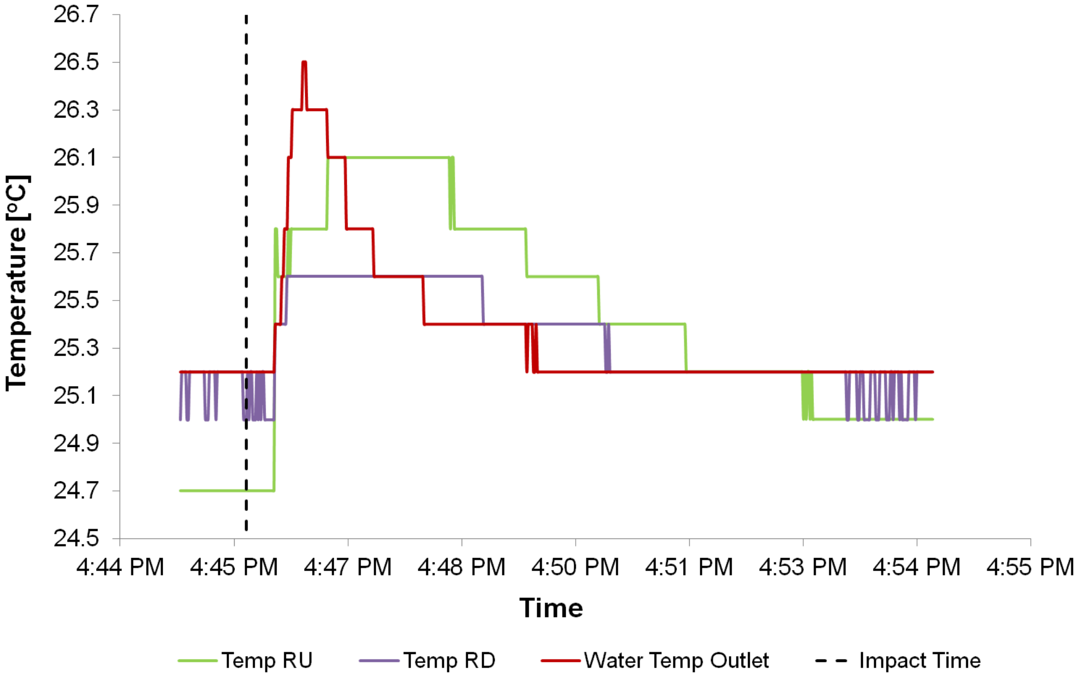

Figure 6.10: Test 3: temperature profiles captured by the RU and RD jaw temperature sensors, and the water outlet temperature sensor. Beam impact at 4:46:20 PM (corresponding to dashed vertical line).

The reason for the low experimental jaw temperature measurements is the high thermal resistance (due to the low contact pressure) between the temperature probe and the support to which it is attached, leading to temperature recordings with a very low sensitivity. This reasoning will be explained in more detail in Section 6.5.3 where it will be shown in Figure 6.19 that the expected temperature reading for the Test 3 beam impact was around 150 °C.

Sound measurements

Rapid energy deposition by the beam on the collimator jaws causes pressure waves inside the jaw material. Microphones capture the response of the whole collimator structure to this impulsive excitation, depending on the acoustic transfer function of the reflective tunnel area specific to each microphone location [132]. The signals in Figure 6.11 show the sound pressure during the test beam impacts.

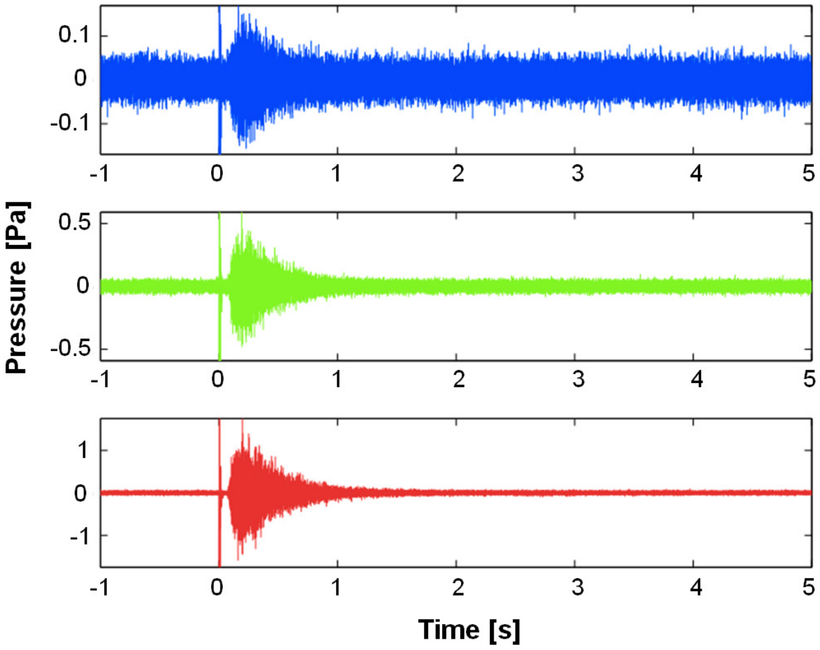

Figure 6.11: Filtered signals during Test 2 (top), Test 1 (middle) and Test 3 (bottom) for Microphone 1 shown in Figure 6.2. A noise spike with a slow refraction decay is generated in the sensor electronics by radiation effects and it can be used as an event trigger of the beam impact. A high-pass filter of 3rd order at 100 Hz removes the slow decay and reveals the real sound data (results obtained in collaboration with D. Deboy, CERN).

6.4.3 Post-irradiation visual inspection

Following the collimator robustness tests, measurements of the residual contact dose rates of the collimator were recorded at different locations. Two months after the experimental tests were performed, the hottest activation point of the collimator was found to be approximately 100 μSv/h located around the middle of the collimator tank. The dose rate levels at the entrance window were much lower at a value of approximately 20 μSv/h. After the necessary cool-down of the irradiated collimator, a preliminary visual inspection (Figure 6.12) was performed at the beginning of 2013 by means of a camera, in order to give a qualitative damage evaluation before further analysis can be carried out.

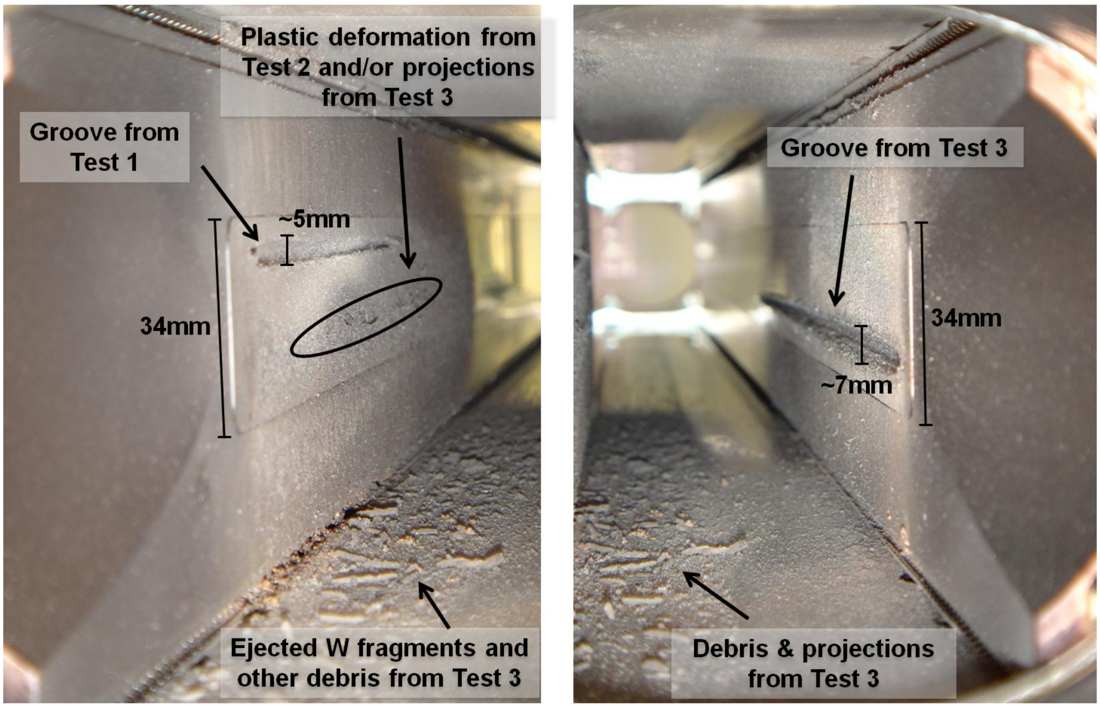

Figure 6.12: Post-irradiation visual inspection of the tested collimator. Damage on the left jaw caused mainly by Test 1 beam impact (left). Damage on the right jaw caused by Test 3 beam impact (right). The marked dimensions of the grooves are known from the 34 mm dimension of the jaw inserts and they only take into account the estimated height of the groove.

Grooves from Test 1 and Test 3 can clearly be identified, showing that there was a local temperature rise exceeding the melting temperature of the Cu-Ni phase of the jaw insert material (approximately 1343 °C). Various fragments of tungsten can also be observed between the jaws on the bottom of the tank. Such projections might compromise the correct functionality of movable parts (such as RF fingers sliding on upper and lower rails). Moreover, vaporisation deposit around the molten region is visible. This implies the extent of the damage caused by the beam impacts, as well as the risk for contamination due to activated tungsten particles, and UHV degradation along the beam-line. A dedicated post-irradiation campaign, including metallographic inspections of the impacted TCT, is foreseen in the near future once the radiation dose will be low enough.

6.5 Numerical benchmarking

6.5.1 Simulation approach

The FLUKA-ANSYS® simulation approach explained in Chapter 3 was used for benchmarking purposes. Table 6.5 showed that a number of SPS bunches were used for the three high-intensity tests to reproduce the LHC accident scenarios to be studied. The high pressure produced in the deposition region after beam impact generates a radially outgoing pressure wave. This is followed by a rarefaction wave that in turn leads to a density reduction between one bunch and the next. In practice, the protons in subsequent bunches will penetrate much deeper into the target. Once the error in density becomes too high, FLUKA should be run iteratively with the modified density distribution obtained from ANSYS® in order to provide an updated energy deposition map [98]. As stated in Section 2.4, a suitable iteration step is considered to be the time interval during which the target density decreases by 15%-20% [91].

In the test cases studied here, the temperature and density variations for Test 3 (most loaded test case) were monitored at 5 sampling points placed at the most loaded longitudinal collimator section. Figure 6.13 gives the temperature plot during the energy deposition at the 5 points indicated on the schematic diagram. Moreover, the density plot in Figure 6.14 shows that the most loaded element, which from the temperature plot in Figure 6.13 is represented by Point 3, has a 12% density reduction which is within the acceptable target density reduction range quoted in [91].

Thus, since for these studied cases, the change in density induced by the impinging particles was within the acceptable density reduction range, it was justified to assume that the density remained constant for the duration of the impact. Therefore, an uncoupled FLUKA-ANSYS® approach was used, meaning that the energy deposition calculated for the first bunch on the pristine material was maintained also for subsequent bunches. The same approach was followed for similar calculations on other structures [95].

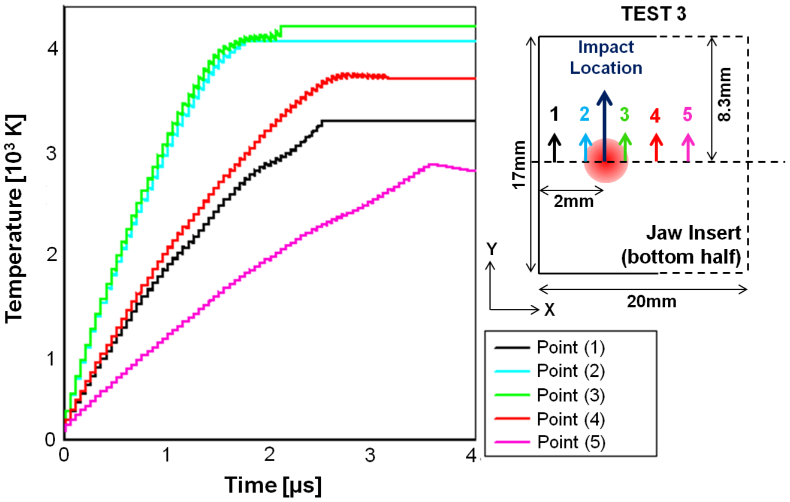

Figure 6.13: Simulated temperature profiles over time for Test 3 at 5 different sampling points placed at the most loaded longitudinal collimator section. The sampling points are located on the same plane as the beam impact, as indicated on the cross-sectional schematic diagram of the bottom half of the jaw insert. Sampling Point 1 is at 0.5 mm from the external surface, Point 2 is 1 mm distant from Point 1, Point 3 is 1 mm from Point 2, and so on for Point 4 and Point 5 (results obtained in collaboration with F. Carra, CERN).

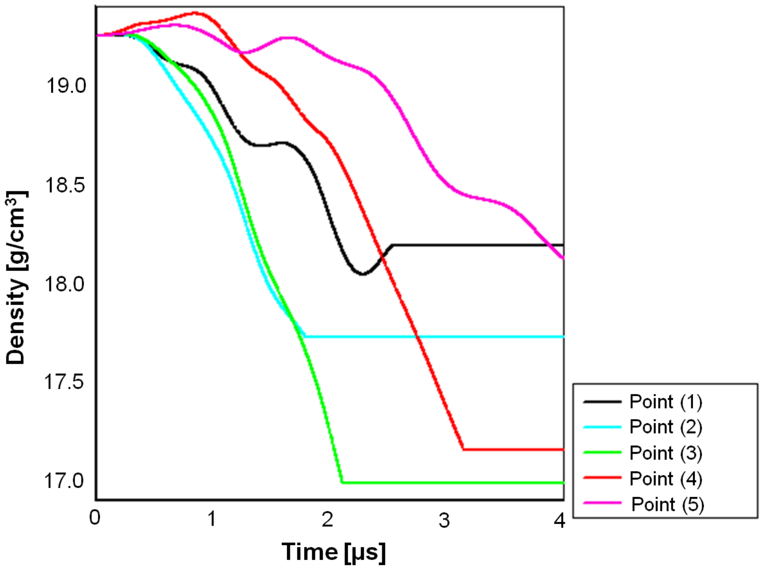

Figure 6.14: Simulated density profiles over time for Test 3 at 5 different sampling points placed at the most loaded longitudinal collimator section. The sampling point locations are the same as indicated on the schematic diagram in Figure 6.13 (results obtained in collaboration with F. Carra, CERN).

6.5.2 FLUKA simulations

Full shower simulations with FLUKA provided energy deposition distributions for the studied accident cases (Figure 6.15).

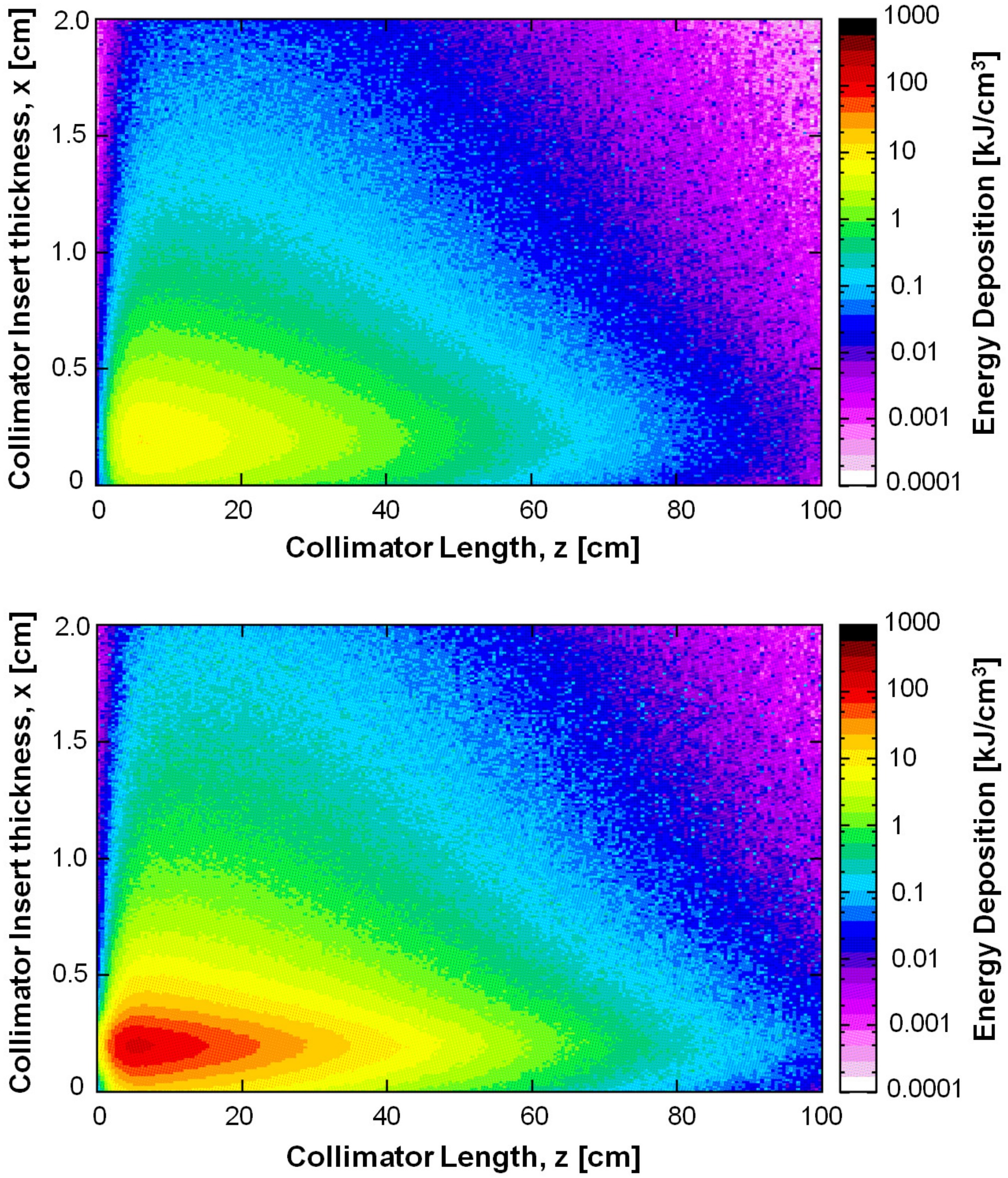

Figure 6.15: Energy deposition cuts at the maximum temperature on the tungsten inserts in longitudinal section, as calculated by FLUKA for Test 1 (top) and Test 3 (bottom) at the end of the beam impact (results obtained in collaboration with L. Lari, CERN).

6.5.3 FEM analysis

The FLUKA energy deposition maps were then used to conduct non-linear transient analyses with ANSYS®. The numerical modelling approach involved FEM simulations that were performed as described in Chapter 3 in order to evaluate the temperature distribution and other thermally induced effects due to the beam impact. The material properties used for the jaw inserts were those obtained from a full thermal characterisation performed on INERMET® 180 as explained in Chapter 5. An overview of the implemented thermo-physical properties is given in Figure 6.16. Table 6.6 then gives a summary of the simulated test parameters, and Figure 6.17 shows the different peak temperatures reached along the jaw length for the three tests.

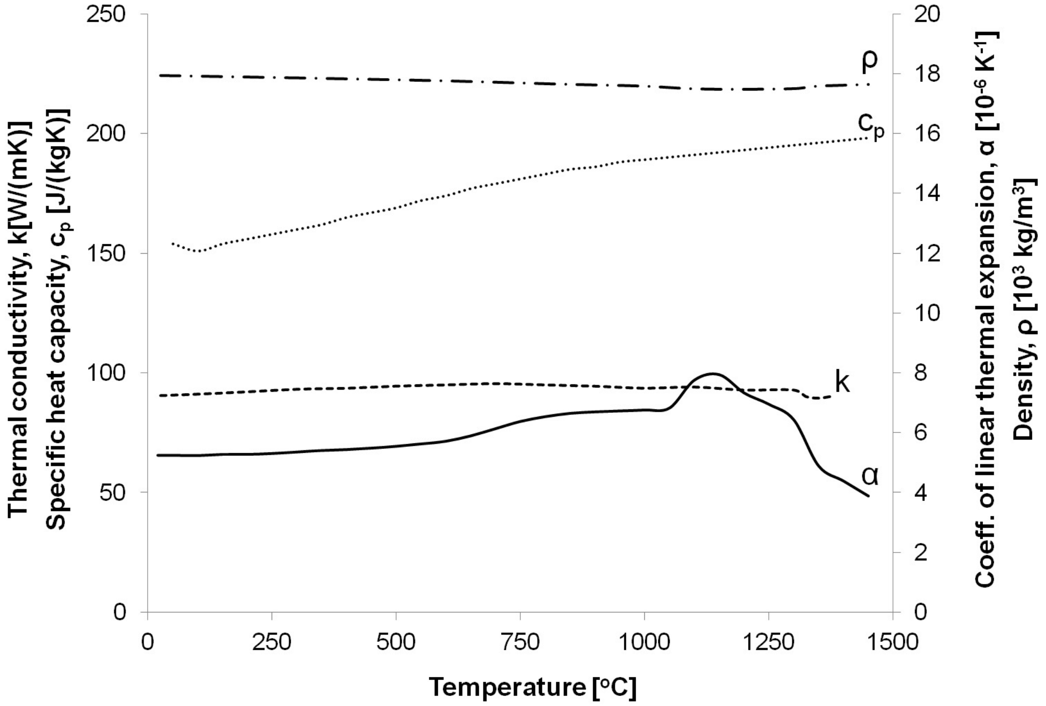

Figure 6.16: An overview of the temperature-dependent thermo-physical properties implemented for INERMET® 180.

Table 6.6: Summary of the test parameters as simulated by ANSYS®.

Test	**1**	**2**	**3**
SPS extraction intensity [10^{12} protons]	3.36	1.04	9.34
Number of bunches	1	1	1
Simulated bunch intensity [10^{12} protons]	3.36	1.04	9.34
Thermal shock duration, τ_{shock} [μs]	1.174	0.256	3.622
Energy on jaw [kJ]	87.89	27.72	249.87
TNT equivalent [g]	21.01	6.62	59.72

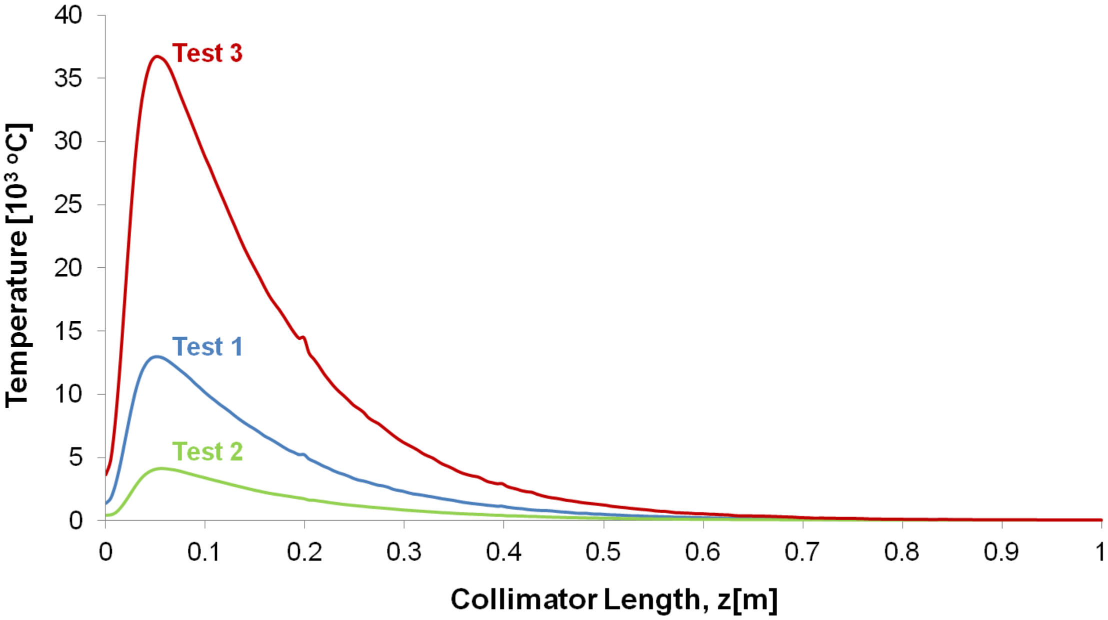

Figure 6.17: Simulated temperature peak profiles within the jaw inserts as a function of distance along the beam direction for Tests 1-3.

Equations 3.7 and 3.8 were used to calculate $\tau_{\text{diffusion}}$ for the jaw inserts, which was found to be approximately 306 μs, considering INERMET® 180 as the material of the jaw inserts, and the transverse edge length of one mesh element (0.1 mm) as the typical dimension of the structure. Table 6.6 shows that τ_{shock} for the three test situations is on the range of a few microseconds (Test 1: 1.174 μs, Test 2: 0.256 μs, Test 3: 3.622 μs), considering a bunch length of 1 ns and a bunch spacing of 50 ns.

Thus, τ_{shock} is much shorter than $\tau_{\text{diffusion}}$, concluding that heat diffusion does not play a significant role and can be neglected during the deposition of the energy. This justifies the assumption to consider the deposited energy as linearly growing during τ_{shock} (Figure 6.18). This enabled the system to be simulated in a way that the local temperature increases linearly with energy deposition (in time) since limited heat diffusion on relatively small volumes prevents the temperature to decrease between one bunch and the following bunch.

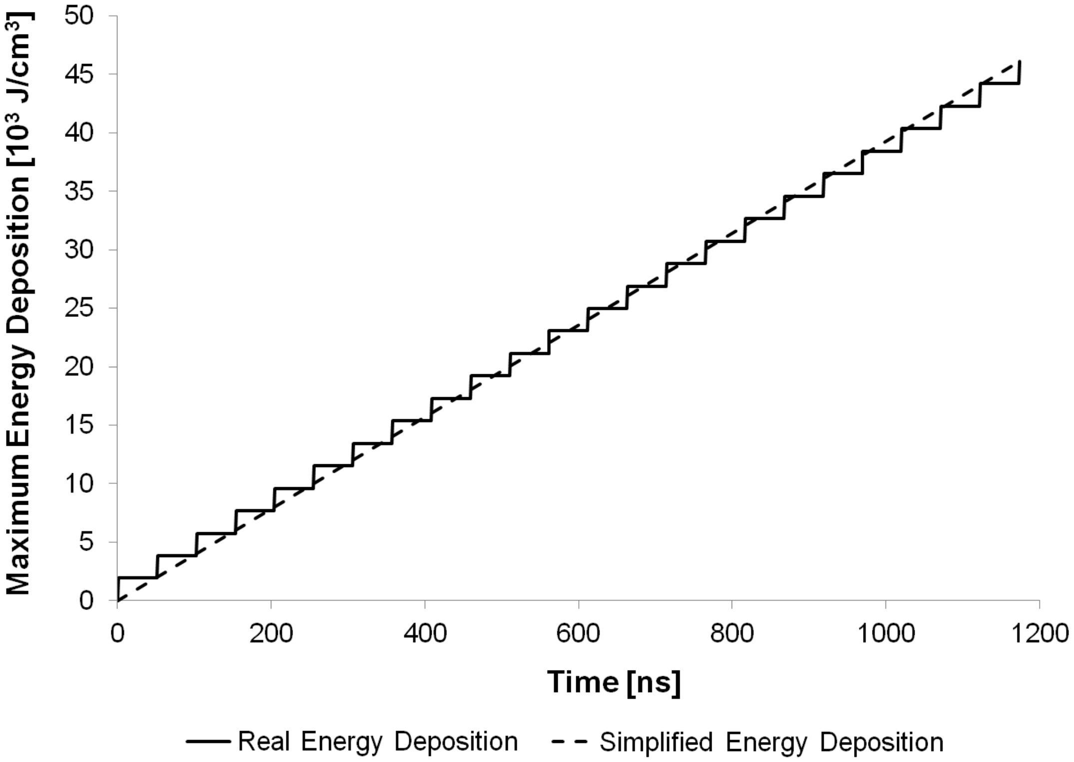

Figure 6.18: Comparison of the real and simplified energy depositions from simulations of Test 1 (24 bunches). The real energy deposition is performed bunch by bunch while in the simplified case, the local temperature is taken to increase linearly with energy deposition (in time) due to the limited heat diffusion assumption.

In order to benchmark numerical simulations, the evolution of temperature as a function of time was simulated for each test. This was done by means of temperature sampling points at the locations where the jaw temperature sensors were installed on the collimator jaws in the experiment. Originally, the direct temperature of the copper housing at the location of the temperature sensors was taken but this showed a greater temperature rise than that captured by the sensors in the experiment.

The temperature sensor was then modelled as a small component placed at the location of the sensor at the back of the copper housing. The thermal conductance value at the contact interface between the sensor and the copper housing was calibrated for the obtained experimental results. Such an approach led to more similar simulated temperature profiles with respect to the experimental ones. In fact, a thermal conductance value of 0.5 W/m^2K was found to give the closest temperature profile, both in terms of maximum temperature reached as well as temperature profile over time. This means that during the experiment, the contact pressure between the temperature sensor and the copper housing was extremely low, leading to a transient temperature reading that proved to have a very low sensitivity. The outcomes for Test 3 are shown in Figure 6.19.

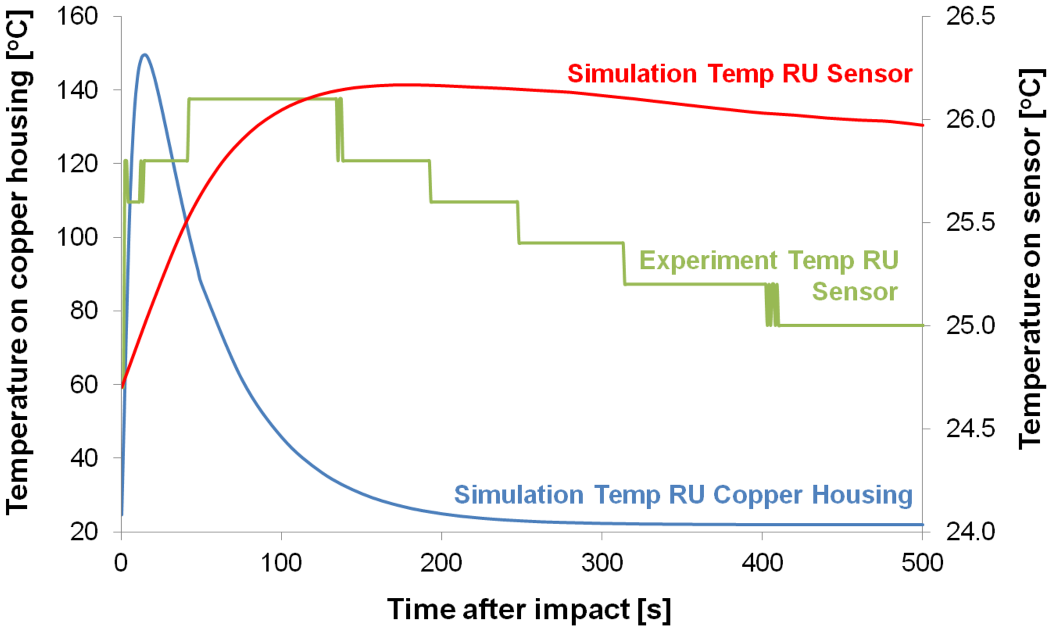

Figure 6.19: Comparison of experimental and simulated thermal transients at the location of the right upstream temperature sensor for Test 3. The left axis represents the temperature on the copper housing at the location of the right upstream temperature sensor (blue curve), while the right axis represents the temperatures given by the right upstream temperature sensor in the experiment (green curve) and in the simulations (red curve).

The tested collimator could not be extensively manipulated immediately after the HiRadMat experiment due to the high radiation level. Thus, based on preliminary observations (no detailed metrology), the only structural comparison between the experiment and the simulations was limited to the dimension and shape of the groove generated by the beam impacts on the jaw inserts.

In order to visualise the groove generated by each beam impact, the molten region was investigated in ANSYS®, considering the melting temperature of INERMET® 180 as 1343 °C. Figures 6.20, 6.21 and 6.22 illustrate the target damage by showing the extent of the molten regions for the three tests, together with qualitative and quantitative comparisons of the shapes and dimensions of the real grooves. It is important to point out that the molten volume is not necessarily exactly identical to the removed volume (observed groove size) since some solid fragments are actually ejected by inner highly energetic volumes as shown in Figure 6.20.

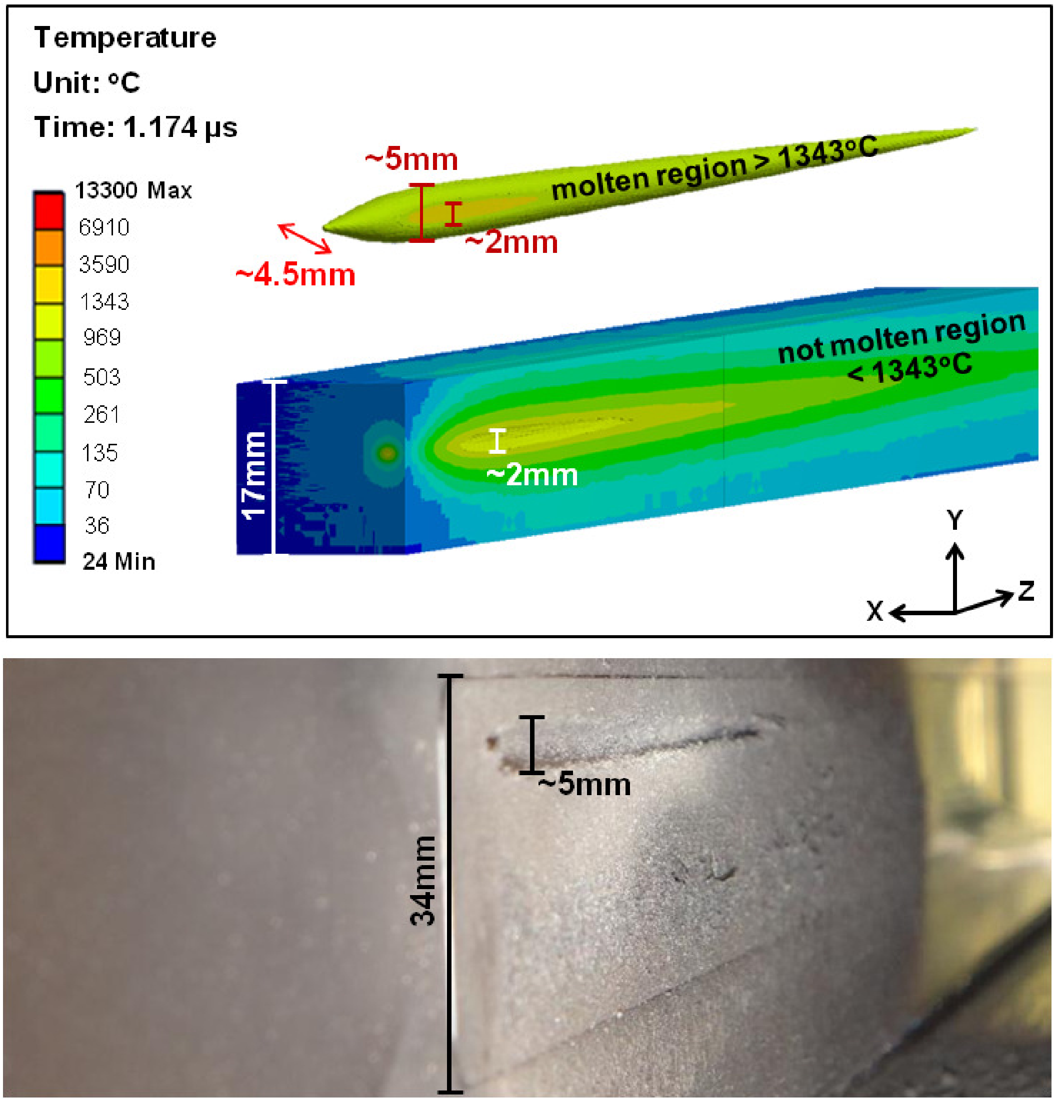

Figure 6.20: Comparison of the extent of the molten region caused by Test 1 beam impact between numerical simulations and post-irradiation analysis. The molten region is simulated by ANSYS® on the left TCT jaw, and a groove with a height of 2 mm is obtained from simulations on the top half of the first INERMET® 180 jaw insert block. However, it results that the volume of molten material is even larger inside the insert block, with the dimension of the simulated molten region being in fact 5 mm. The simulated molten region inside the inserts also extends partly into the second insert block. This is in good agreement with the post-irradiation observations shown. The marked dimensions of the grooves only take into account the estimated height of the groove.

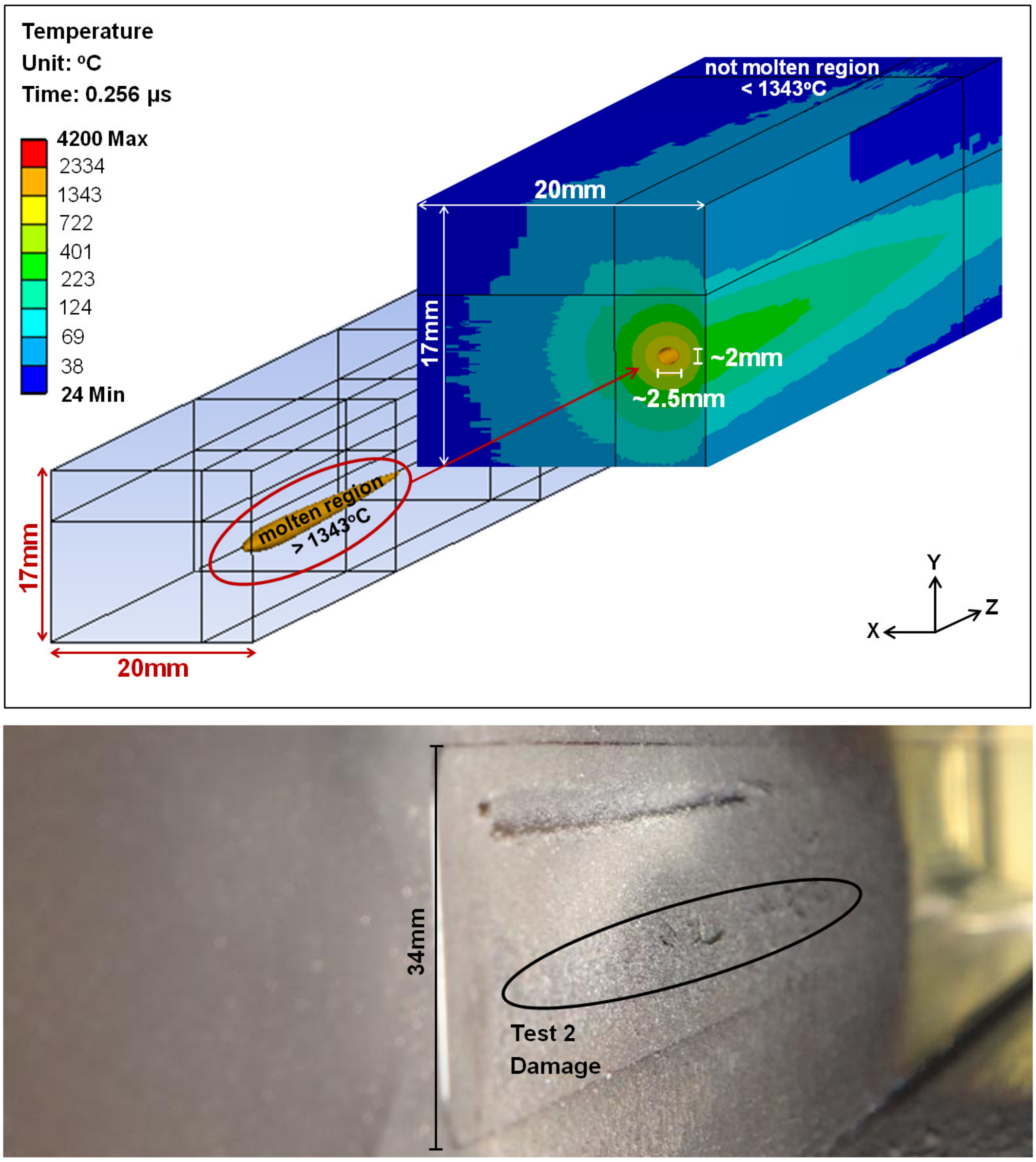

Figure 6.21: Comparison of the extent of the molten region caused by Test 2 beam impact between numerical simulations and post-irradiation analysis. The molten region is simulated by ANSYS® on the left TCT jaw. No groove is obtained from simulations on the surface of the bottom half of the INERMET® 180 jaw insert blocks. However, a small volume of molten material exists within the jaw insert, which means that there may be some structural changes to the material inside the bottom half of the first insert block. This is in good agreement with the post-irradiation observations shown.

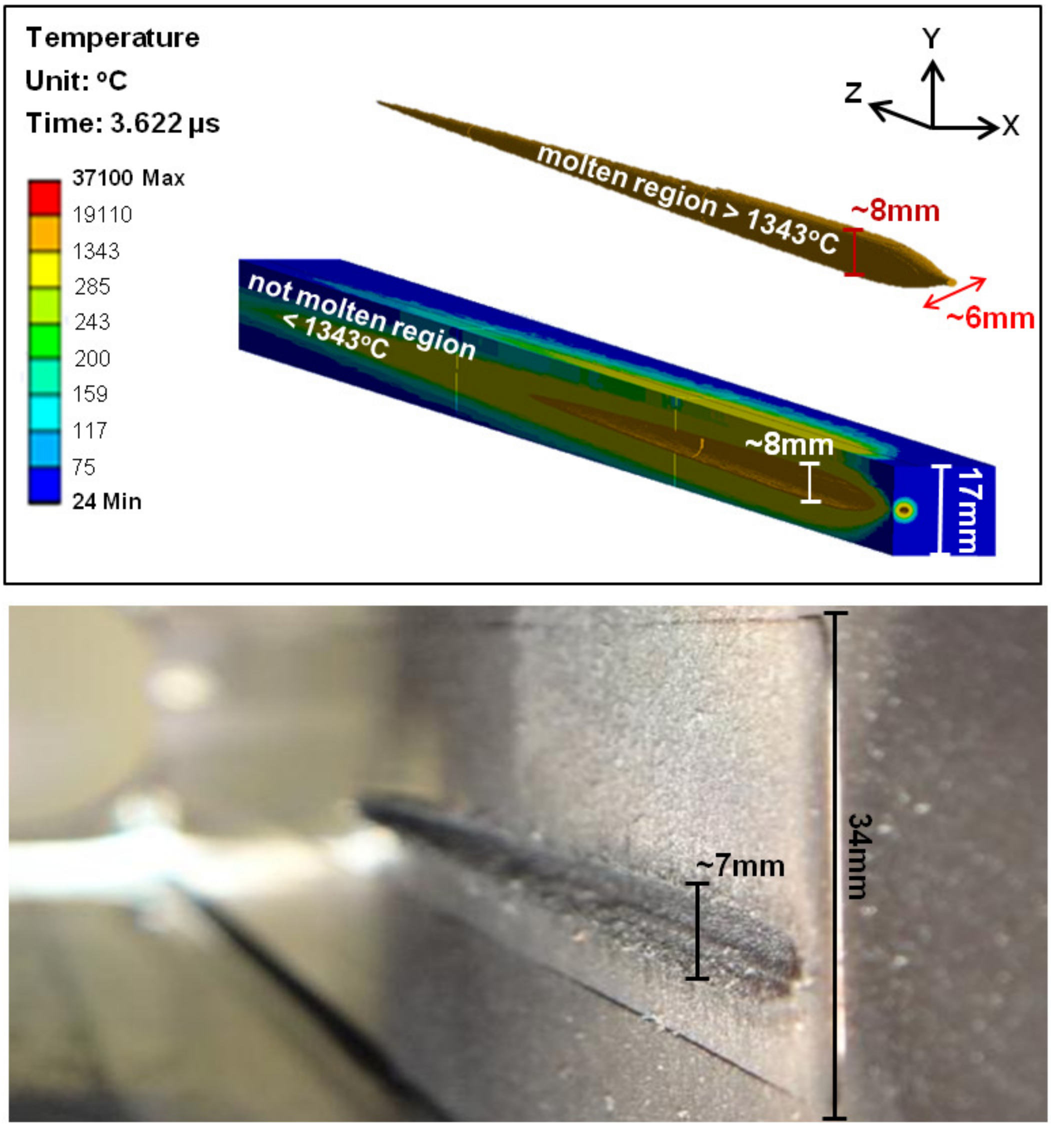

Figure 6.22: Comparison of the extent of the molten region caused by Test 3 beam impact between numerical simulations and post-irradiation analysis. The molten region is simulated by ANSYS® on the right TCT jaw. It can be observed that a groove results from simulations on the bottom half of the first two INERMET® 180 jaw insert blocks, and that the simulated molten region inside the inserts extends partly into the third insert block. This is in good agreement with the post-irradiation observations shown. The marked dimensions of the grooves only take into account the estimated height of the groove.

The graph in Figure 6.23 summarises the groove sizes for the three tests and provides a comparison of the damage extent between the observed and simulated values. Simulation outcomes for the three tests are in good accordance with the post-irradiation visual inspection. Therefore, the preliminary experimental test results have confirmed the reliability of the developed numerical method and the material model adopted to simulate beam impact scenarios on a TCT. In addition, such simulation results have been complemented by simulations performed with AUTODYN® [114].

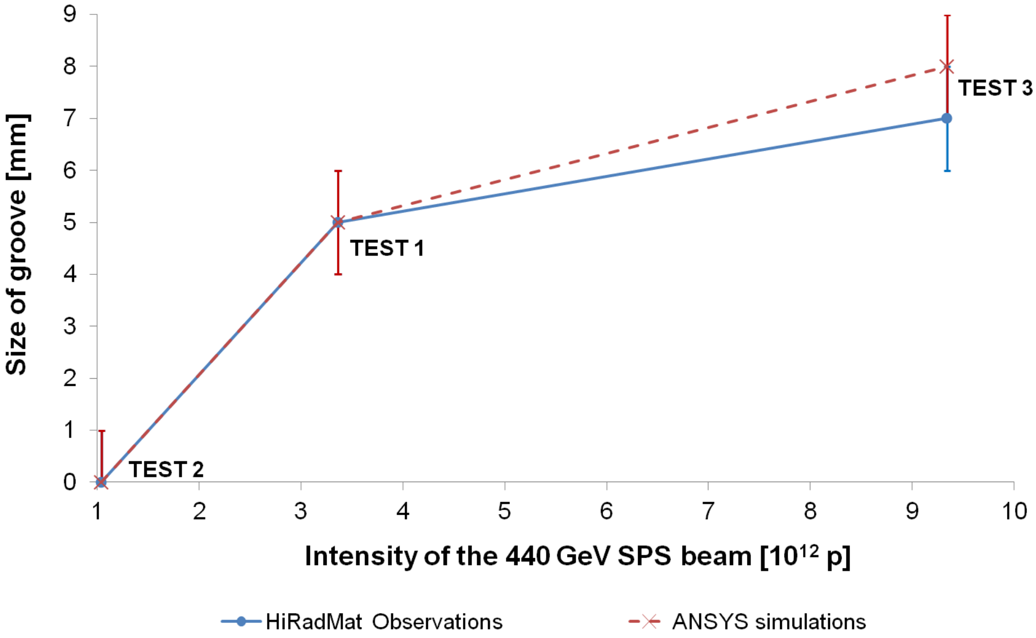

Figure 6.23: Summary plot with a comparison of the damage extent between the observed and the simulated (ANSYS®) values for the three tests.

6.6 Additional experimental outcomes

6.6.1 New collimator robustness limits

The preliminary post-irradiation observations shown in Figure 6.12, together with the outcomes of the advanced materials test [103], have led to some crucial conclusions on safe

7 TeV limits for TCTs, and have in fact helped to update collimator robustness limits. Damage thresholds in case of an asynchronous beam dump accident involving the impact of a 7 TeV bunch, with an impact parameter of 0.5 mm and a beam size of 0.50 mm (σ_{x}) $\times$ 0.50 mm (σ_{y}), on a TCT have been identified [134], and include the following:

- The threshold for the onset of plastic damage is in the order of 10^9 protons.
- The limit for tungsten fragment ejection (with plastic deformation) is set to 2.00×10^{10} protons.
- The limit for 5th axis compensation (with severe plastic deformation and fragment ejection) is set to 1.00×10^{11} protons.

6.6.2 New temperature sensor fixation method

The low experimental temperature measurements given in Section 6.4.2, and the results shown in Figure 6.19, have led to the identification of a new temperature sensor fixation method for the collimators (Figures 6.24 and 6.25). So far, the temperature sensors on the collimators have been held in place with just an adhesive. Following this experiment, a spring has been added to the new collimators installed in the ring for the LHC Run 2 (2015 - 2018) to enable an adequate contact pressure to be achieved between the temperature sensor and the copper housing. This will thus ensure that the required thermal conductance is present between the two surfaces, consequently leading to reliable temperature recordings.

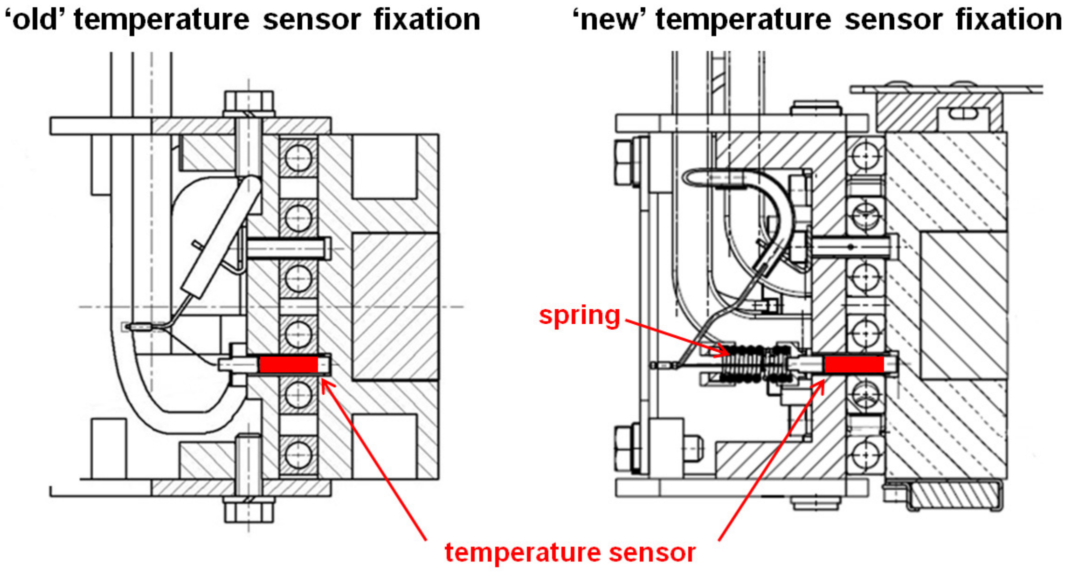

Figure 6.24: Comparison between the old and new temperature sensor fixation methods for the collimators. A spring is introduced in the new configuration to ensure adequate contact pressure is achieved between the temperature sensor and the back of the copper housing.

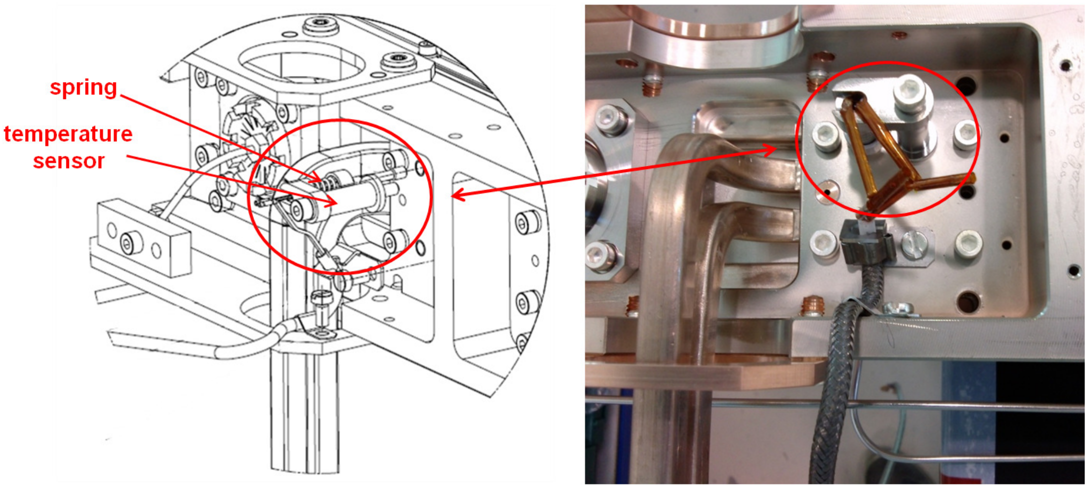

Figure 6.25: New temperature sensor fixation method for the collimators.

6.7 Conclusions

This chapter has given an overview of an experiment that has been designed and recently carried out at the CERN HiRadMat facility. The aim of the experiment was to investigate the robustness and effects of beam accidents on a fully assembled TCT collimator, based on accident scenarios in the LHC which were defined by accelerator physics studies.

The performed tests consisted of the controlled impact of intense and energetic proton pulses on both jaws of a TCT. Preliminary experimental results and post-irradiation visual inspection of the outcome of these tests have been presented and discussed. The extent of the damage caused on the jaws of the collimator could be observed and good agreement with the results of advanced simulations has been achieved. The experiment results have thus confirmed the effectiveness of the numerical method and material models used to reliably predict beam-induced damage. In addition to mechanical damage, potential machine protection issues due to the projection of fragments from the impacted components were also highlighted. Other immediate outcomes from these tests include a new temperature sensor fixation method for the collimators as well as newly defined safe 7 TeV limits for TCTs.

Moreover, an extensive post-irradiation campaign, implying further direct observations, non-destructive and destructive testing on the tested collimator, is foreseen in the near future in order to provide additional valuable information on the beam-induced damage. Such investigations will help to provide an integral assessment of beam accident scenarios together with a more in-depth view of the robustness and effects of beam impacts on a TCT.

Chapter 7

Comparative Analysis: Proton and Heavy Ion Beam Impacts

7.1 Introduction

The LHC mainly operates with proton beams. However, heavy ion collisions have been included in the conceptual design of the LHC from an early stage [135], and collisions between beams of fully stripped lead ($^{208}\mathrm{Pb}^{82+}$) ions have been successfully carried out during the first years of operation of the LHC [136, 137]. Moreover, the success of the first two Pb-Pb runs led the experiments to request a proton-ion run [138], as a first extension to the LHC design, for the last exploitation period before the first long shutdown of the LHC.

While the major hardware systems of the LHC ring are compatible with both proton and heavy ion operation, the physics of the ion beam's interaction with matter varies qualitatively and quantitatively from that of the proton beam, resulting in different beam dynamics and performance limits for the two types of beam [135]. This chapter implements the numerical FEM approach presented in Chapter 3, and the material characterisation results of INERMET® 180 presented in Chapter 5, in order to evaluate and compare the thermo-mechanical response of TCTs in case of critical beam load cases, involving proton and heavy ion beam impacts.

7.2 Particle-matter interactions for protons and heavy ions

The LHC is designed to accelerate and bring into collision high-energy protons as well as heavy ions. The main LHC beam parameters for protons and heavy ions are listed in Table 7.1.

Table 7.1: Design parameters for the LHC's proton and ^{208}Pb^{82+} beams in collision conditions [135].

Particle	**proton**	^{208}**Pb**$^{82+}$
Energy/nucleon [TeV]	7	2.759
Number of bunches	2808	592
Particles/bunch	1.15×10^{11}	7.00×10^{7}
Transverse normalised emittance (1σ) [μm]	3.75	1.5
RMS momentum spread $\langle \delta_p^2 \rangle^{1/2}$	1.13×10^{-4}	1.10×10^{-4}
Stored energy per beam [MJ]	362.00	3.81
Design luminosity $\mathcal{L}$ [cm^{-2}s^{-1}]	10^{34}	10^{27}
Horizontal and vertical β^* [m]	0.55	0.50

The physics of the particle-matter interactions for heavy ions is different from that for protons (Table 7.2), and thus the ion-matter interaction processes in collimators result in ion-specific beam losses [135]. Ions undergo nuclear fragmentation and electro-magnetic dissociation (EMD). An impinging nucleus may lose one or several nucleons, in particular neutrons, through EMD. In an EMD process, one of the lead ions (^{208}Pb^{82+}) makes a transition to an excited nuclear state that then decays with the emission of a neutron, leaving a lighter isotope of lead (^{207}Pb^{82+}). Another important EMD process is the production of a secondary beam of ^{206}Pb^{82+}. However, the rates of transmutation of the lead ions to isotopes of lighter elements are very small compared with the processes in which the lead ion emits one or two neutrons. Moreover, the nuclei may also split up in smaller fragments through nuclear inelastic reactions.

Once the ions have fragmented, the resulting hadronic shower behaves similarly for both particle types (protons and heavy ions), and the heat deposition is proportional to the beam energies [135]. It can be expected that the heat deposition of the heavy ions on the collimators nowhere exceeds that of the protons [135].

Other important physical processes that occur when both heavy nuclei and protons traverse the collimator material are the energy loss through ionisation, and the change of direction through many small-angle scattering events, known as multiple coulomb scattering (MCS). However, the ionisation energy loss is much higher for ions than for protons. The energy loss through ionisation, which is described by the well-known Bethe-Bloch formula [139], rises proportionally with the square of the particle's atomic number (Z). This means that a lead ion will lose more energy per unit path length in a material than, for instance, a proton. Angular deviation can also be caused by nuclear elastic scattering, which is a significant effect for protons but negligible for lead ions.

The role of the primary collimator (TCP) in the LHC collimation system is to intercept halo and off-momentum particles whilst increasing their betatron amplitude by means of MCS. In the case of protons, it can be assumed that the main action of TCPs on an intercepted particle is scattering while energy loss has a comparably small effect on the particle trajectories. This assumption is however no longer valid for heavy ions because:

1. The relative energy loss due to ionisation is two orders of magnitude larger for ions than for protons.
2. Peripheral collisions of heavy ions with collimator nuclei lead to nucleon losses by hadronic fragmentation and EMD, whose effects are comparable to a change of longitudinal particle momentum from a beam dynamics point of view.

3. The RMS scattering angle is proportional to the square root of the penetration depth and the proportionality coefficient is similar for protons and ions.

As a conclusion, due to the complexity of the physical processes involved, the collimation system tends to put ions on trajectories characterised by large momentum errors but of moderate betatron amplitude increase when compared to protons. This is because nuclear fragmentation and EMD in the TCPs create ion fragments with a wide range of Z/A (i.e. atomic number/atomic mass) ratios. In addition, the secondary collimator (TCS) is designed to cut into the betatron amplitude of secondary halo particles scattered out of the TCP. Thus, since ion beam fragments scattered out of the TCPs exhibit only a small betatron amplitude increase with respect to the primary particles, such fragments have a high probability of exiting the TCP without being intercepted by the TCS. These fragments can consequently be lost where the dispersion has grown sufficiently large in the LHC machine.

As a result, the cleaning efficiency for $^{208}\mathrm{Pb}^{82+}$ ion beams in the LHC is substantially worse than for proton beams. The LHC collimation setup, designed as a three-stage system for proton operation, is thus effectively reduced to a one-stage system for ions [135].

Table 7.2: $^{208}\mathrm{Pb}^{+}$ ion-matter interactions in comparison with proton-matter interactions. Values are for particle impact on graphite [135].

Physics Process	**Injection**		**Collision**	
	proton	$^{208}\mathbf{Pb}^{+}$	**proton**	$^{208}\mathbf{Pb}^{+}$
Energy per nucleon [TeV]	0.44	0.1774	7	2.759
Ionisation energy loss, $\frac{dE}{Edx}$ [%/m]	0.12	9.57	0.0088	0.73
Multiple scattering (projected RMS angle) [μrad/m$^{\frac{1}{2}}$]	73.5	73.5	4.72	4.72
Electron capture length [cm]	...	20	...	312
Electron stripping length [cm]	...	0.028	...	0.018
Electron capture pair production (ECPP) interaction length [cm]	...	24.5	...	0.63
Nuclear interaction length (including fragmentation) [cm]	38.1	2.5	38.1	2.2
EMD length [cm]	...	33.0	...	19.0

7.3 Numerical Analysis

7.3.1 FLUKA energy deposition maps

The 3D FLUKA maps provided the spatial distribution of the specific energy deposited on the jaw inserts in the longitudinal (Figure 7.1) and transverse (Figure 7.2) planes. These energy deposition maps were then loaded in the developed FE model in order to provide the input thermal load in terms of power density distribution (in W/m^3).

7.3.2 Finite element modelling

The numerical FEM approach defined in Chapter 3 was applied, and the modelling details, specific to the comparative study considered in this chapter, are described below.

Geometry, component setup and finite element discretisation

FEM simulations for proton and heavy ion beam impacts were performed on the lower symmetrical half of the right collimator jaw assembly. The discretisation of the jaw components was performed as explained in Section 3.3.2.

Material Modelling

Following the material characterisation tests presented in Chapter 5, a complete thermal and structural material model could be implemented for INERMET® 180 in ANSYS®. The thermal model of INERMET® 180 consisted of temperature-dependent thermo-physical properties based on the thermal characterisation results presented in Section 5.3 (Figure 6.16).

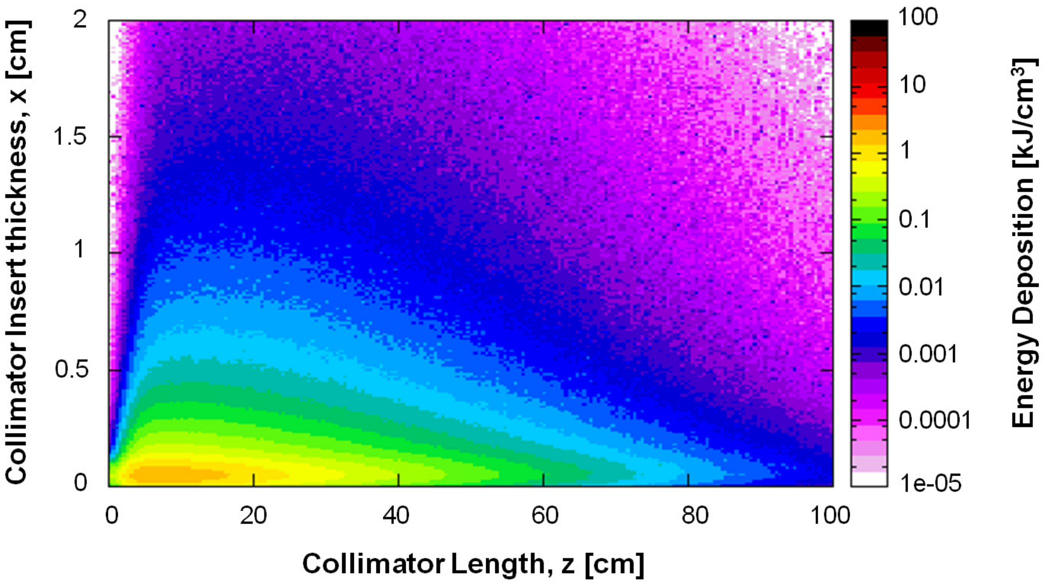

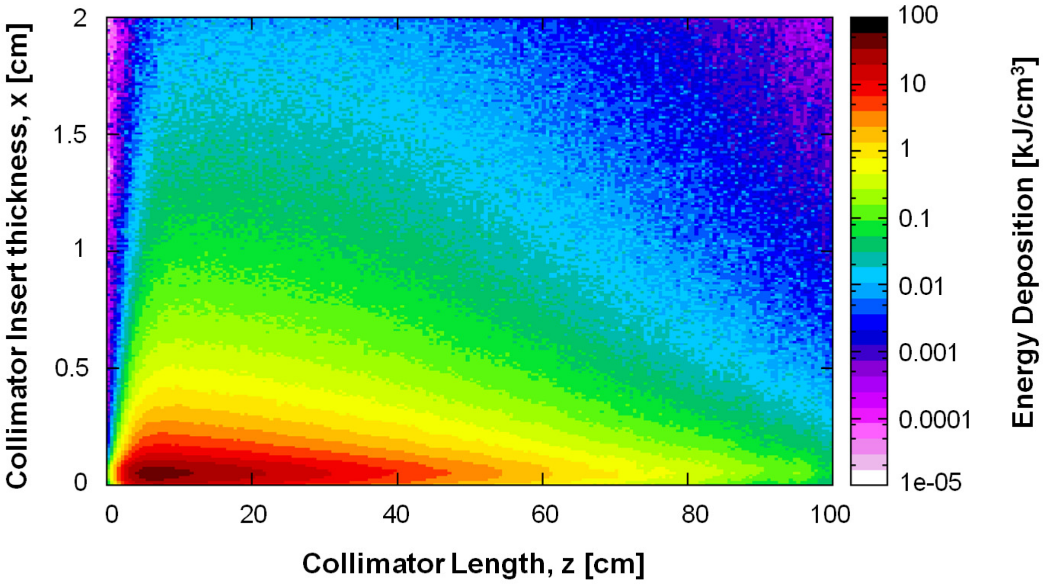

Figure 7.1: Energy deposition cuts in the x-z plane at the collimator insert half-height (symmetry plane) for heavy ions and protons: 1 nominal bunch of lead ions - 7.00×10^7 ions, 2759 GeV/n (top), and 1 nominal bunch of protons - 1.15×10^{11} protons, 7 TeV (bottom) (results obtained in collaboration with L. Lari, CERN).

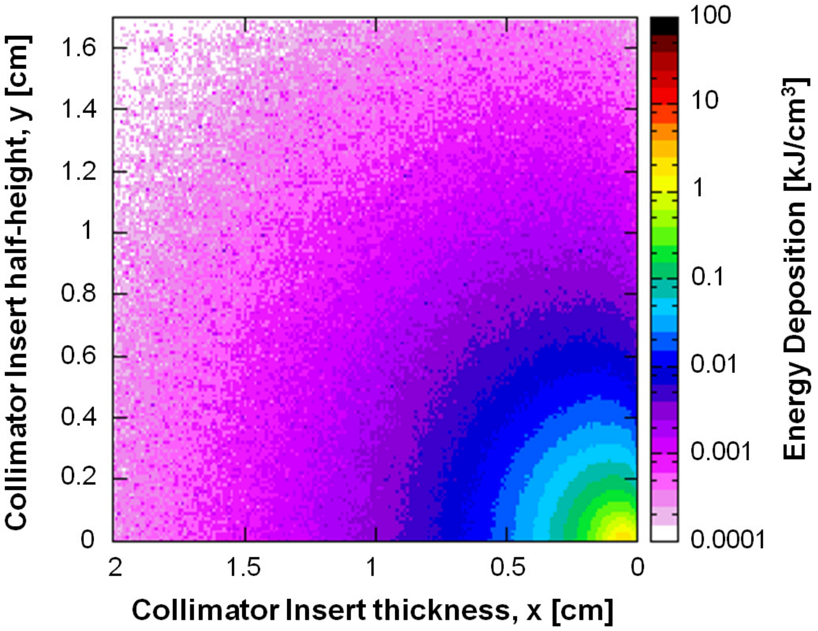

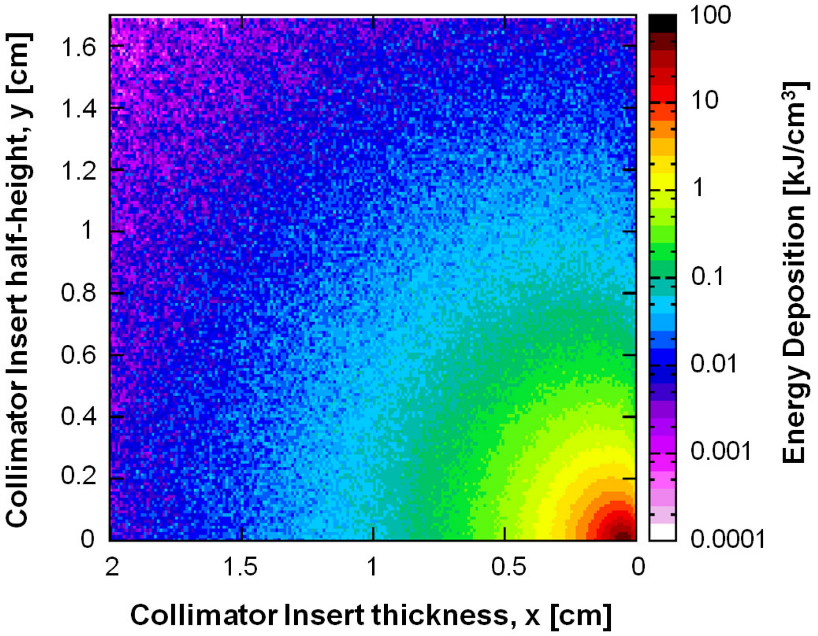

Figure 7.2: Energy deposition cuts in the x-y plane at the location of T_{max} in the z-direction for heavy ions and protons: 1 nominal bunch of lead ions (7.00×10^7 ions, 2759 GeV/n) with T_{max} occurring at $z = 6.5$ cm (top), and 1 nominal bunch of protons (1.15×10^{11} protons, 7 TeV) with T_{max} occurring at $z = 7$ cm (bottom) (results obtained in collaboration with L. Lari, CERN).

Moreover, a multilinear kinematic hardening model at different temperatures was adopted for the collimator jaw insert material, based on the structural characterisation results presented in Section 5.4 (Figure 7.3). The stress-strain results at the fixed strain-rate of 10^{-3} s^{-1} were used in order to be able to investigate the cumulative damage in the part of the component that was still solid after the beam impact. The results at the higher strain-rate of 10^{3} s^{-1} were then used in the study of spallation in order to investigate if the UTS of the material was exceeded in the region subject to high tensile stresses, temperatures and strain-rates close to the beam impact.

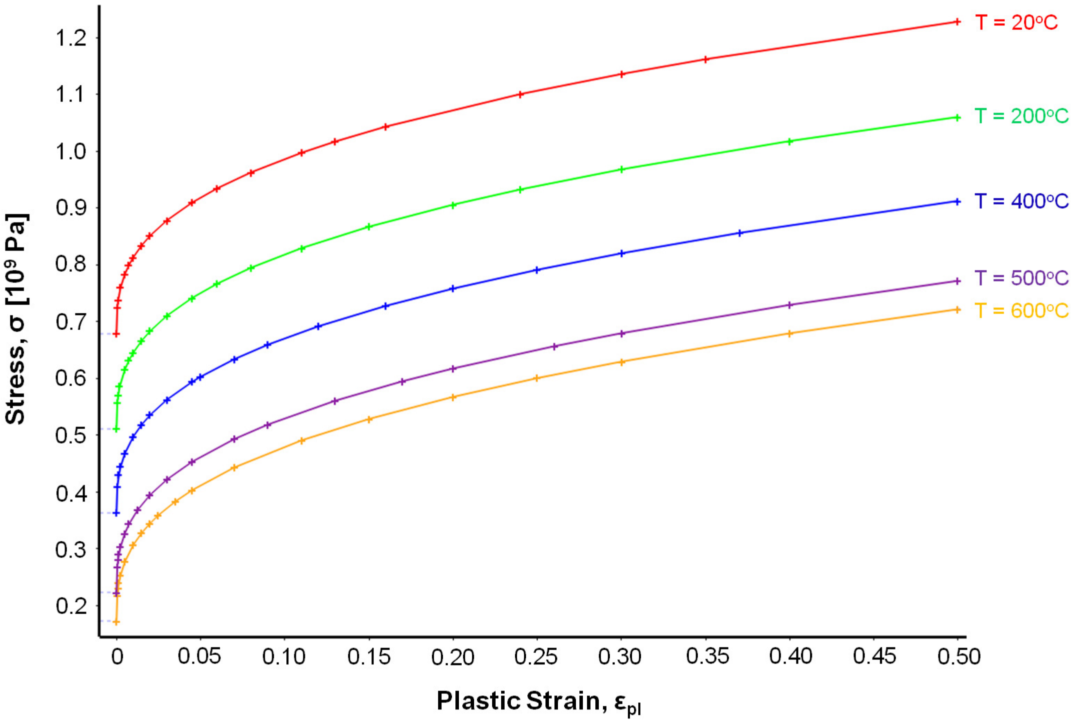

Figure 7.3: The multilinear kinematic hardening model used in ANSYS® for INERMET® 180. This model is based on a modified version of the Z-A model as explained in Section 5.4.6.

The material models of the OFE-Cu block housing, the Cu-Ni cooling pipes and the GlidCop® AL-15 back stiffener were implemented as specified in Section 4.3.2.

Loading and boundary conditions

The typical $\tau_{\text{diffusion}}$ for the INERMET® 180 jaw inserts has already been calculated in Section 6.5.3. Given the rapidity of the beam impact duration (1 ns) when compared with the typical $\tau_{\text{diffusion}}$ (approximately 306 μs), it can be concluded that it is possible to decouple and sequentially solve the non-linear, transient thermal and structural analyses. Thus, the same approach as that presented in Chapter 4 was used for the study of the ion and proton beam impact scenarios.

The first period of flexural oscillation of the jaw assembly was calculated by Equation 3.9, considering INERMET® 180 as the jaw insert material, and it was found to be around 105 Hz. As explained in Section 3.3.4 and implemented in Section 4.3.2, the integration time step (ITS) must be optimised depending on the mesh size. The Courant criterion was calculated using Equation 3.10 and the minimum step size was again fixed to 0.1 μs for the structural analyses. The transient thermal and structural load cases were then implemented as a sequence of load steps, as given in Table 7.3.

Table 7.3: Load step sequences used for the FEM thermal and structural analyses in the comparative study on proton and ion beam impacts. The first load step represents the beam impact. The computational time needed to achieve these transient thermal and structural solutions on a 32 GB RAM 4-core machine with a processor speed of 4.0 GHz was ∼1 day and ∼4 weeks per solution respectively.

Load step number	**Time at end of loadstep** [s]	**Thermal ITS** $\Delta t_{\mathbf{thermal}}$ [s]	**Structural ITS** $\Delta t_{\mathbf{structural}}$ [s]	**Imported Body Load Step Time** [s]
1	1.00×10^{-9}	1.25×10^{-10}	1.25×10^{-10}	1.00×10^{-9}
2	1.00×10^{-6}	1.00×10^{-7}	1.00×10^{-7}	1.00×10^{-6}
3	1.00×10^{-4}	2.50×10^{-6}	1.00×10^{-6}	1.00×10^{-4}
4	2.00×10^{-3}	2.00×10^{-5}	1.00×10^{-5}	2.00×10^{-3}
5	5.00×10^{-3}	2.00×10^{-4}	1.00×10^{-4}	5.00×10^{-3}
6	0.01	2.00×10^{-4}	1.00×10^{-4}	0.01
7	0.02	2.00×10^{-4}	1.00×10^{-4}	0.02
8	0.04	5.00×10^{-4}	2.50×10^{-4}	0.04
9	0.06	5.00×10^{-4}	2.50×10^{-4}	0.06
10	0.12	1.00×10^{-3}	2.50×10^{-4}	0.12
11	0.25	5.00×10^{-3}	1.25×10^{-3}	0.25
12	1.00	0.05	2.50×10^{-3}	1.00
13	5.00	0.20	5.00×10^{-3}	5.00

7.4 Numerical simulation results

7.4.1 Thermal analyses

An initial comparison between protons and lead ions can be done by evaluating the energy deposited by 1 nominal bunch of each particle type on the collimator jaw inserts. It is observed from Figures 7.1 and 7.2 that the energy deposited by a nominal ion bunch is around two orders of magnitude smaller than that for a nominal proton bunch. This results from the fact that the stored energy of the nominal ion beam is only 1% of that of the nominal proton beam (Table 7.1). Figures 7.4 and 7.5 show that a different maximum temperature T_{max} is reached for the nominal proton and ion beam impact cases. This subsequently influences the dimension of the molten region on the jaw inserts and the extent of the beam-induced damage.

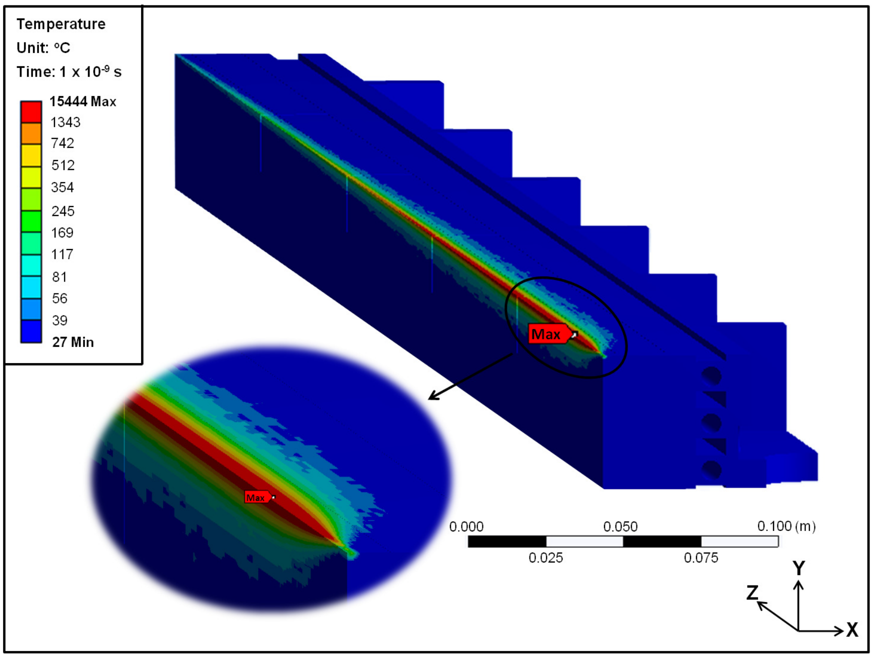

Figure 7.4: Logarithmic temperature distribution provoked by the nominal proton beam impact at 1 ns. The red region represents temperatures above the melting temperature of INERMET® 180 (approximately 1343 °C). This region gives an indication of the molten region caused by the beam impact and of the extent of the resulting groove formed on the surface of the collimator jaw inserts. A detailed view is shown in the inset.

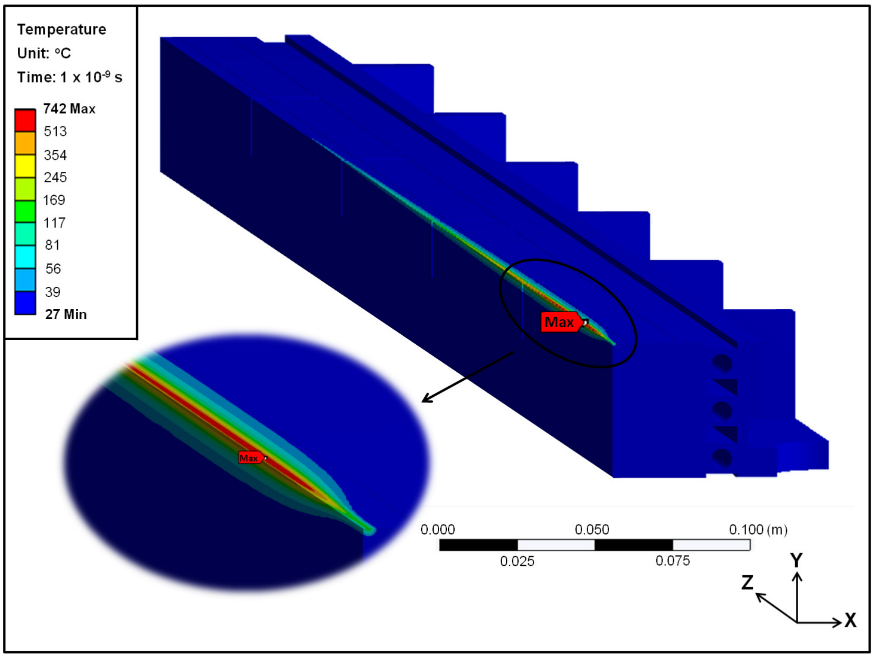

Figure 7.5: Logarithmic temperature distribution provoked by the nominal lead ion beam impact at 1 ns. The melting temperature of INERMET® 180 (approximately 1343 °C) is not exceeded in any region in this case. A detailed view is shown in the inset.

Another interesting aspect was to simulate the number of protons per bunch that would give the same T_{max} as 1 nominal ion bunch, considering the same beam size and the same impact parameter. The graph in Figure 7.6 shows that 4.48×10^9 protons per bunch would in fact give the same T_{max} as 1 nominal ion bunch. This intensity is very close to the intensity of an LHC pilot bunch. However, some differences between the two temperature profiles can be observed. One of the main differences is the discrepancy between the energy deposition values close to the jaw entrance. This difference is caused by ionisation. As shown in Table 7.2, the relative energy loss due to ionisation is two orders of magnitude larger for heavy ions than for protons. This means that ions lose their energy to the target material more quickly than protons.

From the thermal analyses, it can be concluded that the heat deposition, and consequently the damage caused by the impact of a nominal ion bunch, nowhere exceeds that resulting from a nominal proton bunch. Thus, in order to be able to qualitatively compare the effects resulting from the differences between the interactions of protons and heavy ions with matter, it was decided to consider impact cases of the two particle types where the

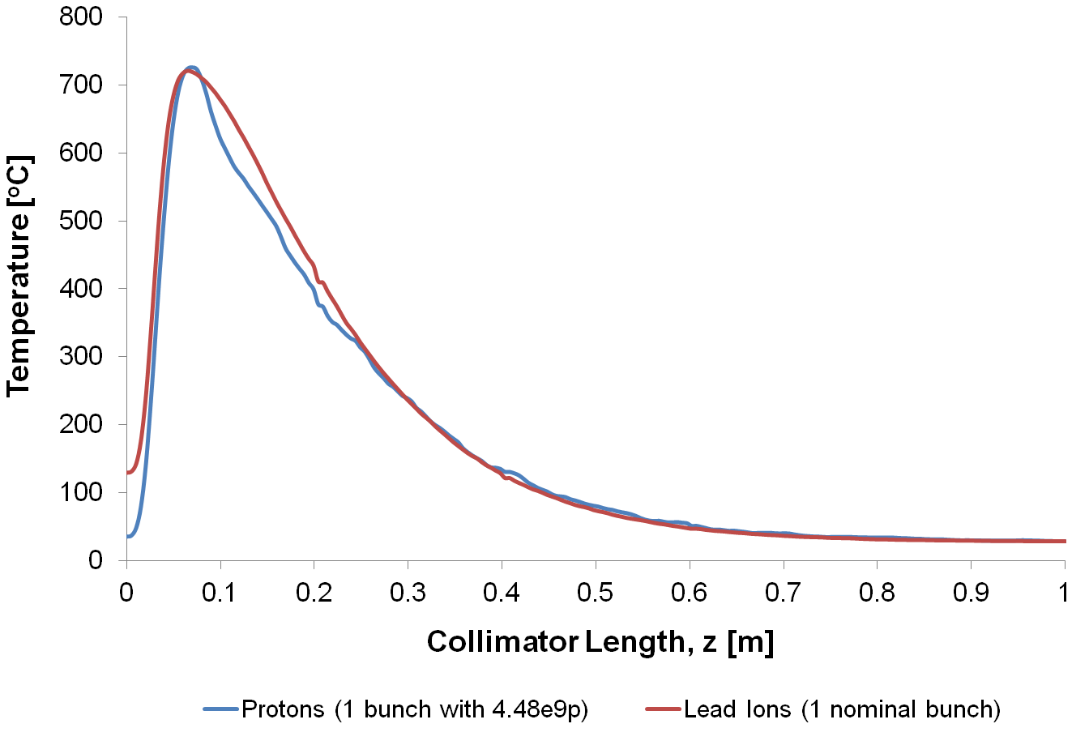

Figure 7.6: Temperature peak profiles within the jaw inserts along the beam direction for heavy ions and protons.

same peak temperature is reached. In fact, some differences in the temperature profiles of these two cases were observed, with such discrepancies mainly arising from ionisation effects. Section 7.4.2 will now discuss if such differences will play any role in the structural behaviour of the collimator when subject to an asynchronous beam dump.

7.4.2 Structural analyses

Once the expected temperature increase was known, the plasticisation provoked by the thermal shock and the range of compressive stresses were estimated by Equations 4.1 and 4.2 respectively. Given that ΔT_{max} and the jaw insert material (INERMET® 180) were set to be the same for the proton and heavy ion cases, the values of $\epsilon_{z_{max}}$ and $\sigma_{z_{max}}^{linear}$ resulted to be the same for these two cases, as expected. Thus, considering the ion beam impact case, Figure 7.7 shows a contour plot of the longitudinal elastic strain on the collimator jaw assembly, following the impact of 1 nominal ion bunch. Good agreement is achieved with the analytical calculation that is performed using Equation 4.1 with $\alpha = 5.25 \times 10^{-6}$ K^{-1} and $T_{\text{max}} = 742$ °C as shown in Figure 7.5.

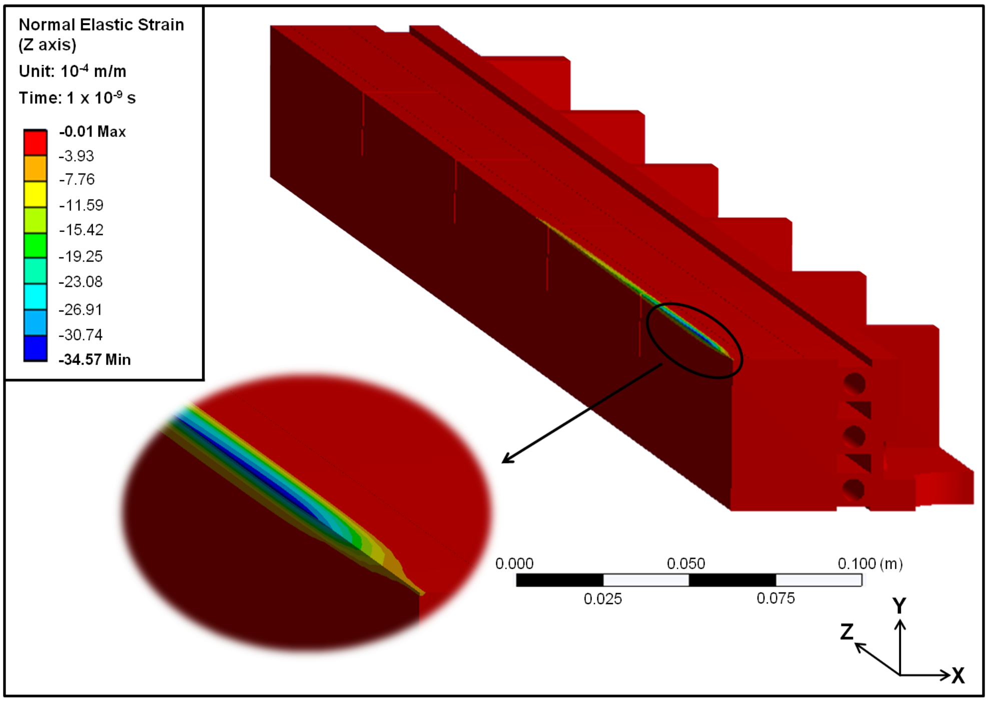

Figure 7.7: Normal elastic strain along the z-direction on the collimator jaw assembly after the nominal ion beam impact. A detailed view is shown in the inset. A similar plot with comparable peak values has been obtained for the case of the proton beam impact (involving 1 bunch with 4.48×10^{9} protons).

The behaviour of the compressive stress developed within the collimator jaw assembly is very similar to that of the normal elastic strain shown in Figure 7.7. A maximum compressive longitudinal stress of around 3 GPa was developed at the same location as the maximum compressive longitudinal strain, both for the ion and proton beam impact cases. This value of maximum compressive stress is also comparable with that achieved with Equation 4.2, using $E = 360$ GPa and $\nu = 0.28$ in addition to $\alpha = 5.25 \times 10^{-6}$ K^{-1} and $T_{\text{max}} = 742$ °C as given previously. Moreover, the longitudinal deformation due to the particle beam impact does not exceed 0.1 mm (Figure 7.8), thus once again justifying the modelling approach of the contact interface between the jaw inserts as described in Section 3.3.1.

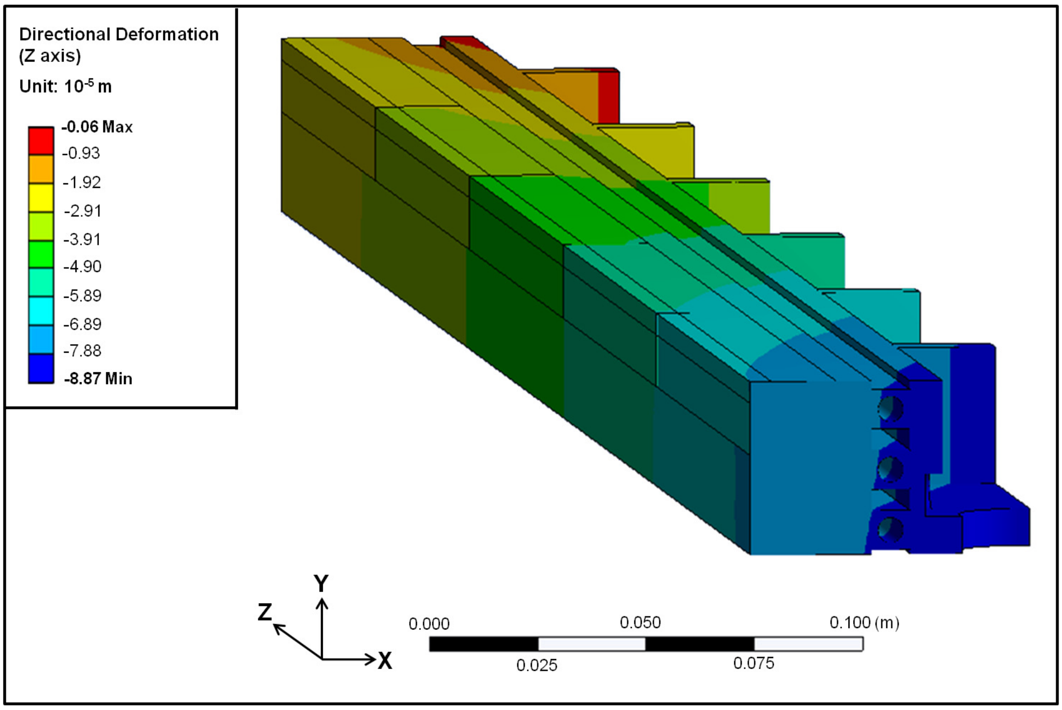

Figure 7.8: Longitudinal deformation (z-direction) of the collimator jaw assembly due to the studied ion beam impact case. The maximum longitudinal deformation is approximately 89 μm.

The numerical results of the dynamic response of the collimator jaw assembly, as calculated by ANSYS®, will now be presented. Figure 7.9 shows that the jaw assembly, hit by the high-energy particle beam, shows a dynamic flexural response with a main frequency of approximately 100 Hz. The main frequency of flexural oscillation, analytically calculated as 105 Hz by Equation 3.9 in Section 7.3.2, is thus once again correctly predicted by numerical simulations.

Moreover, it can be noticed that the jaw assembly vibrates, with an underdamped response, around its quasi-static deflected position. Theoretically, for a given system, the value of the quasi-static deflection should be equal to the value of the dynamic deflection at the end of the dynamic response. It is calculated that for both the proton and the ion case studies, there is a discrepancy of around 3.65% between these two values. Given the complexity of the FEM simulations involved, this is still considered as being within an acceptable limit. The developed dynamic thermal stresses, obtained from the FEM analysis, are also given in Figure 7.10.

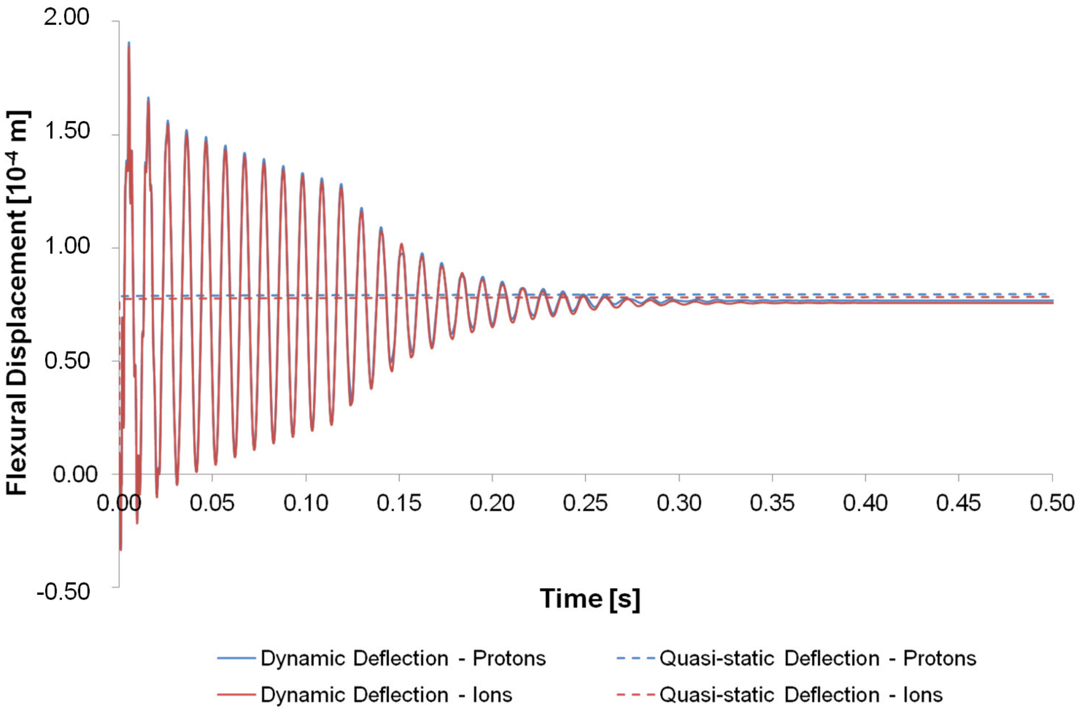

Figure 7.9: Dynamic flexural displacement (x-direction) of the collimator jaw assembly at z = 0.530 m for protons, as provoked by the proton (1 bunch with 4.48×10^9 protons) beam impact, and at z = 0.532 m for ions, as provoked by the ion (1 nominal ion bunch) beam impact. The quasi-static deflection due to the thermal bending moment is also shown for both cases.

As highlighted in Section 2.3.3, spallation is an important mode of failure during high velocity impact. In this study, the maximum principal stress model is used as the spallation criterion. The maximum principal stress on the collimator jaw for the ion case study is shown in Figure 7.11, and it can observed that the highest stresses develop in the region subject to the highest temperatures (Figure 7.5) and strain-rates. An overview of the UTS of INERMET® 180 can be obtained from experimental data presented in Section 5.4.5. It can be deduced from interpolation of Figure 5.25 that under high strain-rate and high temperature ($T_{\max} \approx 742$ °C from Figure 7.5) conditions, the UTS of INERMET® 180 is expected to be approximately 550 MPa. This value is thus used as a limit above which spallation is expected to occur.

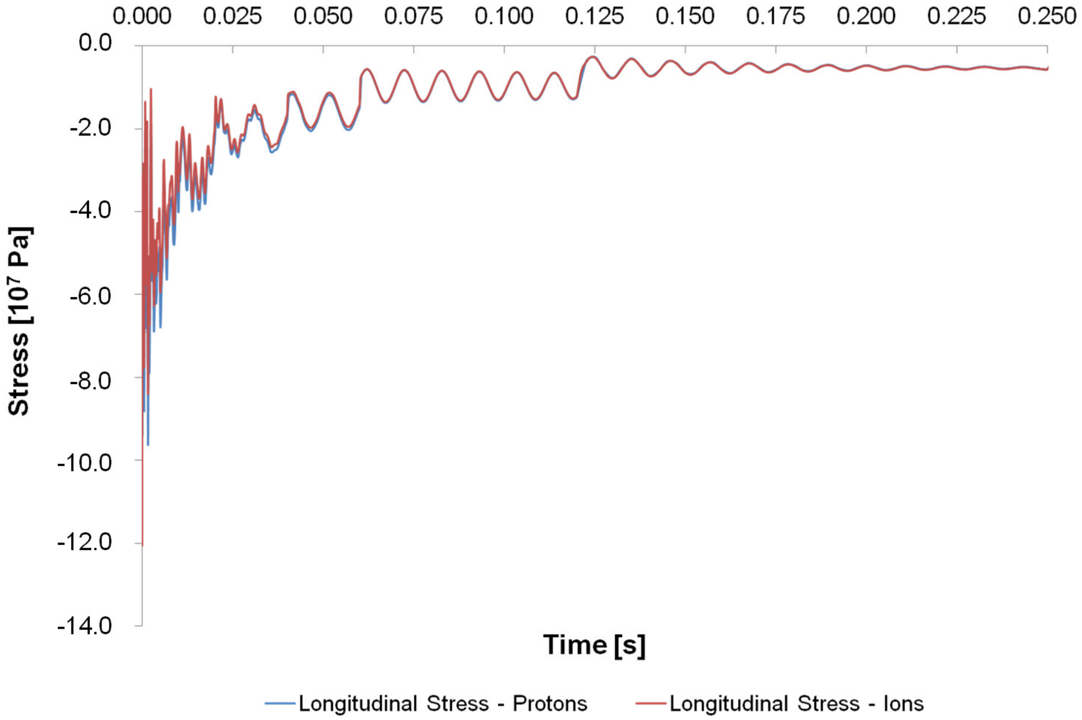

Figure 7.10: Dynamic longitudinal stress (z-direction) of the collimator jaw assembly at z = 0.530 m for protons, as provoked by the proton (1 bunch with 4.48×10^9 protons) beam impact, and at z = 0.532 m for ions, as provoked by the ion (1 nominal ion bunch) beam impact. It can be observed that oscillations start at a frequency range on the order of kHz and settle at a main frequency of approximately 100 Hz, which is approximately equal to the first period of flexural oscillation of the jaw assembly.

A comparison between the ion and proton impact scenarios is given in Figure 7.12, from where it can be seen that the UTS of INERMET® 180 is slightly exceeded in both cases. A slightly larger region can be observed for the ion case, meaning that a slightly larger region of the first jaw insert is subject to the formation of cracks. However, it can be concluded that in both cases, crack formation and other related subsequent damage are limited to a very small region.

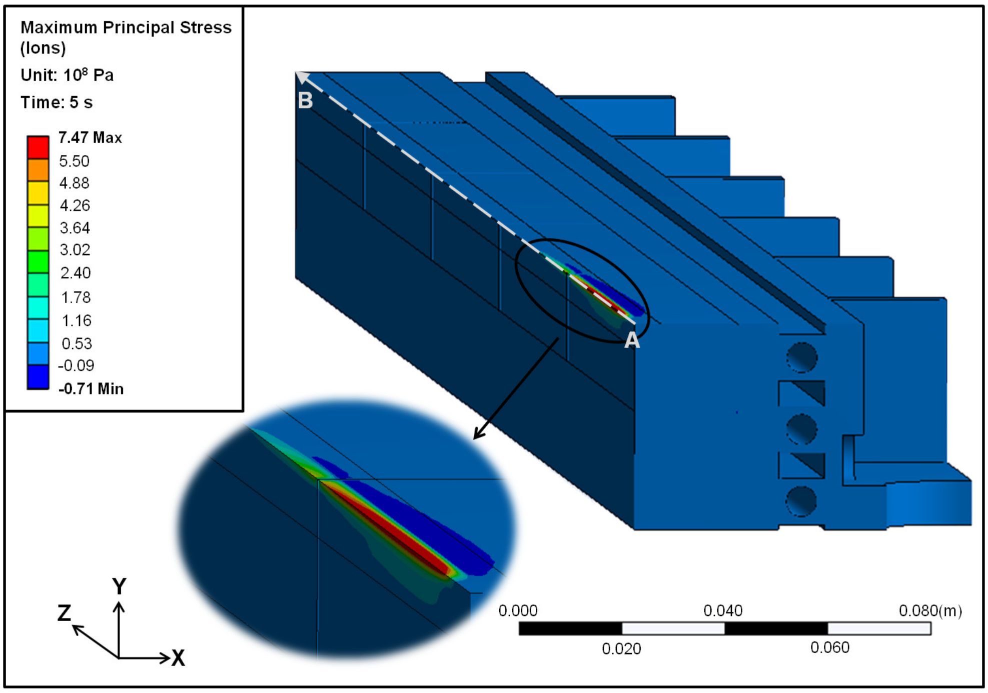

Figure 7.11: Maximum principal stress on the collimator jaw assembly as provoked by the ion (1 nominal ion bunch) beam impact. The red region indicates the region of the jaw where the UTS of INERMET® 180 is exceeded, leading to the formation of micro-cracks and ultimately, spallation.

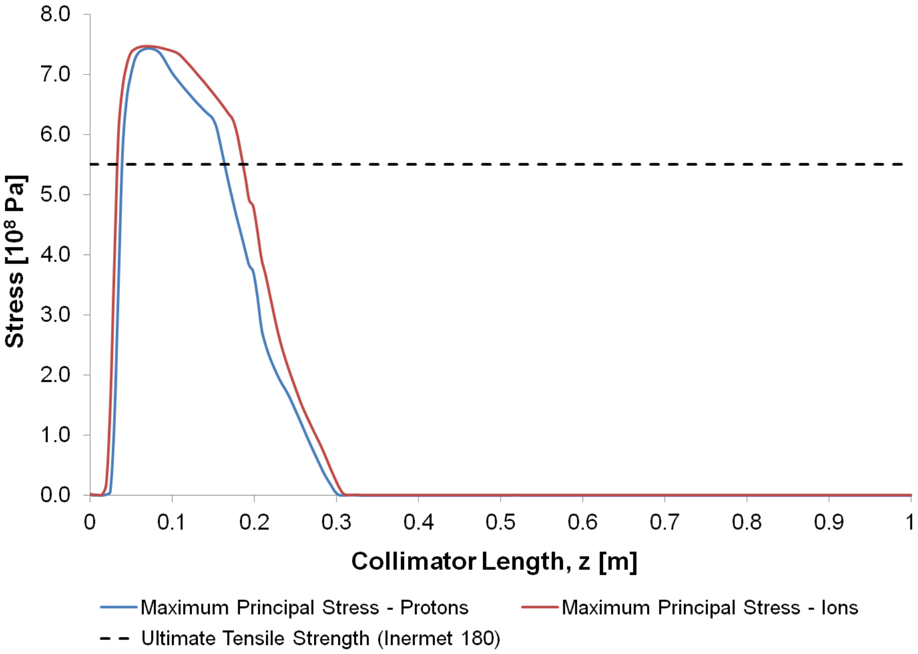

Figure 7.12: Comparison of the maximum principal stress on the collimator jaw assembly for the proton and ion beam impacts. For each case, the maximum principal stress is plotted along Path AB shown in Figure 7.11.

Due to the fact that the beam-induced thermal stresses on the collimator jaw exceed the yield strength of INERMET® 180, the collimator jaw will remain subject to some permanent deformation after the beam impact. Figure 7.13 shows that for the case of the ion beam impact, residual plastic strains lead to a permanent deformation of approximately 94 μm of the collimator jaw assembly. A comparison of the total and flexural deformations for the proton and ion case studies is then given in Figure 7.14, from which it can be observed that there are no significant differences between the two cases.

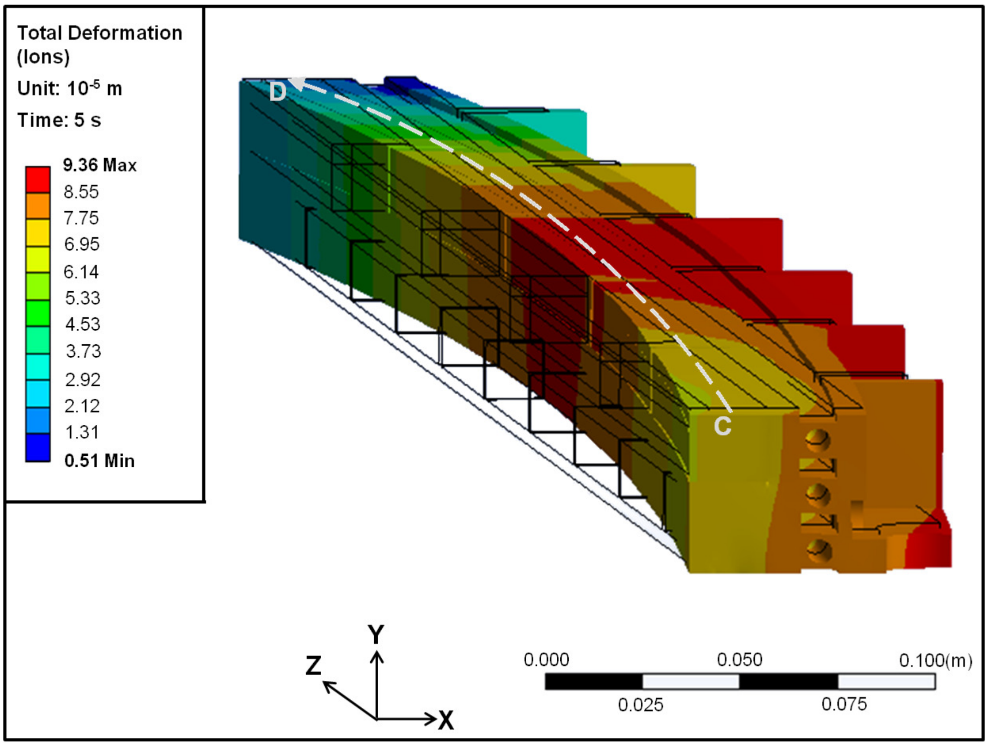

Figure 7.13: Total deformation of the collimator jaw assembly as provoked by the ion (1 nominal ion bunch) beam impact. The deformation scale factor is 280.

It can be noticed that the deformation mode of the collimator jaw in Figure 7.13 varies from that shown in Figure 4.23. The different deformation modes of the collimator jaw are in fact the result of the different temperature distributions resulting from the beam impact. The uniform temperature distribution along the whole collimator length, as a result of the -1 mrad jaw inclination (Figure 4.12), causes the jaw to expand outwards along the whole length, with the result that the jaw remains with a permanent deformation towards the beam as shown in Figure 4.23. On the other hand, the focused temperature development

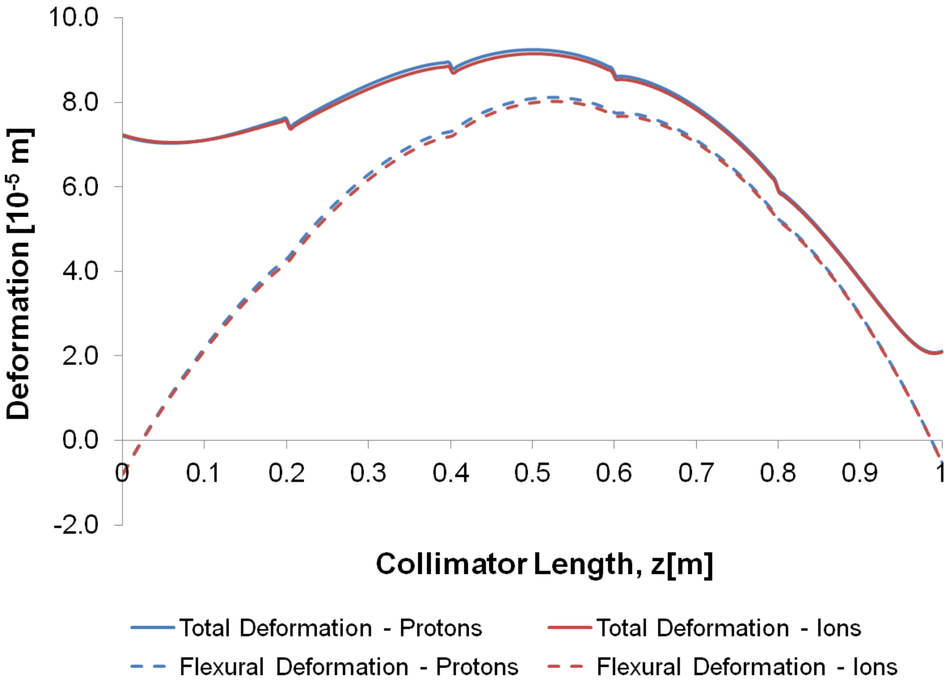

Figure 7.14: Comparison of the total and flexural deformations of the collimator jaw assembly for the proton (1 bunch with 4.48×10^9 protons) and ion (1 nominal ion bunch) beam impacts. The deformations are plotted along Path CD shown in Figure 7.13.

at the upstream part of the jaw (Figure 7.5) due to the parallel jaw-beam setup, together with the structural constraints of the jaw, subject the jaw to a permanent deformation away from the beam as shown in Figure 7.13.

7.5 Conclusions

The LHC is designed to bring high-energy protons as well as heavy ions into collision. Accidents involving impacts on collimators can happen in both cases. This chapter has presented the study performed to compare, for the first time, the thermo-mechanical response of TCTs in case of an asynchronous beam dump, involving proton or heavy ion beam impacts. For both cases, the same impact conditions were assumed, changing only the particle type when simulating the interaction with matter. A numerical FEM approach was implemented, and sequential fast-transient thermo-structural analyses were performed in the elastic-plastic domain. Recent thermo-physical and structural characterisation properties of the collimator jaw insert material, INERMET® 180, were used, thus providing a more precise material model for the analyses.

From the thermal analyses, it has been shown that the heat deposition of 1 nominal ion bunch on TCTs nowhere exceeds that of 1 nominal proton bunch. However, some qualitative differences in the temperature profiles of the proton and ion beam impact case studies were observed, with such discrepancies mainly arising from ionisation effects. Consequently, further detailed studies were carried out in the structural domain to investigate if such variations in energy deposition, resulting from different beam-matter interactions, play any role in the structural behaviour of the collimator structure, when subject to an asynchronous beam dump.

For this structural study, the proton bunch intensity was selected such that it provided the same temperature increase on the jaw as a nominal ion bunch. This bunch intensity corresponded to 4.48×10^9 protons per bunch which is very close to that of an LHC pilot bunch. The thermally-induced dynamic response of the collimator structure was studied, followed by a quasi-static analysis to calculate potential permanent deformations of the structure once the dynamic response had vanished. No major discrepancies resulted between the proton and ion case studies. Both cases had a permanent deformation of approximately 94 μm and a maximum principal stress of approximately 750 MPa on the collimator jaw assembly. It can thus be concluded that heavy ion operation with a nominal ion bunch intensity of 7.00×10^7 ions and a beam size of 0.30 mm (σ_x) × 0.30 mm (σ_y) poses no additional qualitative challenges, when compared to protons, on the structural integrity of collimators in case of an asynchronous beam dump.

Chapter 8

Conclusions

.

8.1 Summary of work achievements

The correct functioning of the collimation system is crucial to safely and successfully operate high-energy particle accelerators such as the LHC. With a nominal stored beam energy of 362 MJ and a beam momentum of 7 TeV/c, the requirements to handle the high-intensity beams are unprecedented. Thus, predicting the consequences of high-energy particle beams impacting protection devices, such as collimators, is a fundamental issue in the accelerator machine design. Accident scenarios must be studied well in order to assess the robustness of collimators in case of possible error scenarios.

One of the serious accident scenarios identified within the LHC is an asynchronous beam dump. In the case of a single dump module pre-fire, one of the 15 pre-charged kicker circuits fires out of time with the abort gap, spraying beam pulses onto LHC machine elements before the MPS can fire the remaining kicker circuits and bring the beam to the dump. If a proton bunch directly hits a collimator during such an event, severe beam-induced damage such as magnet quenches and other equipment damage might result, with consequent downtime for the machine. While the robust TCP and TCS system are designed to withstand such beam impacts, there may be machine conditions that expose the TCTs and put them at risk of damage. This study has thus focused on accident scenarios involving TCTs since they are the first metallic collimators exposed to a high risk of damage in case of an asynchronous beam dump.

The interaction of high-energy particle beams with matter provokes a sudden non-uniform temperature increase on the structure. This gives rise to thermal stresses and deformations that may affect the integrity or the proper functionality of the hit equipment. It is, in this respect, that the implementation of a numerical FEM approach, as opposed to analytical solutions, is imperative for an in-depth study of the fast and complex thermo-mechanical phenomena induced within the impacted structure. Such an approach is also essential for the study of multi-component systems with contact interfaces, as well as for the study of problems exhibiting material non-linearities that have a strong influence on the results. Therefore, a numerical FEM approach found direct application in the framework of the LHC collimation project.

This study has developed and applied a numerical FEM approach based on an implicit algorithm of integration in order to evaluate both thermally induced vibrations on the short time scale as well as permanent deformations on the long time scale resulting from the beam impact. A challenging simulation campaign, especially in terms of computational resources, was set up. Sequential transient thermal and structural analyses were performed in the elastic-plastic domain in order to investigate the consequences of LHC particle beams hitting TCTs.

Detailed energy deposition maps were essential to correctly simulate thermal loads as an input for thermo-mechanical calculations of complex structures. The evaluation of the thermal loads on the TCT for the studied accident cases was provided through simulations with the Monte Carlo based statistical code FLUKA. This work focuses on the thermo-mechanical study of the collimator jaw assembly whose detailed model was set up in ANSYS®. An optimised FE discretisation procedure was implemented, and the heat convection coefficient together with the effect of the water flow pressure on the inner wet surface of the cooling pipes were also taken into account.

The thermo-structural behaviour of the collimator jaw assembly was correctly modelled through the choice of an appropriate integration time step (ITS) based on the Courant criterion. The thermal and structural load cases were implemented as a series of load steps and the solution was then based on three sequential steps. Once the heat load was known, the temperature distribution could be calculated as a function of space and time. The results of the thermal analysis were subsequently used as loads in the structural analysis so that the dynamic stresses and displacements could be evaluated. A final quasi-static step was then necessary to calculate potential permanent deformations of the structure once the dynamic response had vanished.

Material modelling plays an important role in the performance of reliable FEM simulations. Temperature-dependent thermal and structural material properties are required in FEM calculations with large temperature variations as is the case of a beam impact on a TCT. Due to the lack of available temperature-dependent properties for the collimator jaw insert material, INERMET® 180 (composition: 95 wt.% W - 3.5 wt.% Ni - 1.5 wt.% Cu), it was decided to use the more defined temperature-dependent properties of pure tungsten for the initial case studies on the jaw-beam angle effect. The use of pure tungsten instead of INERMET® 180 introduced a 5% modelling error which was nevertheless still considered acceptable in the context of the complex numerical simulations involved.

Two sets of material characterisation tests on INERMET® 180 were then commissioned as part of this study in order to obtain an overview of the temperature-dependent behaviour of the jaw insert material under extreme conditions. Thermo-physical characterisation tests were commissioned at the Energy Department of the Austrian Institute of Technology. Measurements of the coefficient of linear thermal expansion, density, specific heat capacity, thermal diffusivity and thermal conductivity were obtained between room temperature and 1450 °C. Additionally, structural characterisation tests were commissioned at the DYNLab of the Politecnico di Torino, and stress-strain curves at different temperatures and strain-rates were provided. This experimental data was processed via a numerical inverse method and the Z-A model was then used to obtain a unique material strength model with a sufficient level of accuracy.

The probability that a collimator is hit directly by a high-intensity bunch comes as a result of concurrent errors such as collimator settings and orbit errors. In this context, a scenario with such combined errors was defined as a conservative case study in order to understand the consequences of a potentially severe beam impact event on a tungsten-based collimator. Additional case studies presented in this thesis investigate the behaviour of TCTs in the special case that the impacted jaw has a slight inclination of a few milliradians due to misalignment errors of the collimator installation at the beam-line. Specifically, the thermo-mechanical response of TCTs is studied in case their planar collimating surface is either exactly parallel to the beam or is tilted by -1 mrad or ±5 mrad during 3.5 TeV and 7 TeV bunch impacts with 1.30×10^{11} protons.

An estimate of the expected damage for the different jaw error cases could be obtained from the peak temperature profiles. This is because higher temperature values will result in larger deformations and thermal stresses. It was found that a jaw tilt of -1 mrad leads to a better temperature distribution when compared to the other cases. In fact, such a jaw inclination, together with a beam impact parameter of 0.5 mm, mean that the first point of impact of the 0.30 mm (σ_x) × 0.30 mm (σ_y) RMS beam will be spread from z = 0.2 m to z = 0.8 m along the collimator length.

One of the design requirements of LHC collimators is that they must survive proton beam impacts whilst keeping their correct functionality. The deformation of collimator jaws due to thermal loads induced in nominal steady-state conditions must not exceed the limit of 40 μm in order to ensure geometric stability. The accident scenario considered in this study is of a serious nature when compared to steady-state conditions. In this regard, a resulting jaw deformation of approximately 82 μm obtained for the '3.5 TeV, -1 mrad' case could still be considered acceptable, especially when compared to the larger deformation expected for the '3.5 TeV, 0 mrad' case. It has thus been concluded that a -1 mrad tilt of the jaw could actually reduce the beam-induced damage caused by an asynchronous beam dump on a TCT.

Furthermore, the conservative accident scenario that was considered for the jaw-beam angle scanning study was also used as a case study to evaluate and compare, for the first time, the thermo-mechanical response of TCTs to proton and heavy ion beam impacts. The LHC operates with both high-energy protons and heavy ions. The physics of the interaction with matter varies quantitatively as well as qualitatively for the proton and lead ion beams, resulting in different beam dynamics and performance limits for the two types of beam. Case studies were thus considered for both proton and heavy ion beams. The same impact conditions were assumed, changing only the particle type when simulating the interaction with matter.

A qualitative comparison between proton and ion beam impacts was obtained by selecting a proton bunch intensity such that it produced the same temperature increase on the collimator jaw as a nominal ion bunch. Such a proton bunch intensity is, in fact, very close to that of an LHC pilot bunch. Transient thermal and structural analyses were performed for the two scenarios, implementing the material model of INERMET® 180 obtained from the material characterisation tests. No major discrepancies were observed between the proton and ion case studies. It has thus been concluded that heavy ion operation with a nominal ion bunch intensity of 7.00×10^7 ions and an RMS beam size of 0.30 mm (σ_x) × 0.30 mm (σ_y) poses no additional challenges from a collimator damage point of view, when compared to protons, during a beam impact on collimators.

Different damage mechanisms have been described for the impacted collimator and they have been investigated as part of the performed thermo-mechanical analyses. The thermal analyses led to an evaluation of the maximum temperatures reached on the collimator jaw. An estimate of the extent of the molten region was produced through a comparison between the obtained temperature distributions and the melting temperature of the material. No change of state in the material was present in the cases for which a detailed structural analysis was performed with ANSYS® in this study. As concluded by Bertarelli et al.

[47], such cases are usually characterised by the development of stress waves in the plastic domain and thus can still be reasonably well-treated with FE models using an implicit scheme of integration such as ANSYS®. Changes in the density of the material due to the outgoing pressure waves, as resulting from the beam impact, were also accounted for through the use of a temperature-dependent density variation included as part of the material model.

An important mode of failure during high velocity impact occurs when the developed stresses exceed the ultimate tensile strength (UTS) of the material. Therefore, the maximum principal stress model was used as the damage criterion. In this case, sequential stages of the damage include the appearance of micro-cracks, the coalescence of micro-cracks into one major crack and finally, spallation close to the beam impact location. Residual plastic strains and permanent deformations of the collimator jaw assembly were finally studied to investigate the extent of the cumulative damage caused by an accidental beam impact.

Since high-energy and high-intensity beam impacts expose collimators to extreme conditions, the possibility for experimental tests on different accident scenarios is limited. It is therefore crucial to develop reliable computational models that can be efficiently applied to estimate the damage occurring during an impact. Benchmarking of the complex numerical simulations is thus essential and for this reason, a dedicated beam experiment was designed and set up at the CERN HiRadMat facility. This test was designed to investigate the robustness and effects of beam accidents on a fully assembled TCT. The preliminary post-irradiation analysis has confirmed the validity of the developed FEM approach as good agreement was achieved between the dimensions of the observed grooves and the simulated molten regions. Other important experimental outcomes include updated safe 7 TeV limits for TCTs and an improved temperature sensor fixation method for collimators.

The next sub-section will now summarise the main contributions of this work to the development of the research field.

8.2 Main contributions

This thesis has presented a thorough assessment of the thermo-mechanical response of TCTs to accidental beam impacts in a detailed study of various relevant scenarios for the operation of the LHC and its risk optimisation. A more in-depth view of the robustness of TCTs in case of an asynchronous beam dump has been achieved by taking into account all relevant collimator damage limits. The main contributions of this work to the research field consist of:

1. The development of a working and validated numerical FE model has been successfully achieved. All studied cases deal with stress waves generated in the plastic domain whereby an implicit algorithm of integration, as implemented with ANSYS®, is considered sufficient. Such an approach has been found to be highly effective to study both thermally induced vibrations on the short time scale as well as permanent deformations on the long time scale.
2. The developed FE model has been implemented to identify the effectiveness, from a collimator damage point of view, of operating with tilted collimator jaws in case of an asynchronous beam dump accident. Jaw error cases with different beam energies and jaw-beam angles were studied and it has been found that in the case of a jaw inclination of -1 mrad, no region with very focused energy deposition results from the beam impact, leading to an overall lower peak temperature. It has in fact been concluded that a jaw tilt of -1 mrad can mitigate the effect of a beam impact on a TCT. This means that for the same beam impact conditions (beam energy, beam size, impact parameter), the collimator will be subject to less damage and can possibly survive a high-energy beam impact while keeping its correct functionality.
3. The developed FE model has also been used to give an assessment of the thermo-mechanical response of TCTs to proton and heavy ion beam impacts. The physics of the ion beam's interaction with matter varies qualitatively and quantitatively from that of the proton beam. It has however been concluded that

operation with heavy ions (1 nominal bunch, 0.30 mm RMS beam size) poses no additional qualitative challenges, when compared to protons, on the structural integrity of collimators in case of an asynchronous beam dump.

4. Thermal and structural material characterisation tests of INERMET® 180, under varying temperature and strain-rate conditions, have been commissioned and the obtained results have enabled the implementation of a more reliable material model in the FEM simulations. Such test campaigns were challenging both in terms of cost and resources. However, due to the limited temperature-dependent INERMET® 180 data available, such tests were considered an essential contribution to the research field in order to be able to correctly reproduce the material behaviour and to perform the numerical FEM simulations with a higher level of confidence.

5. A dedicated beam experiment has also been designed and carried out at the CERN HiRadMat facility in order to experimentally investigate the effects of beam accidents on the robustness of a fully assembled collimator, and to benchmark the complex numerical simulations. Such an experiment has successfully confirmed the validity and reliability of the developed FE model, thus giving confidence in the prediction of damage by such numerical simulations. This is crucial since the experimental phase in such extreme conditions is also very expensive in terms of cost as well as resources, and the possibility to perform experimental tests to study different accident scenarios is therefore limited. A new temperature sensor fixation method was another important outcome of such tests and it has already been implemented for the new collimators installed in the machine for the LHC Run 2.

8.3 Future work

8.3.1 Post-irradiation analysis of the tested collimator

An extensive post-irradiation campaign on the tested HiRadMat collimator is foreseen in order to provide additional valuable information on the robustness of TCTs in case of beam impacts. The visual inspection presented in this study consisted of preliminary observations done based on photos taken with a camera. Due to the high-radiation level, transportation of the collimator to dedicated laboratories for further analysis has so far been restricted.

Future post-irradiation analysis will involve direct observations including detailed metrology as well as destructive and non-destructive testing of the collimator jaws. Any permanent deformations of the jaws will be investigated, and metallographic inspections will specifically give insight into the damage caused by the beam on the microstructure of the material. These results should then be complemented with numerical simulations in order to validate the FE model developed and presented in this thesis within the structural domain.

8.3.2 Beam damage studies and numerical simulations

This study has investigated the effects of an asynchronous beam dump scenario when combined with other concurrent errors. Further studies on realistic losses in case of an asynchronous beam dump are ongoing [140, 141] and it will be interesting to investigate and compare the thermo-mechanical response of TCTs in these new scenarios.

It was found in this study that a jaw-beam angle of -1 mrad can actually mitigate the effect of the beam-induced damage caused by an asynchronous dump on TCTs. A useful complementary study will be the investigation of the number of escaping high-energy protons in case of such a jaw inclination as such protons can potentially be lost in the SC magnets located downstream of the impacted collimator.

The comparative analysis on proton and heavy ion beam impacts presented in this thesis showed that heavy ion operation creates no additional challenges when it comes to beam impacts on collimators. This investigation was done considering a nominal ion bunch with an RMS beam size of 0.30 mm (σ_{x}) × 0.30 mm (σ_{y}). An interesting aspect will be to study at what intensity, or beam size, heavy ions might potentially become problematic.

Material defects as a result of beam damage can act as hindrance to dislocation movement within the material, and thus future work can also include the study of the effect of beam damage on the material properties at the atomic level.

References

[1] CERN Official Website: `http://www.cern.ch` Accessed: 2014-08-26.

[2] The Official Website of the Nobel Prize: `http://www.nobelprize.org/` Accessed: 2014-11-12.

[3] O. Brüning, P. Collier, P. Lebrun, S. Myers, R. Ostojic, J. Poole, and P. Proudlock, *LHC Design Report*. Geneva: CERN, 2004.

[4] ATLAS Collaboration, "The ATLAS Experiment at the CERN Large Hadron Collider," *JINST*, vol. 3, p. S08003, August 2008. ATLAS Official Website: `http://atlas.web.cern.ch/Atlas/Collaboration/` Accessed: 2014-08-26.

[5] ALICE Collaboration, F. Carminati, P. Foka, P. Giubellino, A. Morsch, G. Paic, J.P. Revol, K. Safarik and Y. Schutz and U.A. Wiedemann (editors), "The ALICE Experiment at the CERN LHC," *JINST*, vol. 3, p. S08002, 2008. ALICE Official Website: `http://aliceinfo.cern.ch/` Accessed: 2014-08-26.

[6] CMS Collaboration, "The CMS Experiment at the CERN LHC," *JINST*, vol. 3, p. S08004, August 2008. CMS Official Website: `http://cms.web.cern.ch/` Accessed: 2014-08-26.

[7] LHCb Collaboration, "The LHCb Detector at the LHC," *JINST*, vol. 3, p. S08005, 2008. LHCb Official Website: `http://lhcb.web.cern.ch/lhcb/` Accessed: 2014-08-26.

[8] Nature Specials - The Large Hadron Collider: `http://www.nature.com/news/specials/lhc/interactive.html` Accessed: 2014-11-14.

[9] CERN Official Website - The Large Hadron Collider: `http://home.web.cern.ch/topics/large-hadron-collider` Accessed: 2014-11-18.

[10] R. Bruce, R. W. Assmann, V. Boccone, C. Bracco, M. Brugger, M. Cauchi, F. Cerutti, D. Deboy, A. Ferrari, L. Lari, A. Marsili, A. Mereghetti, D. Mirarchi, E. Quaranta, S. Redaelli, G. Robert-Demolaize, A. Rossi, B. Salvachua, E. Skordis, C. Tambasco, G. Valentino, T. Weiler, V. Vlachoudis, and D. Wollmann, "Simulations and measurements of beam loss patterns at the CERN Large Hadron Collider," *Phys. Rev. ST Accel. Beams*, vol. 17, p. 081004, Aug 2014.

[11] LHC 2008 Inauguration Official Website: `http://lhc2008.web.cern.ch/LHC2008/inauguration/lhcexpo.html` Accessed: 2014-11-18.

[12] CERN Official Website - Cryogenics: Low temperatures, high performance: `http://home.web.cern.ch/about/engineering/cryogenics-low-temperatures-high-performance` Accessed: 2014-11-22.

[13] F. Close, *Particle Physics - A Very Short Introduction.* New York: Oxford University Press, Inc., 2004.

[14] O. Brüning, P. Collier, P. Lebrun, S. Myers, R. Ostojic, J. Poole, and P. Proudlock, *LHC Design Report - Volume 1, Chapter 2: Beam Parameters and Definitions.* Geneva: CERN, 2004.

[15] R. W. Assmann, O. Aberle, G. Bellodi, A. Bertarelli, C. Bracco, H. Braun, M. Brugger, S. Calatroni, R. Chamizo, A. Dallocchio, *et al.*, "The final collimation system for the LHC," in *Proceedings of the 10th European Particle Accelerator Conference, Edinburgh, Scotland*, pp. 986–988, Jul 2006.

[16] L. Evans and J. Gareyte, "The beam-beam effect in the SPS." Technical Report: SPS Divisional Reports - 1982.

[17] A. Piwinski, "Intra-Beam-Scattering," in *Proceedings of the 9th International Conference on High Energy Accelerators, Stanford, California (Stanford Linear Accelerator Centre, Stanford University, California)*, pp. 405 – 409, May 1974.

[18] Y. Chin, K. Satoh, and K. Yokoya, “Instability of a Bunched Beam With Synchrotron Frequency Spread,” *Particle Accelerators*, vol. 13, pp. 45–66, 1983.

[19] R. W. Assmann, F. Schmidt, F. Zimmermann, and M. Zorzano-Mier, “Equilibrium Beam Distribution and Halo in the LHC,” in *Proceedings of the 8th European Particle Accelerator Conference, Paris, France*, pp. 1326–1328, June 2002.

[20] J. Jeanneret, D. Leroy, L. Oberli, and T. Trenkler, “Quench levels and transient beam losses in LHC magnets,” May 1996. Technical Report: CERN-LHC-Project-Report-44.

[21] E. Holzer, B. Dehning, E. Effinger, J. Emery, G. Ferioli, J. Gonzalez, E. Gschwendtner, G. Guaglio, M. Hodgson, D. Kramer, R. Leitner, L. Ponce, V. Prieto, M. Stockner, and C. Zamantzas, “Beam loss monitoring system for the LHC,” in *Nuclear Science Symposium Conference Record, 2005 IEEE*, vol. 2, pp. 1052–1056, Oct 2005.

[22] E. Holzer, P. Chiggiato, B. Dehning, G. Ferioli, V. Grishin, T. Jimenez, A. Koshelev, D. Kramer, A. Larionov, M. Taborelli, V. Seleznev, M. Sleptsov, A. Sytin, and I. Wevers, “Development, Production and Testing of 4500 Beam Loss Monitors,” in *Proceedings of the 11th European Particle Accelerator Conference, Genoa, Italy*, pp. 1234–1136, June 2008.

[23] M. Stockner, B. Dehning, C. Fabjan, E. Holzer, and D. Kramer, “Classification of the LHC BLM Ionization Chamber,” in *Proceedings of the 8th European Workshop on Beam Diagnostics and Instrumentation for Particle Accelerators, Venice, Italy*, (Geneva), pp. 328–330, May 2007.

[24] CERN Courier, September 2007 Volume 47 Issue 7: `http://cerncourier.com/cws/article/cern/31175` Accessed: 2014-11-16.

[25] E. Gschwendtner, B. Dehning, G. Ferioli, W. Friesenbichler, and V. Kain, “The Beam Loss Detection System of the LHC Ring,” in *Proceedings of the 8th European Particle Accelerator Conference, Paris, France*, pp. 1894–1896, June 2002.

[26] E. Holzer, D. Bocian, T. Böhlen, B. Dehning, D. Kramer, L. Ponce, A. Priebe, M. Sapinski, and M. Stockner, “Generation of 1.5 Million Beam Loss Threshold Values,” in *Proceedings of the 11th European Particle Accelerator Conference, Genoa, Italy*, pp. 3333–3335, June 2008.

[27] O. Brüning, P. Collier, P. Lebrun, S. Myers, R. Ostojic, J. Poole, and P. Proudlock, *LHC Design Report - Volume 1, Chapter 18: Beam Cleaning and Collimation System.* Geneva: CERN, 2004.

[28] R. W. Assmann, J. Jeanneret, and D. Kaltchev, “Efficiency for the imperfect LHC collimation system,” in *Proceedings of the 8th European Particle Accelerator Conference, Paris, France*, pp. 293–296, Jul 2002.

[29] C. Bracco, *Commissioning Scenarios and Tests for the LHC Collimation System.* PhD thesis, Ecole Polytechnique, Lausanne, 2009. CERN-THESIS-2009-031.

[30] R. W. Assmann, “Operational Experience with LHC Collimation,” in *Proceedings of the 23rd Particle Accelerator Conference 2009, Vancouver, Canada*, pp. 789–793, May 2009.

[31] G. Robert-Démolaize, *Design and Performance Optimization of the LHC Collimation System.* PhD thesis, CERN, Geneva, 2006. CERN-THESIS-2006-069.

[32] Project for the LHC Collimation System - Official Website: `http://lhc-collimation-project.web.cern.ch/lhc-collimation-project/` Accessed: 2014-08-28.

[33] R. W. Assmann, “Collimation for the LHC High Intensity Beams,” in *Proceedings of the 46th ICFA Advanced Beam Dynamics Workshop on High-Intensity and High-Brightness Hadron Beams, Morschach, Switzerland*, vol. MOIB03, pp. 21–33, September 2010.

[34] D. Wollmann *et al.*, “First cleaning with LHC collimators,” in *Proceedings of the 1st International Particle Accelerator Conference, Kyoto, Japan*, pp. 1237–1239, May 2010.

[35] B. Salvachua, A. R. W., R. Bruce, M. Cauchi, D. Deboy, L. Lari, A. Marsili, D. Mirarchi, E. Quaranta, S. Redaelli, A. Rossi, and G. Valentino, “LHC Collimation Cleaning and Operation Outlook,” in *Proceedings of the 2012 Evian Workshop on LHC Beam Operation*, pp. 155–160, December 2012.

[36] B. Salvachua, R. W. Assmann, R. Bruce, D. Deboy, A. Marsili, E. Quaranta, S. Redaelli, A. Rossi, D. Mirarchi, G. Valentino, M. Cauchi, and L. Lari, “Cleaning Performance of the LHC Collimation System up to 4 Tev,” in *Proceedings of the 4th International Particle Accelerator Conference, Shanghai, China*, pp. 1002–1004, May 2013.

[37] V. Moens, R. Bruce, S. Redaelli, B. Salvachua, and G. Valentino, “Comparison of LHC Beam Loss Maps Using the Transverse Damper Blow Up and Tune Resonance Crossing Methods,” in *Proceedings of the 4th International Particle Accelerator Conference, Shanghai, China*, pp. 1008–1010, May 2013.

[38] R. Bruce, R. W. Assmann, V. Boccone, G. Bregliozzi, H. Burkhardt, F. Cerutti, A. Ferrari, M. Huhtinen, A. Lechner, Y. Levinsen, A. Mereghetti, N. Mokhov, I. Tropin, and V. Vlachoudis, “Sources of machine-induced background in the ATLAS and CMS detectors at the CERN Large Hadron Collider,” *Nuclear Instruments and Methods in Physics Research Section A: Accelerators, Spectrometers, Detectors and Associated Equipment*, vol. 729, pp. 825 – 840, 2013.

[39] R. W. Assmann, I. Baishev, M. Brugger, L. Bruno, H. Burkhardt, G. Burtin, B. Dehning, C. Fischer, B. Goddard, E. Gschwendtner, *et al.*, “Requirements for the LHC collimation system,” in *Proceedings of the 8th European Particle Accelerator Conference, Paris, France*, pp. 197–199, 2002.

[40] R. W. Assmann, O. Aberle, A. Bertarelli, H. Braun, M. Brugger, O. Brüning, L. Bruno, S. Calatroni, E. Chiaveri, B. Dehning, *et al.*, “An improved collimation system for the LHC,” in *Proceedings of the 9th European Particle Accelerator Conference, Lucerne, Switzerland*, pp. 536–538, July 2004.

[41] S. Redaelli, R. W. Assmann, A. Masi, and R. Losito, "Final Implementation and Performance of the LHC Collimator Control System," in *Proceedings of the Particle Accelerator Conference 2009, Vancouver, Canada*, pp. 4788–4790, May 2009.

[42] R. W. Assmann, G. Bellodi, J. Jowett, E. Metral, T. Weiler, T. Markiewicz, and L. Keller, "Accelerator Physics Concept for Upgraded LHC Collimation Performance ," in *Proceedings of the 23rd Particle Accelerator Conference 2009, Vancouver, Canada*, pp. 3202–3204, May 2009.

[43] N. Tahir, V. Fortov, B. Goddard, D. Hoffmann, V. Kain, I. Lomonosov, A. Piriz, R. Schmidt, A. Shutov, and M. Temporal, "Impact of 7-TeV/c Large Hadron Collider proton beam on a copper target," *Journal of Applied Physics*, vol. 97, no. 8, pp. 83532–1–8, 2005.

[44] P. Sievers, "Elastic stress waves in matter due to rapid heating by an intense high-energy particle beam," Jun 1974. Technical Report: CERN-Lab-2-BT-74-2.

[45] B. Goddard, R. W. Assmann, E. Carlier, J. Uythoven, J. Wenninger, and W. Weterings, "Protection of the LHC against Unsynchronised Beam Aborts," in *Proceedings of the 10th European Particle Accelerator Conference, Edinburgh, UK*, pp. 1514–1516, June 2006.

[46] R. W. Assmann, B. Goddard, E. B. Vossenberg, and E. Weisse, "The consequences of abnormal beam dump actions on the LHC collimation system," May 2002. Technical Report: LHC-PROJECT-NOTE-293.

[47] A. Bertarelli, V. Boccone, F. Carra, F. Cerutti, A. Dallocchio, N. Mariani, L. Peroni, and M. Scapin, "Limits for Beam Induced Damage: Reckless or too Cautious?," in *Proceedings of Chamonix 2011 Workshop on LHC Performance, Chamonix, France*, (Geneva), pp. 183–188, 2011.

[48] R. Bruce, R. W. Assmann, F. Burkart, M. Cauchi, D. Deboy, L. Lari, S. Redaelli, A. Rossi, B. Salvachua, G. Valentino, and D. Wollmann, "Collimation settings and

performance in 2011 and 2012," in *Proceedings of Chamonix 2012 Workshop on LHC Performance, Chamonix, France*, pp. 183–188, 2012.

[49] L. Lari, R. W. Assmann, M. Cauchi, A. Rossi, and A. Faus-Golfe, "Improved robustness of the LHC collimation system by operating with a jaw-beam angle," in *Proceedings of the 3rd International Particle Accelerator Conference, New Orleans, LA, USA*, vol. C1205201, pp. 553–555, May 2012.

[50] A. Bertarelli and R. Perret, "LHC collimator design," in *Proceedings of 1st LHC Project Workshop, Chamonix, France*, pp. 112–117, 2004.

[51] A. Bertarelli, O. Aberle, R. W. Assmann, E. Chiaveri, T. Kurtyka, M. Mayer, R. Perret, and P. Sievers, "The Mechanical Design for the LHC Collimators," in *Proceedings of the 9th European Particle Accelerator Conference, Lucerne, Switzerland*, pp. 545–547, 2004.

[52] L. Lari, L. Rivkin, and V. Vlachoudis, *Beam-Machine Interaction Studies for the Phase II LHC Collimation System.* PhD thesis, Ecole Polytechnique, Lausanne, 2010.

[53] S. Redaelli, R. W. Assmann, P. Gander, M. Jonker, M. Lamont, R. Losito, A. Masi, and M. Sobczak, "The LHC Collimator Controls Architecture - Design and beam tests," in *Proceedings of the 22nd Particle Accelerator Conference, Albuquerque, NM, USA*, pp. 344–346, June 2007.

[54] A. Masi and R. Losito, "LHC Collimators Low Level Control System," *Nuclear Science, IEEE Transactions on*, vol. 55, pp. 333–340, Feb 2008.

[55] D. Deboy, R. W. Assmann, C. Baccigalupi, F. Burkart, M. Cauchi, C. Derrez, J. Lendaro, A. Masi, G. Spiezia, and D. Wollmann, "Acoustic measurements in the collimation region of the LHC," in *Proceedings of 2nd International Particle Accelerator Conference, San Sebastian, Spain*, pp. 3759–3761, September 2011.

[56] V. Baglin, G. Bregliozzi, J. Jimenez, and J. Kamiya, “Vacuum Performances of some LHC Collimators,” in *Proceedings of the 1st International Particle Accelerator Conference, Kyoto, Japan*, pp. 3867–3869, May 2010.

[57] J. Kamiya, V. Baglin, J. Jimenez, and G. Bregliozzi, “Outgassing measurement of an LHC collimator and estimation for the NEG performances,” *Vacuum*, vol. 85, no. 12, SI, pp. 1178–1181, 2011.

[58] G. Valentino, R. W. Assmann, R. Bruce, S. Redaelli, A. Rossi, N. Sammut, and D. Wollmann, “Semiautomatic beam-based lhc collimator alignment,” *Phys. Rev. ST Accel. Beams*, vol. 15, p. 051002, May 2012.

[59] Plansee GmbH, “DENSIMET® and INERMET® Tungsten Alloys.” `http://www.plansee.com/en/Materials-Tungsten-heavy-alloys-1577.htm` Accessed: 2014-11-09.

[60] S. Calatroni, R. Perret, and W. Vollenberg, “RF Contacts for the LHC Collimators,” *Nuclear Instruments and Methods in Physics Research Section A: Accelerators, Spectrometers, Detectors and Associated Equipment*, vol. 566, no. 2, pp. 205 – 211, 2006.

[61] H. Burkhardt, G. Arduini, R. W. Assmann, F. Caspers, M. Gasior, A. Grudiev, O. Rhodri-Jones, T. Kroyer, S. Redaelli, G. Robert-Démolaize, F. Roncarolo, D. Schulte, R. Steinhagen, J. Wenninger, and F. Zimmermann, “Measurements of the LHC Collimator Impedance with Beam in the SPS,” in *Proceedings of the 21st IEEE Particle Accelerator Conference, Knoxville, TN, USA*, pp. 1132–1134, July 2005.

[62] P. Sievers, “Appropriate Materials for LHC Collimators,” in *Proceedings of Chamonix XII Workshop on LHC Performance - Operating with Unprecedented Stored Beam Energy, Chamonix, France*, pp. 171–173, 2003.

[63] A. Ferrari, P. R. Sala, A. Fassò, and J. Ranft, *FLUKA: A multi-particle transport code (program version 2005).* Geneva: CERN, 2005.

[64] G. Battistoni, F. Cerutti, A. Fassò, A. Ferrari, S. Muraroi, J. Ranft, S. Roesler, and P. Sala, "The FLUKA code: Description and benchmarking," *AIP Conf. Proc.*, vol. 896, no. SLAC-REPRINT-2007-184, pp. 31–49. 19 p, 2007.

[65] A. Fassò, A. Ferrari, and P. Sala, "Electron-photon transport in FLUKA: status," in *Advanced Monte Carlo for Radiation Physics, Particle Transport Simulation and Applications*, pp. 159–164, Springer, 2001.

[66] S. Eidelman, K. Hayes, K. Olive, M. Aguilar-Benitez, C. Amsler, D. Asner, K. Babu, R. Barnett, J. Beringer, P. Burchat, *et al.*, "Review of particle physics," *Physics Letters B*, vol. 592, no. 1–4, pp. 1 – 5, 2004. Review of Particle Physics.

[67] A. Ferrari and P. Sala, "The Physics of High Energy Reactions," in *Proceedings of the Workshop on Nuclear Reaction Data and Nuclear Reactors Physics, Design and Safety, International Centre for Theoretical Physics, Miramare-Trieste, Italy, 15 April - 17 May 1996*, vol. 2, p. 424, 1998.

[68] "ANSYS® Mechanical, Academic Research, Release 12.1, Help System, Workbench User's Guide," 2009.

[69] A. Bertarelli, O. Aberle, R. W. Assmann, S. Calatroni, A. Dallocchio, T. Kurtyka, M. Mayer, R. Perret, S. Redaelli, and G. Robert-Demolaize, "Mechanical Design for Robustness of the LHC Collimators," in *Proceedings of the 21st IEEE Particle Accelerator Conference, Knoxville, TN, USA*, pp. 913–915, July 2005.

[70] A. Bertarelli, A. Dallocchio, and T. Kurtyka, "Dynamic Response of Rapidly Heated Cylindrical Rods: Longitudinal and Flexural Behavior," *Journal of Applied Mechanics*, vol. 75, no. 3, p. 13, 2008.

[71] A. Bertarelli, O. Aberle, R. W. Assmann, A. Dallocchio, T. Kurtyka, M. Magistris, M. Santana-Leitner, and M. Mayer, "Permanent Deformation of the LHC Collimator Jaws Induced by Shock Beam Impact: an Analytical and Numerical Interpretation," in *Proceedings of the 10th European Particle Accelerator Conference, Edinburgh, Scotland*, pp. 1801–1803, July 2006.

[72] A. Dallocchio, *Study of Thermo-Mechanical Effects Induced in Solids by High Energy Particle Beams: Analytical and Numerical Methods.* PhD thesis, Polytechnic University of Turin, Turin, 2008. CERN-THESIS-2008-140.

[73] N. Tahir, V. Fortov, I. Lomonosov, A. Shutov, R. Piriz, and R. Schmidt, "Simulations of the Full Impact of the LHC Beam on Solid Copper and Graphite Targets," in *Proceedings of the 1st International Particle Accelerator Conference, Kyoto, Japan*, pp. 1375–1377, May 2010.

[74] B. Gladman *et al.*, "LS-DYNA® Keyword User's Manual. Volume I. Version 971.," 2007.

[75] "ANSYS® Autodyn, Release 13.0, Help System, User Manual," 2010.

[76] L. Peroni, M. Scapin, and A. Dallocchio, "Thermo-mechanical modelling of metal structures subjected to high energy particle beam impacts," 2011. Technical Report: EuCARD-CON-2011-077.

[77] M. Scapin, L. Peroni, and A. Dallocchio, "Damage evaluation in metal structures subjected to high energy deposition due to particle beams," *Journal of Physics: Conference Series*, vol. 305, no. 012062, p. 10, 2011.

[78] L. Peroni, M. Scapin, A. Bertarelli, and A. Dallocchio, "Numerical simulations of tungsten targets hit by LHC proton beam," in *Proceedings of IV International Conference on Computational Methods for Coupled Problems in Science and Engineering, COUPLED PROBLEMS 2011, Kos, Greece*, June 2011.

[79] W. S. Lee, G. L. Xiea, and C. F. Lin, "The strain rate and temperature dependence of the dynamic impact response of tungsten composite," *Materials Science and Engineering: A*, vol. 257, no. 2, pp. 256 – 267, 1998.

[80] B. Muddle, "Interphase boundary precipitation in liquid phase sintered w-ni-fe and w-ni-cu alloys," *Metallurgical Transactions A*, vol. 15, no. 6, pp. 1089–1098, 1984.

[81] L. Hu, P. Miller, and J. Wang, “High strain-rate spallation and fracture of tungsten by laser-induced stress waves,” *Materials Science and Engineering: A*, vol. 504, no. 1–2, pp. 73 – 80, 2009.

[82] V. Lubarda, M. Schneider, D. Kalantar, B. Remington, and M. Meyers, “Void growth by dislocation emission,” *Acta Materialia*, vol. 52, no. 6, pp. 1397 – 1408, 2004.

[83] I. Rohr, H. Nahme, K. Thoma, and C. A. Jr., “Material characterisation and constitutive modelling of a tungsten-sintered alloy for a wide range of strain rates,” *International Journal of Impact Engineering*, vol. 35, no. 8, pp. 811 – 819, 2008.

[84] M. Pasalic, F. Rustempasic, S. Iyengar, S. Melin, and E. Noah, “Fatigue testing and microstructural characterization of tungsten heavy alloy densimet 185,” *International Journal of Refractory Metals and Hard Materials*, vol. 42, pp. 163 – 168, 2014.

[85] T. Weerasooriya and J. Clayton, “Failure behaviour of a tungsten heavy alloy at different strain rates under different tensile loading,” in *Proceedings of the 2006 International Conference on Tungsten, Refractory & Hardmetals VI, Metal Powder Industries Federation, Orlando, Florida*, February 2006.

[86] H. Tan, “Spallation and Fragmentation,” 2008. iMechanica, Web of Mechanics and Mechanicians: `http://imechanica.org/files/spall-I_0.pdf` Accessed: 2014-11-09.

[87] N. Tahir, V. Fortov, V. Gryaznov, D. H. Hoffmann, V. Kain, I. Lomonosov, A. Piriz, R. Schmidt, A. Shutov, and M. Temporal, “The CERN Large Hadron Collider as a tool to study high-energy density matter,” *Phys. Rev. Lett.*, vol. 94, no. 13, pp. 135004/1–4, 2005.

[88] N. Tahir, R. Schmidt, M. Brugger, A. Shutov, I. Lomonosov, A. Piriz, and D. Hoffmann, “Simulations of Full Impact of the LHC Beam With a Solid Graphite Target,” *Laser Part. Beams*, vol. 27, p. 475, 2009.

[89] N. Tahir, A. Shutov, J. Blanco Sancho, R. Schmidt, and A. Piriz, "LHC Beam Impact on Materials considering the Time Structure of the Beam," 2011. Technical Report: EuCARD-CON-2011-073.

[90] V. Fortov, B. Goel, C.-D. Munz, A. Ni, A. Shutov, and O. Y. Vorobiev, "Numerical simulations of nonstationary fronts and interfaces by the godunov method in moving grids," *Nuclear Science and Engineering*, vol. 123, no. 2, pp. 169–189, 1996.

[91] N. Tahir, J. Blanco Sancho, A. Shutov, R. Schmidt, and A. Piriz, "Impact of high energy high intensity proton beams on targets: Case studies for Super Proton Synchrotron and Large Hadron Collider," *Phys. Rev. Spec. Top. Accel. Beams*, vol. 15, p. 051003, 2012.

[92] N. Tahir, R. W. Assmann, M. Brugger, V. Fortov, D. Hoffmann, I. Lomonosov, A. Piriz, R. Schmidt, and A. Shutov, "Simulation Studies of Impact of SPS Beam with Collimator Materials," in *Proceedings of the 11th European Particle Accelerator Conference, Genoa, Italy*, pp. 2689–2691, June 2008.

[93] R. Schmidt, J. Blanco Sancho, F. Burkart, D. Grenier, D. Wollmann, N. A. Tahir, A. Shutov, and A. R. Piriz, "First experimental evidence of hydrodynamic tunneling of ultra-relativistic protons in extended solid copper target at the CERN HiRadMat facility," *Physics of Plasmas (1994-present)*, vol. 21, no. 8, pp. –, 2014.

[94] I. Efthymiopoulos, C. Hessler, H. Gaillard, D. Grenier, M. Meddahi, P. Trilhe, A. Pardons, C. Theis, N. Charitonidis, S. Evrard, H. Vincke, and M. Lazzaroni, "HiRadMat: A New Irradiation Facility for Material Testing at CERN," in *Proceedings of 2nd International Particle Accelerator Conference, San Sebastian, Spain*, vol. C110904, pp. 1665–1667, 2011.

[95] M. Scapin, L. Peroni, and A. Dallocchio, "Effects induced by LHC high energy beam in copper structures," *Journal of Nuclear Materials*, vol. 420, pp. 463–472, Jan. 2012.

[96] Scapin, M., Peroni, L., Dallocchio, A., and Bertarelli, A., “Shock loads induced on metal structures by LHC proton beams: modelling of the thermo-mechanical effects,” *Applied Mechanics and Materials*, vol. 82, pp. 338–343, 2011.

[97] M. Scapin, L. Peroni, and A. Dallocchio, “Thermo-mechanical modelling of high energy particle beam impacts,” in *Numerical Modeling of Materials Under Extreme Conditions* (N. Bonora and E. Brown, eds.), vol. 35 of *Advanced Structured Materials*, pp. 87–106, Springer Berlin Heidelberg, 2014.

[98] M. Scapin, L. Peroni, V. Boccone, and F. Cerutti, “A LS-DYNA/FLUKA coupling for the numerical simulation of high energy particle beam interaction with matter,” in *Proceedings of V International Conference on Computational Methods for Coupled Problems in Science and Engineering, COUPLED PROBLEMS 2013, Ibiza, Spain*, June 2013.

[99] M. Scapin, L. Peroni, V. Boccone, and F. Cerutti, “Effects of high-energy intense multi-bunches proton beam on materials,” *Comput. Struct.*, vol. 141, pp. 74–83, Aug. 2014.

[100] J. Bennett, C. Booth, R. Brownsword, C. Densham, R. Edgecock, and G. Škoro, “LS-DYNA calculations of shocks in solids,” *Nuclear Physics B - Proceedings Supplements*, vol. 155, no. 1, pp. 293 – 294, 2006.

[101] J. Bennett, G. Škoro, C. Booth, S. Brooks, R. Brownsword, T. Edgecock, C. Densham, S. Gray, A. McFarland, N. Simos, and D. Wilkins, “Thermal shock measurements and modelling for solid high-power targets at high temperatures,” *Journal of Nuclear Materials*, vol. 377, no. 1, pp. 285 – 289, 2008.

[102] N. Mokhov, “MARS Code System.” Fermi National Accelerator Laboratory: `http://www-ap.fnal.gov/MARS/` Accessed: 2014-12-05.

[103] A. Bertarelli, E. Berthome, V. Boccone, F. Carra, F. Cerutti, N. Charitonidis, C. Charrondiere, A. Dallocchio, P. Fernandez Carmona, P. Francon, *et al.*, “An experiment to test advanced materials impacted by intense proton pulses at CERN

HiRadMat facility," *Nuclear Instruments and Methods in Physics Research Section B: Beam Interactions with Materials and Atoms*, vol. 308, pp. 88–99, 2013.

[104] I. Leitao, "Development, Validation and Application of a Novel Method for Estimating the Thermal Conductance of Critical Interfaces in the Jaws of the LHC Collimation System," in *Proceedings of the 4th International Particle Accelerator Conference, Shanghai, China*, vol. C130512, pp. 3430–3432, May 2013.

[105] B. Snaith, S. Probert, and P. O'Callaghan, "Thermal resistances of pressed contacts," *Applied Energy*, vol. 22, no. 1, pp. 31 – 84, 1986.

[106] F. Carra, "Screwed solutions for the new tertiary collimator jaw assembly," September 2014. Presentation during the BUFAB visit to CERN: `https://indico.cern.ch/event/338824/contribution/1/material/slides/3.pdf` Accessed: 2014-12-10.

[107] F. P. Incropera, D. P. Dewitt, T. L. Bergman, and A. S. Lavine, *Introduction to Heat Transfer*. No. ISBN 978-0-471-45727-5, John Wiley & Sons, Inc., 5th ed., 2007.

[108] P. P. Benham, R. J. Crawford, and C. G. Armstrong, *Mechanics of Engineering Materials*. No. ISBN 0-582-25164-8, Pearson Education Limited, 2nd ed., 1996.

[109] ANSYS, Inc., "ANSYS Mechanical Structural Nonlinearities," December 2010. Lecture 5 - Rate Independent Plasticity: `http://inside.mines.edu/~apetrell/ENME442/Labs/1301_ENME442_lab7.pdf` Accessed: 2014-12-14.

[110] W. Kalbreier, W. Middelkoop, and P. Sievers, "External targets at the SPS," Feb 1974. Technical Report: CERN-Lab-2-BT-74-1.

[111] R. Courant, K. Friedrichs, and H. Lewy, "On the partial difference equations of mathematical physics," *IBM Journal of Research and Development*, vol. 11, pp. 215–234, March 1967.

[112] O. Brüning, P. Collier, P. Lebrun, S. Myers, R. Ostojic, J. Poole, and P. Proudlock, *LHC Design Report - Volume 1, Chapter 17: Beam Dumping System*. Geneva: CERN, 2004.

[113] W. Weterings, T. Antonakakis, B. Balhan, J. Borburgh, B. Goddard, C. Maglioni, and R. Versaci, “Upgrade of the LHC Beam Dumping Protection Elements,” in *Proceedings of the 3rd International Particle Accelerator Conference, New Orleans, Louisiana, USA*, vol. C1205201, pp. 556–558, July 2012.

[114] M. Cauchi, O. Aberle, R. W. Assmann, A. Bertarelli, F. Carra, K. Cornelis, A. Dallocchio, D. Deboy, L. Lari, S. Redaelli, A. Rossi, B. Salvachua, P. Mollicone, and N. Sammut, “High energy beam impact tests on a LHC tertiary collimator at the CERN high-radiation to materials facility,” *Phys. Rev. ST Accel. Beams*, vol. 17, p. 021004, Feb 2014.

[115] Plansee GmbH, “Tungsten - Material Properties and Applications.” `http://www.plansee.com/en/Materials-Tungsten-403.htm` Accessed: 2014-11-09.

[116] Erik Lassner and Wolf-Dieter Schubert, *Tungsten - Properties, Chemistry, Technology of the Element, Alloys, and Chemical Compounds.* No. ISBN 978-1-4615-4907-9, Kluwer Academic / Plenum Publishers, New York, XXI ed., 1999.

[117] J. Das, G. A. Rao, and S. Pabi, “Microstructure and mechanical properties of tungsten heavy alloys,” *Materials Science and Engineering: A*, vol. 527, no. 29 - 30, pp. 7841 – 7847, 2010.

[118] P. Lorenzo, M. Miralda, S. Iyengar, S. Melin, and E. Noah, “Fatigue properties and characterization of tungsten heavy alloys IT180 & D176,” *International Journal of Refractory Metals and Hard Materials*, vol. 41, pp. 250 – 258, 2013.

[119] W. Hohenauer, “Thermophysical Characterisation Methods and Uncertainty Considerations,” 2015. Technical Report: Theoretical part of accredited AIT reporting of thermophysical measurements.

[120] Working Group 1 of the Joint Committee for Guides in Metrology (JCGM/WG 1), “Evaluation of measurement data - Guide to the expression of uncertainty in measurement,” 1999. Standard DIN V ENV 13005:1999.

[121] NETZSCH-Gerätebau GmbH, "Dilatometry - Method, Instruments, Applications - from -180^{o}C to 2800^{o}C," January 2014. `http://www.netzsch-thermal-analysis.com/en/products-solutions/dilatometer/dil-402-c.html` Accessed: 2015-01-07.

[122] NETZSCH-Gerätebau GmbH, "Differential Scanning Calorimetry - Method, Technique, Applications," June 2013. `http://www.netzsch-thermal-analysis.com/en/products-solutions/differential-scanning-calorimetry/dsc-404-f1-pegasus.html` Accessed: 2015-01-07.

[123] NETZSCH-Gerätebau GmbH, "Laser Flash Analysis (LFA) - Method, Technique, Applications," September 2013. `http://www.netzsch-thermal-analysis.com/en/products-solutions/thermal-diffusivity-conductivity/lfa-427.html?utm_source=offline&utm_medium=print&utm_content=lfa427&utm_campaign=brochure-lfa427` Accessed: 2015-01-07.

[124] Peroni, L., Scapin, M., and Peroni, M., "Identification of strain-rate and thermal sensitive material model with an inverse method," *EPJ Web of Conferences*, vol. 6, p. 39004, 2010.

[125] Vikas Prakasch, "Compression-and-shear deformation of amorphous polycarbonate," March 2012. Society of Plastics Engineers: `http://www.4spepro.org/pdf/004085/004085.pdf` Accessed: 2015-01-09.

[126] J. William D. Callister, *Materials Science and Engineering, An Introduction.* No. ISBN 0-471-73696-1, John Wiley & Sons, Inc., 7th ed., 2007.

[127] P. Skoglund, "Constitutive modelling and mechanical properties of a tungsten heavy metal alloy," November 2002. Tehnical Report: FOI-R–0723–SE, ISSN 1650-1942.

[128] Johnson, G. R. and Cook, W. H., "A constitutive model and data for metals subjected to large strains, high strain rates and high temperatures," in *Proceedings of the 7th International Symposium on Ballistics, The Hague, The Netherlands*, pp. 541–547, 1983.

[129] Zerilli, Frank J. and Armstrong, Ronald W., "Dislocation-mechanics-based constitutive relations for material dynamics calculations," *Journal of Applied Physics*, vol. 61, no. 5, pp. 1816–1825, 1987.

[130] D. Samantaray, S. Mandal, U. Borah, A. Bhaduri, and P. Sivaprasad, "A thermo-viscoplastic constitutive model to predict elevated-temperature flow behaviour in a titanium-modified austenitic stainless steel," *Materials Science and Engineering: A*, vol. 526, no. 1–2, pp. 1 – 6, 2009.

[131] A. Fabich and C. Hessler, "HiRadMat Beam Parameters," September 2010. Technical Report: HiRadMat Project - 2010-02.

[132] D. Deboy, O. Aberle, R. W. Assmann, F. Carra, M. Cauchi, L. J., A. Masi, and R. S., "Remote Estimation of Collimator Jaw Damages with Sound Measurements during Beam Impacts," in *Proceedings of the 4th International Particle Accelerator Conference, Shanghai, China*, no. CERN-ACC-2013-0061, pp. 951–953, May 2013.

[133] F. Carra, A. Bertarelli, A. Dallocchio, L. Lari, and M. Mariani, "Expected Damage on TCTA Collimator during HRMT09-LCOL Experiment in HiRadMat Facility," July 2012. Presentation in the Collimation Working Group at CERN: `https://indico.cern.ch/event/201418/contribution/2/material/slides/1.pdf` Accessed: 2015-01-12.

[134] A. Bertarelli, R. Bruce, F. Carra, A. Dallocchio, M. Guinchard, M. Mariani, L. Lari, S. Redaelli, and A. Rossi, "Updated Damage Limits for Collimator Materials," in *Proceedings of the 2013 MPP Workshop on LHC Machine Protection* (M. Jonker, ed.), (Geneva), pp. 108–112, April 2014.

[135] O. Brüning, P. Collier, P. Lebrun, S. Myers, R. Ostojic, J. Poole, and P. Proudlock, *LHC Design Report - Volume 1, Chapter 21: The LHC as a Lead Ion Collider*. Geneva: CERN, 2004.

[136] D. Manglunki, M. Angoletta, P. Baudrenghien, G. Bellodi, A. Blas, T. Bohl, C. Carli, E. Carlier, S. Cettour-Cave, M. Chanel, K. Cornelis, H. Damerau, A. Findlay,

S. Gilardoni, S. Hancock, J. Jowett, D. Küchler, S. Maury, E. Métral, S. Pasinelli, M. Schokker, G. Tranquille, B. Vandorpe, J. Wenninger, and U. Wehrle, “Ions for LHC: performance of the injector chain,” in *Proceedings of 2nd International Particle Accelerator Conference, San Sebastian, Spain*, pp. 2529–2531, September 2011.

[137] D. Manglunki, M. Angoletta, H. Bartosik, G. Bellodi, A. Blas, T. Bohl, C. Carli, E. Carlier, S. Cettour-Cave, K. Cornelis, H. Damerau, I. Efthymiopoulos, A. Findlay, S. Gilardoni, S. Hancock, J. Jowett, D. Küchler, S. Maury, M. O’Neil, Y. Papaphilippou, S. Pasinelli, R. Scrivens, G. Tranquille, B. Vandorpe, U. Wehrle, and J. Wenninger, “Performance of the CERN heavy ion production complex,” in *Proceedings of 3rd International Particle Accelerator Conference, New Orleans, LA, USA*, vol. C1205201, pp. 3752–3754, May 2012.

[138] D. Manglunki, M. Angoletta, H. Bartosik, G. Bellodi, A. Blas, M. Bodendorfer, T. Bohl, C. Carli, E. Carlier, S. Cettour-Cave, K. Cornelis, H. Damerau, A. Findlay, S. Gilardoni, S. Hancock, J. Jowett, D. Küchler, M. O’Neil, Y. Papaphilippou, S. Pasinelli, R. Scrivens, G. Tranquille, B. Vandorpe, U. Wehrle, and J. Wenninger, “The first LHC p-Pb run: performance of the heavy ion production complex,” in *Proceedings of 4th International Particle Accelerator Conference, Shanghai, China*, pp. 2648–2650, May 2013.

[139] R. M. Barnett *et al.*, “Review of particle physics. Particle Data Group,” *Phys.Rev.*, vol. D54, pp. 1–720, 1996.

[140] L. Lari, R. W. Assmann, V. Boccone, R. Bruce, F. Cerutti, A. Rossi, V. Vlachoudis, A. Mereghetti, and A. Faus-Golfe, “Accelerator physics studies on the effects from an asynchronous beam dump onto the LHC experimental region collimators,” in *Proceedings of 3rd International Particle Accelerator Conference, New Orleans, Louisiana, USA*, vol. C1205201, pp. 547–549, May 2012.

[141] L. Lari, R. Bruce, and S. Redaelli, “Collimator Fast Failure Losses for Various HL-LHC Configurations,” in *Proceedings of 5th International Particle Accelerator Conference, Dresden, Germany*, pp. 157–159, June 2014.